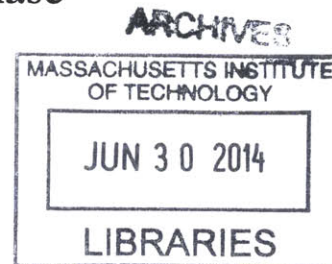


Microreactor Technology: Scale-up of Multiphase Continuous Flow Chemistries

by

María José Nieves Remacha

B.S. Chemical Engineering, Universidad Complutense de Madrid, 2008
M.S. Chemical Engineering Practice, Massachusetts Institute of Technology, 2009



SUBMITTED TO THE DEPARTMENT OF CHEMICAL ENGINEERING IN PARTIAL FULFILLMENT OF THE REQUIREMENTS FOR THE DEGREE OF

DOCTOR OF PHYLOSOPHY IN CHEMICAL ENGINEERING AT THE MASSACHUSETTS INSTITUTE OF TECHNOLOGY

JUNE 2014

© 2014 Massachusetts Institute of Technology. All rights reserved.

Signature redacted

Author

.....
María José Nieves Remacha
Department of Chemical Engineering
June 2014

Signature redacted

Certified by .

.....
Klavs F. Jensen
Warren K. Lewis Professor of Chemical Engineering
Professor of Materials Science and Engineering
Thesis Supervisor

Signature redacted

Accepted by

.....
Patrick S. Doyle
Professor of Chemical Engineering
Chairman, Committee for Graduate Students

Microreactor Technology: Scale-up of Multiphase Continuous Flow Chemistries

by

María José Nieves Remacha

Submitted to the Department of Chemical Engineering on May 16, 2014
in partial fulfillment of the requirements for the degree of
Doctor of Philosophy in Chemical Engineering

Abstract

Microreactors have been demonstrated to provide many advantages over conventional process technologies for the synthesis of chemical compounds and kinetic studies at the laboratory scale. High heat and mass transfer rates, rapid mixing, and higher selectivities and conversions can be achieved in these microdevices thanks to the small characteristic dimensions, enabling the synthesis of compounds that cannot be synthesized in conventional reactors. In the past years, efforts have been directed towards the application of microreactor technology for production purposes, especially in the pharmaceutical and fine chemicals industry. The challenge is how to get benefit of the transport rates inherent to microreactors while increasing the throughput for production applications. Two approaches to increase production rate are possible: a) *scale-out* by parallelization of units; b) *scale-up* by increase in channel size and flow rates. Scale-out would require thousands of units to achieve kg/min of production rates and development of very expensive and complex control systems to ensure identical operating conditions in each unit for a perfect and predictable overall reactor performance. On the other hand, scale-up by increase in channel size risks losing mass and heat transfer performance. The Advanced-Flow Reactor (AFR) manufactured by Corning Inc. combines both approaches being able to yield production rates of 10 – 300 g/min per module. If the AFR is demonstrated to perform efficiently and to be easily scalable, it may become an alternative for process intensification and transition from batch to continuous in the pharmaceutical and fine chemicals industry. Additional advantages include shorter process development times thanks to the scalability of the reactor modules, higher selectivities and yields, greener production processes, and possibility of introducing new chemistries. In this context, fundamental understanding of the hydrodynamics for multiphase systems is essential and critical for process development and scale-up purposes. The objective of this thesis is to study both experimentally and through computational fluid dynamic simulations the hydrodynamic characteristics of the AFR to demonstrate the capabilities of this technology using non-reactive (hexane/water) and reactive systems (carbon dioxide/water, ozone/alkene) at ambient conditions.

Thesis Supervisor: Klavs F. Jensen
Title: Department Head, Chemical Engineering
Warren K. Lewis Professor of Chemical Engineering
Professor of Materials Science and Engineering

Acknowledgements

My PhD experience has been a long journey since I came to Boston in August 2008. During this time I have met a lot of friends, some of which have left, some of which are still here. This is now the time to leave for me and I would like to thank many people who have contributed to my life experience here in the east coast.

First, I would like to thank my advisor professor Klavs F. Jensen for his support, patience, and guidance throughout my entire PhD and for providing me a lot of freedom to pursue my research ambitions. I also thank my thesis committee members, professors William M. Deen, Alan T. Hatton, and Timothy Jamison, for the helpful discussions provided during our meetings. Special thanks to Patrick Heider, who helped me get started in the lab, Simon Kühn, Yanxiang, and Lu for their helpful discussions and insights regarding CFD simulations, as well as the members of the Jensen lab for their kindness and discussions during group meetings. Special thanks also to the Novartis Center for Continuous Manufacturing members and Berthold S., Markus K., for providing helpful insights and a different perspective to our research problems.

I would like to acknowledge Corning Inc. for the Advanced-Flow Reactor for this research, Dr. Jim Bales from the Edgerton Center at MIT for the high speed Phantom camera, Novartis-MIT Center for Continuous Manufacturing for financial support, and Fundacion Cajamadrid for the Fellowship (2008-2010) to pursue Postgraduate studies.

I would like to thank José for his unconditional support, my friends for the wonderful moments we have shared: Jorge A., Yajaira G., Ana, my ChemE friends Jen, Tanya, Yuko, Kristin, and Vasiliki; the Windsor family: Daniel S., Jorge C., Maite B., Carlos P., baby Carlos, Cecilia R., Ada Y., Mariana R., María de S., María Pont, and Bruno A.; the Spain@MIT family, in special Roberto S., Rubén G., David J., Maite P., Noel S., Javi H., Isa, Bernat S., Patricia G., Helena, Rafael M., Enrique L., Paula S., Ana D., María P., José María, Mar, and all the members of our community for supporting our events. I also would like to thank my friends in my home country who are and will always be there: Belén, Sara, Lorena, Ana M., Sandra, y Paco.

And last, but not least, my family in Spain: to my parents, who have always been supportive and are always there despite of the long distance and time difference. To my brother Javier and his wife Ruth because, together with my parents, help me grow in all aspects of my life. To my cousins, uncles, and aunts, who I have shared beautiful moments with while living in Spain, and to the memory of my grandparents who I always will keep in my heart.

Table of Contents

Abstract	3
Acknowledgements	4
List of Figures	11
List of Tables	22
1 Introduction, motivation, and objectives	25
1.1 Microreactor technology	25
1.2 Multiphase flow in microreactors	28
1.2.1 Gas-liquid	28
1.2.2 Liquid-liquid.....	30
1.3 Challenges in scale-up and scale-out	31
1.4 Chemistry applications of microreactor technology	36
1.5 Scope of this work	38
1.6 Specific objectives	39
1.7 Thesis outline.....	39
1.8 References	41
2 Experimental study of gas – liquid hydrodynamics in the Advanced-Flow Reactor..	44
2.1 Abstract	44
2.2 Introduction	44
2.3 Experimental.....	46
2.4 Results and discussion	49
2.4.1 Flow regimes	49

2.4.2	Vertical orientation.....	52
2.4.2.1	Bubble size distribution.....	52
2.4.2.2	Gas holdup.....	54
2.4.2.3	Specific interfacial area.....	55
2.4.2.4	Properties of dispersion along the flow path.....	56
2.4.2.5	Mass transfer coefficients	58
2.4.3	Horizontal orientation.....	63
2.4.3.1	Bubble size distribution.....	63
2.4.3.2	Gas holdup.....	65
2.4.3.3	Specific interfacial area.....	66
2.4.3.4	Properties of dispersion along the flow path.....	66
2.4.3.5	Mass transfer coefficients	68
2.4.4	Pressure drop.....	68
2.4.5	Comparison of AFR with other gas-liquid reactors.....	74
2.5	Conclusions.....	78
2.6	Notation	78
2.7	References	80
3	Experimental study of liquid – liquid hydrodynamics in Advanced-Flow Reactor...	83
3.1	Abstract	83
3.2	Introduction.....	83
3.3	Experimental.....	85
3.4	Results and discussion.....	87
3.4.1	Flow regimes.....	87
3.4.2	Drop size distribution.....	90

3.4.3	Drop size variation along flow path	95
3.4.4	Hexane hold-up	95
3.4.5	Specific interfacial area	100
3.4.6	Mass transfer coefficients.....	101
3.4.7	Pressure drop	104
3.4.8	Comparison of AFR with other liquid-liquid contactors	106
3.5	Conclusions.....	110
3.6	Notation	110
3.7	References	113

4	Experimental determination of residence time distribution in the Advanced-Flow Reactor.....	117
4.1	Abstract	117
4.2	Introduction	117
4.2.1	Tanks in series model	119
4.2.2	Dispersion model	120
4.2.3	Two-zone model	120
4.3	Experimental.....	121
4.3.1	Analysis of experimental data.....	123
4.4	Results and discussion	124
4.4.1	Experimental data	124
4.4.2	Models.....	126
4.4.2.1	Tanks in series model	126
4.4.2.2	Dispersion model.....	128
4.4.2.3	Two-zone model	130

4.4.3	Comparison among models.....	135
4.5	Conclusions.....	136
4.6	Notation.....	136
4.7	References.....	138
5	Computational fluid dynamic simulations: single-phase flow.....	139
5.1	Abstract.....	139
5.2	Introduction.....	139
5.2.1	Basic physical equations.....	140
5.2.2	Numerical approach.....	142
5.2.3	Mesh.....	144
5.2.4	Boundary conditions.....	145
5.2.5	Analysis of results.....	146
5.3	Results and discussion.....	148
5.3.1	Velocity fields, streamlines, and swirling strength.....	148
5.3.2	Pressure fields.....	154
5.3.3	Residence time distribution.....	158
5.3.4	Effect of reactor design.....	163
5.4	Conclusions.....	172
5.5	Notation.....	172
5.6	References.....	174
6	Computational fluid dynamic simulations: two-phase flow.....	177
6.1	Abstract.....	177

6.2	Introduction	177
6.3	Modeling two-phase flow using OpenFOAM.....	179
6.3.1	interFoam solver validation	183
6.3.1.1	Static bubble	186
6.3.1.2	Rising bubble	192
6.3.1.3	Microchannels and T-junctions	195
6.3.2	Application to the Advanced-Flow Reactor.....	213
6.4	Conclusions.....	217
6.5	Notation	218
6.6	References	221
7	Computational fluid dynamic simulations: modeling mass transfer between immiscible phases in the Advanced-Flow Reactor	226
7.1	Abstract	226
7.2	Introduction	226
7.3	Implementation of solver.....	228
7.4	Solver validation.....	232
7.5	Application to the Advanced-Flow Reactor	241
7.5.1	Effect of fluid properties	251
7.5.1.1	Effect of viscosity	251
7.5.1.2	Effect of surface tension.....	254
7.5.1.3	Effect of contact angle.....	256
7.5.2	Effect of reactor design.....	258
7.6	Conclusions.....	260
7.7	Notation	261
7.8	References	262

8	Ozonolysis	264
8.1	Abstract	264
8.2	Introduction	264
8.3	Experimental.....	269
8.3.1	Materials.....	269
8.3.2	Experimental setup	269
8.4	Results and discussion	272
8.5	Conclusions.....	278
8.6	Notation	279
8.7	References	279
9	Summary, conclusions, and future research direction.....	281
9.1	Summary and conclusions	281
9.2	Future research direction	282

List of Figures

Chapter 1

Figure 1.1	Multistep continuous-flow microchemical synthesis involving multiple reactions and separations.....	26
Figure 1.2	Diagram of the experimental setup for multistep synthesis of amides from alcohols and amines: packed bed microreactor, gas-liquid membrane separator, spiral-channel microreactor.....	26
Figure 1.3	Example of multistep microfluidic polymerization reactions in droplets.....	26
Figure 1.4	Passive mixing techniques applied in microfluidic systems.....	27
Figure 1.5	Flow regime diagram for gas-liquid flow.....	29
Figure 1.6	Representative photographs of flow patterns for gas-liquid flow in a microchannel of 1.09 mm hydraulic diameter and semi-triangular test section.....	30
Figure 1.7	Regime diagram for liquid-liquid flows in microfabricated systems.....	31
Figure 1.8	Different scale-up approaches using microreactor technology concepts.....	33
Figure 1.9	Corning Generation 1 fluidic modules.....	34
Figure 1.10	Generations of Corning Advanced-Flow Reactors.....	35
Figure 1.11	Corning Advanced-Flow Reactors throughput for Gen 1, Gen 2, Gen 3, and Gen 4 module designs.....	35

Chapter 2

Figure 2.1	Schematic of experimental set-up for gas-liquid flow visualization experiments.....	47
Figure 2.2	Details of the structure of the Advanced-Flow Reactor Gen 1.....	47
Figure 2.3	Gas-liquid flow in the AFR for vertical orientation at $Q_L = 80$ mL/min and $Q_G = 106$ mL/min.....	51
Figure 2.4	Variation in average bubble size with inlet gas flow rate in vertical orientation for different water flow rates.....	53

Figure 2.5	Variation in gas holdup with flow rate ratio in vertical orientation for different water flow rates.....	54
Figure 2.6	Variation in specific interfacial area with flow rate ratio in vertical orientation at different water flow rates.....	55
Figure 2.7	Variation in a) bubble number and b) bubble size along reactor length in vertical orientation for different gas and liquid flow rates	57
Figure 2.8	Variation in slip velocity with bubble size in vertical orientation for different water flow rates.....	59
Figure 2.9	Variation in a) individual and b) overall mass transfer coefficients with gas flow rate in vertical orientation for different water flow rates.....	60
Figure 2.10	Overall mass transfer coefficients for different water and gas flow rates in vertical orientation using different methods.....	62
Figure 2.11	Variation in average bubble diameter with flow rate ratio in horizontal orientation for different water flow rates.....	64
Figure 2.12	Variation in gas holdup with flow rate ratio in horizontal orientation for different water flow rates.....	65
Figure 2.13	Variation in specific interfacial area with inlet flow rate ratio in horizontal orientation for different water flow rates.....	66
Figure 2.14	Flow patterns in horizontal orientation for different water and gas flow rates	67
Figure 2.15	Variation in a) individual and b) overall mass transfer coefficients with gas flow rate in horizontal orientation for different water flow rates	69
Figure 2.16	Variation in pressure drop with a) superficial gas velocity and b) gas holdup in vertical orientation for different water flow rates	71
Figure 2.17	Comparison of experimental and predicted pressure drop in vertical orientation.....	73
Figure 2.18	Variation in power consumption with flow rate ratio in vertical orientation for different water flow rates	74
Figure 2.19	Comparison of overall mass transfer coefficients in function of power consumption among different gas-liquid contactors.....	75

Figure 2.20	Experimental versus predicted overall mass transfer coefficients for all gas and liquid flow rates. Dashed lines indicate relative error of 15%.....	77
-------------	--	----

Chapter 3

Figure 3.1	Schematic of experimental set-up for liquid-liquid flow visualization experiments.....	86
Figure 3.2	Flow patterns of hexane/water in the Advanced-Flow Reactor.....	91
Figure 3.3	Effect of flow rate on droplet formation regime.....	91
Figure 3.4	Effect of flow rate on drop size and number of drops.....	93
Figure 3.5	Drop size versus capillary number.....	94
Figure 3.6	Relationship between mean droplet size and flow regimes in the Advanced-Flow Reactor.....	94
Figure 3.7	Average drop size variation with position in the Advanced-Flow Reactor.....	96
Figure 3.8	Ratio of average drop size in row/Sauter diameter in row versus row in AFR.....	97
Figure 3.9	Hexane hold-up variation with flow rate ratio.....	98
Figure 3.10	Hexane hold-up variation with capillary number.....	99
Figure 3.11	Hexane hold-up variation with water Weber number.....	100
Figure 3.12	Specific interfacial area variation with capillary number.....	101
Figure 3.13	Overall mass transfer coefficient variation with flow rate ratio.....	103
Figure 3.14	Overall mass transfer coefficient variation with residence time.....	103
Figure 3.15	Pressure drop variation with Reynolds number.....	104
Figure 3.16	Experimental and predicted two-phase pressure drop.....	105
Figure 3.17	Relative error in prediction of pressure drop.....	105
Figure 3.18	Drop size versus power consumption for different liquid-liquid contactors.....	107
Figure 3.19	Specific interfacial area versus power consumption for different liquid-liquid contactors.....	108

Figure 3.20	Overall mass transfer coefficient versus power consumption for different liquid – liquid contactors	109
Chapter 4		
Figure 4.1	Schematic of two-zone RTD model.....	121
Figure 4.2	Experimental set-up for RTD measurements	122
Figure 4.3	Experimental residence time distribution $E(\theta)$ versus θ for different water flow rates	125
Figure 4.4	Predicted RTD by tanks in series model at different flow rates.....	127
Figure 4.5	Peclet number versus liquid flow rate for dispersion model.....	129
Figure 4.6	Comparison of tanks in series model with dispersion model for different water flow rates	130
Figure 4.7	Effect of static holdup on dimensionless variance.....	131
Figure 4.8	Effect of flow path length on a) dimensionless variance, and b) mean residence time for different water flow rates.....	131
Figure 4.9	$E(t)$ predicted by two-zone model for different flow rates.....	134
Chapter 5		
Figure 5.1	Detail of mesh for single-phase CFD simulations with simpleFoam: a) unstructured; b) structured.....	145
Figure 5.2	Velocity profiles and streamlines for 2D and 3D meshes in Advanced-Flow Reactor.....	149
Figure 5.3	Streamlines of 3D mesh for different Advanced-Flow Reactor heights at 5 mL/min	150
Figure 5.4	Swirling strength for different water flow rates	150
Figure 5.5	Velocity profiles for different turbulent flow models at 80 mL/min.....	151
Figure 5.6	Velocity profile along cross-section on side of heart cell in first row of AFR.....	152
Figure 5.7	Velocity profile along cross-section at center of heart cell in first row of AFR.....	153

Figure 5.8	Non-dimensional pressure field for incompressible water in structured 3D mesh.....	154
Figure 5.9	Pressure drop in AFR for incompressible water at different Reynolds numbers using simpleFoam.....	156
Figure 5.10	Comparison of RTD simulation for a) 2D mesh versus b) 3D mesh at two different times (5.4 s and 7.5 s); c) F(t) curve; d) E(t) curve.....	159
Figure 5.11	Dimensionless residence time distribution E(θ) for different flow rates.....	160
Figure 5.12	Comparison of CFD and experimental residence time distribution, E(θ).....	162
Figure 5.13	Geometry for three AFR designs studied.....	163
Figure 5.14	Comparison of velocity fields and streamlines among three different AFR designs.....	165
Figure 5.15	Dimensionless residence time distributions E(θ) for different AFR designs.....	166
Figure 5.16	Effect of reactor design on pressure drop.....	167
Figure 5.17	Pressure drop for LFR and comparison with AFR.....	168
Figure 5.18	Velocity profiles and streamlines in LFR.....	169
Figure 5.19	Residence time distribution in LFR.....	169
Figure 5.20	Conversion of reagent A in first order kinetics ($r = kC_A$) for irreversible reaction $A + B \rightarrow C$	170

Chapter 6

Figure 6.1	Illustration of the different continuum methods for describing the evolution of deforming interfaces.....	179
Figure 6.2	Schematic of the Continuum Surface Force (CSF) approach.....	181
Figure 6.3	Schematic of the static bubble test case.....	186
Figure 6.4	Comparison between interFoam and poreFoam solvers for bubble diameter of 0.4 mm.....	187
Figure 6.5	Velocity fields showing spurious currents for 0.4 mm bubble size using a) interFoam; b) poreFoam.....	188

Figure 6.6	Comparison between interFoam and poreFoam solvers for two different bubble diameters	189
Figure 6.7	Velocity fields showing spurious currents for different bubble sizes: a) 0.4 mm; b) 0.2 mm	189
Figure 6.8	Comparison between different compression terms using interFoam solver, for bubble size 0.2 mm	190
Figure 6.9	Reduction of spurious currents with poreFoam solver for a stagnant bubble 0.4 mm using different time steps	190
Figure 6.10	Terminal velocity of air bubbles in water at 20 °C. Reprinted from Clift et al.....	192
Figure 6.11	Rising velocity for air bubble in water for different bubble sizes as function of compression term cAlpha	194
Figure 6.12	Bubble shape for air bubble rising in water for different bubble sizes	195
Figure 6.13	Schematic of T-junction with channel size d for two-phase simulations, adapted from Qian and Lawal.....	196
Figure 6.14	Effect of mesh resolution on slug flow for $V_G = 0.02$ m/s, $V_L = 0.08$ m/s and $d = 0.5$ mm	199
Figure 6.15	Effect of mesh resolution on streamlines and velocity profiles for $V_G = 0.02$ m/s, $V_L = 0.08$ m/s and $d = 0.5$ mm	200
Figure 6.16	Effect of inlet velocities on slug size for $d = 0.5$ mm	201
Figure 6.17	Effect of inlet channel width on slug length for $V_G = 0.02$ m/s, $V_L = 0.02$ m/s: a) $W = 0.5$ mm; b) $W = 1$ mm; c) $W = 0.25$ mm; $d = 0.5$ mm	202
Figure 6.18	Effect of inlet configuration on slug length, simulations with interFoam, $V_G = 0.02$ m/s, $V_L = 0.02$ m/s; $d = 0.5$ mm	202
Figure 6.19	Effect of inlet channel length on slug length, simulations with OpenFOAM: a) short inlet channels; b) long inlet channels; interFoam, cAlpha = 4; $d = 0.5$ mm	203
Figure 6.20	Effect of contact angle on slug flow and slug shape: a) interFoam, cAlpha = 1; b) interFoam, cAlpha = 4; c) comparison with literature values	204
Figure 6.21	Effect of a) liquid viscosity and b) interfacial tension on liquid and gas slug lengths	206

Figure 6.22	Microchannel geometry and computational grid, as shown by Raj et al.....	207
Figure 6.23	Comparison among Fluent (Raj et al), OpenFOAM, and experimental results (Garstecki et al) of slug formation for Geometry A, $Q_{\text{water}} = 0.14 \mu\text{L/s}$, $Q_{\text{oil}} = 0.083 \mu\text{L/s}$	208
Figure 6.24	Effect of oil flow rate on slug formation; comparison among experiments (Garstecki et al), Fluent (Raj et al), and OpenFOAM (this work, 2D mesh 15,448 cells, and 3D mesh 77,240 cells with 5 cells in Z); Geometry A, $Q_{\text{water}} = 0.14 \mu\text{L/s}$; a) $Q_{\text{water}}/Q_{\text{oil}} = 0.343$; b) $Q_{\text{water}}/Q_{\text{oil}} = 1.129$; c) $Q_{\text{water}}/Q_{\text{oil}} = 7.179$	209
Figure 6.25	Effect of water flow rate on slug formation; comparison among experiments (Garstecki et al), Fluent (Raj et al), and OpenFOAM (this work, 2D mesh); Geometry A, $Q_{\text{oil}} = 0.028 \mu\text{L/s}$; a) $Q_{\text{water}}/Q_{\text{oil}} = 0.143 \mu\text{L/s}$; b) $Q_{\text{water}}/Q_{\text{oil}} = 1.8 \mu\text{L/s}$; c) $Q_{\text{water}}/Q_{\text{oil}} = 3.96 \mu\text{L/s}$	210
Figure 6.26	Effect of Courant number on slug formation. Geometry A, $Q_{\text{water}} = 0.050 \mu\text{L/s}$ and $Q_{\text{oil}} = 0.028 \mu\text{L/s}$. a) $Co = 0.5$; b) $Co = 0.1$; c) Experimental ⁴⁷ ; d) Fluent (Raj et al ⁴⁵).....	210
Figure 6.27	Effect of contact angle on slug formation; Geometry A, $Q_{\text{water}} = 0.14 \mu\text{L/s}$, $Q_{\text{oil}} = 0.408 \mu\text{L/s}$, $Q_{\text{water}}/Q_{\text{oil}} = 0.343$	211
Figure 6.28	Effect of increasing mesh resolution on liquid film.....	212
Figure 6.29	Effect of distributor configuration on slug formation, Geometry B, $Q_{\text{water}} = 0.14 \mu\text{L/s}$, $Q_{\text{oil}} = 0.408 \mu\text{L/s}$, $Q_{\text{water}}/Q_{\text{oil}} = 0.343$: a) cross-flow T-junction; b) co-flow T-junction; c) Y-junction.....	213
Figure 6.30	CFD simulations of carbon dioxide/water and comparison with experiments. a) $Q_w = 10$, $Q_{\text{CO}_2} = 13.3$, vertical orientation; b) $Q_w = 10$, $Q_{\text{CO}_2} = 20.8$, horizontal orientation.....	215
Figure 6.31	Detail of detachment point at different times for carbon dioxide/water system. $Q_w = 10$, $Q_{\text{CO}_2} = 13.3$, vertical orientation.....	215
Figure 6.32	CFD simulations of hexane/water and comparison with experiments. Phase flow rate (mL/min): a) $Q_w = 10$, $Q_h = 10$; b) $Q_w = 20$, $Q_h = 20$; c) $Q_w = 40$, $Q_h = 10$	216

Figure 6.33	CFD simulations of hexane/water and comparison with experiments ⁵¹ . Phase flow rate (mL/min): a) $Q_w = 40, Q_h = 40$; b) $Q_w = 60, Q_h = 60$; c) $Q_w = 80, Q_h = 80$	217
-------------	---	-----

Chapter 7

Figure 7.1	Schematic of the system for validation of mass transfer of species under static conditions and constant volume fraction field	233
Figure 7.2	Concentration profiles for $DT1 = DT2 = 10^{-5} \text{ m}^2/\text{s}$, $He = 100$ for different times = 1 s, 5 s, 10 s, 20 s, 30 s, 40 s, 100 s	234
Figure 7.3	Concentration profiles for $DT1 = 10^{-5} \text{ m}^2/\text{s}$, $DT2 = 10^{-7} \text{ m}^2/\text{s}$, $He = 100$ for different times = 1 s, 2 s, 5 s, 10 s, 20 s, 50 s, 100 s	234
Figure 7.4	Schematic of the system for validation of mass transfer of species under dynamic conditions and constant volume fraction field.....	235
Figure 7.5	Velocity profile for a fully developed flow at steady-state for two immiscible fluids. $dP/dx = -10 \text{ Pa s}$; $\mu_1 = 0.001 \text{ Pa.s}$, $\mu_2 = 0.0003 \text{ Pa.s}$, $\alpha_1 = 63.46$, $\alpha_2 = 211.54$, $\beta_1 = 0$, $\beta_2 = -0.45$	236
Figure 7.6	Concentration profiles obtained in OpenFOAM using HarounTransportFoam.....	237
Figure 7.7	Concentration profiles obtained with Matlab using the two-fluid formulation with boundary conditions specified at the interface	238
Figure 7.8	Validation of reactInterFoam for a first order irreversible reaction in static conditions. $He = 1$ and $k_1 = 0, k_2 = -0.01$	240
Figure 7.9	Validation of reactInterFoam for a first order reversible reaction in static conditions. $k_1 = 0, k_2 = -0.01$; $k_{1rev} = 0, k_{2rev} = 0.01$	240
Figure 7.10	Flow patterns for hexane/water system using HarounTransportFoam (OpenFOAM) for different flow rates; a) $Q_w = 10 \text{ mL/min}$, $Q_h = 10 \text{ mL/min}$; b) $Q_w = 20 \text{ mL/min}$, $Q_h = 10 \text{ mL/min}$; c) $Q_w = 40 \text{ mL/min}$, $Q_h = 10 \text{ mL/min}$; d) $Q_w = 80 \text{ mL/min}$, $Q_h = 10 \text{ mL/min}$	243
Figure 7.11	Effect of water flow rate at 10 mL/min hexane flow rate on a) concentration in hexane; b) average drop size; c) specific interfacial area; d)	

	hexane hold-up; e) individual mass transfer coefficient; f) overall mass transfer coefficient	246
Figure 7.12	Flow patterns for hexane/water system using HarounTransportFoam (OpenFOAM) for different flow rates; a) $Q_w = 10$ mL/min, $Q_h = 10$ mL/min; b) $Q_w = 40$ mL/min, $Q_h = 40$ mL/min; c) $Q_w = 80$ mL/min, $Q_h = 80$ mL/min.....	247
Figure 7.13	Effect of total flow rate at hexane to water flow rate ratio = 1 on a) concentration in hexane; b) average drop size; c) specific interfacial area; d) hexane hold-up; e) individual mass transfer coefficient; f) overall mass transfer coefficient	250
Figure 7.14	Effect of viscosity on flow patterns at 40 mL/min water and 10 mL/min hexane, for a) $\mu/\rho=10^{-5}$ m ² /s; b) $\mu/\rho=10^{-6}$ m ² /s.....	252
Figure 7.15	Effect of viscosity on a) concentration in hexane phase; b) droplet size; c) specific interfacial area; d) hold-up; e) individual mass transfer coefficient; f) overall mass transfer coefficient	253
Figure 7.16	Effect of surface tension on flow patterns at 40 mL/min water and 10 mL/min hexane, for σ (N/m): a) 0.052; b) 0.043; c) 0.035; d) 0.0068.....	254
Figure 7.17	Effect of surface tension at 40 mL/min water and 10 mL/min hexane on a) concentration in hexane phase; b) average drop size; c) specific interfacial area; d) hexane holdup; e) individual mass transfer coefficient; f) overall mass transfer coefficient	255
Figure 7.18	Effect Effect of contact angle on flow patterns at 40 mL/min water and 10 mL/min hexane, for a) $\theta = 0^\circ$; b) $\theta = 75^\circ$; c) 150°	256
Figure 7.19	Effect of contact angle at 40 mL/min water and 10 mL/min hexane on a) bulk concentration in hexane; b) average drop size; c) specific interfacial area; d) hexane holdup; e) individual mass transfer coefficient; f) overall mass transfer coefficient	257
Figure 7.20	Effect of contact angle at 40 mL/min water and 10 mL/min hexane on flow patterns	258
Figure 7.21	Effect of contact angle at 40 mL/min water and 10 mL/min hexane on a) bulk concentration in hexane; b) average drop size; c) specific interfacial	

area; d) hexane holdup; e) individual mass transfer coefficient; f) overall mass transfer coefficient	259
---	-----

Chapter 8

Figure 8.1	Examples of ozonolysis using microreactor technology: a) multichannel microreactor 8; b) falling film microreactor 9, 10; c) semipermeable Teflon AF-2400 11; d) Vapourtec technology	266
Figure 8.2	Characteristics of the ozone molecule. a) ozone molecule; b) reaction for the generation of ozone	266
Figure 8.3	Mechanistic steps in ozonolysis reaction according to Criegee	267
Figure 8.4	Experimental setup for ozonolysis.....	270
Figure 8.5	Reactors used in the ozonolysis experiments a) multichannel microreactor; b) LFR; c) AFR.....	271
Figure 8.6	Alkene conversion (%) versus molar ratio ozone/alkene	274
Figure 8.7	Images for ozonolysis of Sudan Red 7B dye 1mM in AFR with 100 mL/min gas flow rate at 10 % wt.	275
Figure 8.8	Images for ozonolysis of Sudan Red 7B dye 1mM in LFR at 1.5 mL/min and 10 % wt. ozone in gas phase.....	277
Figure 8.9	Predicted and experimental conversion of alkene	277

Appendices

Figure A.1.1	Gas-liquid flow images in AFR module as function of flow rates (mL/min) in horizontal orientation	285
Figure A.1.2	Gas-liquid flow images in AFR module as function of flow rates (mL/min) in vertical orientation.....	287
Figure A.2	Bubble size distribution in the AFR at different gas and liquid flow rates for vertical orientation	289
Figure A.3	Change in the fractional gas holdup along the length of the AFR for (A-B) Vertical orientation of module, (C-D) horizontal orientation of module.....	290
Figure A.4	Bubble size distribution in the horizontal orientation of the AFR.....	291

Figure A.5	Variation in the bubble number and bubble size along the length of the AFR in horizontal orientation.....	292
Figure A.6.1	Drop size distribution for hexane/water system in AFR. $Q_w = 10$ mL/min.....	294
Figure A.6.2	Drop size distribution for hexane/water system in AFR. $Q_w = 20$ mL/min.....	295
Figure A.6.3	Drop size distribution for hexane/water system in AFR. $Q_w = 40$ mL/min.....	296
Figure A.6.4	Drop size distribution for hexane/water system in AFR. $Q_w = 60$ mL/min.....	297
Figure A.6.5	Drop size distribution for hexane/water system in AFR. $Q_w = 80$ mL/min.....	298
Figure A.7	Hold-up estimation: packing structures in the AFR.....	299
Figure A.8	Comparison of effective interfacial area vs. power consumption for different liquid-liquid contactors	300
Figure A.9	Figure A.9: Drop size of dispersed phase versus power consumption for different liquid-liquid contactors	300
Figure A.10	Evolution of pressure and velocity components at fixed location (center of inlet of heart cell) with number of iterations for 2D unstructured mesh	301
Figure A.11	Residuals for velocity and pressure evolution with number of iterations for 2D unstructured mesh.....	301
Figure A.12	Evolution of pressure (kPa) and velocity components at a fixed location with number of iterations in 3D unstructured mesh.....	302
Figure A.13	Evolution of residuals for pressure and velocity components with number of iterations in 3D unstructured mesh.....	302
Figure A.14	Validation of modified interFoam solver based on two-phase scalarTransportFoam for a irreversible reaction $A+B \rightarrow C$	303
Figure A.15	Hexane/water two-phase flow simulated with interFoam using a 2D unstructured mesh	303
Figure A.16	Simulation of hexanw/water with interFoam using a 2D structured mesh	304
Figure A.17	Simulation of hexane/water flow using interfoam in AFR for a 3D mesh.....	305

List of Tables

Chapter 1

Table 1.1	Flow regime classifications according to Coleman and Garimella.....	30
-----------	---	----

Chapter 2

Table 2.1	Fluid properties of water and carbon dioxide at 25 °C.....	46
Table 2.2	Comparison of individual and overall mass transfer coefficients and specific interfacial areas among different gas-liquid contactors.....	76

Chapter 3

Table 3.1	Fluid properties of hexane and water at 20 °C.....	86
Table 3.2	Comparison of effective interfacial area and mass transfer coefficients in liquid – liquid contactors	108

Chapter 4

Table 4.1	Experimental mean residence time and variance.....	123
Table 4.2	Number of tanks in tanks in series model	126
Table 4.3	Peclet number for dispersion model.....	128
Table 4.4	Dimensional analysis of two-zone model equations	132
Table 4.5	Model parameters for two-zone dynamic-static model	133
Table 4.6	Relative error (%) in mean residence time and variance in prediction by two-zone model.....	134
Table 4.7	Comparison between models based on sum of square of errors.....	135

Chapter 5

Table 5.1	Linear solvers.....	143
Table 5.2	Preconditioner options.....	144
Table 5.3	Comparison of experimental and CFD results for pressure drop in AFR.....	155

Table 5.4	Transition regime for different microchannel geometry, hydraulic diameters, and materials.....	157
Table 5.5	Comparison of conversion (%) between different reactor designs	171

Chapter 6

Table 6.1	Fluid properties of air and water at 25°C.....	186
Table 6.2	Flow characteristic numbers for air rising bubble in water.....	192
Table 6.3	Effect of mesh resolution on gas and liquid slug lengths for different air and water inlet velocities.....	197
Table 6.4	Effect of inlet channel width on slug length for 0.02 m/s air and 0.02 m/s water inlet velocities.....	198
Table 6.5	Effect of cAlpha on slug length for 0.02 m/s air and 0.02 m/s water inlet velocities, configuration C	198

Chapter 7

Table 7.1	CEqn.H file including species conservation equation for solver including mass transfer using approaches of Haroun and Marschall.....	230
Table 7.2	Modified species conservation equation in CEqn.H in MarschallInterFoam solver for irreversible reaction $A \rightarrow B$	231
Table 7.3	Modified species conservation equation in CEqn.H in MarschallInterFoam solver for reversible reaction $A \leftrightarrow B$	231
Table 7.4	Boundary conditions for 1D validation case	232
Table 7.5	Solver validation. Jump concentration at interface at 5 s from CFD results as function of Henry constant	233
Table 7.6	Solver validation. Jump concentration at interface from CFD results for different diffusion coefficients as function of Henry constant	233
Table 7.7	Boundary conditions for validation of mass transfer solvers	236
Table 7.8	HarounInterFoam.C. Formulation of coupled species conservation and momentum equations within OpenFOAM solver	239

Table 7.9	Mass transfer efficiency, concentration, and hexane hold-up for constant hexane flow rate	243
Table 7.10	Comparison of experimental and CFD k_L and a	244
Table 7.11	Comparison of experimental and CFD $k_L a$	245
Table 7.12	Mass transfer efficiency, concentration, and hexane hold-up for constant hexane flow rate	248
Table 7.13	Comparison of experimental and CFD k_L and a for unity flow rate ratio	248
Table 7.14	Comparison of experimental and CFD $k_L a$ for unity flow rate ratio	249

Chapter 8

Table 8.1	Operating conditions and conversion results for ozonolysis of 1-decene in multichannel microreactor, LFR, and AFR	273
Table 8.2	Operating conditions and conversion results for ozonolysis of ethylsorbate in LFR and AFR	274

Appendices

Table A.1.1	Reproducibility of measurements for gas-liquid flow. Case a) Single bubble	293
Table A.1.2	Reproducibility of measurements for gas-liquid flow. Case b) Single heart cell	293
Table A.2.1	Reproducibility of measurements for liquid-liquid flow. Case a) Single bubble	299
Table A.2.2	Reproducibility of measurements. for liquid -liquid flow Case b) Single heart cell	299

1 Introduction, motivation, and objectives

1.1 Microreactor technology

Microreactors are “small, continuous flow reactors” with channel dimensions on the order of microns which have been demonstrated to provide many advantages over conventional process technologies for the synthesis of chemical compounds. Some of these include: high transport rates, rapid mixing, and high selectivities and conversions, enabling the synthesis of compounds that cannot be synthesized in conventional reactors. The small characteristic dimensions of microchannels increase the gradients for momentum, concentration, and temperature, thus increasing the driving forces or diffusional flux for heat and mass transport. In addition, the surface area to volume ratio also increases at small channel sizes, increasing the total area available for mass and heat transfer. These two factors also result in shorter response times leading to simpler process control. ¹ The use of microreactors in the laboratory scale for process development is an environmentally friendly alternative since small amounts of reagent are used and small waste volumes are generated. Furthermore, the higher selectivities and yields achieved in addition to better transport rates allow more efficient processes in comparison to conventional reactors.

An additional feature of microreactors is their modular design, which allows to increase the throughput by direct parallelization of units, and the possibility of incorporating a series of microreactors with separation steps allowing a multistep synthesis. Examples include the work by Sahoo et al (Figure 1.1) ², Liu X. et al for the synthesis of amides from alcohols and amines (Figure 1.2) ³, and Li W. et al in a multistep microfluidic polymerization reactions in droplets (Figure 1.3) ⁴, among others ⁵.

Microreactor devices allow the specification of different reaction conditions at different locations, enabling a single device to have different heating zones. In addition, in-line continuous separation devices enable removal of unreacted reagents and by-products, making it possible to realize a series of reactions and separations without leaving the microreactor environment. ^{2,9}

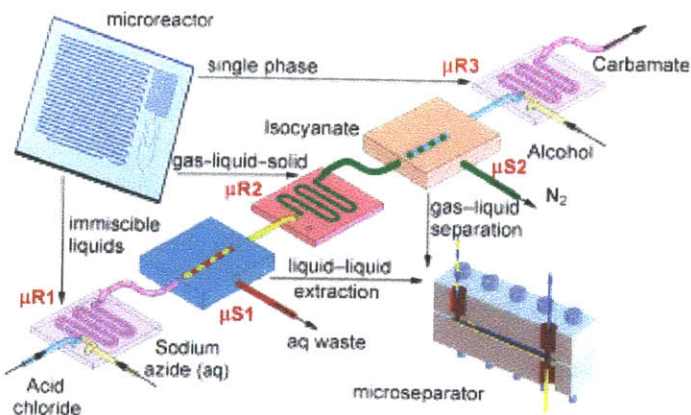


Figure 1.1: Multistep continuous-flow microchemical synthesis involving multiple reactions and separations. Schematics for carbamate synthesis: reaction steps are conducted in microreactors $\mu R1$, $\mu R2$, $\mu R3$, and separation steps in microseparators $\mu S1$, $\mu S2$.²

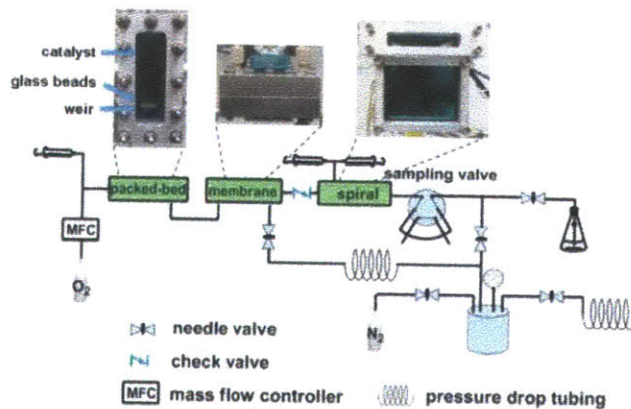


Figure 1.2: Diagram of the experimental setup for multistep synthesis of amides from alcohols and amines: packed bed microreactor, gas-liquid membrane separator, spiral-channel microreactor.³

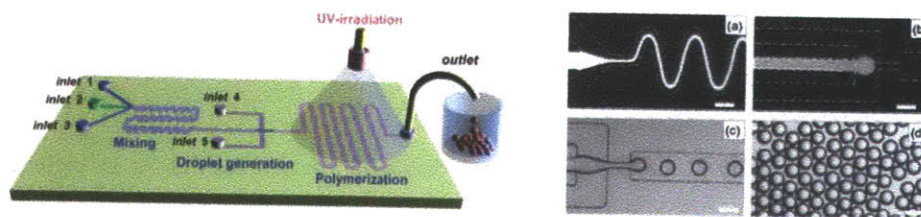


Figure 1.3: Example of multistep microfluidic polymerization reactions in droplets. (left) Schematic of microfluidic reactor composed by mixing zone, droplet generation, and polymerization by UV-irradiation; (right) fluorescence microscopy images of the mixture of monomers (a) in the mixing zone and (b) in the central channel of the droplet generator; (c) microfluidic emulsification of PU-pre/TPGDA in aqueous phase; (d) droplets collected at outlet of the microfluidic reactor without exposure to UV-irradiation.⁴

Mixing in microreactors occurs without the need of mechanical agitation or external forces, and that is called “passive micromixing”, which is essentially determined by the channel geometry: lamination (Y-channel), flow focusing (T-junction), converging and diverging flows (micromixers with posts, packed beds). In immiscible gas-liquid and liquid-liquid slug flows, mixing occurs within each droplet due to interior circulations, as shown in Figure 1.4 – b, c), and each droplet behaves as a single batch reactor. Active micromixing can also be achieved by applying periodic flow switching, acoustic streaming, ultrasonic waves, or electrokinetic/electrowetting induction, among others.⁵

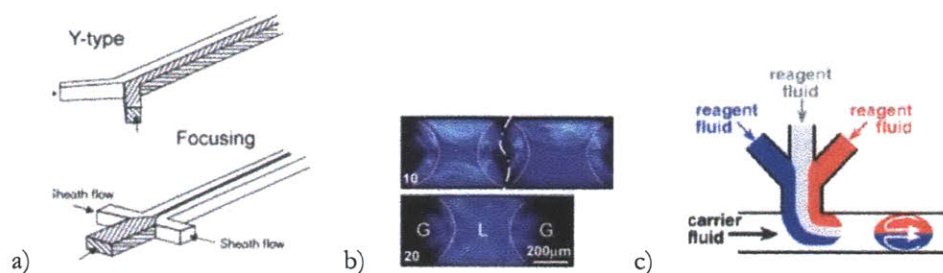


Figure 1.4: Passive mixing techniques applied in microfluidic systems: a) lamination by Y-type geometry and flow focusing⁶; b) recirculation streamlines in gas-liquid segmented flow⁷; c) encapsulated mixing in dispersed liquid slugs⁸

In addition to the already reported advantages offered by microreactors, it is important to emphasize on the advantage of operating continuously in contrast to the traditional batch mode, in which most pharmaceutical and fine chemicals industries usually operate, reducing the operation time by eliminating the load and cleaning times required in batch. It has been reported in many scientific publications that reaction times can be reduced when substituting laboratory batch reactors by continuous microreactor technology, i.e. in Aldol reactions, from hours to minutes.¹⁰ Many safety issues related to the accumulation of unstable intermediates in batch can be overcome by operating in continuous mode, where the required reaction volumes are smaller. Based on the study of several synthesis processes by Roberge, 50% of the reactions would benefit from a continuous process, most of which would prefer a microreactor device. Although it is clear that microreactors provide significant benefits against conventional batch reactors, especially for

homogeneous, gas-liquid and liquid-liquid systems, handling solids is still a challenge that limits the applicability of microreactors to heterogeneous systems involving solids.¹¹

1.2 Multiphase flow in microreactors

Multiphase flows are created “when two or more partially or totally immiscible fluids are brought into contact”.¹² Multiphase reactive systems are very frequent in the pharmaceutical and fine chemicals industry. Examples include hydrogenations, nitrations, oxidations, fluorinations, hydrogenations, ozonolysis, and carbonylations. Some reactive systems require the presence of more than a single phase because the different reagents are found naturally in different phases. For example, in oxidation or ozonolysis reactions, oxygen and ozone are transported from the gas phase to an organic liquid phase, where the reaction occurs. A second group of multiphase reactions are those wherein the reaction occurs in a single phase, but the presence of a second immiscible phase enhances the reaction performance by reducing the axial dispersion, minimizing side reactions, driving the reaction to higher yields, enhancing mass and heat transport at the interfaces by inducing recirculation, or isolating determined components in droplets from contact the reactor wall.¹² The understanding of the hydrodynamics and mass transfer for different gas-liquid and liquid-liquid systems is important for a comprehensive reactor design and optimization.

1.2.1 Gas-liquid

The understanding and knowledge of the gas-liquid flow patterns in the reactor are crucial for engineering design purposes and evaluation of practical performance. Most of the studies of gas-liquid flow have been performed in micro and milli straight channels. These studies have determined the transition lines between flow regimes, void fraction, pressure drop, liquid film thickness, and internal mixing quality.^{13, 14} Different flow patterns develop in channels depending on the different velocities of the gas and liquid phases^{12, 14-16} (Table 1.1). The different flow regimes are generally represented in map flows in terms of the gas and liquid superficial velocities (Figures 1.5 and 1.6) or in terms of fluid properties as coordinates. Several experimental studies in microchannels have been reported to date^{12, 14, 16-21}. However, each flow map has

been obtained under specific conditions, and factors such as temperature, cross-sectional shape of the channel and surface roughness has not been studied yet. In addition, most of the experiments have been developed for air/water systems. Therefore, transition lines in these diagrams depend on the fluid properties, the material of the channel wall (wetting characteristics, roughness) and the hydraulic diameter and shape (cross-section) of the channel.^{12, 14} Thus, generalized correlations that account for fluid properties would be very useful to predict reactor performance.

The hydrodynamic behavior in the AFR may be completely different than those observed in micro or millichannels, due to the complex geometry in the form of a series of convergent/divergent sections and larger operating flow rates (10-200 mL/min). In addition, it is expected that the hydrodynamics in the AFR will be different for varying fluid properties and wetting characteristics. Unlike microchannels, where the flow patterns are determined by the balance among interfacial, inertial (generally negligible due to the low velocities), and viscous forces, in macrochannels gravitational forces may become significant. The effect of gravity is also studied in the AFR for gas/liquid systems.

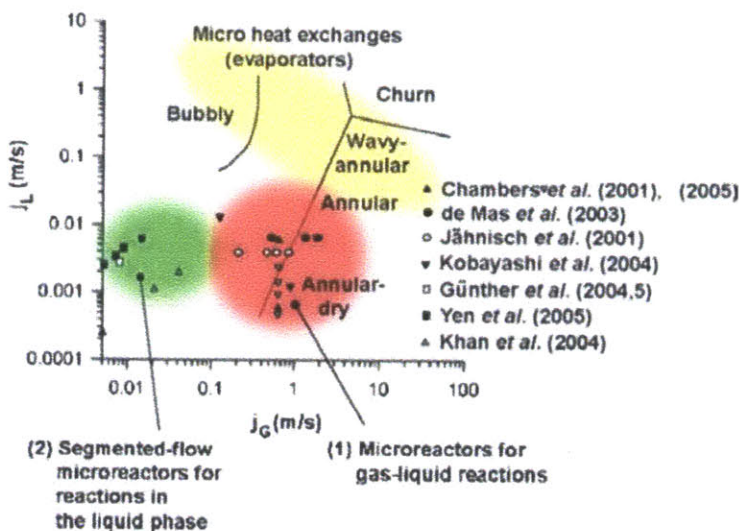


Figure 1.5: Flow regime diagram for gas-liquid flow. Plane spanned by the liquid (j_L) and gas (j_G) superficial velocities. Characteristic regions for micro-heat exchangers, segmented-flow microreactors for reactions in the liquid phase and gas-liquid reactions in microreactors are shaded.¹²

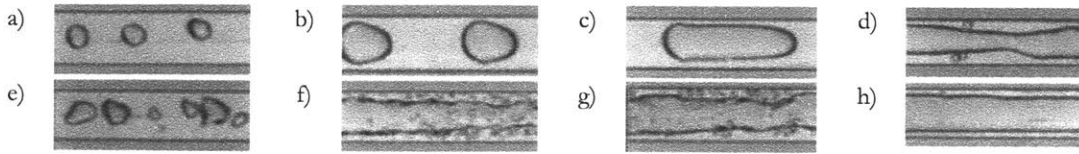


Figure 1.6: Representative photographs of flow patterns for gas-liquid flow in a microchannel of 1.09 mm hydraulic diameter and semi-triangular test section: a), b) bubbly; c), d) slug; e), f) churn; g) slug-annular; i) annular; ¹⁷

Table 1.1: Flow regime classifications according to Coleman and Garimella ¹⁴

Flow Regime	Flow Patterns	Description
Stratified	Stratified smooth	Parallel flow
	Stratified wavy	
Intermittent	Elongated bubble (plug)	Discontinuities in the liquid and gas flow, with a thin liquid film coating the wall and surrounding elongated gas bubbles
	Slug flow	
Annular	Wavy annular	Flowing gas core surrounded by the liquid phase coating the walls
	Annular	
Bubbly	Bubbly flow	Bubbles smaller than the characteristic dimension of the channel and a continuous liquid phase
	Dispersed flow	

1.2.2 Liquid-liquid

Liquid-liquid systems are also numerous in the pharmaceutical industry. However, gas-liquid systems have been more extensively studied than liquid-liquid systems. ²² In liquid-liquid flow, wetting properties of both liquids and the reactor wall become important, the viscosity of both liquid phases need to be considered (as compared to the gas-phase where viscosity is treated as negligible versus the liquid viscosity), and both liquids are incompressible. ¹² The transition lines between flow regimes in microchannels for liquid-liquid systems (isolated drops, pearls necklaces, stratified flow, and pears) have been measured (Figure 1.7). It has been reported that wetting properties of the microchannel walls, particularly at low continuous phase velocities, in addition to the inlet geometry, affect flow regimes. The preferred flow pattern is normally isolated regular-sized drops, which requires high velocities of the carrier fluid and low superficial velocities of the dispersed phase. This regime can be extended towards lower continuous phase velocity if the microchannel walls are preferentially wetted by the continuous phase or if the interfacial tension is reduced by

surfactants. Similarly to the liquid phase in gas-liquid systems, axial dispersion in the discontinuous phase is reduced and there is no contact with the walls, which makes the droplet regime suitable for nanoparticle synthesis or crystallization applications ¹². But again, this data has been obtained for specific substances, and generalized maps still need to be obtained. In addition, the AFR has a different design than straight channels and these results cannot be extrapolated directly.

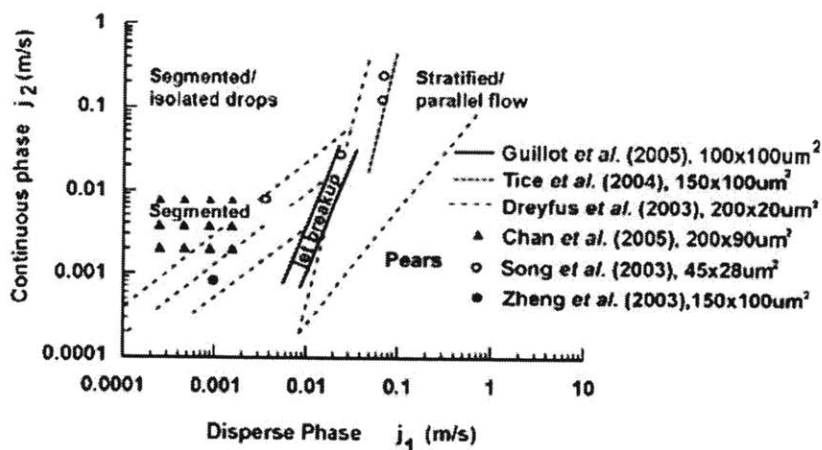


Figure 1.7: Regime diagram for liquid-liquid flows in microfabricated systems. Transition lines and operating conditions for different literature data. ¹²

1.3 Challenges in scale-up and scale-out

There are two concepts that need to be distinguished in the context of scaling in microreactors. One is the conventional “scaling up”, or increase in reactor size and flow rate. A second concept is the “numbering up” or “scaling out”, which consists of the assembly of a large number of microchannels in parallel in order to operate with macroscopic flow rates while maintaining the performance offered locally by small characteristic dimensions ^{23, 24}. The problems associated with conventional scale-up procedures could be overcome through microreactor scale-out or numbering-up by parallelization of microreactor units to achieve the required production level. This enables the possibility of optimization of a single unit and further expansion to higher production levels by just numbering-up. Ideally, the performance of the global reactor operating at identical conditions would be the same as in the single optimized microreactor, provided that the

flow distribution is uniform and the heat management is equal in all the units that compose the overall scaled out device. The microchannel network should be designed properly to avoid flow maldistribution and maintain the performance of the individual microreactors ²⁴⁻²⁶. In this regard, different designs of flow splitters have been studied to guarantee uniform flow distribution ²⁷. The advantage of scaling-out is that the production level can be adjusted in terms of supply and demand without the necessity of applying the traditional tedious procedure of scaling-up, which requires redesign and validation of the reaction methodology. ²⁸

Although the current application of microreactors is on process development and industrial research, its potential application to production levels has acquired an increasing interest in the industrial sector, especially for the manufacture of high value products, such as pharmaceuticals and specialty chemicals. The challenge in scaling microreactors is how to use the increased transport rates inherent to microreactor technology while increasing the throughput for production applications. Scale-out by direct parallelization of units is not feasible for target production rates on the order of kg/min. The reason is that this approach requires thousands of units and development of very expensive and complex control systems to guarantee identical operating conditions in each one of the units for a perfect and predictable overall reactor performance. In order to overcome this limitation, a compromise between the “scale up” and “scale out” approaches must be achieved. Increasing the channel size helps increase the throughput and reduce the number of units required for parallelization, but at the same time risks reducing the mass and heat transfer performance. For this reason, it is necessary to investigate the effects of increasing the reactor size and flow rates from the microscale to the milliscale, and study whether the mass and heat transfer performance of microreactors is still kept in the milliscale.

Several companies have investigated microreactors for chemical production using different reactor systems, such as those developed by Corning, Forschungszentrum Karlsruhe, Alfa Laval, Institut für Mikrotechnik Mainz (IMM), Velocys, Lonza, and Ehrfeld BTS ²⁹. They differ in the scale-up technique, materials, dimensions, and geometries. Except for Corning, the other reactors are fabricated in metal and

their designs are based on a heat exchange configuration, with multiple channels for the reaction mixture and channels for the heating/cooling fluid. The Falling Film Microreactor developed by IMM works with liquid films of a few tens of micrometer thickness and interfacial areas of up to $20,000 \text{ m}^2/\text{m}^3$ combined with an effective heat exchange.²³

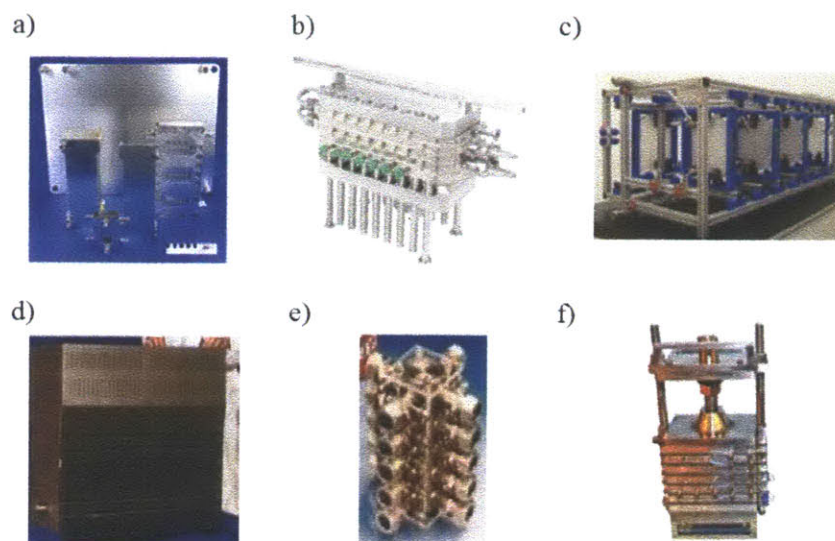


Figure 1.8: Different scale-up approaches using microreactor technology concepts: a) IMM (Institute für Mikrotechnik Mainz); b) Alfa Laval; c) Corning Advanced-Flow Reactor; d) Velocys; e) Forschungszentrum Karlsruhe; f) Lonza

Scaling of microreactors still needs to be addressed in more detail in microreactor technology. Very frequently, publications refer to scaling-out microreactors but they do not provide any further details about the work that has been done in this specific field. It has not been studied in detail yet and some of the applications in larger scales have been developed by companies that do not provide sufficient information due to confidentiality issues.

Within the context of scale-up, the motivation for using a reactor configuration such as the Advanced-Flow Reactor (AFR) manufactured by Corning Inc. against other available options in the market, is its special design for multiphase systems with a series of converging/diverging sections and the material of construction (glass) that enables the experimental observation of the hydrodynamics. The AFR has minimum dimensions

of 1 mm and handles flow rates from 10 to 200 mL/min, thus allowing the direct parallelization of a reasonable number of units (tens) to achieve production rates of kg/min. Here, the challenge of achieving flow uniformity across all parallelized units becomes a manageable problem.

The Corning Advanced-Flow glass reactor is an assembly of glass fluidic modules connected together through appropriate piping and connectors and works with a liquid flow rate range from 10 to 200 mL/min. Figure 1.9 includes two types of modules, heart shaped for mixing and straight channels to provide longer residence times. The heart-shaped module has a special design to promote mixing of phases. Two shaped posts interrupt the flow within each heart cell, inducing break up of bubbles at the entrance of the heart and further coalescence at the outlet, therefore enhancing mass transfer. The modules are composed by three layers: a reaction layer sandwiched by two layers for the cooling/heating fluid. Different hydrodynamic regimes encountered can be achieved in the Corning system by varying the operating conditions ³¹. Glass is chemically compatible with a wide spectrum of chemicals and solvents over a wide range of temperatures (from - 60°C to 230°C) and pressures up to 18 barg (maximum pressure dependent on working temperature). Reactions such as hydrogenations, nitrations and oxidations have been already tested successfully in Corning reactors.

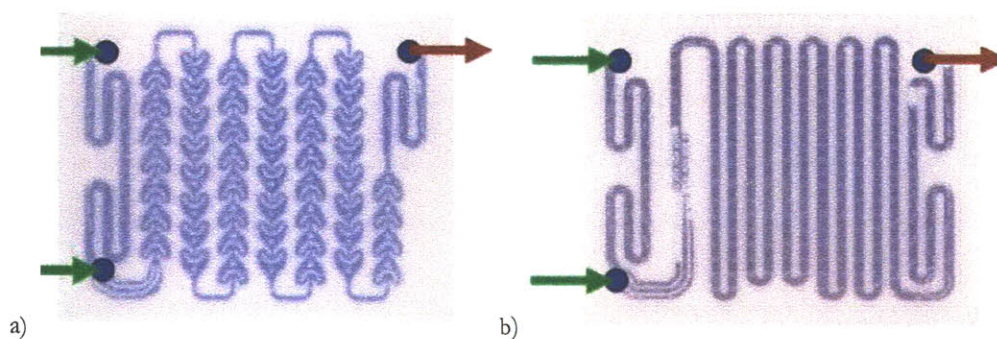


Figure 1.9: Corning Generation 1 fluidic modules. a) Heart design for mixing, b) i-mixer coupled with straight channel residence time.

Within the context of reactor scale up, Corning Inc. offers several options with different reactor volumes, as shown in Figure 1.10, following the same heart design with series of convergent/divergent

sections. The Low-Flow reactor (LFR) has an internal volume of 0.45 mL and height dimensions of 0.35 mm. This design provides a tool for the development phase allowing kinetic studies with small amount of reagents and waste (throughput of 0.1 – 0.6 kg/h). The larger versions of the Advanced-Flow Reactor Gen 1, Gen 2, Gen 3, and Gen 4, have larger internal volumes (shown in Figure 1.10) and provide larger throughputs that can go up to 120 kg/h in the Gen 3 or 300 kg/h in the Gen 4 reactor (see Figure 1.11).

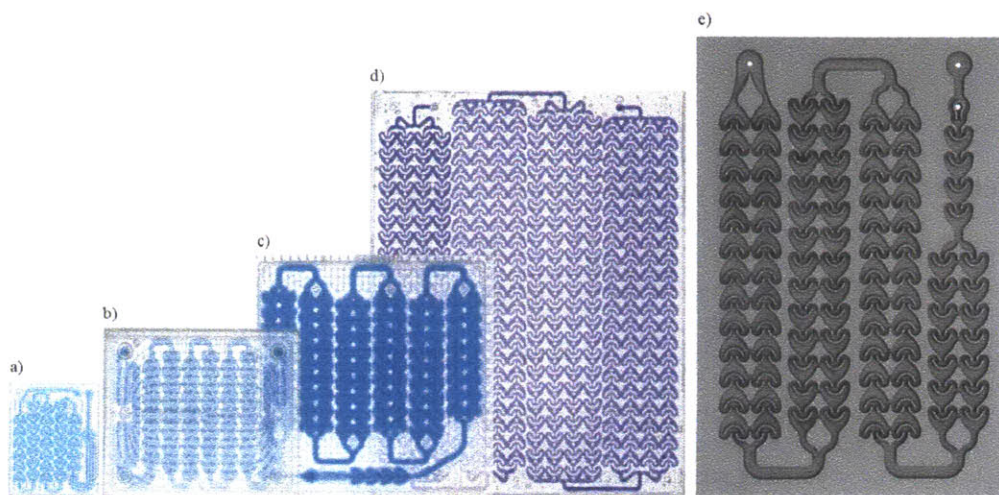


Figure 1.10: Generations of Corning Advanced-Flow Reactors: a) Low-Flow reactor, 0.45 mL; b) Gen 1, 8 – 11 mL; c) Gen 2, 21 – 25 mL; d) Gen 3, 55 – 65 mL; e) Gen 4, ceramic, 200 - 260 mL ³²

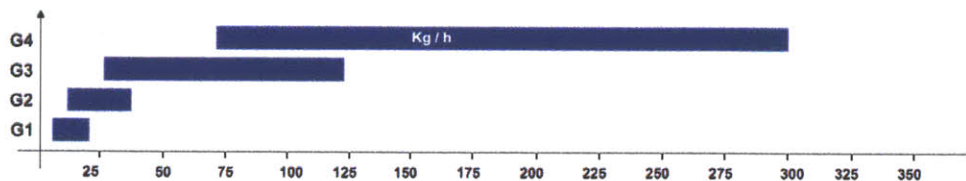


Figure 1.11: Corning Advanced-Flow Reactors throughput for Gen 1, Gen 2, Gen 3, and Gen 4 module designs. ³³

Although the essence of the heart design is kept among the different generations, there are slight differences which may affect the hydrodynamic characteristics of each reactor design. For instance, the LFR

replaces the “two-post” design typical of the Gen 1 AFR, with a single triangle-shaped post that occupies almost the entire zone within the two posts of the Gen 1. The Gen 4 AFR removes the second post in the shape of a cylinder with respect to Gen 1 AFR. Another difference is the significant increase of the channel size from the LFR (height is 0.35 mm) to the Gen 1 AFR (height is 1.1 mm). Finally, reactors Gen 2, Gen 3, and Gen 4, use the scale out concept within each module to achieve higher throughputs by having two (Gen 2, Gen 4) or four (Gen 3) rows of hearts in parallel. This is an excellent approach to provide a compact configuration for further scale out by modules.

1.4 Chemistry applications of microreactor technology

One of the most important steps in the definition of this thesis is the selection of relevant reactions for the pharmaceutical industry that are suitable for application using microreactor technology. Roberge et al.²⁹ published a classification of reactions based on physico-chemical properties: reaction kinetics and phases involved (gas, liquid or solid). The reactions according to kinetics were classified into three different types:

- Type A reactions: very fast reactions (<1 s) and controlled by the mixing process.
- Type B reactions: fast reactions (10 s - 20 min) and kinetically controlled.
- Type C reactions: slow reactions (> 20 min) and often operated in batch mode, as opposed to semibatch.

The characteristic enhanced mass and heat transfer in microreactors make them particularly suitable to carry out kinetically fast reactions that are otherwise slow due to the limitation caused by transport processes (type A reactions) enabling higher yields than using conventional reactors. In kinetically controlled reactions (type B reactions), microreactors enable higher yields through precise control of the residence time and heat management. Finally, microreactors enable the safe performance of hazard reactions that involve large heat accumulation in batch reactors (type C reactions), by the rapid heat transfer achieved in microreactors.

The most frequent type of reactions is the heteroatom alkylation and arylation, particularly N- and O-containing molecules. One reported example is the synthesis of sibenadet hydrochloride, a highly potent drug for treatment of patients with chronic obstructive pulmonary disease ³⁴. The O-C, S-C and N-C bonds are formed by phase-transfer alkylation of an alcohol, free radical addition to an olefin and conjugate addition of an amine to a vinyl sulfone, respectively. Of particular interest is the highly exothermic radical thiol addition, which requires dilution with toluene for scale-up. This is therefore a clear example of potential improvement that can be achieved through microreactor technology. The high surface to volume ratio and enhanced heat transfer in microchannels can reduce the amount of solvent required to carry out the reaction, as compared to the conventional reactors.

Oxidation reactions, either with oxygen or ozone, are normally avoided for safety reasons. Many oxidizing agents are highly energetic compounds, giving rise to thermal hazards and low selectivities. ³⁵ Of particular interest is the ozonolysis reaction, with a great relevance in the pharmaceutical industry for the manufacture of different drugs, such as cefitibuten (3G cephalosporin antibiotic), cefaclor (2G cephalosporin antibiotic), artemisinin (antimalarial stable peroxide), and oxandrolone (anabolic steroid). More examples can be found in the review by Van Ornum et al. ³⁶ However, ozonolysis is a reaction that requires extreme heat management conditions (temperatures of $-78\text{ }^{\circ}\text{C}$) and suffers from mass transfer limitations, with accumulation of highly energetic intermediates which can lead to explosions in conventional reactors. For these reasons, this type of oxidation reaction can benefit from the advantages of high transport rates of microreactors and reduction of accumulation of intermediates in continuous flow. Whether the mass transport rates in the Advanced-Flow reactor are sufficient to perform the ozonolysis reaction efficiently still remains unknown.

1.5 Scope of this work

In every scale-up process it is essential to know the hydrodynamic characteristics of each reactor unit for the fluid system in addition to the intrinsic kinetics of the reaction of interest. This includes pressure drop, residence time distribution, and mass and heat transfer coefficients. This thesis is focused on the study of the hydrodynamics of the AFR for two-phase systems under constant ambient temperature conditions. Heat transfer studies are beyond the scope of this work. The hydrodynamics are determined both experimentally and computationally.

Experiments can be tedious, expensive and generate large amounts of waste. In addition, experiments do not reveal enough information of the local behavior of the reactor, since it is impossible to have access to measure concentrations, velocities, and temperatures at each point along the reactor. Simulations can be used for optimization of operating conditions, selection of fluid properties, and provide insight in the interpretation of experimental data. Furthermore, the costs of fabrication of new reactors with the purpose of studying them experimentally can be reduced if computational fluid dynamic (CFD) simulations are first used to screen different reactor designs. Thus, the development of a computational tool capable of predicting flow characteristics in a reactor for any fluid system can save time and costs. Here the open source software OpenFOAM is used to study the hydrodynamics of the AFR through CFD simulations. One of the main challenges in simulating two-phase flow in channels of small characteristic dimensions is that surface tension effects are important. Many dynamic events in the reactor happen simultaneously, such as droplet detachment, deformation, break-up, and coalescence, and a simulation method that can predict these phenomena is required. The volume-of-fluid method (VOF) has become a frequent choice in Eulerian models to track interfaces when these topology changes are present. After validating the simulation method for simple geometries, such as rising bubbles in quiescent liquids and T-junctions, the flow is simulated through the AFR and CFD results are compared with the experimental results obtained from flow visualization techniques. In addition, after modification of the standard *interFoam* solver to account for mass

transfer and reaction, CFD simulations to predict overall mass transfer coefficients for different fluid systems are performed.

The final step is to demonstrate experimentally the scale-up of multiphase reactions from a microreactor to the AFR. The exothermicity of the ozonolysis reaction, and its mass transfer limited nature, make it the perfect model to be studied in the micro and the milli scales. Comparison with ozonolysis performed in different reactors at different scales is also included.

1.6 Specific objectives

The main objective of this thesis is to study the scale-up process of multiphase continuous flow chemistries from micro scales to milli scales by means of microreactor technology and Advanced-Flow Reactors provided by Corning Inc. More specifically,

- Understand single-phase and two-phase hydrodynamics in the AFR using experimental methods.
- Develop a computational tool that is able to predict single-phase and two-phase flows and, ultimately, mass transfer coefficients in the AFR, after validation with experiments.
- Understand the motivation for the specific reactor design and study design variations and effect of fluid properties on two-phase hydrodynamics and mass transfer coefficients.
- Apply the knowledge acquired in the characterization of hydrodynamics of the AFR to study experimentally the scale-up procedure from a microreactor to the AFR using ozonolysis as the model reaction.

1.7 Thesis outline

The thesis is structured in 8 Chapters, the first one devoted to introduce the thesis topic, motivation and objectives, and the content of following Chapters is summarized here:

- **Chapters 2 and 3** include a complete analysis of the results from visualization techniques applied to study flow patterns for gas-liquid (Chapter 2) and liquid-liquid (Chapter 3) systems in AFR and their variation with operating conditions. Bubble/drop size distributions, specific interfacial areas, dispersed phase holdup, and mass transfer coefficients are studied. Correlations to estimate pressure drop are developed based on the Lockhart-Martinelli approach ^{37, 38}. Comparison of mass transfer performance of AFR with other conventional multiphase contactors is performed.
- **Chapter 4** focuses on residence time distribution (RTD) measurement in the AFR for different flow rates. Different models (tanks in series, dispersion, and two-zone models) are developed and assessment against experimental data is performed.
- **Chapter 5** includes computational fluid dynamic (CFD) simulations using OpenFOAM (open source software) for single-phase flow in the AFR. CFD results are compared with experimental measurements of pressure drop and residence time distributions for different flow rates. The influence of reactor design in pressure drop, velocity profiles, streamlines, stagnant zones, and residence time distributions is also studied.
- **Chapter 6** includes the results of applying the Volume-of-Fluid (VOF) method to predict flow patterns of two-phase flow. Challenges encountered in modeling multiphase flow at small scales are presented with test cases, such as rising bubbles in stagnant liquids or flow through T-junctions in microchannels. The results are compared with available data in the literature and the CFD tool applied to model hexane/water and carbon dioxide/water flows in the AFR.
- **Chapter 7** focuses on modeling mass transfer across interfaces between immiscible phases. The interFoam solver is extended to include mass transfer and reaction terms in the VOF formulation based on the approaches followed by Marschall ³⁹ and Haroun ⁴⁰⁻⁴¹. Validation with simple test cases and application to AFR is performed. The CFD tool is applied to the AFR to study the influence of

fluid properties and reactor design on two-phase flow patterns, bubble/drop size distributions, specific interfacial areas, holdup, pressure drop, and mass transfer coefficients.

- **Chapter 8** includes experimental results that demonstrate the scale-up using a multichannel microreactor, LFR, and AFR using ozonolysis as the model reaction.
- **Chapter 9** includes a summary of the work done, conclusions, recommendations, and future work to follow in this investigation.

1.8 References

- (1) Ehrfeld, W.; Hessel, V.; Haverkamp, V.; Microreactors. Institute für Mikrotechnik Mainz GmbH. *Ullmann's Encyclopedia of Industrial Chemistry*, **2012**, Wiley-VCH Verlag GmbH & Co. KGaA, Weinheim. DOI: 10.1002/14356007.b16_b37
- (2) Sahoo, H. R.; Kralj, J. G.; Jensen, K. F. Multistep continuous-flow microchemical synthesis involving multiple reactions and separations. *Angewandte Chemie*, **2007**, *119*, 30, pages 5806–5810. DOI: 10.1002/ange.200701434
- (3) Liu, X. and Jensen, K. F. Multistep synthesis of amides from alcohols and amines in continuous flow microreactor systems using oxygen and urea hydrogen peroxide as oxidants. *Green Chem.*, **2013**, *15*, 1538-1541. DOI: 10.1039/C3GC40407B
- (4) Li, W.; Pham, H. H.; MacDonald, B.; Günther, A.; Kumacheva, E. Multi-Step Microfluidic Polymerization Reactions Conducted in Droplets: The Internal Trigger Approach. *J. Am. Chem. Soc.*, **2008**, *130*, 30, 9935 - 9941. DOI:10.1021/ja8029174
- (5) Hartman, R. L.; Jensen, K. F. Microchemical systems for continuous-flow synthesis. *Lab Chip*, **2009**, *9*, 2495 – 2507. DOI: 10.1039/B906343A
- (6) Nguyen, N. T.; Wu, Z. G.; *J. Micromech. Microeng.*, **2005**, *15*, R1–R16
- (7) Gunther, A.; Jhunjhunwala, M.; Thalmann, M.; Schmidt, M. A.; K. F. Jensen, *Langmuir*, **2005**, *21*, 1547–1555
- (8) Song, H.; Chen, D. L.; Ismagilov, R. F. *Angew. Chem. Int. Ed.*, **2006**, *45*, 7336–7356
- (9) Sahoo, H. Design and Operation of microchemical systems for multistep chemical synthesis. Ph.D.Thesis, **2008**, Cambridge: Massachusetts Institute of Technology
- (10) Hessel, V., & Löwe, H. Organic Synthesis with Microstructured Reactors. *Chemical Engineering Technology*, **2005**, *28*, 3, 267 - 284
- (11) Roberge, D. M.; Ducry, L.; Bieler, N.; Cretton, P.; Zimmermann, B. Microreactor Technology: A Revolution for the Fine Chemical and Pharmaceutical Industries? *Chemical Engineering Technology*, **2005**, *28*, 3, 318 – 323

- (12) Günther, A.; Jensen, K. F. Multiphase microfluidics: from flow characteristics to chemical and materials synthesis. *Lab on a Chip*, **2006**, *6*, 1487 – 1503
- (13) Serizawa, A., Feng, Z., & Kawara, Z. Two-phase flow in microchannels. *Experimental Thermal and Fluid Science*, **2002**, *26*, 703-714
- (14) Waelchli, S., & von Rohr, R. P. Two-phase flow characteristics in gas–liquid microreactors. *International Journal of Multiphase Flow*, **2006**, *32*, 791–806
- (15) Shui, L., Eikjel, J. C., & van den Berg, A. Multiphase flow in microfluidic systems - Control and applications of droplets and interfaces. *Advances in Colloid and Interface Science*, **2007**, *133*, 35-49
- (16) Günther, A.; Khan, Saif. A.; Thalmann, M.; Trachsel, F.; Jensen, K. F. Transport and Reaction in Microscale Segmented Gas-Liquid Flow. *Lab Chip*, **2004**, *4*, 278 - 286
- (17) Triplett, K. A. et al. Gas-liquid two-phase flow in microchannels. Part I: two-phase flow patterns. *International Journal of Multiphase Flow*, **1999**, *25*, 377-394
- (18) Triplett, K. A. et al. Gas-liquid two-phase flow in microchannels. Part II: void fraction and pressure drop. *International Journal of Multiphase Flow*, **1999**, *25*, 395 - 410
- (19) de Mas, N; Günther, A.; Schmidt, M. A.; Jensen, K. F. Microfabricated multiphase reactors for the selective direct fluorination of aromatics. *Ind. Eng. Chem. Res.*, **2003**, *42*, 698-710
- (20) Coleman, J. W., & Garimella, S. Characterization of two-phase flow patterns in small diameter round and rectangular tubes. *Int. J. Heat Mass Transfer*, **1999**, *42*, 2869-2881
- (21) Kawahara, A., Chung, P. M., & Kawaji, M. Investigation of two phase flow pattern, void fraction and pressure drop in a microchannel. *Int. J. Multiphase Flow*, **2002**, *28*, 9, 1411-1435
- (22) Gavriilidis, A.; Angeli, P.; Cao, E.; Yeong, K.K.; Wan, Y.S.S. Technology and Applications of Microengineered Reactors. *Trans IChemE*, **2002**, *80*, Part A, 3-30
- (23) Markowz, G. Microstructured Reactors for Heterogeneously Catalyzed Gas-Phase Reactions on an Industrial Scale. *Chemical Engineering Technology*, **2005**, *28*, 4, 459 - 464
- (24) Commenge, J. M.; Falk, L.; Corriu, J. P.; Matlosz, M. Optimal Design for Flow Uniformity in Microchannel Reactors. *AIChE Journal*, **2002**, *48*, 2, 345 - 358
- (25) Saber, M.; Commenge, J. M.; Falk, J. Microreactor numbering-up in multi-scale networks for industrial-scale applications: Impact of flow maldistribution on the reactor performances. *Chemical Engineering Science*, **2010**, *65*, 372 - 379
- (26) Amador, C.; Gavriilidis, A.; Angeli, P. Flow distribution in different microreactor scale-out geometries and the effect of manufacturing tolerances and channel blockage. *Chemical Engineering Journal*, **2004**, *101*, 379 - 390
- (27) Schenk, R.; Hessel, V.; Hofmann, C.; Kiss, J.; Löwe, H.; Ziogas, A. Numbering-up of micro devices: a first liquid-flow splitting unit. *Chemical Engineering Journal*, **2004**, *101*, 421 - 429
- (28) Haswell, S. J.; Skelton, V. Chemical and biochemical microreactors. *Trends in Analytical Chemistry*, **2000**, *19*, 6, 389 - 395
- (29) Roberge, D.; Gottsponer, M; Eyholzer, M.; Kockmann, N. Industrial design, scale-up, and use of microreactors. *Chemistry Today*, **2009**, *27*, 4, 8-11
- (30) Vankayala, B. K.; Löb, P; Hessel, V.; Menges, G.; Hofmann, C.; Metzke, D.; Krtschil, U.; Kost, H. Scale-up of Process Intensifying Falling Film Microreactors to Pilot Production Scale. *International Journal of Chemical Reactor Engineering*, **2007**, *5*, 1, 1542 – 6580 DOI: 10.2202/1542-6580.1463

- (31) Corning. Corning Advanced-Flow™ glass reactor. Avon (France): *Application & Reactor Engineering*, 2009, Corning Inc.
- (32) Corning Brochure: The future flows through. Corning® Advanced-Flow™ glass reactors. Corning S. A. S. Corning European Technology Center, France, 2009, Corning Inc. www.corning.com
- (33) Vizza, A.; Guidat, R.; Lavric, D. Corning® Advanced-Flow™ Reactor Technologies: from lab to production, a seamless scale-up. Corning reactor technologies, Corning European Technology Center, France. 2013, Corning Inc.
- (34) Giles et al. Development of a Manufacturing Process for Sibenadet Hydrochloride, the Active Ingredient of Viozan. *Organic Process Research and Development*, 2004, 8, 628 – 642
- (35) Carey, J. S., Laffan, D., Thomson, C., & Williams, M. T. Analysis of the reactions used for the preparation of drug candidate molecules. *Org. Biomol. Chem.*, 2006, 4, 2337 - 2347
- (36) Van Ornum, S. G. Ozonolysis applications in drug synthesis. *Chem. Rev.*, 2006, 106, 2990-3001
- (37) Lockhart, R. W.; Martinelli, R. C. Proposed correlation of data for isothermal, two-phase, two-component flow in pipes. *Chemical Engineering Progress*, 1949, 45, 39-48
- (38) Chisholm, D. A theoretical basis for the Lockhart-Martinelli correlation for two-phase flow. *International Journal of Heat and Mass Transfer*, 1967, 10, 1767-1778
- (39) Marschall, H.; Hinterberger, K.; Schuler, C.; Habla, F.; Hinrichsen, O. Numerical simulation of species transfer across fluid interfaces in free-surface. *Chemical Engineering Science*, 2012, 78, 111–127
- (40) Haroun, Y.; Legendre, D.; Raynal, L. Volume of fluid method for interfacial reactive mass transfer: application to a stable liquid film. *Chemical Engineering Science*, 2010, 65, 2896 - 2909
- (41) Haroun, Y.; Raynal, L.; Legendre, D. Mass transfer and liquid hold-up determination in structured packing by CFD. *Chemical Engineering Science*, 2012, 75, 342 - 348

2 Experimental study of gas – liquid hydrodynamics in the Advanced-Flow Reactor

2.1 Abstract

Hydrodynamics and mass transfer of gas-liquid flow are explored under ambient conditions in an Advanced-Flow Reactor (AFR) using carbon dioxide/water as the model system. Phase flow rates range from 5.6 to 103 mL/min and 10 – 80 mL/min for carbon dioxide and water, respectively. Bubble size distribution, gas holdup (ε_g), specific interfacial area (a), pressure drop (ΔP), and mass transfer coefficients ($k_{L,a}$) are determined from flow visualization experiments and compared with conventional gas-liquid contactors. Average bubble sizes ($\overline{d_B}$) of 0.9 – 3.8 mm, gas holdup of 0.04 – 0.68, specific interfacial areas of 160 – 1,300 m^2/m^3 , and overall mass transfer coefficients of 0.2 – 3 s^{-1} are obtained for the vertical orientation of the AFR and are seen to vary with the inlet flow rates. Although the effect of gravity is present for this system at the lowest flow rates, it is concluded that no significant effect on the hydrodynamic properties exists. The measured pressure drop for vertical orientation (3.6 – 53.4 kPa) is used to estimate power consumption, a metric that serves to compare the mass transfer efficiency among different gas-liquid contactors. A power law relationship was obtained for overall mass transfer coefficients in terms of power input and gas holdup, given by $k_{L,a} = 0.101P_w^{0.44}\varepsilon_G^{0.46}$. Measured interfacial areas and mass transfer coefficients in the AFR are one order of magnitude larger than bubble columns (50 – 600 m^2/m^3 ; 0.005 – 0.24 s^{-1}) and spray columns (75 – 170 m^2/m^3 ; 0.015 – 0.022 s^{-1}), but one order of magnitude smaller than gas-liquid microchannels (3,400 – 9,000 m^2/m^3 ; 0.3 – 21 s^{-1}) or falling film reactors (20,000 m^2/m^3). However, the AFR is the most efficient contactor providing high throughputs with the smallest power consumption.

2.2 Introduction

Microreaction technology^{1,2} has been demonstrated to be a useful concept for the chemical synthesis at laboratory scale, pilot scale³ and also at commercial scale manufacturing. A large number of review papers and applications of engineering principles for the analysis of reactions/processes indicate the potential of this

concept as a future chemical processing technology.⁴⁻⁷ Over the last two decades, microreactors have been shown to be useful for synthesis of chemicals (viz. natural products, API, perfumery chemicals, dyes, polymers and polymer composites, radiopharmaceutical drugs, etc.) and nanomaterials. However, very few reaction systems have been extended for large scale manufacturing.^{3, 8-10} One of the reasons for the paucity of such examples is the non-availability of a device that can be reliably used for large scale synthesis while maintaining most of the advantages that a typical microreactor offers, such as high heat and mass transfer coefficients.

A few options for pilot and large scale continuous flow production of chemicals that are available include: Alfa Laval Plate Reactor or Open Plate Reactor¹¹, FZK (Forschungszentrum Karlsruhe) reactors¹², Hitachi reactors¹⁰, microreactors by Lonza¹³, MIPROWA[®] systems by Ehrfeld-BTS, Cylindrical Falling film microreactor by IMM¹⁴ and Advanced Flow Reactor[®] of Corning Ltd⁸. For individual devices some information on the applicability for specific reactions is quoted, but general guidelines are typically missing for use in new reactions. One of the challenges is the absence of any information on the expected values of hydrodynamic parameters for specific operating conditions. Although there are studies on the hydrodynamics in channels at the millimeter scale, none of them accounts for the complex geometry characteristic of the AFR and results may not be directly extrapolated to this reactor. Thus, it is necessary to explore and quantify its hydrodynamic features to provide the understanding needed for the selection of flow configuration and correct operating parameters.

The *Experimental* section provides details of the experimental set-up, measurement devices used and experimental procedure. The section on *Results and Discussion* includes the analysis of hydrodynamic parameters measured for two orientations of the AFR and comparison with other gas-liquid contactors. Finally, the important observations useful in identifying operating conditions yielding a desired range of hydrodynamic parameters are summarized.

2.3 Experimental

A schematic of the experimental setup is shown in Figure 2.1. Carbon dioxide and water (Millipore Academic) are the two fluids of the model system to study the hydrodynamics properties of gas-liquid flow in the AFR (fluid properties are shown in Table 2.1). Water is pumped at constant flow rate using an ISCO syringe pump. Gas is supplied from a cylinder and the gas flow rate is controlled using a pre calibrated mass flow controller. Experiments are carried out at room temperature (~ 22 °C) at different gas (5.6 – 103 mL/min) and liquid flow rates (10 – 80 mL/min). The outlet is kept open to atmospheric pressure.

Table 2.1: Fluid properties of water and carbon dioxide at 25 °C. ¹⁵

Fluid	Density (kg/m ³)	Viscosity (Pa·s)	Surface tension (N/m)
Water	998.2	$1.0 \cdot 10^{-3}$	0.072
Carbon dioxide	1.8	$1.5 \cdot 10^{-5}$	

A typical AFR mixing module consists of four structured glass surfaces confined to yield a reaction zone sandwiched by two layers devoted for the flow of heating/cooling fluid (Figure 2.2 a). The heat transfer area available per unit volume of reacting fluid is (788.5 m⁻¹) and the volume of the reaction zone is 8.7 ml. The heat transfer zones have one inlet and one outlet, and a network of obstacles in the flow space to achieve uniform flow distribution. The reaction zone has two inlets and a single outlet, and it is made of several heart-shaped cells connected in series (Figure 2.2 b). A detail of the cell and typical dimensions is shown in Figure 2.2 c). The arrangement of multiple modules (either heart-shaped or with straight channels) according to the requirements of the reaction of interest, yields a configuration such as that shown in Figure 2.2 d). Moreover, this configuration can be scaled-out by parallelization in order to achieve larger production rates to satisfy the demand.

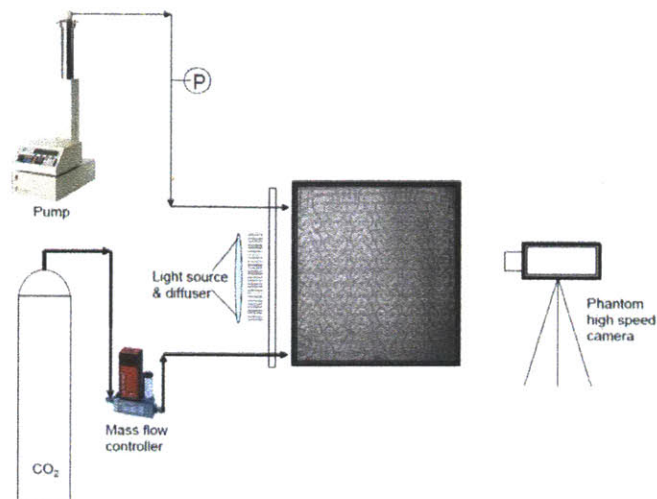


Figure 2.1: Schematic of experimental set-up for gas-liquid visualization experiments. Liquid flow is introduced through ISCO pump to the Advanced-Flow Reactor and carbon dioxide from gas cylinder using a mass flow controller. Light source and high speed camera for flow visualization experiments.

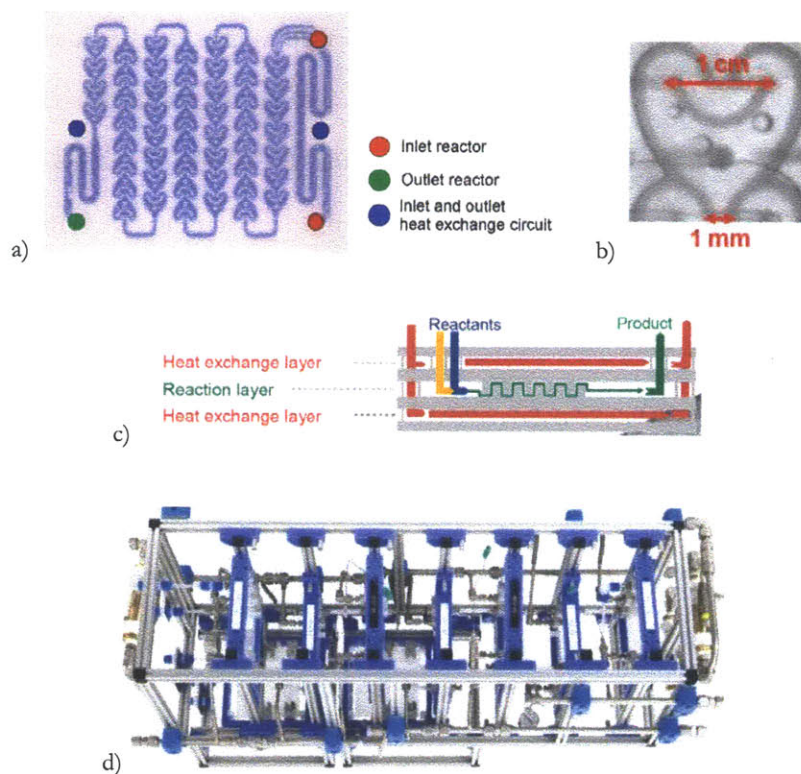


Figure 2.2: Details of the structure of the Advanced-Flow Reactor (AFR) Gen 1: a) front view of the AFR mixing module; b) detail of a heart-shaped cell; c) lateral cross-section of a single AFR module showing reaction and heat transfer zones; d) typical AFR system with multiple connected plates.

The following sections summarize details of the measurement devices used for these studies.

- *Pressure drop:* pressure drops were measured using a pressure gauge installed on the tube carrying the liquid from the pump to the AFR just before entering the reactor.
- *Flow visualization by high speed imaging:* measurement of bubble sizes, gas holdup, and effective interfacial area was performed with a Phantom v7.1 high speed camera (maximum resolution 800x600 pixels at speeds up to 4,800 fps). The acquisition rate was varied in the range of 200 – 4,000 fps. In all cases, the visibility of the object was enhanced using back illumination with suitable light diffuser.

One frame of each movie recorded at steady-state was analyzed using the software ImageJ^{®16} for the measurement of bubble size distribution. The bubble size (d_{bi}) and number of bubbles (N) were measured in every heart cell along the entire AFR for each combination of water and carbon dioxide flow rates. The so-obtained data was further used to estimate the specific interfacial area (a) and gas holdup (ε_g). The gas holdup was used to estimate the slip velocity (v_s) between phases, and mass transfer coefficients (k_L) were calculated theoretically using the surface renewal theory of Danckwerts¹⁷. Overall mass transfer coefficients ($k_L a$) were then obtained from the specific surface area and theoretically estimated k_L .

- *Experimental measurement of overall mass transfer coefficient:* gas-liquid mass transfer coefficients were determined by measuring the concentration of carbon dioxide absorbed into MilliQ water for different gas and liquid flow rates. The amount of carbon dioxide was measured at the outlet of the AFR after collection in a beaker by titration. For each 2 ml sampled water, 2 ml of 0.5 M NaOH were added. Each mole of dissolved carbon dioxide in water reacts with two moles of NaOH to yield Na_2CO_3 . From titration with 0.1 N HCl the amount of non-reacted NaOH is determined and thus, the original amount of carbon dioxide dissolved in

water is back-calculated. Titration of three blank samples of MilliQ water were also performed to correct for the possible amount of carbon dioxide dissolved in water naturally.

2.4 Results and discussion

2.4.1 Flow regimes

In microchannels, flow maps of different flow regimes are presented based on the Reynolds numbers and superficial velocities of each phase. Experiments are normally performed for straight channels with constant cross-sectional area. Thus, the definition of dimensionless numbers for these systems is straightforward. However, the non-constant width dimensions in the AFR makes difficult to define a single Reynolds number and superficial velocity for each phase. As reference, here the definition of superficial velocities and dimensionless numbers is based at the inlet of the heart cell ($w = 1 \text{ mm}$, $h = 1.1 \text{ mm}$). The Reynolds number is calculated as given by eq 2.1:

$$Re = \frac{VD_h\rho}{\mu} \quad (2.1)$$

The Reynolds numbers for the individual liquid and gas phases at the largest flow rates calculated at the inlet of the heart cell are 170 – 1,330 and 12 – 210, respectively. Using average fluid properties (density and viscosities) and the total superficial velocities of the two phases, the range for the two-phase Reynolds number is 260 – 3,000. While the flow patterns in microchannels are very well defined and characterized with a laminar regime, the two-phase flow in the AFR can change from laminar to turbulent.

Similarly, the Weber and Capillary numbers are calculated using eq 2.2 and eq 2.3 to estimate the relative importance of inertial-versus-interfacial stresses and viscous-versus-interfacial stresses, respectively. The Weber numbers for the gas phase are on the order of 10^{-4} to 10^{-2} from the lowest to the highest gas flow rates, and the Capillary number on the order of 10^{-3} to 10^{-2} , respectively. Thus, capillary forces are relevant at

the operating conditions tested, and inertial and viscous forces become more relevant at the highest flow rates.

$$We = \frac{V^2 d_B \rho}{\sigma} \quad (2.2)$$

$$Ca = \mu V / \sigma \quad (2.3)$$

The relative importance of forces in the AFR is different from microchannels, where bubble formation is highly influenced by surface tension and inertial effects are negligible. However, the AFR operates with flow rates on the order of 10 – 100 mL/min and inertial effects become important. In addition, the cross section in the AFR is not constant as it usually is in microchannels. Thus, different velocities are encountered along the flow path and the capillary number is reduced in specific locations leading to breakup of bubbles.

A typical image of the two-phase flow for carbon dioxide/water is presented in Figure 2.3. The fluid enters the heart-shaped cell through a narrow channel and impacts a first curved post which splits the flow into two streams, each one travelling close to the walls leaving a zone of low velocity between the two obstacles. After reaching a second cylindrical post, the two streams merge into a single stream, which enters the next heart cell. This design provides a convergent-divergent configuration that causes continuous splitting and merging of the flow enhancing the mass transfer along the reactor. This results in a decrease in bubble size and number of bubbles from the inlet towards the outlet of the reactor due to the absorption of carbon dioxide into water. Different average bubble size and size distributions are obtained depending on the inlet flow rates. This contrasts with the narrow bubble size distributions obtained in microchannels, and the broad size distributions obtained in stirred vessels.

From the visualization experiments it is observed that the two-phase flow in the AFR is characterized by a sequence of dynamic events: detachment, elongation, deformation, breakup, and coalescence of bubbles as they travel through the continuous phase. These dynamic events are influenced by the confined geometry, small dimensions, and presence of obstacles that disturb the flow. This is different from stirred vessels, where distances are so large that wall effects are negligible. In stirred reactors the bubble size distribution depends

on the agitation speed, the design and type of impeller, and the physical properties of the fluids. The flow patterns in microchannels are also affected by the operating conditions, fluid properties, and other fixed factors (channel dimensions, device geometry), but all variables related to agitation are absent. Thus, dispersion characteristics are device dependent and an independent study of the effect of different variables in the AFR is needed.

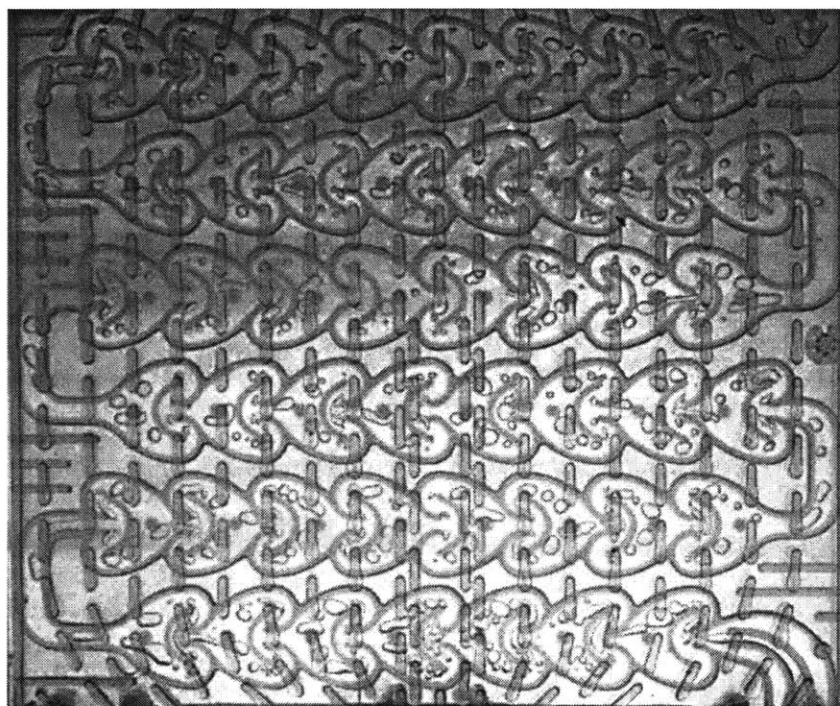


Figure 2.3: Gas-liquid flow in the Advanced-Flow Reactor for vertical orientation at $Q_L = 80$ mL/min and $Q_G = 106$ mL/min. (Images at other combinations of flow rates for horizontal and vertical orientations are given in Figures A.1.1 and A.1.2 of the Appendix)

The AFR module is normally kept in vertical position so that the heat transfer fluid flows upward without leaving air-pockets in its way. Gravity effects may be significant in two-phase flow within the reaction zone for very different fluid densities as it may occur in the water/carbon dioxide system. Indeed, the calculated Froude number using eq 4 for total flow rates between 10 mL/min and 180 mL/min ranged from 0.48 to 8.7. Thus, the influence of gravity on the flow patterns and derived variables may not be negligible at

least at the lowest flow rates. In order to quantify this effect the hydrodynamic features of the AFR for both orientations are studied here.

$$Fr = \frac{v}{\sqrt{gw}} \quad (2.4)$$

2.4.2 Vertical orientation

2.4.2.1 Bubble size distribution

Bubble size distributions and number-average bubble sizes are measured from the images obtained in the visualization experiments. The individual bubble size d_{Bi} is measured using *ImageJ*® software by drawing the bubble perimeter and calculating the equivalent diameter of a circle having the same area as the bubble as seen from above. It is observed for all flow rates that only one bubble exists along the height of the reactor, so the image analysis of bubble size from the top of the reactor gives a good approximation of d_{Bi} . For further calculations of gas holdup, the bubble volume is calculated as a sphere for bubble diameters smaller than the reaction layer height, whereas the remaining bubble volumes are calculated from the measured area and channel height.

The number-average bubble size ($\overline{d_B}$) is calculated from the individual bubble sizes over the entire AFR module for each experiment. Its dependence with gas and liquid flow rates is shown in Figure 2.4. At constant gas flow rate (Q_G), the bubble size decreases continuously with increasing liquid flow rate (Q_L). This observation is explained from the early detachment of bubbles at the inlet orifice for co-current flow, which depends on the high shear produced by the continuous phase flowing on the outer section.¹⁷ It is also observed that right at the detachment point, increasing the gas flow rate for a constant liquid flow rate generates smaller bubble sizes. However, at the highest gas flow rates, the numerous and small bubbles generated right at the inlet coalesce resulting in larger effective bubble sizes at the detachment point. Coalescence dominates over breakup and, overall, gas holdup and bubble size increases with increasing gas flow rate for a constant water flow rate.

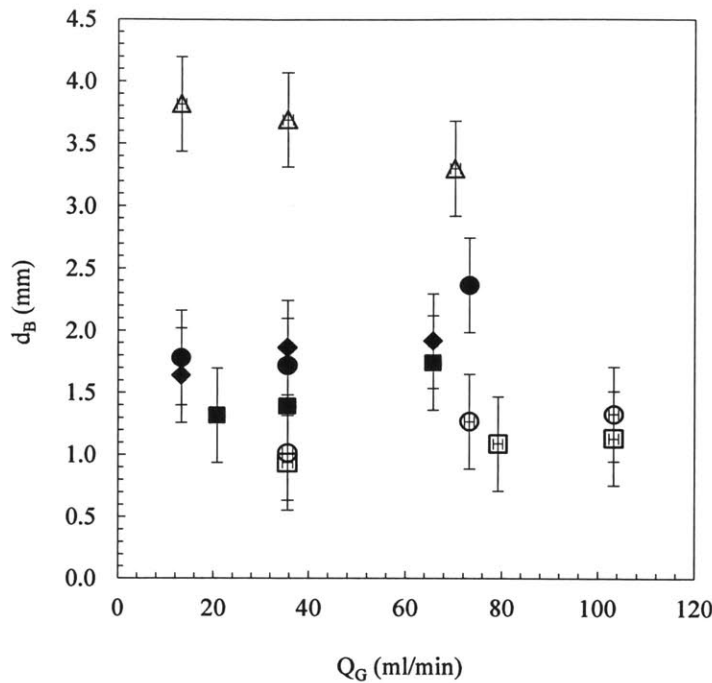


Figure 2.4: Variation in average bubble size with inlet gas flow rate in vertical orientation for different water flow rates (mL/min): Δ , 10; \bullet , 20; \blacklozenge , 30; \blacksquare , 40; \circ , 60; \square , 80;

The bubble size distributions in vertical orientation for liquid flow rates of 20, 30, 60, and 80 mL/min and different gas flow rates are shown in the *Appendix – Chapter 2*. As it is observed, the average-bubble size and bubble size distribution depend only on the gas and liquid flow rates. However, in stirred tank reactors the agitation speed also affects the bubble size distribution decreasing the average bubble size and narrowing the bubble size distribution at higher impeller speeds.¹⁸ At 10 mL/min of water large bubbles occupy almost half of the hearts and are connected to each other from heart to heart at the largest gas flow rates (36 mL/min, 70 mL/min). Having large bubbles are in detriment of mass transfer since the specific interfacial area is significantly reduced. This experiment shows also that gravity has an effect on the hydrodynamics when the AFR module is located in vertical position and working at low water flow rates.

Broader bubble size distributions are observed at low flow rates (20 mL/min). Increasing the gas flow rate broadens the bubble size distribution with a larger effect at the lowest flow rates, whereas increasing the liquid flow rate narrows the size distribution. For example, at 20 mL/min, increasing the gas flow rate from

13 mL/min to 66 mL/min increases the maximum of the bubble size interval from 2.1 to 4.4 mm. At 80 mL/min, increasing the gas flow rate from 36 to 103 mL/min increases the maximum bubble size from 1.6 to 2.5 mm only.

2.4.2.2 Gas holdup

Gas holdup is an important variable for the estimation of the pressure drop and the specific interfacial area. It is calculated from the number of bubbles and bubble size, assuming that the number of bubbles seen from above is exactly the number actually existing in the entire channel height. At constant Q_L gas holdup increases with increasing Q_G , as it is shown in Figure 2.5. It is also observed that gas holdup depends significantly on the inlet flow rate ratio Q_L/Q_G and it can be correlated according to eq 2.5.

$$\varepsilon_G = 0.125 (Q_L/Q_G)^{-1.04} \quad (2.5)$$

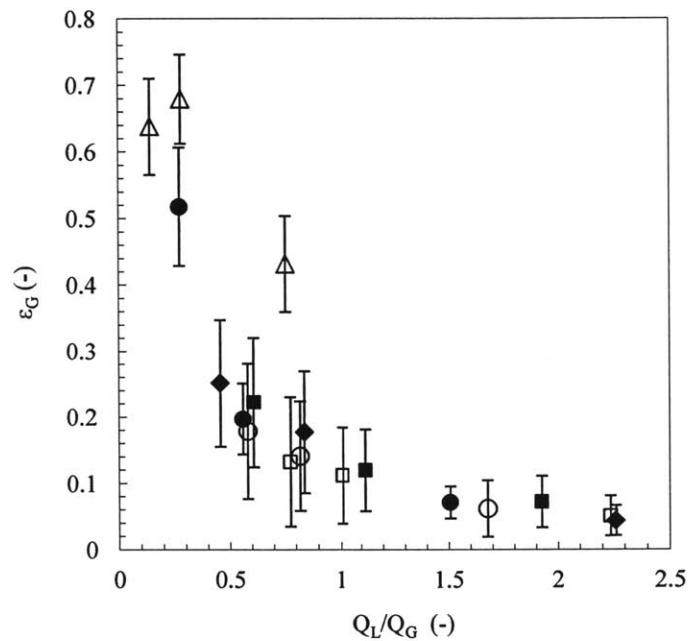


Figure 2.5: Variation in gas holdup with flow rate ratio in vertical orientation for different water flow rates (mL/min): Δ , 10; \bullet , 20; \blacklozenge , 30; \blacksquare , 40; \circ , 60; \square , 80;

These experiments were conducted with the outlet at atmospheric pressure. It is definitely interesting to study the effect of adding back pressure to the system on the gas holdup and other hydrodynamic

parameters. This is important in gas-liquid systems where the gas is compressible and solubility can be affected by pressure.

2.4.2.3 Specific interfacial area

The specific interfacial area (a) is related to the gas holdup (ϵ_g) and the mean bubble diameter ($\overline{d_B}$) by eq 2.6. The results were plotted versus the flow rate ratio Q_L/Q_G in Figure 2.6. A power law behaviour of a with respect to the ratio Q_L/Q_G is given by eq 2.7.

$$a = 6\epsilon_g/\overline{d_B} \quad (2.6)$$

$$a = 466.9 (Q_L/Q_G)^{-0.673} \quad (2.7)$$

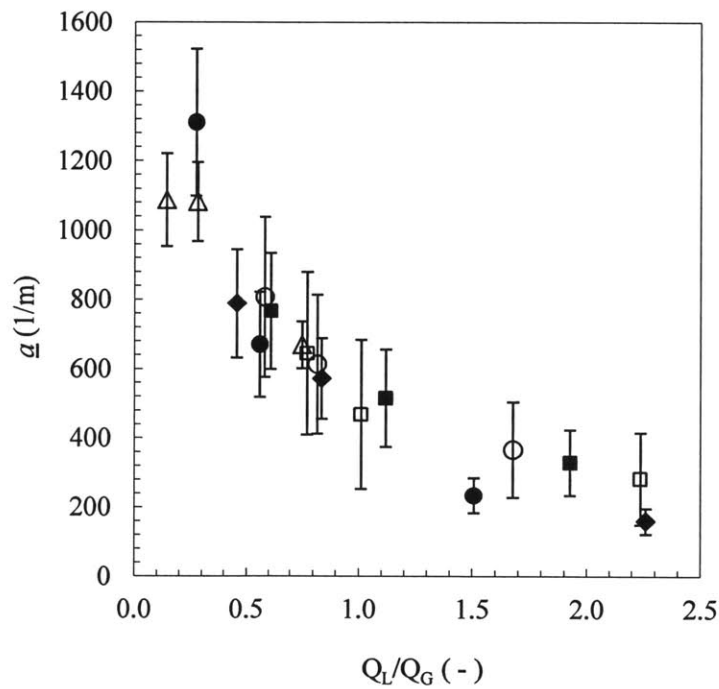


Figure 2.6: Variation in specific interfacial area with flow rate ratio in vertical orientation at different water flow rates (mL/min): Δ , 10; \bullet , 20; \blacklozenge , 30; \blacksquare , 40; \circ , 60; \square , 80;

Specific interfacial areas for this gas-liquid system are in the range of 160-1,300 m²/m³ and depend on the combination of flow rates. These values corresponding to the range of flow rates tested are of the same order of magnitude as other gas-liquid contactors, such as stirred tanks, static mixers, vertical tube reactors, and couette-Taylor flow reactors.¹⁹ However, a better metric for comparison is in done terms of mass transfer efficiency versus power consumption (Section *Comparison of AFR with other gas-liquid contactors*).

2.4.2.4 Properties of dispersion along the flow path

As discussed in the *Experimental* section, the AFR module contains six rows of heart-shaped cells connected to each other in series. The hydrodynamic properties change from the inlet towards the outlet due to the convergent/divergent configuration that enhances mass transfer between phases. In Figure 2.7 the number of bubbles and bubble diameter are presented along the flow path for two liquid flow rates ($Q_L = 40$ and 80 mL/min) and three gas flow rates ($Q_G = 13, 36,$ and 73 mL/min). The abscissa corresponds to the row number in the AFR module, from the inlet (row 1) towards the outlet (row 6).

It is seen that the total number of bubbles increases with increasing gas flow rate and decreases along the reactor flow path for a constant gas flow rate due to the chemical absorption into water. For $Q_L = 40$ mL/min, the bubble size decreases at low Q_G (13 mL/min) towards the outlet due to the absorption into water. However, at the highest Q_G (73 mL/min) absorption coexists with coalescence of bubbles causing the bubble size to increase, although the overall effect is to decrease the gas holdup since the bubble number also decreases. For $Q_L = 80$ mL/min, the higher shear rates decrease the bubble size, which remains almost constant over the entire flow path. The reduction of the number of bubbles for approximately the same bubble size decreases the gas holdup along the flow path.

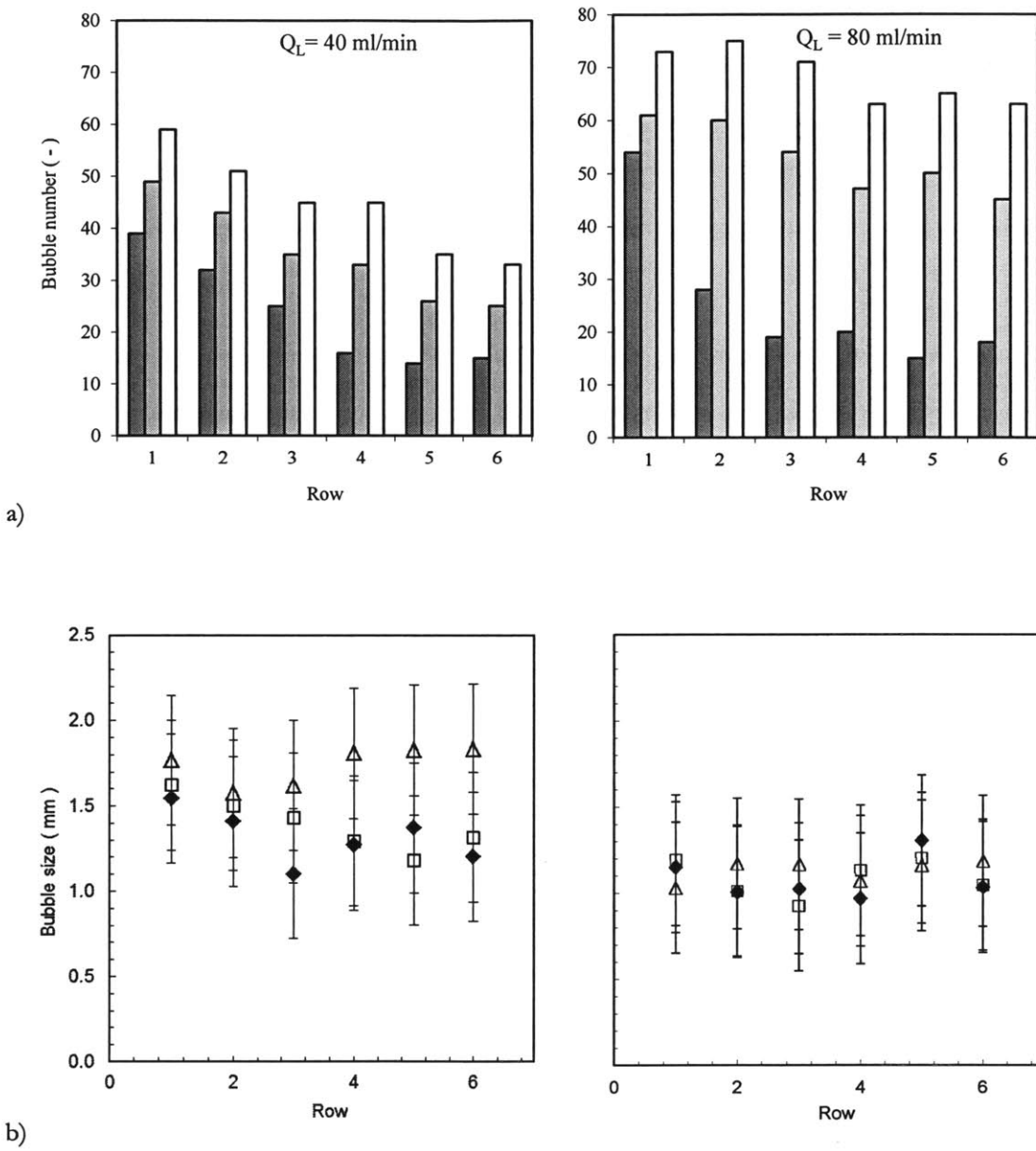


Figure 2.7: Variation in a) bubble number and b) bubble size along reactor length in vertical orientation for different gas and liquid flow rates. Legend Q_G (mL/min): a) dark grey ■, 13; soft grey ■, 36; white □, 73; b) bubble size at different gas flow rates (mL/min): ♦, 13; □, 36; △, 73; for different liquid flow rates: left, $Q_L = 40$ mL/min, and right, $Q_L = 80$ mL/min

2.4.2.5 Mass transfer coefficients

Individual mass transfer coefficients (k_L) were estimated using Calderbank's modification of surface renewal theory ²⁰ from the bubble slip velocities and average bubble size over the entire AFR for each operating condition. The bubble slip velocity was estimated from the experimental holdup and superficial gas and liquid velocities using eq 2.8 for a gas-liquid reactor with co-current flow ^{21,22}.

$$V_S = \left(\frac{V_G}{\varepsilon_G}\right) - \left(\frac{V_L}{\varepsilon_L}\right) \quad (2.8)$$

It can be seen in Figure 2.8 that the slip velocity decreases with increasing bubble size, which is consistent with the observation of large bubbles at lower inlet liquid velocities. The variation in the values at a given liquid flow rate are due to the nature of the flow at a given gas-liquid flow rate combination, which governs the local shear rate and hence, the average bubble size.

In the penetration theory ²³ the mass transfer across the interface is considered as an unsteady state process, whereas, for all eddies, equal age-distribution is considered. This assumption yields the expression given by eq 2.9 for the individual mass transfer coefficient.

$$k_L = 2\sqrt{\frac{D_L}{\pi t}} \quad (2.9)$$

The k_L values depend on the interface mobility, which in turn can be given in terms of time span for a size specific surface renewal. Following these arguments Calderbank ²⁴ derived the value of contact time (t) in a bubbling system, in terms of the average bubble size ($\overline{d_B}$) and the average bubble slip velocity (V_B):

$$k_L = 2\sqrt{\frac{D_L V_B}{\pi \overline{d_B}}} \quad (2.10)$$

The variable V_B is the terminal rise velocity of a bubble in a stagnant liquid, but in dispersion it is the slip velocity of the bubble, i.e. V_S . After these considerations, the values of slip velocity and dispersed phase holdup were used for the calculation of k_L . Overall mass transfer coefficients ($k_L a$) were estimated using the so-calculated individual mass transfer coefficients (k_L) and the obtained specific surface area (a) from the flow visualization experiments.

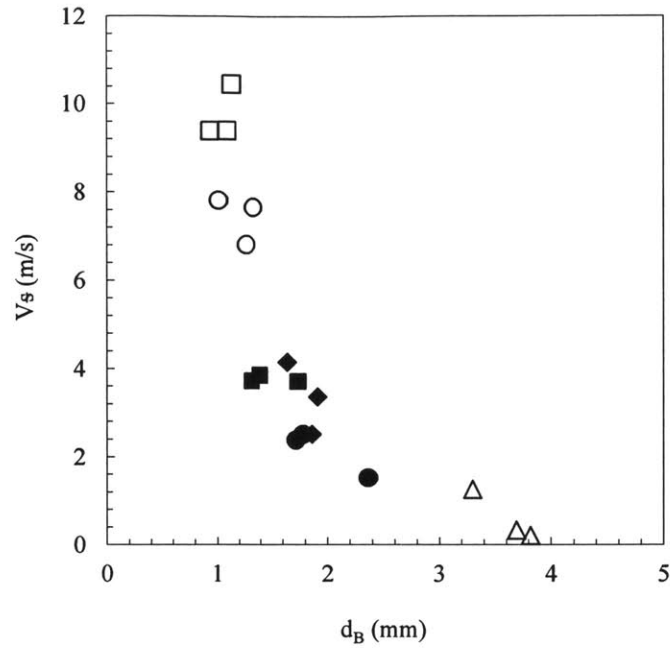
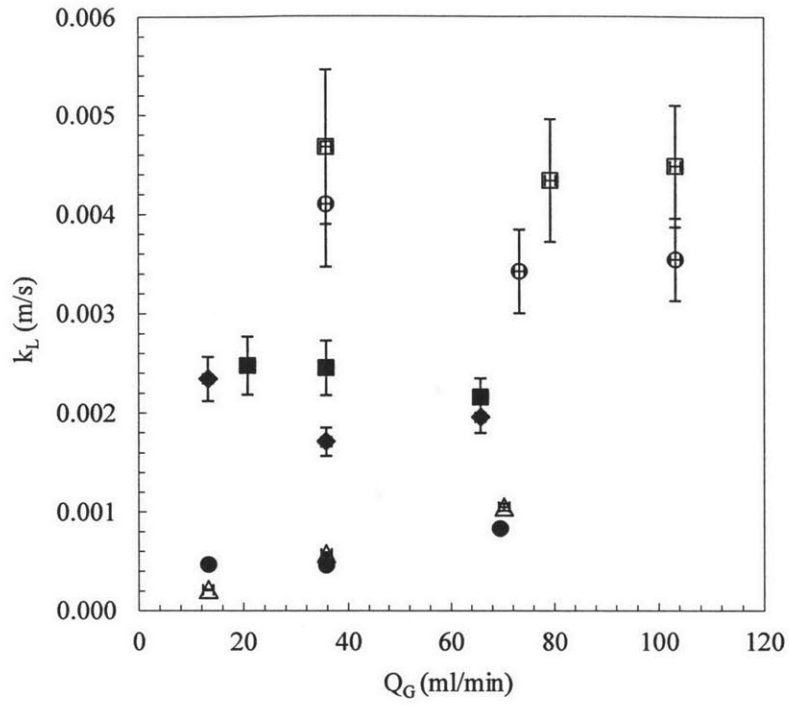


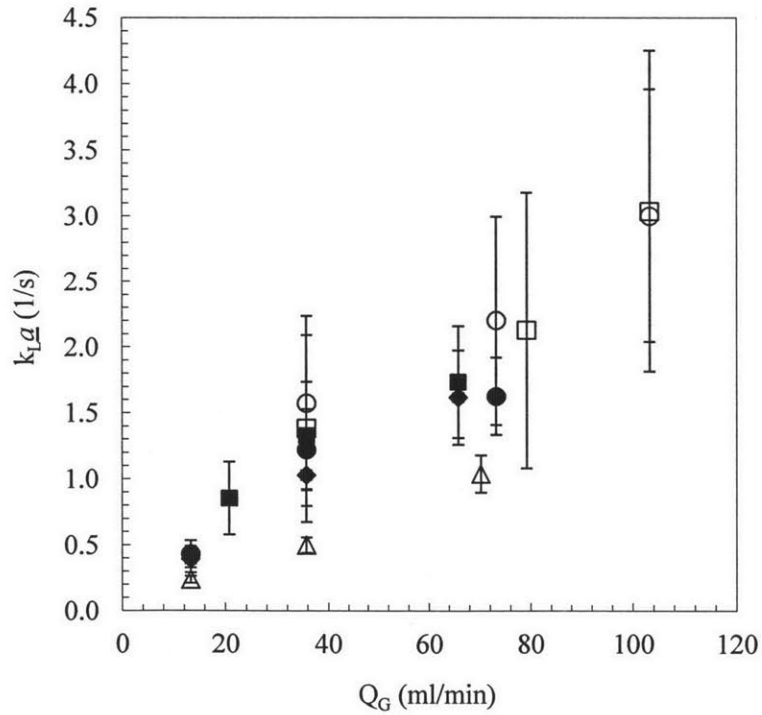
Figure 2.8: Variation in slip velocity with bubble size in vertical orientation for different water flow rates (mL/min): \triangle , 10; \bullet , 20; \blacklozenge , 30; \blacksquare , 40; \circ , 60; \square , 80;

The observations on the estimated individual and overall mass transfer coefficients are shown in Figures 2.9 a) and b). Water flow rate has an important effect on k_L increasing its value for higher flow rates, whereas gas flow rate affects more significantly $k_L a$ due to its effect on the specific interfacial area. Thus, both gas and liquid flow rates have the effect of increasing $k_L a$ values.

The obtained k_L and $k_L a$ in the AFR are about one order of magnitude larger than those of conventional contactors, such as bubble columns, counter-current packed columns, tube reactors, and stirred tanks ²⁵. A comparison of $k_L a$ as a function of specific power consumption for different contactors is discussed in section *Comparison of AFR with other gas-liquid contactors*.



a)



b)

Figure 2.9: Variation in a) individual and b) overall mass transfer coefficients with gas flow rate in vertical orientation for different water flow rates (mL/min): Δ , 10; \bullet , 20; \blacklozenge , 30; \blacksquare , 40; \circ , 60; \square , 80;

Overall mass transfer coefficients were measured by titration for water flow rates of 10, 20, and 40 mL/min. The experimental results and comparison with estimated values using two different methods are presented in Figure 2.10. “Method I” corresponds to estimated $k_{L,a}$ from modified surface renewal theory and flow visualization experiments (already shown in Figure 2.9), and “Method II” corresponds to $k_{L,a}$ values obtained from a mass balance of CO₂ along the reactor. For this approach it is necessary to know the gas holdup variation from row 1 to row 6 in the AFR which was taken from the flow visualization experiments. The absorbed amount of CO₂ into water was estimated from the decrease in gas holdup from the inlet towards the outlet, and $k_{L,a}$ from the contact time and equilibrium concentration in water at the operating pressure and temperature. The $k_{L,a}$ values for 10 and 20 mL/min show better agreement with the experiments than for 40 mL/min. The contact time based slip velocity and bubble size model holds for well-behaved laminar flows. The flow in the AFR actually undergoes continuous splitting and merging in a confined domain, and this may be the reason for the lack of agreement between the experiments and Modell II, especially for 40 mL/min. The calculation of $k_{L,a}$ is very sensitive to variables such as contact time between phases, and gas and liquid velocities. These are values that change locally along the flow path in the AFR and thus, the estimated values should only be considered as order of magnitude estimations.

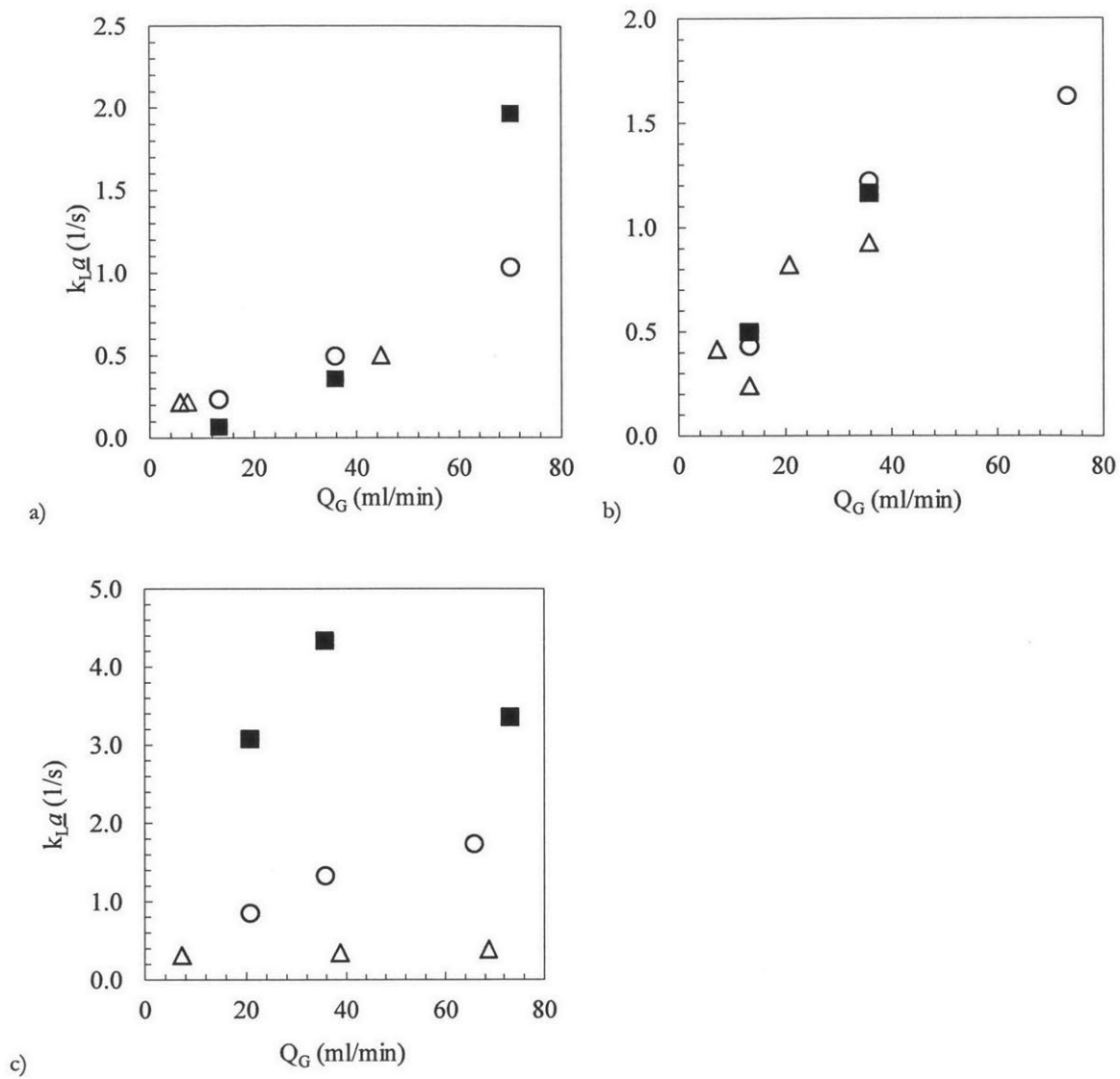


Figure 2.10: Overall mass transfer coefficients for different water and gas flow rates in vertical orientation using different methods. a) $Q_L = 10$ mL/min, b) $Q_L = 20$ mL/min, c) $Q_L = 40$ mL/min. Legend: \square , Titration; \circ , Method I; \blacksquare , Method II;

2.4.3 Horizontal orientation

As mentioned previously, the AFR modules are normally used in vertical orientation in order to guarantee a good performance in terms of heat transfer by reducing possible channelling effects of the heating/cooling fluid. However, at sufficiently high flow rates of the heat transfer fluid, the issue of channelling is irrelevant and similar to the posted microreactors²⁸ the modules can be kept in horizontal orientation. In that case the AFR is expected to show a different behaviour than the suggested vertical orientation, in which gravity effects are significant at low flow rates. The observations of our experiments using the horizontal configuration are reported in this section.

2.4.3.1 Bubble size distribution

The variation in the measured number-average $\overline{d_B}$ with flow rate ratio is shown in Figure 2.11. At constant Q_L , the average bubble size increases with increasing Q_G , whereas at constant Q_G , the bubble size decreases with increasing Q_L due to the early bubble detachment caused by increased shear rates at the inlet. Although this trend is independent of the AFR module orientation, the average bubble size for the horizontal orientation is larger than the vertical orientation by approximately 1.6 times depending upon the specific gas and liquid flow rates. The difference can be explained based on the gravitational effects observed in the vertical configuration, which enhances bubble breakup. In the horizontal orientation the detachment of bubbles at the inlet is dominated by shear, which yields relatively large bubbles. At low liquid flow rates (10 and 20 mL/min) the average bubble size decreases rapidly with the liquid-to-gas flow rate ratio. This variation is relatively smaller at higher liquid flow rates (60-80 mL/min), which indicates the change of flow regime in the system.

The bubble size distributions for different gas and liquid flow rates in horizontal orientation are included in Figure A.2 of the *Appendix*. Unimodal bubble size distributions are obtained at all combinations of flow rates. For a constant liquid flow rate, increasing the gas flow rate shifts the average bubble size to larger values. At low liquid flow rates (10-20 mL/min of water), broader bubble size distributions are

obtained and they become broader when increasing gas flow rates. For instance, for 10 mL/min of water, the bubble size spans up to 39 mm for the lowest gas flow rate (6 mL/min), and increases up to 106 mm for the largest gas flow rate (36 mL/min). Increasing the liquid flow rate narrows the bubble size distribution decreasing the interval of bubble sizes encountered. In addition, at high water flow rates (60 and 80 mL/min), the effect of the gas flow rate on the bubble size is less strong. For example, at 60 mL/min of water, increasing the gas flow rate from 24 to 78 mL/min increases the maximum bubble size from 9.2 to 17 mm. This effect is reduced at 80 mL/min, where all the bubble size intervals fall in the range 2.0 - 13 mm almost independently of the gas flow rate (36, 73, and 88 mL/min).

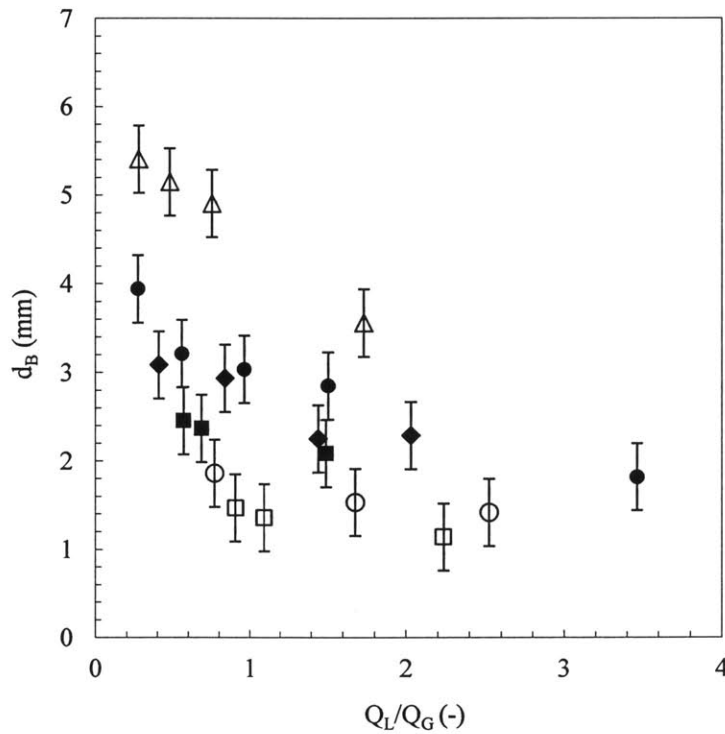


Figure 2.11: Variation in average bubble diameter with flow rate ratio in horizontal orientation for different water flow rates (mL/min): Δ , 10; \bullet , 20; \blacklozenge , 30; \blacksquare , 40; \circ , 60; \square , 80;

2.4.3.2 Gas holdup

The gas holdup (shown in Figure 2.12) was estimated following the procedure already discussed for the vertical orientation. The results show that the gas holdup is a very strong function of the ratio Q_L/Q_G , increasing with Q_G at constant Q_L , and correlates with the flow rate ratio according to eq 2.11.

$$\epsilon_G = 0.2468(Q_L/Q_G)^{-1.205} \quad (2.11)$$

Here it is important to notice that the gas holdup at the lowest water flow rates (10 and 20 mL/min) and highest gas flow rates is very high, corresponding to a flow regime where most part of the hearts are filled with gas phase and barely bubble breakup occurs. This translates into a poor mass transfer performance for the lowest water flow rates, and thus, operating at larger liquid flow rates for high gas flow rates is recommended in order to create a high quality distribution of the dispersed phase flow.

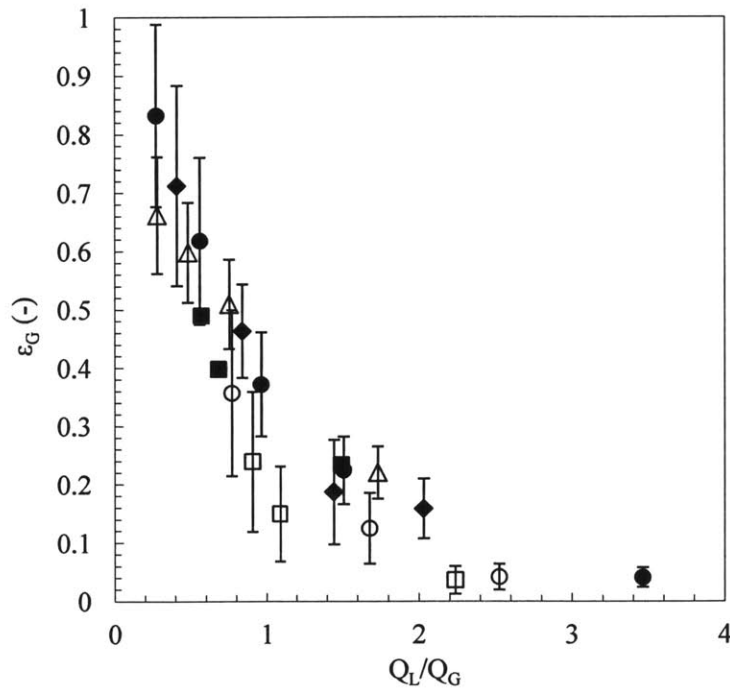


Figure 2.12: Variation in gas holdup with flow rate ratio in horizontal orientation for different water flow rates (mL/min): \triangle , 10; \bullet , 20; \blacklozenge , 30; \blacksquare , 40; \circ , 60; \square , 80;

2.4.3.3 Specific interfacial area

The specific interfacial area shown in Figure 2.13 is estimated from the gas holdup and the average bubble size for the horizontal orientation and correlated to the flow rate ratio, according to eq 12.

$$a = 602.7 (Q_L/Q_G)^{-0.783} \quad (2.12)$$

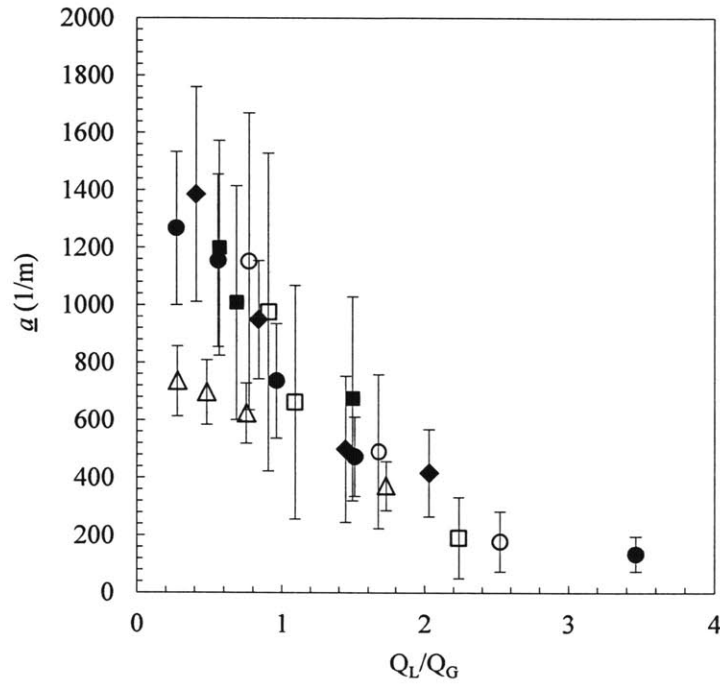


Figure 2.13: Variation in specific interfacial area with inlet flow rate ratio in horizontal orientation for different water flow rates (mL/min): Δ , 10; \bullet , 20; \blacklozenge , 30; \blacksquare , 40; \circ , 60; \square , 80;

2.4.3.4 Properties of dispersion along the flow path

Similar to the vertical orientation case, the bubble diameter in the horizontal orientation also changes continuously along the flow path. The bubble size distributions within the entire module and the variation of bubble size and number of bubbles by row along the flow path were quantified from the image analysis. In general, both bubble size and number of bubbles decrease towards the end of the flow path, which

corresponds to a decrease in gas holdup. This is an empirical evidence of the absorption of carbon dioxide into water and the trends are similar to those in the vertical orientation of AFR module. All the observations discussed about the dispersion characteristics for different gas and liquid flow rates are shown through images in the first and sixth rows of the AFR in Figure 2.14.

Complete absorption of carbon dioxide occurs for sufficiently high water-to-gas flow rate ratio and long contact times. This behavior being observed in this reactive system was not observed in flow visualization experiments performed in the AFR for the non-reactive hexane-water system.²⁷

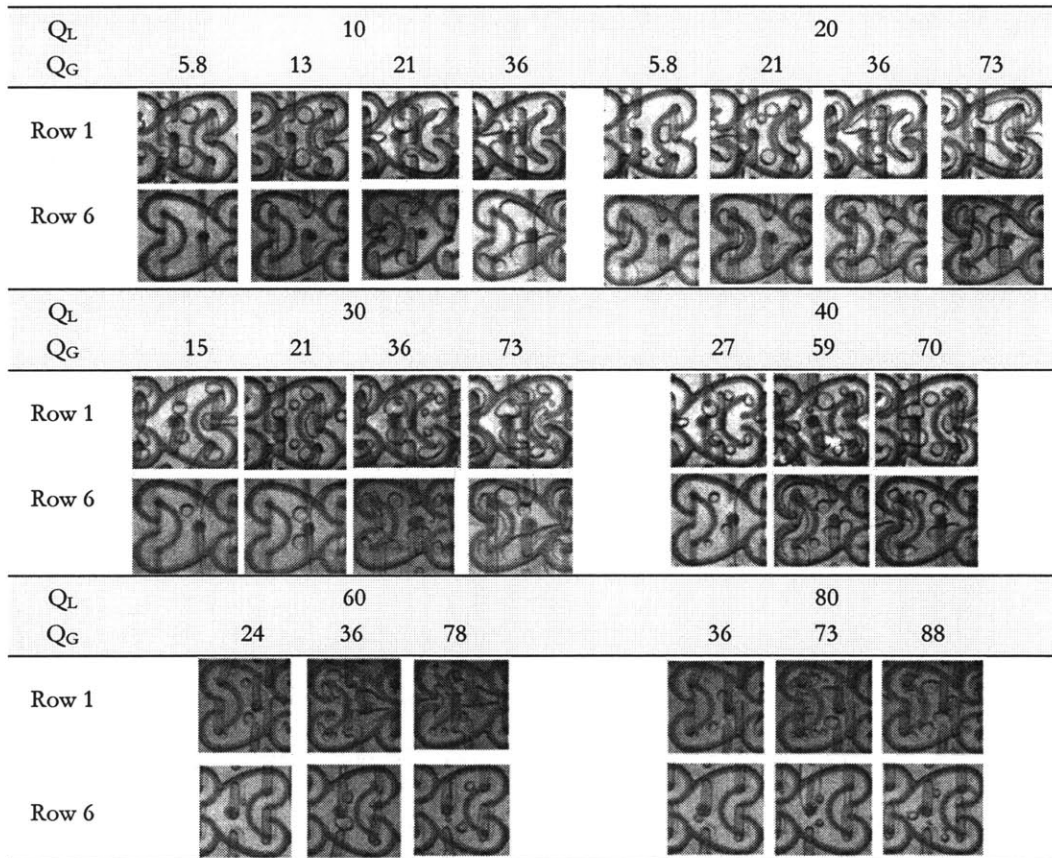


Figure 2.14: Flow patterns in horizontal orientation for different water Q_L and gas flow rates Q_G (mL/min). Row 1 indicates the first row in the flow path (closer to the inlet), and row 6 indicates the sixth row (closer to the outlet). Droplet size, holdup, and number of bubbles decrease from row 1 (inlet) to row 6 (outlet) due to absorption of carbon dioxide into water.

2.4.3.5 Mass transfer coefficients

The bubble slip velocity was estimated from the gas holdup obtained from the image analysis and superficial phase velocities using eq 2.8. Similar to the case of vertical orientation of the AFR, the slip velocity decreases with increasing bubble size. This means that for larger bubbles, the difference between velocities of each phase becomes smaller, lowering the interfacial mass transfer rates. The slip velocities and average bubble size were used for the estimation of individual (k_L) and overall mass transfer coefficients ($k_{L\bar{a}}$). The values of k_L and $k_{L\bar{a}}$ for different liquid flow rates in term of gas flow rate are shown in Figure 2.15. It was observed that $k_{L\bar{a}}$ increases with increasing Q_G , which is largely due to an increase in \bar{a} . Both Q_G and Q_L have a positive effect on the overall mass transfer coefficient.

2.4.4 Pressure drop

Pressure drop measurements were used to estimate the power consumption in the AFR and a correlation based on the Lockhart-Martinelli method ²⁸ was developed using modified friction factors as a function of the gas holdup and Reynolds number. Typically, in a conventional stirred tank energy is given to the liquid through agitation, which generates a flow field specific to the impeller for a given energy or power input. In an AFR, the energy is given to the liquid by pumping it at specific flow rates such that the pressure energy gets converted into kinetic energy resulting in mixing and dispersion.

The experimental pressure drop data is shown Figure 2.16. Pressure drop increases with inlet superficial gas velocity and two-phase Reynolds number. At a given liquid flow rate, the two-phase pressure drop is greater than that of single-phase. This reflects the additional pressure drop that is present in this type of flow with bubbles moving through a continuous liquid phase. Not only friction of single-phase due to the walls is present, but also, friction for each bubble flowing in water, breakup of bubbles dissipating energy, and impact of bubbles against obstacles throughout the reactor causing pressure loss.

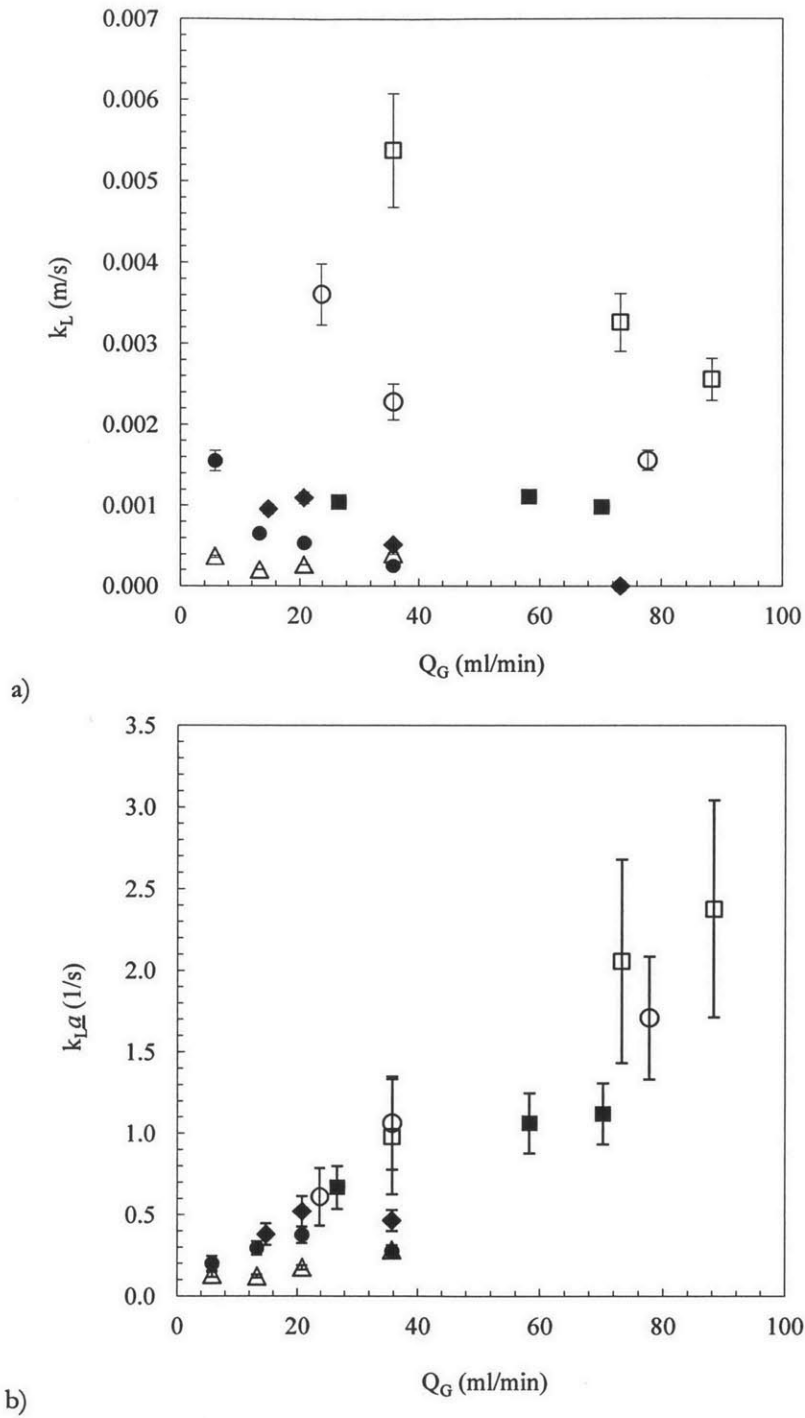


Figure 2.15: Variation in a) individual and b) overall mass transfer coefficients with gas flow rate in horizontal orientation for different water flow rates (mL/min): Δ , 10; \bullet , 20; \blacklozenge , 30; \blacksquare , 40; \circ , 60; \square , 80; k_L decreases with gas flow rate but increases with liquid flow rate; $k_L a$ increases with gas and liquid flow rates.

From theoretical and empirically verified dependencies, the total pressure drop $(\Delta p/\Delta L)_{TP}$ in a two-phase flow can be given by eq 2.13.

$$\left(\frac{\Delta p}{\Delta L}\right)_{TP} = \left(\frac{\Delta p}{\Delta L}\right)_{TPF} + \left(\frac{\Delta p}{\Delta L}\right)_a + \left(\frac{\Delta p}{\Delta L}\right)_H \quad (2.13)$$

The different terms indicate the pressure drop corresponding to different subscripts: TP is total pressure drop; TPF , two-phase frictional flow; a , acceleration; and H , the hydrostatic head. In general, for confined systems without significant height, the last two terms are negligible, which is the case for the system of study. Thus, the total pressure drop is equal to the two phase frictional pressure drop, which is calculated according to the Lockhart–Martinelli method using eq 2.14.

$$\left(\frac{\Delta p}{\Delta L}\right)_{TPF} = \phi_l^2 \left(\frac{\Delta p}{\Delta L}\right)_l = \phi_g^2 \left(\frac{\Delta p}{\Delta L}\right)_g \quad (2.14)$$

Each term is considered as a result of a single-phase flow of medium and is estimated individually using eq 2.15 and 2.16.

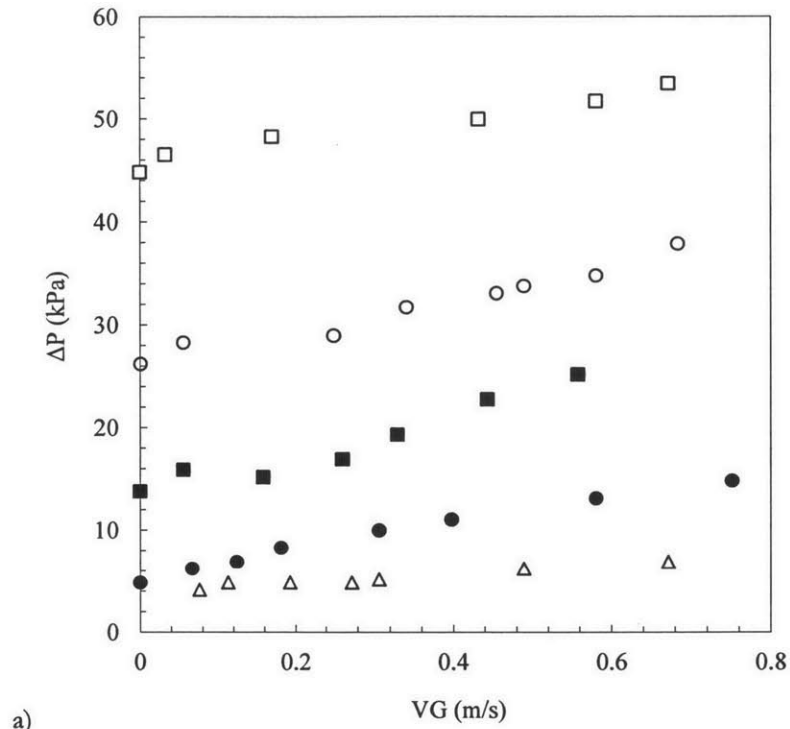
$$(\Delta p/\Delta L)_l = \lambda_l (1/d) (\rho_l V_l^2 / 2) \quad (2.15)$$

$$(\Delta p/\Delta L)_g = \lambda_g (1/d) (\rho_g V_g^2 / 2) \quad (2.16)$$

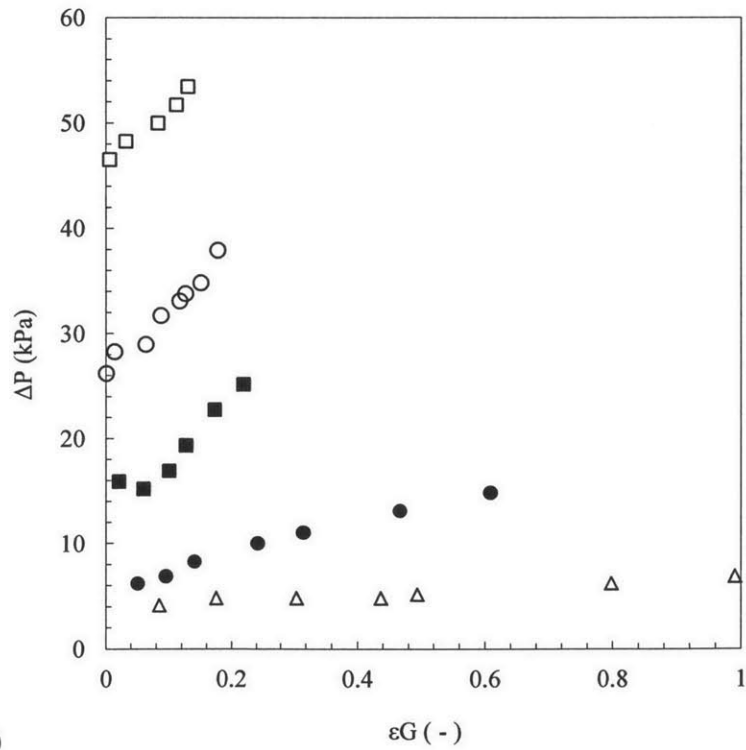
The parameters ϕ_l and ϕ_g in eq 2.14 are single-phase flow friction factors that depend on the Lockhart–Martinelli parameter χ through eq 2.17 and eq 2.18²⁹, respectively.

$$\phi_l^2 = 1 + \frac{C}{\chi} + \frac{1}{\chi^2} \quad (2.17)$$

$$\phi_g^2 = 1 + C\chi + \chi^2 \quad (2.18)$$



a)



b)

Figure 2.16: Variation in pressure drop with a) superficial gas velocity and b) gas holdup in vertical orientation for different water flow rates (mL/min): \triangle , 10; \bullet , 20; \blacksquare , 40; \circ , 60; \square , 80;

The Chisholm parameter (C) is a function of the tube diameter and the flow pattern for straight tubes. Mishima and Hibiki ³⁰ shown that this parameter decreases when decreasing the channel diameter. Here a correlation that accounts for the dependence of C on the mass flux proposed by Niu et al. ³¹ in terms of the Re for each phase and We number is used.

$$C = 0.0049 Re_L^{-0.98} Re_G^{1.08} We^{-0.86} \quad (2.19)$$

The estimated pressure drop using this correlation is shown in Figure 2.17 a) with the experimental values in terms of gas holdup. Figures 2.17 a) and b) show a good agreement between experimental and predicted values with relative errors that are within 15%, except for 10 mL/min of water flow rate, for which the errors are much higher.

The power consumption in the AFR was estimated directly from the experimental pressure drop data and flow rates, since the fluid pumping is the only source of power into the reactor. The results are shown in Figure 2.18 in terms of liquid-to-gas flow rate ratio. At constant liquid flow rate, the power consumption decreases with increasing the flow rate ratio (or decreasing gas flow rate). However, at constant flow rate ratio, the power consumption increases linearly with liquid flow rate, which indicates that the frictional pressure drop has a significant contribution to the total pressure drop, and in consequence, the power consumption.

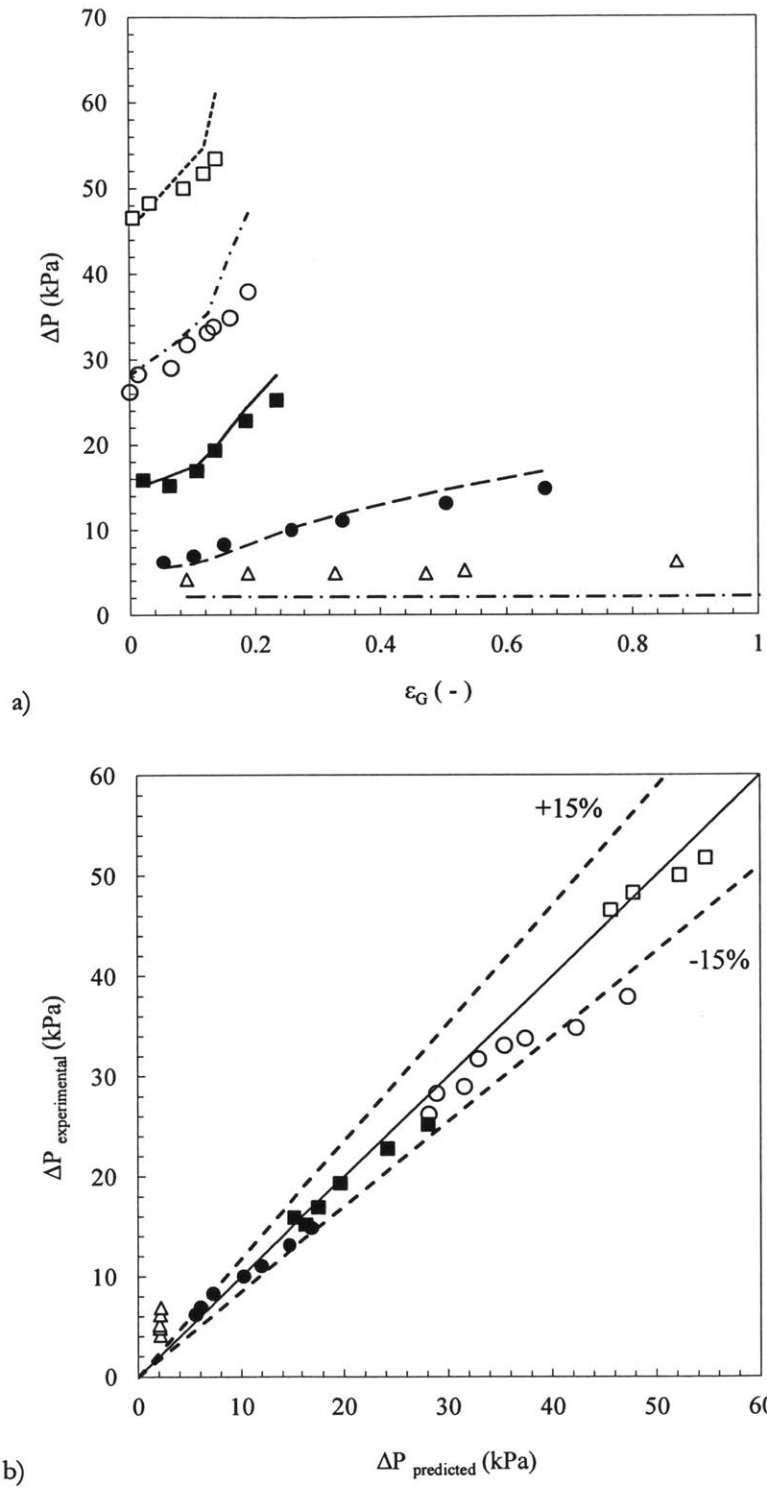


Figure 2.17: Comparison of experimental and predicted pressure drop in vertical orientation a) in function of gas holdup; b) experimental versus predicted pressure drop values. Symbols indicate different water flow rates (mL/min): \triangle , 10; \bullet , 20; \blacksquare , 40; \circ , 60; \square , 80; Lines indicate predictions.

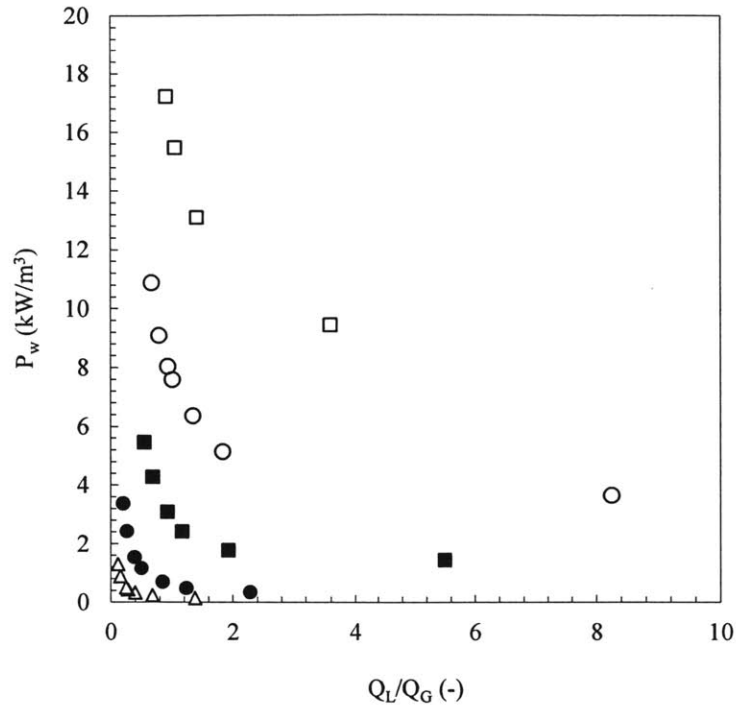


Figure 2.18: Variation in power consumption with flow rate ratio in vertical orientation for different water flow rates (mL/min): Δ , 10; \bullet , 20; \blacksquare , 40; \circ , 60; \square , 80;

2.4.5 Comparison of AFR with other gas-liquid reactors

The obtained hydrodynamic parameters for gas-liquid flow in the AFR are compared with other gas-liquid contactors to measure the reactor performance (Figure 2.19 and Table 2.2). The overall mass transfer coefficient depends on the energy input introduced in the system. Therefore, a good metric to compare the reactor performance is in terms of overall mass transfer coefficients versus power consumption. Typical overall mass transfer coefficients for stirred tanks of different volumes are in the range of $0.003 - 0.10 \text{ s}^{-1}$ for power consumptions of $80 - 2,000 \text{ W/m}^3$. Mass transfer coefficients one order of magnitude larger can be achieved in the AFR ($0.2 - 3 \text{ s}^{-1}$) for power inputs of $90 - 17,000 \text{ W/m}^3$. The main difference between the stirred vessel and the Corning system is that additional power is required to provide agitation in the stirred tank, whereas the AFR only consumes energy to pump the fluids through the reactor and create interfacial area.

A forced circulation pumped loop reactor provides overall mass transfer coefficients higher than an airlift reactor with no external pumping, particularly for liquid circulation rates larger than 1 m³/h. Overall mass transfer coefficients of 0.015-0.06 s⁻¹ for power consumptions of 375-550 and 800-1,080 W/m³ for liquid circulation rates of 1.5 and 2.0 m³/h, respectively, are achieved. Similar values for $k_L a$ (0.015 – 0.04 s⁻¹) are obtained using aero-ejectors working in bubble flow regime, for power consumption of 200 – 800 W/m³. Other gas-liquid contactors with gas-inducing impellers, ring sparkers and surface aeration systems, provide smaller mass transfer coefficients for the same power input.

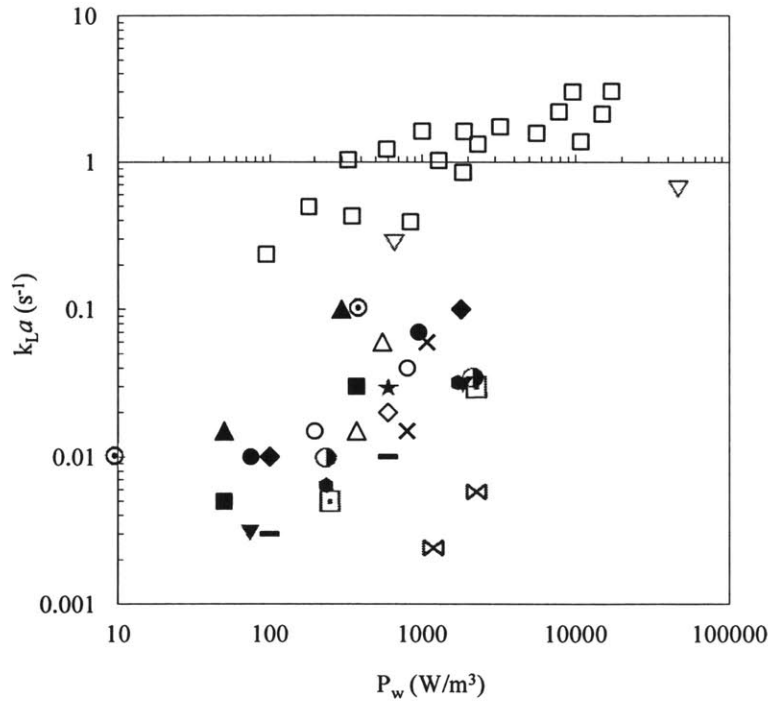


Figure 2.19: Comparison of overall mass transfer coefficients in function of power consumption among different gas-liquid contactors^{19,32-38}: □, Corning AFR; ■, Novel forced circulation loop reactor I; △, Novel forced circulation loop reactor II; ×, Novel forced circulation loop reactor III; ◇, Stirred tank; ▢, Stirred tank (2 L); ▼, Stirred tank (20 L); ◆, Stirred tank (500 L); ●, Stirred tank (1000 L); ●, Bubble column with membrane I; ▲, Bubble column with porous II; ○, Aero ejector bubble flow; ★, Oscillatory flow; ⊙, Miniature lab bubble bioreactor; ⊖, Six-bladed concave gas-inducing impeller; ⊞, Six-bladed concave impeller with ring sparker; ⊗, Six-bladed concave impeller with surface aeration; ∇, Monolith loop reactor

The AFR provides specific interfacial areas on the same order of magnitude as static mixers, packed columns, stirred tanks, and vertical tube reactors ($100 - 1,000 \text{ m}^2/\text{m}^3$), as it is shown in Table 2.2. Extremely high specific surface areas ($3,400 - 9,000 \text{ m}^2/\text{m}^3$) and overall mass transfer coefficients ($0.30 - 21 \text{ s}^{-1}$) can be achieved in gas-liquid microchannels. Falling film microchannels operating in annular flow can provide interfacial areas on the order of $10,000 \text{ m}^2/\text{m}^3$ depending on the reactor dimensions.²⁵ However, the throughput in microchannels is not sufficient for commercial scale applications. The AFR overcomes this problem with larger channel sizes and a special design of the flow path, and provides better mass transfer performance than many other commonly used gas-liquid contactors.

Table 2.2: Comparison of individual and overall mass transfer coefficients and specific interfacial areas among different gas-liquid contactors¹⁹

Type of contactor	$k_L 10^5$ (m/s)	a (m^2/m^3)	$k_L a 10^2$ (s^{-1})	Citations from ref.
Bubble columns	10-40	50-600	0.5-24	Charpentier, 1981
Couette-Taylor flow reactor	9-20	200-1,200	3-21	Diuska et al., 2004
Impinging jet absorbers	29-66	90-2,050	2.5-122	Herskowits et al., 1990
Packed columns, concurrent	4-60	10-1,700	0.04-102	Charpentier, 1981
Packed columns, counter-current	4-20	10-350	0.04-7	Charpentier, 1981
Spray column	12-19	75-170	1.5-2.2	Kies et al., 2004
Static mixers	100-450	100-1,000	10-250	Heyouni et al., 2002
Stirred tank	0.3-80	100-2,000	3-40	Kies et al., 2004
Tube reactors, horizontal and coiled	10-100	50-700	0.5-70	Charpentier, 1981
Tube reactors, vertical	20-50	100-2,000	2-100	Charpentier, 1981
Gas-liquid microchannel	40-160	3,400-9,000	30-2,100	Yue et al., 2007
Corning system: vertical	46-490	160-1,300	39-303	This work
Corning system: horizontal	20-540	140-1,400	13-150	This work

The individual mass transfer coefficient and the specific interfacial area depend on the power consumption per unit volume. For bubble columns and aerated stirred vessels both variables scale with the energy dissipation rate as: $k_L \sim \varepsilon^{0.25}$ and $a \sim \varepsilon^{0.40}$,³⁹ so that the overall mass transfer coefficient, $k_L a \sim \varepsilon^{0.65}$ according to Kolmogorov's inertial range hypothesis. The intercept of this dependence clearly indicates the value of $k_L a$ at the lowest value of power consumed per unit volume. It is necessary to study this aspect in

detail and develop methods that can help understanding the relationship between fluid turbulence, interfacial transport and device geometry. While the rate of energy dissipation is proportional to the power consumption per unit volume, the exact dependence may vary from system to system. For the AFR, it was observed that $k_{L,a}$ depends on both power input and gas holdup, and a correlation based on both variables was obtained (eq 2.22) Predictions agreed with the experimentally measured values, with most of the relative errors below 15%, as shown in Figure 2.20.

$$k_{L,a} = 0.101 P_w^{0.443} \varepsilon_G^{0.459} \quad (2.22)$$

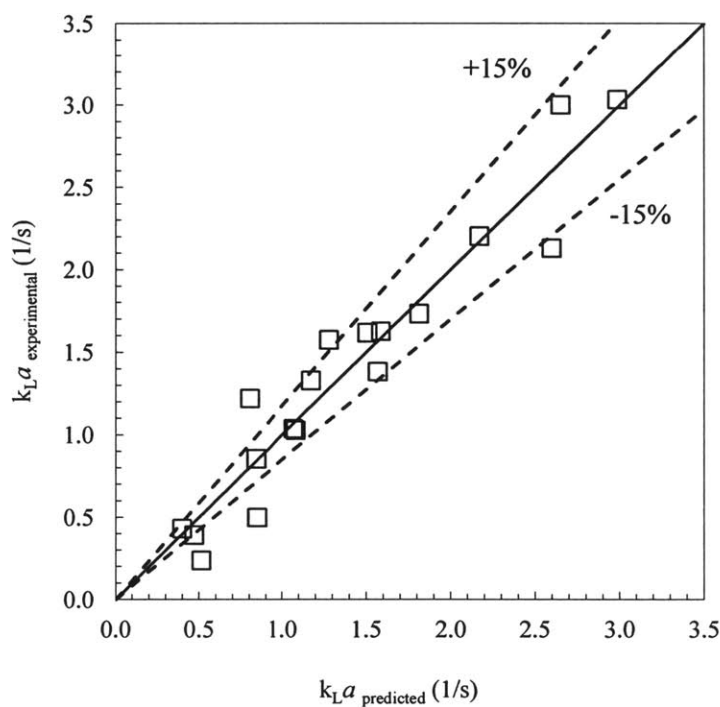


Figure 2.20: Experimental versus predicted overall mass transfer coefficients for all gas and liquid flow rates. Dashed lines indicate relative error of 15%.

Although the performance parameters in terms of hydrodynamics favour the AFR, other issues such as capacity of the reactors, capital cost, return on investment, or payback period, among others, will determine the viability of the process and, consequently, the selection of the reactor for a specific gas-liquid reaction.

2.5 Conclusions

The hydrodynamics for two-phase gas-liquid flow in a Corning Advanced Flow Reactor® (AFR) mixing module were studied experimentally. Carbon dioxide-water was used the gas-liquid model system and experiments were performed at ambient temperature (~ 22 °C) and atmospheric pressure, for gas and liquid flow rates ranging from 5.6 – 103 mL/min and 10 – 80 mL/min, respectively. The effect of the orientation of the AFR on the hydrodynamics was quantitatively analyzed and was found not to be significant for the operating conditions tested. The key observations are: (i) For both orientations, the bubble size distribution is strongly affected by the gas and liquid flow rates. The trends observed for the bubble size are independent of the module orientation, except for the actual values of bubble size. (ii) At constant gas flow rates, the average bubble size decreases continuously with increasing liquid flow rate and increases with gas flow rate. (iii) High interfacial mass transfer rates in the AFR lead to a decrease in the number of bubbles and gas holdup along the reactor length, which indicates that it would be useful to have the gas phase in excess while conducting gas-liquid reactions in AFR. (iv) The gas holdup and the effective interfacial area show a power law relationship with the ratio Q_L/Q_G . (v) The pressure drop for two-phase flow is larger than for single-phase flow and can be correlated using the Lockhart-Martinelli method. (vi) Overall mass transfer coefficients increase with power consumption and gas holdup by a power law relationship. (vii) With respect to hydrodynamics, the AFR is more efficient in comparison with other commonly used gas-liquid contactors.

2.6 Notation

a	Effective interfacial area (m^2/m^3)
C	Chisholm parameter (-)
d_{Bi}	Individual bubble size (m)
$\overline{d_B}$	Average bubble size over the entire AFR module (m)
D_h	Hydraulic diameter (m)

D_L	Diffusion coefficient (m^2/s)
g	Gravity acceleration (m/s^2)
h	Channel height (h)
w	Channel width (m)
k_L	Individual mass transfer coefficient (m/s)
k_{Lg}	Overall mass transfer coefficient ($1/\text{s}$)
P_w	Power consumption (W/m^3)
Q_G	Volumetric gas flow rate (mL/min)
Q_L	Volumetric liquid flow rate (mL/min)
t	Contact time (s)
v_B	Terminal rise velocity of a bubble in stagnant liquid (m/s)
V_G	Gas superficial velocity (m/s)
V_L	Liquid superficial velocity (m/s)
V_S	Slip velocity of the bubble (m/s)

Dimensionless numbers

Ca	Capillary number (-)
Fr	Froude number (-)
Re	Reynolds number (-)
We	Weber number (-)

Greek Symbols

ε_G	Gas holdup (-)
ε_L	Liquid holdup (-)
λ	Friction factor (-)
ρ	Density (kg/m^3)
$\frac{\Delta p}{\Delta L}$	Pressure drop per unit length (Pa/m)

ε	Energy dissipation rate (m^2/s^3)
σ	Surface tension (N/m)
μ	Viscosity (Pa s)
Φ_l	Correction factor for liquid phase pressure drop depending on χ (-)
Φ_g	Correction factor for gas phase pressure drop depending on χ (-)
χ	Lockhart–Martinelli parameter (-)

Subscripts

L	Liquid phase
G	Gas phase
TP	Total pressure drop
TPF	Two phase frictional flow
a	Acceleration
H	Hydrostatic head

2.7 References

- (1) Jensen, K. F. Microreaction engineering — is small better? *Chem. Eng. Sci.*, **2001**, *56*, 293-303.
- (2) Hessel, V. From Microreactor Design to Microreactor Process Design. *Chem. Eng. Tech.*, **2005**, *28*, 243-243.
- (3) Wakami, H.; Yoshida, J. Grignard exchange reaction using a microflow system: from bench to pilot plant. *Org. Proc. Res. Dev.*, **2005**, *9*, 787-791.
- (4) Hartman, R. L.; McMullen, J. P.; Jensen, K. F. Deciding whether to go with the flow: evaluating the merits of flow reactors for synthesis. *Angewandte Chemie International Edition in English* **2011**, *50*, 7502-7519.
- (5) Roberge, D. M.; Ducry, L.; Bieler, N.; Cretton, P.; Zimmermann, B. Microreactor technology: a revolution for the fine chemical and pharmaceutical industries? *Chem. Eng. Tech.*, **2005**, *28*, 318-323.
- (6) Roberge, D. M.; Zimmermann, B.; Rainone, F.; Gottsponer, M.; Eyholzer, M.; Kockmann, N. Microreactor technology and continuous processes in the fine chemical and pharmaceutical industry: is the revolution underway? *Org. Proc. Res. Dev.*, **2008**, *12*, 905-910.
- (7) Hessel, V. Novel process windows - gate to maximizing process intensification via flow chemistry. *Chem. Eng. Tech.*, **2009**, *32*, 1655-1681.

- (8) Calabrese, G. S.; Park, S.; Pissavini, S. From batch to continuous flow processing in chemicals manufacturing. *AIChE J.* **2011**, *57*, 828-834.
- (9) Iwasaki, T.; Kawano, N.; Yoshida, J.-ichi Radical polymerization using microflow system: numbering-up of microreactors and continuous operation. *Org. Proc. Res. Dev.*, **2006**, *10*, 1126-1131.
- (10) Togashi, S.; Miyamoto, T.; Asano, Y.; Endo, Y. Yield improvement of chemical reactions by using a microreactor and development of a pilot plant using the numbering-up of microreactors. *J. Chem. Eng. Japan*, **2009**, *42*, 512-519.
- (11) Prat, L.; Devatine, A.; Cognet, P.; Cabassud, M.; Gourdon, C.; Elgue, S.; Chopard, E. Performance evaluation of a novel concept "open plate reactor" applied to highly exothermic reactions. *Chem. Eng. Tech.*, **2005**, *28*, 1028-1034.
- (12) Janicke, M. The controlled oxidation of hydrogen from an explosive mixture of gases using a microstructured reactor/heat exchanger and Pt/Al₂O₃ catalyst. *J. Catalysis*, **2000**, *191*, 282-293.
- (13) Roberge, D. M.; Gottsponer, M.; Eyholzer, M.; Kockmann, N. Industrial design, scale-up, and use of microreactors. *Chemistry Today*, **2009**, *7*, 8-11.
- (14) Vankayal, B. K.; Hessel, V.; Menges, G.; Hofmann, C.; Metzke, D.; Krtschil, U.; Kost, H. Scale-up of process intensifying falling film microreactors to pilot plant production scale. *International J. Chem. Reactor Eng.*, **2007**, 1-10.
- (15) National Institute of Standards and Technology (NIST).
- (16) ImageJ, Image analysis and processing in Java.
- (17) Danckwerts, P. V. Significance of Liquid-Film Coefficients in Gas Absorption. *Eng. Process Dev.*, **1951**, *43*, 1460-1467.
- (18) Mayinger, F.; Feldmann, O. Bubbly flows. Analysis, Modelling and Calculation; Sommerfeld, P. D.-I. M., Ed.; *Springer Berlin Heidelberg*: Garching, Germany, **2004**, 319-335.
- (19) Yue, J.; Chen, G.; Yuan, Q.; Luo, L.; Gonthier, Y. Hydrodynamics and mass transfer characteristics in gas-liquid flow through a rectangular microchannel. *Chem. Eng. Sci.*, **2007**, *62*, 2096 – 2108.
- (20) Calderbank, P. H.; Lochiel, A. C. Mass transfer coefficients, velocities and shapes of carbon dioxide bubbles in free rise through distilled water. *Chem. Eng. Sci.*, **1964**, *19*, 485-503.
- (21) Lapidus, L.; Elgin, J. C. Mechanics of vertical-moving fluidized systems. *AIChE J.*, **1957**, *3*, 63-68.
- (22) Lockett, M. J.; Kirkpatrick, R. D. Ideal bubbly flow and actual flow in bubble columns. *Transactions of the Institution of Chemical Engineers*, **1975**, *53*, 267-273.
- (23) Higbie, R. The rate of absorption of a pure gas into a still liquid during short periods of exposure. *Transactions of the American Institute of Chemical Engineers*, **1935**, 365-389.
- (24) Calderbank, P. H.; Korchinski, I. J. O. Circulation in liquid drops (a heat transfer study). *Chem. Eng. Sci.*, **1956**, *6*, 65-78.
- (25) Kashid, M. N.; Renken, A.; Kiwi-Minsker, L. Gas-liquid and liquid-liquid mass transfer in microstructured reactors. *Chem. Eng. Sci.*, **2011**, *66*, 3876-3897.
- (26) Hill, G. A. Measurement of overall volumetric mass transfer coefficients for carbon dioxide in a well-mixed reactor using a pH probe. *Ind. Eng. Chem. Res.*, **2006**, *45*, 5796-5800.
- (27) Nieves-Remacha, M. J.; Kulkarni, A. a.; Jensen, K. F. Hydrodynamics of liquid-liquid dispersion in an Advanced-flow reactor. *Ind. Eng. Chem. Res.*, **2012**, *51*, 16251-16262.
- (28) Lockhart, R. W.; Martinelli, R. C. Proposed correlation of data for isothermal, two-phase, two-component flow in pipes. *Chem. Eng. Progress*, **1949**, *45*, 39-48.

- (29) Chisholm, D. A theoretical basis for the Lockhart-Martinelli correlation for two-phase flow. *Int. J. Heat and Mass Transfer*, **1967**, *10*, 1767-1778.
- (30) Mishima, K.; Hibiki, T. Some characteristics of air-water two-phase flow in small diameter vertical tubes. *Int. J. Multiphase Flow*, **1996**, *22*, 703-712.
- (31) Niu, H. N.; Pan, L. W.; Su, H. J.; Wang, S. D. Flow pattern, pressure drop, and mass transfer in a gas-liquid concurrent two-phase flow microchannel reactor. *Ind. Eng. Chem. Res.*, **2009**, *48*, 1621-1628.
- (32) Kashid, M. N.; Renken, A.; Kiwi-Minsker, L. Gas-liquid and liquid-liquid mass transfer in microstructured reactors. *Chem. Eng. Sci.*, **2011**, *66*, 3876-3897.
- (33) Doig, S. D.; Ortiz-Ochoa, K.; Ward, J. M.; Baganz, F. Characterization of oxygen transfer in miniature and lab-scale bubble column bioreactors and comparison of microbial growth performance based on constant $k_L a$. *Biotechnology progress*, **2005**, *21*, 1175-82.
- (34) Garcia-Ochoa, F. Theoretical prediction of gas-liquid mass transfer coefficient, specific area and hold-up in sparged stirred tanks. *Chem. Eng. Sci.*, **2004**, *59*, 2489-2501.
- (35) Markopoulos, J.; Christofi, C.; Katsinaris, I. Mass transfer coefficients in mechanically agitated gas-liquid contactors. *Chem. Eng. Tech.*, **2007**, *30*, 829-834.
- (36) Fadavi, a; Chisti, Y. Gas-liquid mass transfer in a novel forced circulation loop reactor. *Chem. Eng. J.*, **2005**, *112*, 73-80.
- (37) Forrester, S. E.; Rielly, C. D.; Carpenter, K. J. Gas-inducing impeller design and performance characteristics. *Chem. Eng. Sci.*, **1998**, *53*, 603-615.
- (38) J. Heiszwolf, J.; B. Engelvaart, L.; G. van den Eijnden, M.; T. Kreutzer, M.; Kapteijn, F.; A. Moulijn, J. Hydrodynamic aspects of the monolith loop reactor. *Chem. Eng. Sci.*, **2001**, *56*, 805-812.
- (39) Kawase, Y.; Moo-Young, M. Mathematical models for design of bioreactors: applications of Kolmogoroff's theory of isotropic turbulence. *Chem. Eng. J.*, **1990**, *43*, B19-B41.

3 Experimental study of liquid – liquid hydrodynamics in the Advanced-Flow Reactor

3.1 Abstract

Hydrodynamics and mass transfer of immiscible liquid-liquid flows are explored in an Advanced-Flow Reactor (AFR). With hexane/water as a model system, flow visualization techniques are used to determine drop size distribution, dispersed phase hold-up, and specific interfacial areas for a phase flow rate range of 10 to 80 mL/min. The complex geometry of the AFR with its continuously changing cross-section along the flow path and strategically placed obstacles creates pressure changes that cause drop break-up and enhance mass transfer. Observations show that a wide range of average drop size (0.33 - 1.3 mm) can be achieved in the AFR depending upon the inlet flow rates and inlet composition. Pressure drop measurements are performed to estimate the power consumption and are used to compare the efficiency of the AFR with conventional liquid-liquid contactors. The analysis shows that similar to microreactors, the AFR can provide overall mass transfer coefficients (1.9 to 41 s⁻¹) one order of magnitude larger than conventional stirred tank reactors and specific interfacial areas (1,000 - 10,000 m²) one order of magnitude higher than static mixers.

3.2 Introduction

A significant number of reactions in the Pharmaceutical industry involve multiphase systems¹⁻⁴, where the overall rate of reaction is largely limited by the interfacial mass transfer or by the ability to maintain isothermal condition. In particular, liquid – liquid systems are of huge relevance in chemical processes, including two-phase reactions (viz. nitration of aromatic substrates), solvent extractions, phase-transfer catalysis or reactive extractions⁵⁻⁸. Over the last two decades, microreactor technology has emerged as a promising technique in chemical processing with significant advantages over conventional process technologies, facilitating the usage of microreactors for the synthesis of highly energetic compounds or reactions where the selectivity is strongly sensitive to local temperatures. In addition, they are used in the

laboratory scale for performing kinetic studies, catalyst screening, optimization of reaction conditions, and elucidation of reaction mechanisms⁹⁻¹⁵.

There exists a growing interest in applying this technology to production levels in industry. However, direct increase of the throughput by parallelization of microreactor units (“scale-out” concept)^{11,12,16-21} becomes an expensive challenge. Overall good reactor performance is only guaranteed by achieving identical reaction conditions (flow uniformity, heat management, residence time distribution, pressure drop, etc) in each unit²², but tens or hundreds of microreactors in parallel would be required to obtain production rates of the order of kg/min. The alternative is to find an intermediate scale device with larger channel dimensions that still provides high transport rates and permits increasing the production rate by parallelization of a reasonable number of reactor units. Among a few commercially available options, the Advanced-Flow Reactor (AFR) ® manufactured by Corning Inc., which can handle flow rates on the order of 10 – 100 mL/min, was used in this study. Its design introduces a series of heart-shaped connected cells, which yield excellent mixing, large heat transfer areas (and hence, high heat transfer coefficient) and very good mass transfer. Although the channel size is greater than a typical microreactor, the design of individual cells helps compensate for the expected loss in the heat and mass transfer rates²³.

The overall reaction rate in multiphase reactions is determined by the competing intrinsic reaction kinetics and the mass transfer rates between the two phases. Studies of the hydrodynamics and mass transfer of liquid-liquid flow in microchannels have been reported in the literature²⁴⁻²⁸. While microreactors operate in a laminar regime with well-defined flow patterns and narrow drop size distributions²⁹⁻³¹, conventional stirred reactors usually operate in turbulent mode³² generating dispersions having wider drop size distributions. The behavior cannot be easily extrapolated to the AFR because of the many factors (viz. confined geometry, high shear regions, etc.) affecting the flow and the additional difficulties introduced by the geometry of the AFR, which is similar to a sequence of converging-diverging segments. Static mixers are typically used for enhancing mixing by splitting and recombining the flow stream through a pipe/tube with the heat transfer done entirely through the pipe wall. They are known for mixing miscible liquids, generating dispersions and emulsions of immiscible phases, liquid-liquid extraction, etc. Typically, the mixing scales for static mixers are

much larger than the system under consideration here. This in addition to the abovementioned applications of static mixers, because of the very high heat transfer area the AFR can be efficiently used for conducting reactions.

While the AFR is reported to offer excellent performance for specific reactions, a thorough analysis of the hydrodynamics for liquid-liquid systems is necessary. In view of this, Chapter 3 aims to study the hydrodynamics of the AFR for a model system (hexane-water). In the next section we discuss the experimental set-up, details of the different measurement techniques and the experimental method, followed by which the analysis of experimental data has been discussed. In order to evaluate the performance of the AFR in terms of hydrodynamic properties the results are compared with conventional liquid-liquid contactors and static mixers.

3.3 Experimental

A schematic view of the experimental set-up is shown in Figure 3.1. The system consisted of a single mixing unit of the Advanced-Flow Reactor ® (AFR), a dual ISCO syringe pump, and a pressure gauge apparatus. A high speed color Phantom camera model ir300 was connected to a computer and the control software Vision Research v7.3 was used to acquire the sequence of images. The acquisition rate was set to 500 fps and the exposure time to 100 μ s to obtain high quality of images with a resolution of 1152x896 pixels. In all cases, the visibility of the object was enhanced using back illumination and a suitable light diffuser.

MilliQ water (Millipore) and hexane were used in our experiments as the immiscible non-reacting liquid-liquid system with the properties shown in Table 3.1. The hexane phase was stained with Sudan red dye to easily identify the phases during high speed imaging. The two immiscible liquids, aqueous and organic, were pumped from their respective reservoirs at constant flow rate using a 500 mL ISCO dual syringe pump (1 μ L/min – 200 mL/min) with the two parts operating independently. Experiments were conducted at room temperature (~ 22 °C) at different water (0 – 80 mL/min) and hexane flow rates (0 – 80 mL/min). The outlet was kept open to atmospheric pressure.

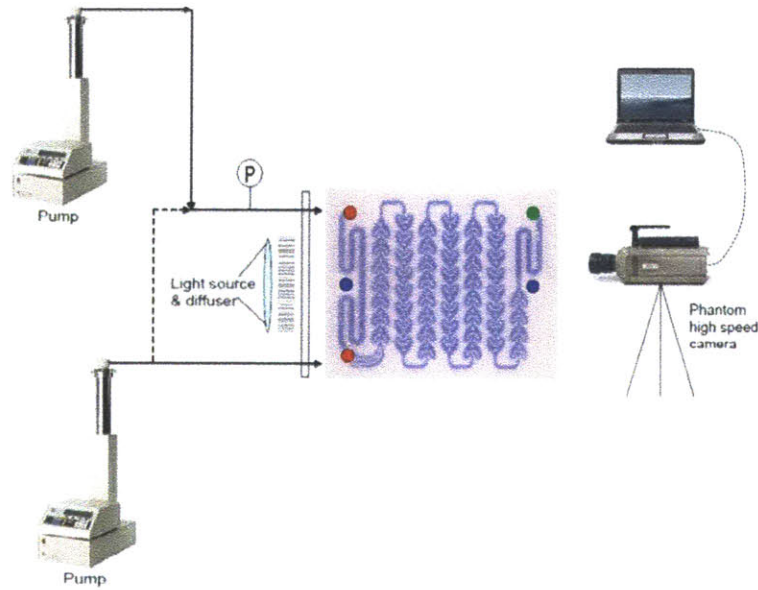


Figure 3.1: Schematic of experimental set-up for liquid-liquid flow visualization experiments. Liquids are pumped into the Advanced-Flow Reactor through a dual ISCO pump. Flow visualization experiments conducted using a high-speed Phantom camera connected to a computer

Table 3.1: Fluid properties of hexane and water at 20 °C ³³

Contactor type	Density (kg/m ³)	Viscosity (Pa·s)	Interfacial tension (kg/s ²)
Hexane	659.4	0.0003	0.0511
Water	998.2	0.001	

One frame of each five seconds-movie recorded at steady-state flow was analyzed using ImageJ® software to extract the number of drops and the drop size. The so-obtained data was further used to estimate the specific surface area (a) and hexane hold-up (ϵ_h). The phase hold-up was used to estimate the slip velocity (v_s) between phases. Mass transfer coefficients (k_L) were calculated theoretically using the Dankwert's surface renewal theory. Overall mass transfer coefficients ($k_L a$) were obtained from the specific interfacial area (a) from the flow visualization and the true mass transfer coefficients (k_L) from the theoretical estimation.

The pressure drop across the AFR was measured at different flow rates with the pressure gauge installed on the PFA tubing carrying both liquid phases and the outlet opened at atmospheric pressure. A correlation based on the Lockhart-Martinelli method³⁴ was developed from these measurements.

3.4 Results and discussion

3.4.1 Flow regimes

All the experiments were run at room temperature and atmospheric pressure at the outlet for hexane and water flow rates ranging from 10 to 80 mL/min. A typical image of the AFR module at steady-state liquid-liquid flow is shown in Figure 3.2. As opposed to the case of flow in channels, where the cross-section dimensions and shape is constant, the channel width in the AFR changes along the flow path in every heart shape cell. A few dimensionless numbers were used for the quantitative analysis of the data. Reynolds number (Re) for AFR was estimated on the basis of dimensions and velocity at the inlet of the heart shape as given by eq 3.1.

$$Re = \frac{VD_h\rho}{\mu} \quad (3.1)$$

Two-phase Re at the inlet (based on average fluid density and viscosity) ranged from 460 to 3700, while the Re of individual phases based on superficial velocities ranged from 180 to 1400 and 390 to 3200, respectively, for hexane and water. Thus, unlike the typical microreactors with very well defined and predictable flow patterns, the flow regime in an AFR is expected to range from laminar to turbulent. Similarly, the Weber number (We) for each phase was estimated using the superficial phase velocity²⁴ defined by eq 3.2:

$$We_i = \frac{v_i^2 d_p \rho_i}{\sigma} \quad (3.2)$$

For the range of flow rates tested (10-80 mL/min of each phase), the We for hexane and water vary in a range of 0.30-19 and 0.45-29, respectively. Both interfacial and inertial forces are important in the AFR and the later ones gain more relevance at higher flow rates. In the process of drop formation, the orientation of the droplet with respect to the main flow and its deformation process both depend on the competing

hydrodynamic and interfacial stresses. The viscous forces act on the droplet tending to elongate it, whereas the surface tension tends to keep the shape of the droplet as spherical, minimizing the drop surface to volume ratio ³⁵ and are estimated in terms of the Capillary number (Ca) defined by eq 3.3:

$$Ca = \frac{\mu V}{\sigma} \quad (3.3)$$

The range of Ca for the operating conditions studied here varies from 0.003 to 0.024, which reflects a larger contribution of surface tension to the droplet formation. It has been reported that droplet formation in microfluidics is dominated by surface tension effects and geometrical confinement. Typically in microreactors, at low velocities inertial effects are usually negligible and a critical Ca decides the droplet break-up and fluid-fluid interaction ³⁶. During two phase flow in a microfluidic system, as the fluid filament stretches and thins down, the capillary number decreases and when it becomes less than a critical value (i.e. ~ 0.1 to 0.01), the surface tension forces break the liquid filament into droplets thereby minimizing the interfacial area. However, the flow rates in the AFR are of the order of 10-100 mL/min and in the transient to turbulent regime, the hydrodynamic characteristics of AFR would be different when compared to simple straight microchannels. Thus, in an AFR, for a non-reactive system, while the viscosity and surface tension would remain unchanged, the superficial velocity varies significantly depending upon the cross-sectional area. Thus, regions along the flow path can exist where the Ca can be lower than the critical levels that lead to droplet break-up. Since in our range of experimental conditions, the values of Ca at the inlet of AFR (which has dimensions similar to the inlet for individual heart shapes) are in the critical level range, the local shear and Ca would govern the droplet break-up.

The two other dimensionless numbers that used for the analysis are the Eötvös number (Eo) and Morton number (Mo). The former (also called Bond number, given by eq 3.4) is normally used together ³⁷ with the later (eq 3.5) to characterize the shape of bubbles or drops in multiphase systems. They are defined as:

$$Eo = \frac{\Delta \rho g a_p^2}{\sigma} \quad (3.4)$$

$$Mo = \frac{\Delta\rho g \mu_c^4}{\rho_c^2 \sigma^3} \quad (3.5)$$

Specific to the hexane-water system, the Morton number was 2.5×10^{-11} . Typically, the droplet formation undergoes a sequence of phenomena viz. dispersed phase fluid displacement, its elongation, deformation and detachment events, and as the drops flow through the continuous phase, they undergo break-up and/or coalescence. These dynamic processes are significantly affected by the presence of walls in small channels (confined geometries as in the AFR) as compared to conventional stirred vessels, where the large dimensions make wall effects negligible.³⁸ It is observed from the visualization experiments that water is always the continuous phase, regardless of the operating flow rates of each phase. The hydrophilic material of construction of the AFR (glass) keeps the hexane dispersed in drops, while the water phase wets the walls. This observation is not found in conventional stirred vessels, where the initial conditions as well as the power input determines the possibility of phase inversion³⁹. In a stirred reactor, the droplet size depends on the input energy (agitation), the design, type of impeller used, and the physical properties of the two liquids. Studies in microchannels demonstrate that the flow patterns are affected by numerous factors: some of them variable (operating conditions, fluid properties), and others, fixed (channel dimensions, and device geometry). Thus, the dispersion characteristics are device-dependent and it is almost impossible to establish general rules to predict the drop size. In the AFR, with a fixed design, the phase flow rates and the physical properties of the two liquids also govern the drop size. In this Section the relevant observations are discussed in a quantitative manner.

Most of the studies on liquid-liquid flow (dispersion or slugs or annular flow) have been performed for single droplets generated in T-junctions or flow-focusing devices³¹. However, dispersions, such as those generated in the AFR, behave differently than single droplets, with inter-drop interactions that affect the flow³⁸. Because of the confined geometry of the AFR and the small flow paths, both shear rates and detachment dynamics affect the dispersion characteristics. The dominant flow pattern along the AFR is drop flow, with drop sizes smaller than the device characteristic dimension. Slug flow also exists in the straight sections

connecting the first two rows, where the drop size is still larger than the channel cross-section and the drops get squeezed by the walls forming slugs.

Another important observation from Figures 3.3 and 3.4 is that unlike in a microreactor ⁴⁰ (where very narrow drop size distributions are obtained), depending on the flow rates the AFR leads to the formation of droplets with a relatively broad size distribution.

3.4.2 Drop size distribution

Drop size distributions and number average drop sizes are measured from the images obtained from the visualization experiments. The Sauter diameter (d_{32}) calculated as shown in eq 3.6 is also used to characterize the dispersions. Its magnitude depends on both the maximum and minimum drop size as well as the shape of the drop size distribution ⁴¹.

$$d_{32} = \frac{\sum_i n_i d_i^3}{\sum_i n_i d_i^2} \quad (3.6)$$

Examples of the effect of hexane flow rate on the drop size distribution for water flow rates ranging from 10 to 80 mL/min are shown in Figures A.6.1–5 of the Appendix. The number density functions for the drop size resemble log-normal distributions, with a stronger effect at the lowest water flow rates, for which the breakage of drops is more difficult due to the low inertia of the continuous phase to overcome the interfacial force. High shear is needed to induce break-up of drops, which is obtained at high total flow rates. The drops remain small at high flow rates, where the continuous phase prevents coalescence. It is also observed that the narrowest size distributions and smaller drop size are obtained at high total flow rates. This is generally desirable for most applications, as smaller drops offer high effective interfacial area for mass transfer (m^2/m^3).

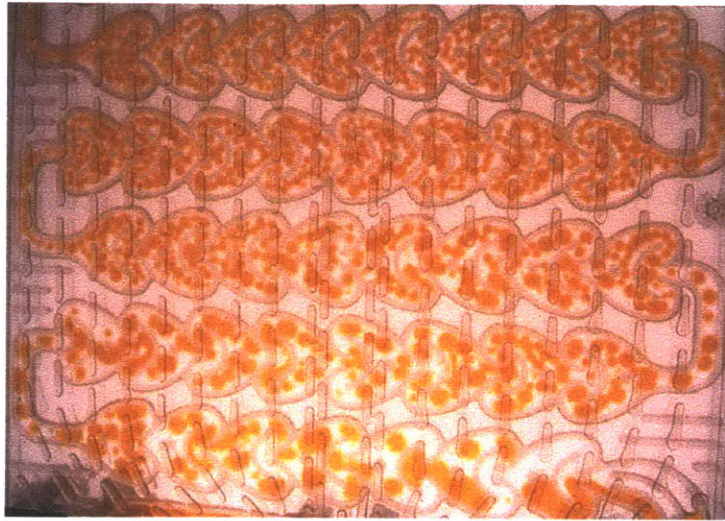


Figure 3.2: Flow patterns of hexane/water in the Advanced-Flow Reactor. Drop size decreases from inlet to outlet after breakup enhanced by reactor design through convergent/divergent channels in the form of heart-shaped cells in series

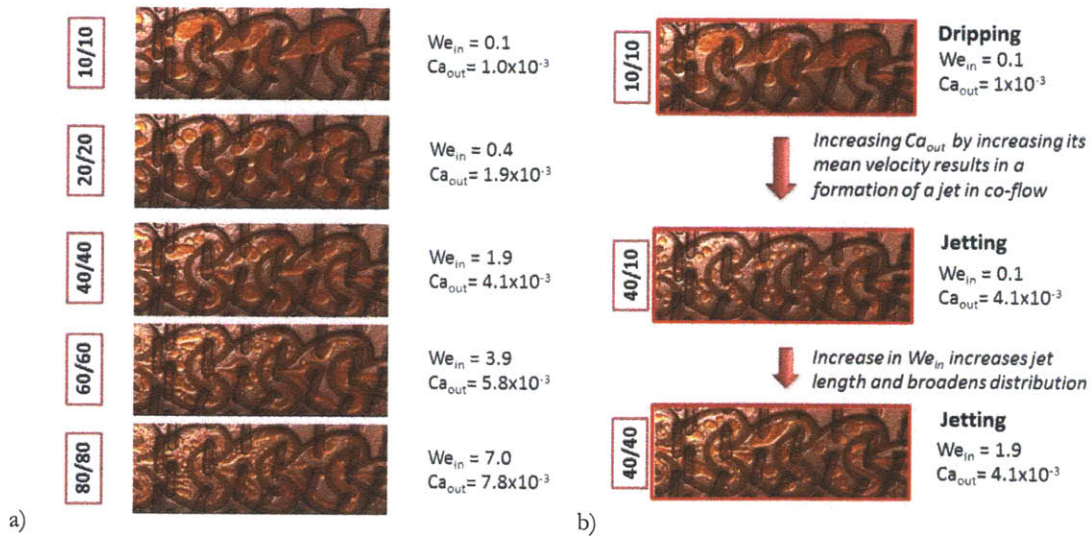


Figure 3.3: Effect of flow rate on droplet formation regime: a) water/hexane flow rate ratio = 1, b) water flow rate/hexane flow rate = 1, 4, and 1 for total flow rates changing from 20 mL/min, 50 mL/min to 80 mL/min.

The Sauter diameter remains within the interval 0.37 – 1.5 mm for most flow rates, except for the lowest water flow rates (10 and 20 mL/min) and highest hexane flow rates (60 mL/min and 80 mL/min of hexane for 10 mL/min of water, and 80 mL/min for 20 mL/min of water) for which the Sauter diameter exceeds 2 mm. This behavior is in accordance with the experimental observation at these low water flow rates, for which it was observed that drop break-up was difficult due to the very small amount of water present. Coexistence of very large drops with very small drops was observed which affects the Sauter diameter estimated through the statistical moments of the drop size distributions.

The different regimes of droplet formation are shown in Figure 3.4 b) for a constant water-to-hexane flow rate ratio for increasing total flow rate. For a vertical configuration of the AFR, gravity affects the biphasic flow at the lowest flow rates (10 mL/min of each phase) and the lightest phase (hexane) occupies the upper half of the heart cell. As the total flow rate increases, inertia overcomes buoyancy effects. At low flow rates of both phases (total flow rate of 40 mL/min), a dripping regime is observed, with a periodic formation of individual drops that pinch-off at the inlet of the heart cell. Increasing the total flow rate results in the formation of a jet, which subsequently breaks to yield drops of different sizes. The shear rate increases with total flow rate producing drops of smaller size and broadening the size distribution. The jet length also increases with increasing flow rate. The transition from the dripping to the jetting regime is observed by increasing the outer flow rate, which increases the viscous drag (Figure 3.3 b) and yields smaller drop sizes. Increasing the inner flow rate in the jetting regime increases the jet length and broadens the drop size distribution.

The average drop size of hexane decreases with both hexane and water flow rates, however the change in drop size for water flow rates of 10 and 20 mL/min with hexane flow rate is more significant than the change observed for larger drop sizes. In the decision of selecting the operating conditions, it is important to notice also that water flow rate determines mainly the droplet size, whereas the hexane flow rate determines the number of drops. This effect can be visualized in Figure 3.4, where three very representative cases of the hexane-water flow are shown. In “Case 1” the low flow rates of water (10 mL/min) and hexane (10 mL/min) generate drop sizes of about 1 mm. If “Case 1” is taken as basis for comparison, increasing water flow rate

from 10 mL./min to 80 mL./min while keeping hexane flowing at 10 mL./min (which brings us to “Case 3”) causes mainly a reduction in drop size with an approximately same number of droplets. Increasing hexane flow rate from 10 mL./min to 80 mL./min, while water flows at 80 mL./min (“Case 2”) increases the number of drops whereas the drop size remains almost unchanged.

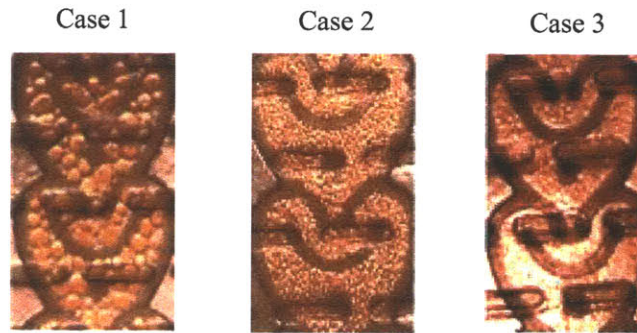


Figure 3.4: Effect of flow rate on drop size and number of drops: case 1) $Q_h = 10, Q_w = 10$; case 2) $Q_h = 80, Q_w = 80$; case 3) $Q_h = 10, Q_w = 80$ (flow rates in mL./min)

The effect of the capillary number (Ca) in the hexane drop size is shown in Figure 3.5, with hexane flow rate as parameter. It was found that both Ca and Q_h have a strong impact on determining the droplet size. At low Ca , the effect of hexane flow rate is significantly larger than at higher Ca , with a general tendency to reduce the droplet size. There is a compromise between droplet size and power consumption, since flow rate increase results in increasing the energy input (increasing water flow rate is equivalent to increasing Ca). There is a point from which increasing the energy input to pump the hexane phase does not result in a significant reduction in drop size. Nevertheless, it has an impact on the interfacial area and the mass transfer coefficients, since the hexane phase has larger influence on the number of drops.

The effect of the hexane Weber number (We) in the average drop size, shown in Figures 3.6 a) and b), reflects a change in the flow regime: at low We_h , surface tension effects dominate over inertia, while at higher We_h inertial effects take over and dominate interfacial forces. The effect of We_w (continuous phase) has a stronger effect than We_h (dispersed phase) on the droplet size, as was already reflected by the stronger

influence of the water flow rate as compared to hexane flow rate. The same observation is seen in rectangular microchannels for kerosene/water system.²⁴

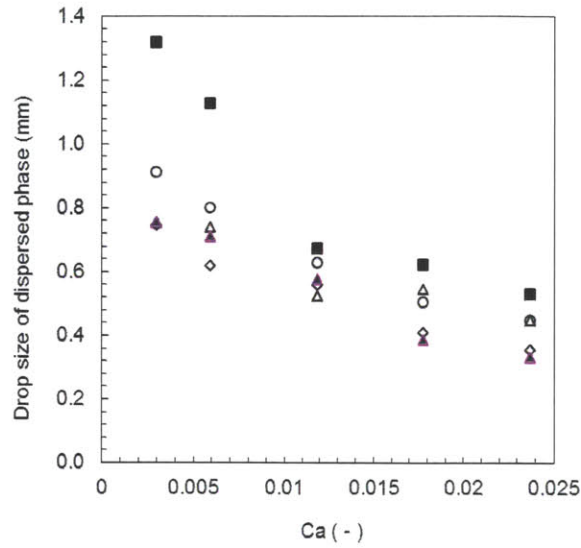


Figure 3.5: Drop size versus capillary number. Hexane flow rate as parameter (mL/min): ■, 10; ○, 20; △, 40; ◇, 60; ▲, 80

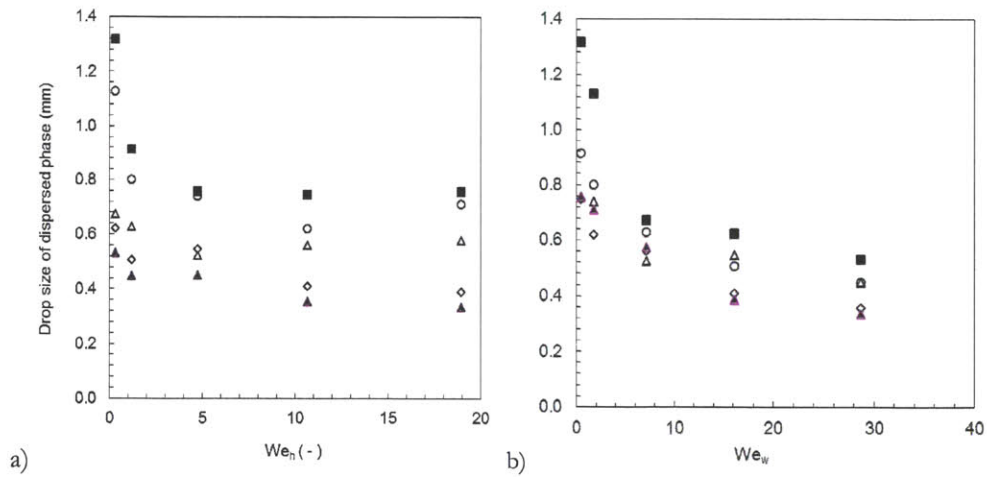


Figure 3.6: Relationship between mean droplet size and flow regimes in Advanced-Flow Reactor: a) drop size of dispersed phase versus hexane Weber number; b) drop size of dispersed phase versus water Weber number. Legend: a) water flow rate, b) hexane flow rate (mL/min): ■, 10; ○, 20; △, 40; ◇, 60; ▲, 80

3.4.3 Drop size variation along flow path

The AFR shows a different behavior with respect to microchannels operating in slug flow regime. While microchannels have slugs of defined size, as shown in Figures 3.3 and 3.4 the AFR has a distribution of drop sizes along the flow path. The system hexane-water is not reactive but still shows a reduction of drop size along the flow path, as shown in Figure 3.7. One interesting result is that, regardless of the water flow rate, the drop size remains almost constant from the fourth row, which could correspond to an equilibrium drop size. In order to show that an equilibrium state has been reached, the ratio of average drop size in each row/Sauter diameter is shown in Figure 3.8. It is seen that the equilibrium size (ratio = 1) is reached in earlier rows at higher flow rates.

3.4.4 Hexane hold-up

The hexane hold-up, which is important to determine the slip velocity, was measured as the volume fraction of hexane using the information provided by the images. The number of drops was counted in each heart cell as those seen from a plane parallel to the plane of the AFR. Since the AFR layer thickness is 1.1 mm, two possibilities of coexisting drops exist: floating drops and stacked drops. In the first case, the hexane hold-up can be calculated easily from the number of drops and drop size, since the number of droplets seen from the above is exactly the number of drops actually existing in the entire channel height. In the second case, the stack of droplets makes impossible to know exactly how many drops exist when seen from above, and some assumptions need to be made. Depending on the packing structure of droplets, the number of drops that can coexist in the thickness will be slightly different. Two packing configurations have been considered: simple cubic packing and close-packing (Appendix, Figure A.7). Neglecting the end effects along the width of the channel and focusing on the end effects on the height, the close-packing is able to hold a larger number of drops (ratio simple cubic packing / close packing = 0.67). Close-packing was selected for the calculation of the hold-up fraction as it was considered to be in better agreement with experimental observations.

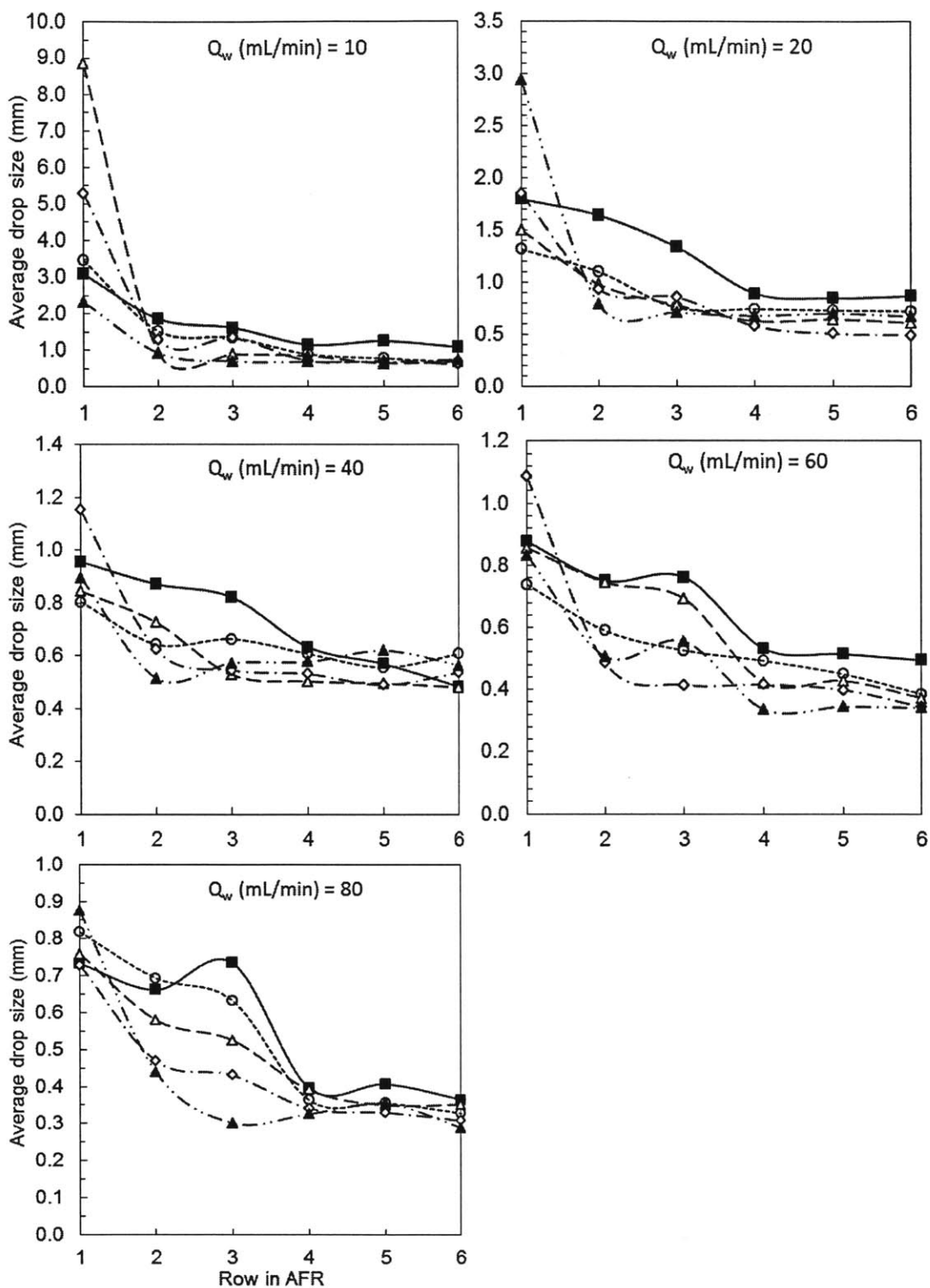


Figure 3.7: Average drop size variation with position in Advanced-Flow Reactor. Hexane flow rate as parameter (mL/min): ■, 10; ○, 20; △, 40; ◇, 60; ▲, 80. Row 1 means inlet, row 6, outlet.

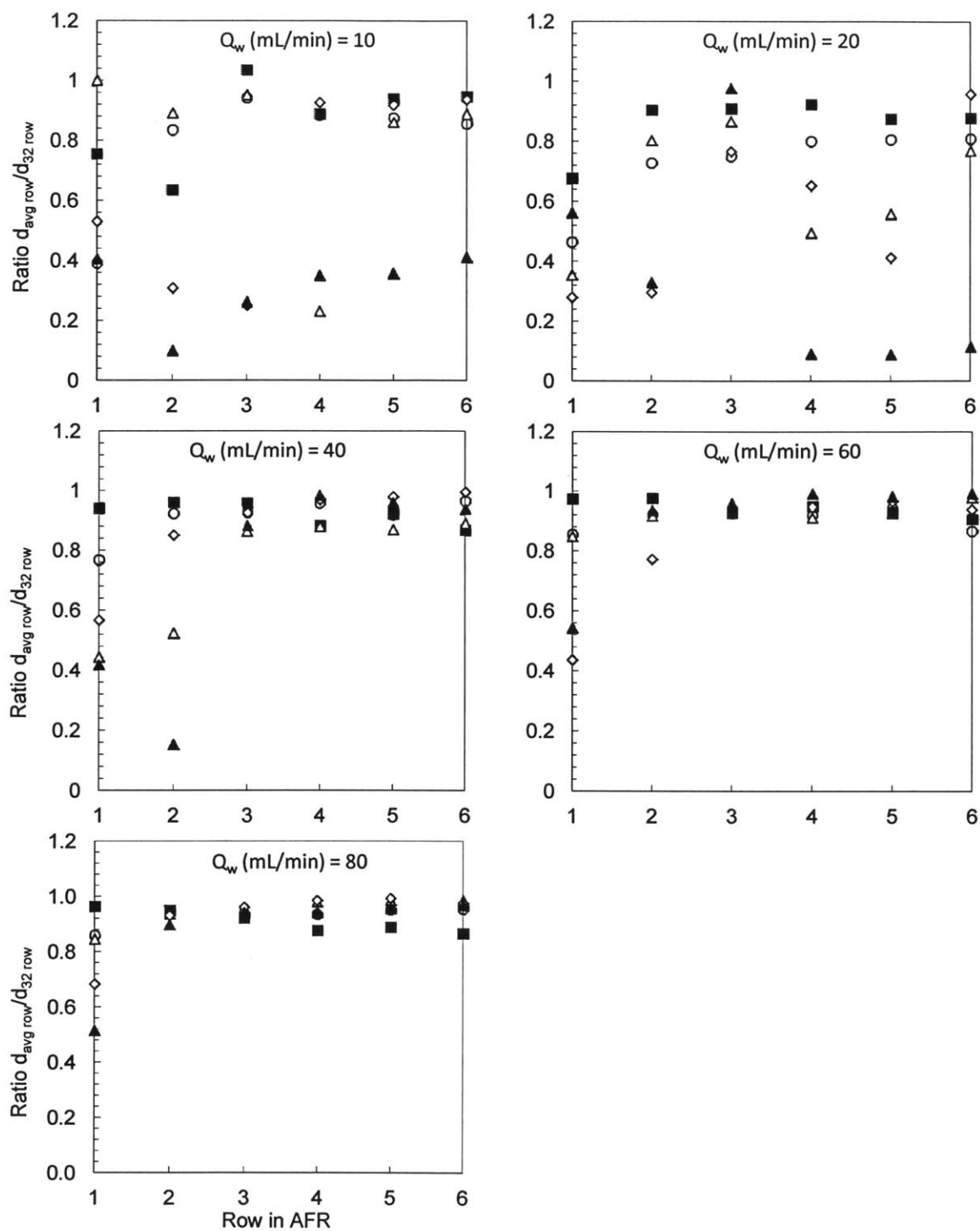


Figure 3.8: Ratio of average drop size in row/Sauter diameter in row versus row in AFR. Legend: hexane flow rate (mL/min): ■, 10; ○, 20; △, 40; ◇, 60; ▲, 80

Two limitations to the calculation of the hold-up fraction were encountered. First, only one droplet size (the average) has been considered for each heart cell. Second, each row has been assumed to be composed of heart cells with identical drop size distributions, but the droplet size actually decreases continuously from the inlet to the outlet of the AFR. However, calculating the hexane hold-up from an averaged drop size for each row can be used as a first approximation for the estimation of mass transfer coefficients.

The hexane hold-up is shown in Figure 3.9 as a function of the flow rate ratio Q_w/Q_h . The fractional hexane hold-up is seen to decrease with increasing water to hexane flow ratio (at almost all water and hexane flow rate combinations). There are some deviations at very low water-to-hexane ratios may be because the hexane flow rate is so high that the continuous phase inertia is not enough to break drops. It was not possible to obtain a good correlation connecting phase hold-up with flow rate ratios. This is probably due to surface tension effects.

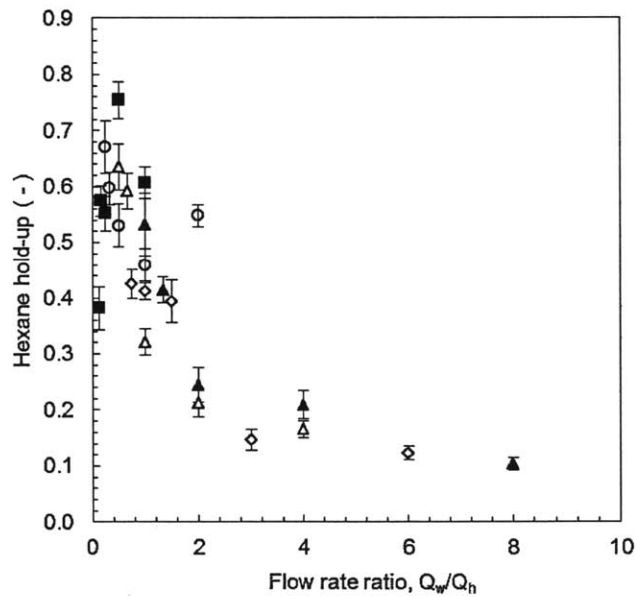


Figure 3.9: Hexane hold-up variation with flow rate ratio. Water flow rate as parameter (mL/min): ■, 10; ○, 20; △, 40; ◇, 60; ▲, 80

The effect of Ca on the hexane hold-up is shown in Figure 3.10. It is seen that hexane hold-up decreases when increasing the Ca , which indicates the effect of inertial forces over the surface tension force. It is important also to notice that there is a drastic reduction in hexane hold-up when the hexane flows at 10 and 20 mL/min for low Ca . A decrease was observed by increasing the two-phase Re , being this drop more drastic at lower Re . Increasing We of the continuous phase also reduced the hexane hold-up, with a larger effect at the lower hexane flow rates (Figure 3.11).

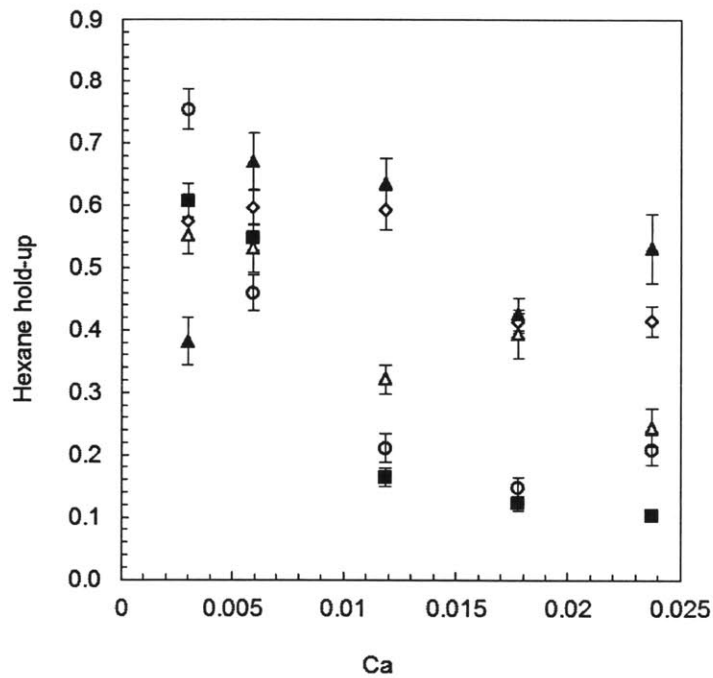


Figure 3.10: Hexane hold-up variation with capillary number. Hexane flow rate as parameter (mL/min): ■, 10; ○, 20; △, 40; ◇, 60; ▲, 80

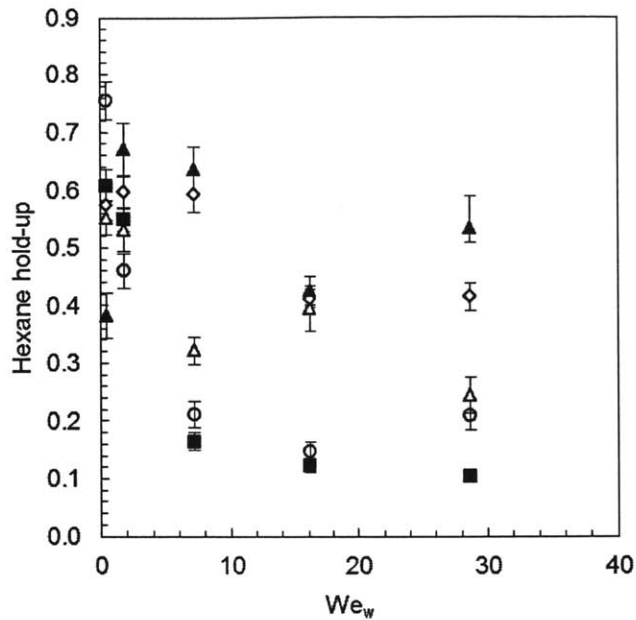


Figure 3.11: Hexane hold-up variation with water Weber number. Hexane flow rate as parameter (mL/min): ■, 10; ○, 20; △, 40; ◇, 60; ▲, 80

3.4.5 Specific interfacial area

The interfacial area was calculated from the number average drop size and the experimental hexane hold-up using eq 3.7.

$$a = 6\epsilon_h/d_p \quad (3.7)$$

High specific interfacial areas were observed at low flow rate ratios Q_w/Q_h and high water flow rates. The rate of increase of interfacial area with Reynolds number was seen to increase with water flow rates and slows down at larger hexane flow rates. The effect of the Capillary number on the effective interfacial area is shown in Figure 3.12. The variation in a is a strong function of the hexane flow rate as the dispersed phase flow rate controlled the number of drops. The values of a decrease slightly with Ca at low hexane flow rates and its effect is negligible beyond 40 mL/min, which is a typical operating condition for pilot or industrial scale production. However, for the largest hexane flow rates, 60 and 80 mL/min, a continuous increase in the effective interfacial area is observed with Ca .

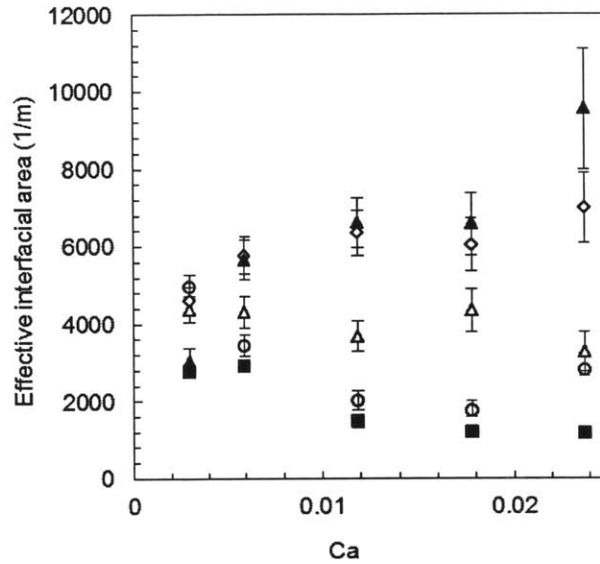


Figure 3.12: Specific interfacial area variation with capillary number. Hexane flow rate as parameter (mL/min): ■, 10; ○, 20; △, 40; ◇, 60; ▲, 80

3.4.6 Mass Transfer Coefficients

Mass transfer coefficients were estimated using the Calderbank's modification of surface renewal theory ⁴². In the original penetration theory of Higbie for gas-liquid mass transfer ⁴³, the mass transfer across the interface is considered as an unsteady process, where the continuous liquid surface is considered to be formed by small elements of fluid which contact the gas phase for some time, after which they penetrate the bulk fluid, to be replaced by new elements of fluid at the gas-liquid interface. The true mass transfer coefficient (k_L) based on the surface renewal theory is given by eq 3.8:

$$k_L = 2 \sqrt{\frac{D_L}{\pi t}} \quad (3.8)$$

The contact time was calculated as the ratio of droplet size to drop terminal velocity ^{44, 45}. The slip velocity (v_s) is essential for the determination of mass transfer coefficients and is estimated using eq 3.9, which needs the superficial velocity of each phase and the hold-up measured from the visualization

experiments. The formula is analogous to the bubble slip velocity for a gas-liquid reactor with co-current flow^{46, 47} and has been used also for liquid-liquid systems in many other contactors.

$$v_s = \frac{v_h}{\epsilon_h} - \frac{v_w}{\epsilon_w} \quad (3.9)$$

The overall mass transfer coefficients are plotted in Figure 3.13 in terms of water-to-hexane flow rate ratio. A general decrease in the mass transfer coefficients is observed as Q_w/Q_h increases. For a constant water flow rate Q_w , the overall mass transfer coefficient ($k_L a$) increases with the hexane flow rate. This variation is related to the decrease in drop size with flow rates, which increases the interfacial area, and the increase in internal circulations within the droplets with higher shear rates and velocities. For a constant hexane flow rate Q_h , the mass transfer coefficients increase for larger water flow rates. Thus, it is recommended for kinetically controlled reactions to operate at high water and hexane flow rates. Also, high overall mass transfer coefficients indicate that it is necessary to have short residence times (Figure 3.14) in the reactor. Thus, less number of AFR plates would actually be sufficient for such cases thereby providing a pilot or commercial scale production for fast reactions that are completed in the smaller residence time. On the other hand, slow reactions need long residence times to achieve reasonable conversions and increasing the temperature and/or connecting several AFR units in series could solve this problem without compromising on the overall mass transfer coefficient. The requirements for each reaction are specific and thus, the operating conditions need to be chosen carefully.

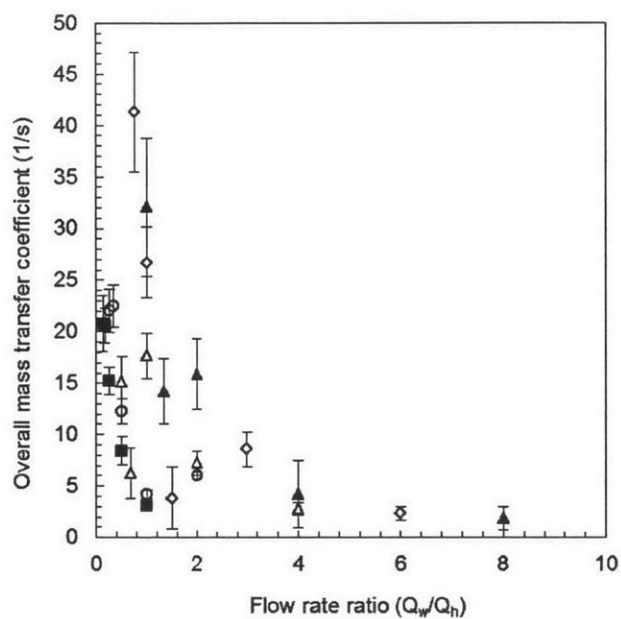


Figure 3.13: Overall mass transfer coefficient variation with flow rate ratio. Water flow rate as parameter (mL/min): ■, 10; ○, 20; △, 40; ◇, 60; ▲, 80

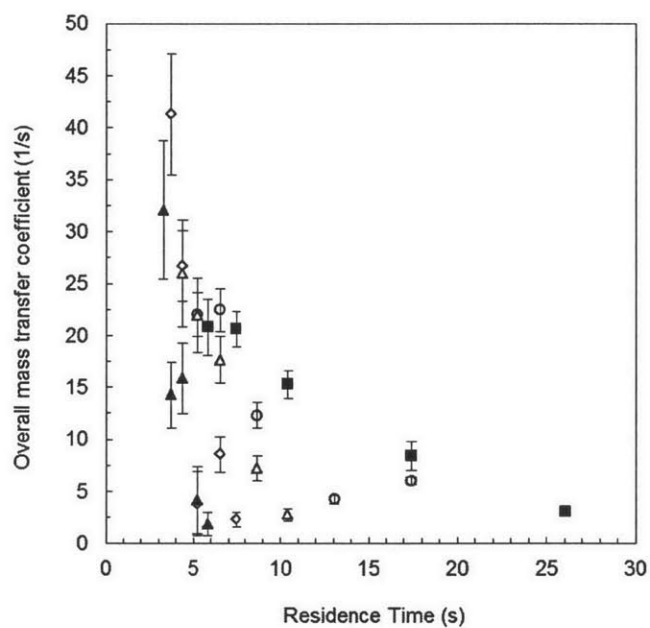


Figure 3.14: Overall mass transfer coefficient variation with residence time. Water flow rate as parameter (mL/min): ■, 10; ○, 20; △, 40; ◇, 60; ▲, 80

3.4.7 Pressure drop

Pressure drop measurements were used for the estimation of the power consumption which directly dictates the specific interfacial area as well as the mass transfer rates. In the AFR only the pumping of the two liquids into the device is required and no additional power to provide agitation as in the case of stirred vessels is needed. The experimentally measured pressure drop at different inlet two-phase Re is shown in Figure 3.15. A correlation to estimate the pressure drop for hexane/water was developed using the framework of Lockhart-Martinelli method³⁴. This is one of the most used methods to predict two-phase pressure drop and it can be used within a broad range of flow regimes of both phases (laminar-laminar, laminar-turbulent, turbulent-laminar, turbulent-turbulent) by modifying the value of specific parameters. A modified correction factor of the Chisholm parameter (C^*) was calculated to fit the experimental data. A good prediction of the experimental data, shown in Figure 3.16, was seen when one correlation for the correction factor for each water flow rate in terms of the ratio $Q_h/(Q_w+Q_h)$ was used. The relative errors were reduced from 0.43 – 170 % to 0.16 – 37 % and randomized, with respect to a single correlation for the correction factor not depending on the water flow rate, as shown in Figure 3.17. It was also seen that the larger errors were obtained for the lowest flow rates (combination of 10 and 20 mL/min flow rates of each phase).

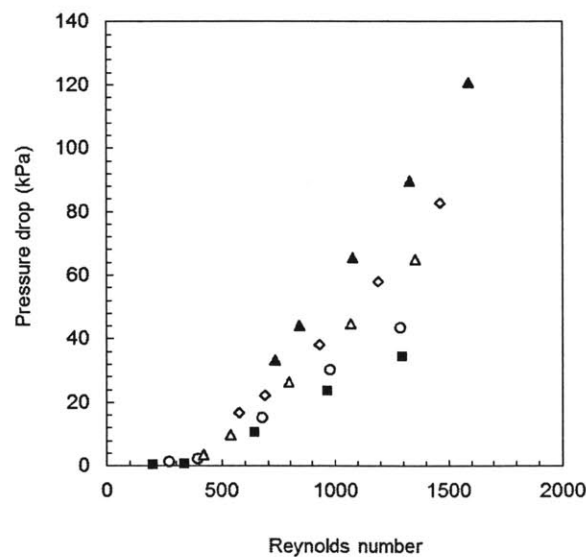


Figure 3.15: Pressure drop variation with Reynolds number. Water flow rate as parameter (mL/min): ■, 10; ○, 20; △, 40; ◇, 60; ▲, 80

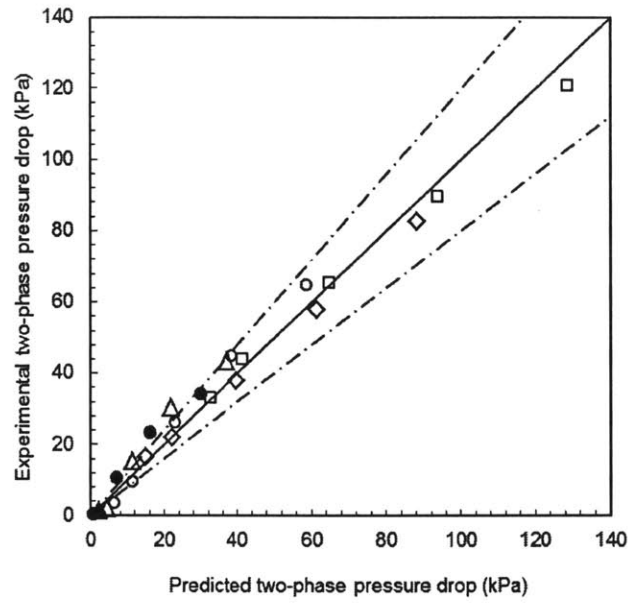


Figure 3.16: Experimental versus predicted two-phase pressure drop. Different correction factor in terms of Q_h/Q_{total} for each water flow rate. Water flow rate (mL/min): ■, 10; ○, 20; △, 40; ◇, 60; □, 80

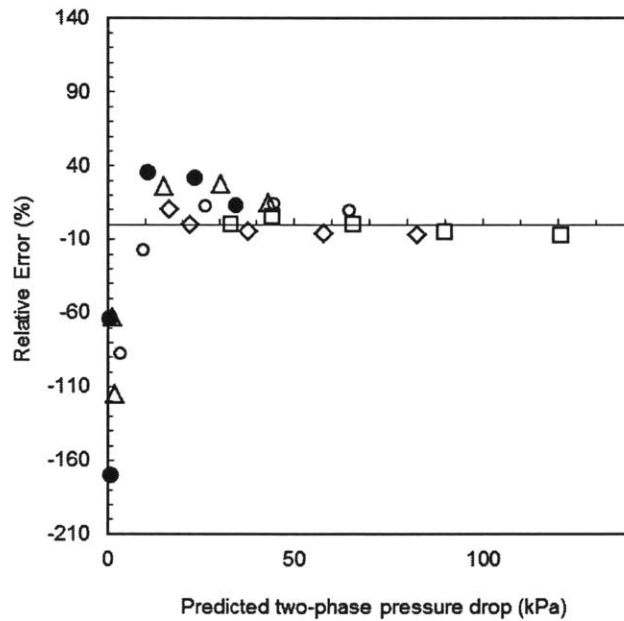


Figure 3.17: Relative error in prediction of pressure drop. Different correction factor in terms of Q_h/Q_{total} for each water flow rate. Water flow rate as parameter (mL/min): ■, 10; ○, 20; △, 40; ◇, 60; □, 80

3.4.8 Comparison of AFR with other liquid-liquid contactors

The different hydrodynamic parameters for AFR that are presented can be compared with the similar parameters that are reported in the literature for different conventional liquid-liquid contactors and static mixers. Values of different parameters at identical power consumption per unit volume were considered as the basis for comparison. The average drop size is presented versus power consumption in Figure 3.18. First of all, it is seen that for a specific device, i.e. a vibromixer^{48,49} the achieved drop size depends on the physical properties of the liquid-liquid system. It can be seen here that the AFR does not provide the smallest drop sizes. However, it is important to consider not only the drop size, but also the number of generated drops, because this affects the total interfacial area, and therefore, the overall mass transfer coefficients.

The values of effective interfacial area for the AFR operating with flow rates from 10 to 80 mL/min are in the range 1,000 to 10,000 m²/m³, which are one order of magnitude higher than those obtained in conventional stirred vessels, where interfacial areas are on the order of 500 m²/m³⁵². Effective interfacial areas typical of other liquid-liquid contactors are presented in Table 3.2. Packed bed columns and RTL extractors are not able to generate interfacial areas as high as those provided by the AFR. However, impinging jet reactors and microchannels present a larger capability in producing specific surface areas, but as it will be shown later, the mass transfer coefficients are smaller than those obtained in the AFR, mainly due to smaller drop sizes and higher hold-up values in the AFR. A better metric for comparison of specific interfacial areas takes into account the power consumption, as shown in Figure 3.19. According to this metric, the AFR is more efficient than other liquid-liquid contactors in creating interfacial area, probably due to its design with a series of divergent/convergent sections through heart-shaped cells along the flow path that cause continuous break-up and coalescence of the dispersed phase creating a large number of small droplets which increase the interfacial area, requiring only energy input for pumping the fluids. However, other contactors require extra energy input to provide agitation and there is probably higher energy dissipation which is not devoted to the creation of new surface between phases.

Very few data on interfacial area and mass transfer coefficients for static mixers is available in the literature, being more predominant data related to drop size. Here we provide some information about mass transfer and interfacial areas for gas/liquid and liquid/liquid systems in static mixers for comparison. Overall mass transfer coefficients for immiscible liquids in screen-type static mixers⁵³ are in the range of 1 to 10 s⁻¹ for energy dissipation rates from 10 to 100 W/kg. HEV static mixer is reported to be more efficient than other mixers, with interfacial areas ranging from 3x10² to 3x10³ m²/m³ for power consumptions of 0.1 to 1 J/kg⁵⁴. Interfacial areas are on the same order of magnitude as the values obtained in capillary microchannels and not very far from the values obtained in the AFR.

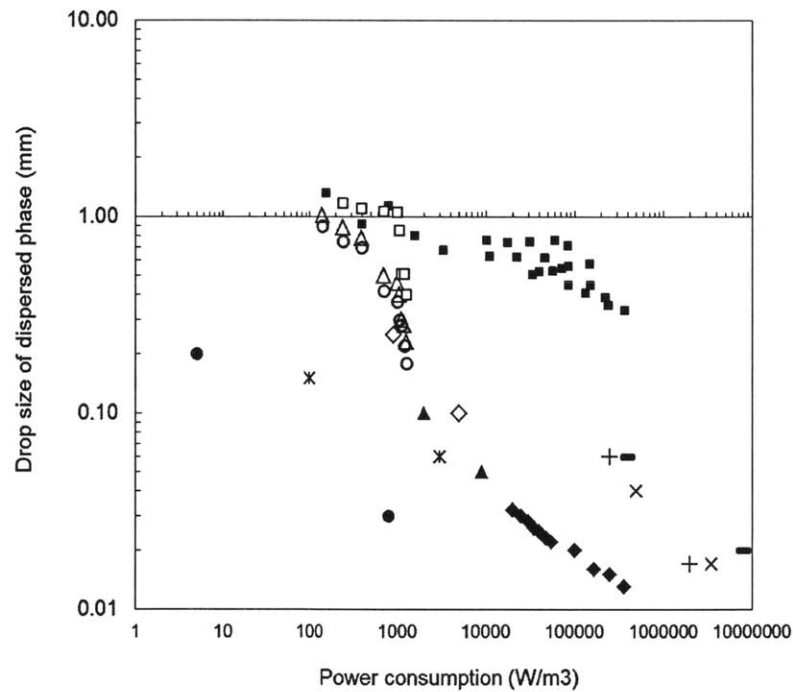


Figure 3.18: Drop size versus power consumption for different liquid-liquid contactors.^{49, 50, 51}
 Legend: ■, Corning; △, vibromixer (kerosene-water); ◆, annular centrifugal extractor (silicon oil-water); ◇, unbaffled shaking flask; *, stirred tank; ○, vibromixer (paraffin oil-water); □, vibromixer (methyl silicon oil-water); ●, stirred tank fermentor 14 L; ▲, baffled shaking flask 300 mL; +, static mixer I; ×, static mixer II; --, static mixer III

Table 3.2: Comparison of effective interfacial area and mass transfer coefficients in liquid-liquid contactors⁵⁵

Contactor type	a (m^2/m^3)	$k_L a$ (s^{-1})	Reference
Agitated contactor	32-311	$(48-83)10^{-3}$	Fernandes and Sharma, 1967
Packed bed column (Pall/Raschig ring, Intalox saddles)	80-450	$(3.4-5)10^{-3}$	Verma and Sharma, 1975
RTL Extractor (Graesser raining bucket)	90-140	$(0.6-1.3)10^{-3}$	Alper, 1988
Air operated two impinging jet reactors	350-900	0.075	Dehkordi, 2002
Two impinging jet reactors	1000-3400	0.28	Dehkordi, 2001
Capillary microchannel	830-3200	0.88-1.67	Kashid et al., 2007
Static mixers	300-3000 ^a	1-10 ^b	^a Lemenand, T. Et al, 2005 ^b Taweel, A. M., et al. 2007

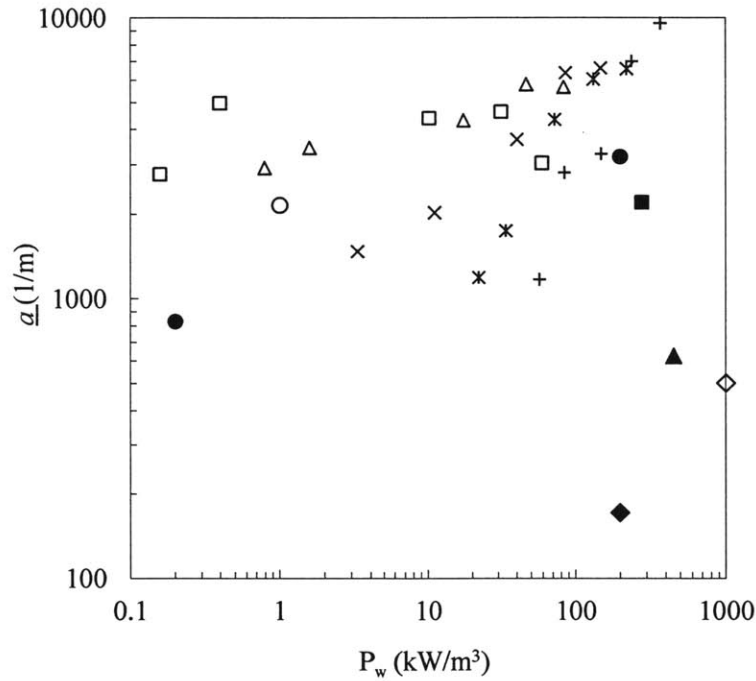


Figure 3.19: Specific interfacial area versus power consumption for different liquid-liquid contactors. Legend: \square Corning $Q_w = 10$ mL/min \triangle Corning $Q_w = 20$ mL/min \times Corning $Q_w = 40$ mL/min $*$ Corning $Q_w = 60$ mL/min $+$ Corning $Q_w = 80$ mL/min \bullet Capillary microchannel; \blacksquare Two impinging jets reactor; \blacktriangle Air operated two impinging jet reactors; \blacklozenge Agitated contactor; \diamond Sulzer static mixer; \circ HEV static mixer⁴¹

It is known that in conventional vessels higher mass transfer rates can be achieved by increasing the shear at the cost of higher power consumption rates. The relationship between mass transfer coefficients and power input is therefore a measurement of the efficiency of the device and can be used as a metric to compare different liquid-liquid contactors. Some typical values for batch reactors, static mixers and packed microchannels are shown in Figure 3.20, together with the AFR results. While agitated vessels need energy to pump the liquids and also stir their fluid content, microchannels and the AFR work in a way that they do not need to provide extra power for agitation. It is seen from the results and the mass transfer data from the literature that the AFR is superior in terms of mass transfer versus power consumption, with values of $k_{L,a}$ within the range 1.9 – 41 s⁻¹ and power input of 0.2 – 400 kW/m³. Capillary and packed microchannels are the closest contactors in performance to the AFR, while the agitated vessels and the Koch static mixer⁵⁶ are the furthest.

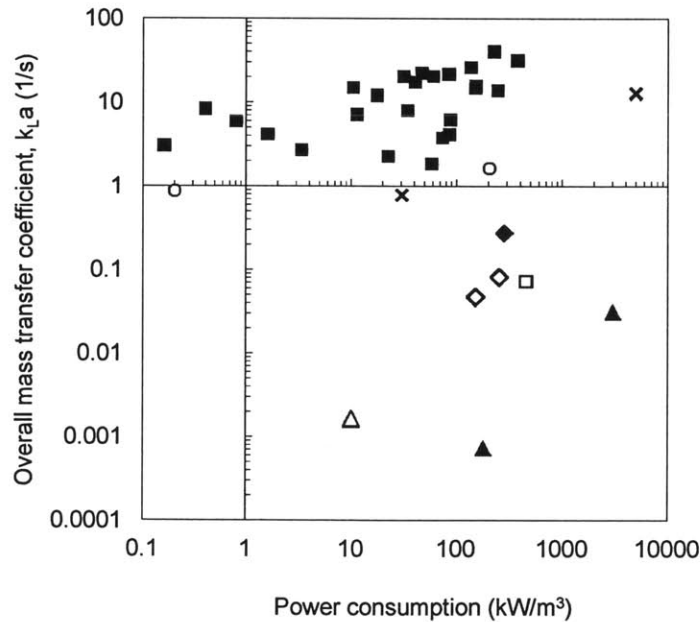


Figure 3.20: Overall mass transfer coefficient versus power consumption for different liquid – liquid contactors⁵⁷. Legend: ■ Corning, △ Batch reactor, ▲ Static mixer, × Packed microchannel, □ Air operated two impinging jet reactors, ○ Capillary microchannel, ◇ Agitated contactor, ◆ Two impinging jets reactor

3.5 Conclusions

In the context of microreactor technology, the Advanced-Flow Reactor® by Corning Inc. appears as one of the commercially available options to scale-up multiphase reactions from the laboratory (micro) scale to the production levels (mili scale). The complex geometry of the AFR with a continuously changing cross-section along the flow path and obstacles within the heart cells creates pressure changes that cause drop break-up and enhance mass transfer. It has been shown the superior performance of this device versus other conventional liquid-liquid contactors in terms of overall mass transfer coefficients and power consumption. For the recommended operating conditions in the AFR ranging from 10 to 80 mL/min of each phase, the values of drop sizes as small as 0.3 mm and mass transfer coefficients on the order of $1 - 10 \text{ s}^{-1}$ were achieved. Since the fluid properties have a strong impact on the characteristic of the dispersion (drop size distribution, dispersed phase hold-up, interfacial tension, etc), more investigations using fluids having a wider range of properties need to be explored. Further analysis of the effect of fluid properties is included in Chapter 6 using computational fluid dynamic simulations.

3.6 Notation

a	Effective interfacial area (m^2/m^3)
A_{heart}	Total surface of one single heart cell (m^2)
C	Chisholm parameter (-)
C^*	Correction factor based on the fractional phase hold-up of the dispersed phase (-)
CI	Confidence interval
$d_{p,i}$	Individual drop size (mm)
$\bar{d}_{p,\text{heart}}$	Number average drop size over one heart cell (m)
\bar{d}_p	Number average drop size over the entire plate (m)

d_{32}	Sauter diameter (mm)
D_h	Hydraulic diameter (m)
D_L	Diffusion coefficient (m^2/s)
H	Channel height (m)
k_L	True mass transfer coefficient (m/s)
k_{Lg}	Overall mass transfer coefficient (1/s)
N_{heart}	Number of drops in each heart cell (-)
n_i	Number of drops of size d_{pi} (-)
M	Number of measurements (-)
N	Number of rows in the AFR (-)
P_w	Specific power consumption (W/m^3)
Q_h	Volumetric hexane flow rate (mL/min)
Q_w	Volumetric water flow rate (mL/min)
s	Standard deviation
t	Time (s)
V_p	Terminal rise velocity of a drop in stagnant liquid (m/s)
V	Superficial velocity (m/s)
V_h	Hexane superficial velocity (m/s)
V_w	Water superficial velocity (m/s)
V_s	Slip velocity of the droplet (m/s)
$V_{heart,i}$	Total volume of drops in one heart cell (m^3)

V_p	Volume of one single droplet (m^3)
W	Channel width (m)
X_i	Individual measurement of variable X
\bar{X}	Mean value of M measurements of variable X
$\Delta P/\Delta L$	Pressure drop per unit length (Pa/m)

Dimensionless numbers

Ca	Capillary number (-)
EO	Eötvös number (-)
Fr_{HOM}	Froude number for homogeneous flow (-)
Mo	Morton number (-)
Re	Reynolds number (-)
We	Weber number (-)
We_{HOM}	Weber number for homogeneous flow (-)

Greek letters

α, α'	Parameters in drop size prediction (m)
$\beta, \gamma, \delta, \delta'$	Constant parameters in drop size prediction (-)
ε	Energy dissipation rate (m^2/s^3)
ε_h	Fractional hexane hold-up (-)
ε_w	Fractional water hold-up (-)
ρ	Density (kg/m^3)
λ	Friction factor (-)

φ_w, φ_h	Correction factor depending on Lockhart–Martinelli parameter χ
σ	Surface tension (N/m)
μ^2	Second statistical moment of distribution (s ²)
μ^3	Third statistical moment of distribution (s ³)
χ	Lockhart–Martinelli parameter (-)

Subscripts

w	Water phase
h	Hexane phase
TP	Total pressure drop
TPF	Two phase frictional flow
a	Acceleration
H	Hydrostatic head

3.7 References

- (1) Dugger, R. W.; Ragan, J. A.; Ripin, D. H. B. Survey of GMP bulk reactions run in a research facility between 1985 and 2002. *Organic Process Research & Development* **2005**, *9*, 253-258.
- (2) Carey, J. S.; Laffan, D.; Thomson, C.; Williams, M. T. Analysis of the reactions used for the preparation of drug candidate molecules. *Organic & biomolecular chemistry* **2006**, *4*, 2337-47.
- (3) Constable, D. J. C.; Dunn, P. J.; Hayler, J. D.; Humphrey, G. R.; Leazer, Jr., J. L.; Linderman, R. J.; Lorenz, K.; Manley, J.; Pearlman, B. a.; Wells, A.; Zaks, A.; Zhang, T. Y. Key green chemistry research areas-a perspective from pharmaceutical manufacturers. *Green Chemistry* **2007**, *9*, 411-420.
- (4) Mckenzie, P.; Kiang, S.; Tom, J.; Rubin, A. E.; Futran, M. Can pharmaceutical process development become high tech? *AIChE Journal* **2006**, *52*, 3990-3994.
- (5) Fedoryński, M.; Jezierska-Zieba, M.; Kakol, B. Phase transfer catalysis in pharmaceutical industry - where are we? *Acta Poloniae Pharmaceutica* **2008**, *65*, 647-654.
- (6) Ahmed-Omer, B.; Barrow, D.; Wirth, T. Biphasic reactions in microreactors. *In Multi-Material Micro Manufacture*, **2008**, 2-4.

- (7) Wilhite, B. A.; Jensen, K. F.; Hill, T. F.; Epstein, A. H.; Livermore, C. Design of a silicon-based microscale trickle-bed system for singlet-oxygen production. *AIChE Journal* **2008**, *54*, 2441-2455.
- (8) Ajmera, S. K.; Losey, M. W.; Jensen, K. F.; Schmidt, M. A. Microfabricated packed-bed reactor for phosgene synthesis. *AIChE Journal* **2001**, *47*, 1639-1647.
- (9) Zhang, X.; Stefanick, S.; Villani, F. J. Application of microreactor technology in process development. *Organic Process Research & Development* **2004**, *8*, 455-460.
- (10) Gavrilidis, A.; Angeli, P.; Cao, E.; Yeong, K. K.; Wan, Y. S. S. Technology and applications of microengineered reactors. *Trans IChemE* **2002**, *80*, 3-30.
- (11) Saber, M.; Commenge, J. M.; Falk, L. Microreactor numbering-up in multi-scale networks for industrial-scale applications: Impact of flow maldistribution on the reactor performances. *Chemical Engineering Science* **2010**, *65*, 372-379.
- (12) Roberge, D. M.; Gottspomer, M.; Eyholzer, M.; Kockmann, N. Industrial design, scale-up, and use of microreactors. *Chemistry Today* **2009**, *7*, 8-11.
- (13) Jensen, K. F. Microreaction engineering — is small better? *Chemical Engineering Science* **2001**, *56*, 293-303.
- (14) Watts, P.; Haswell, S. J. The application of micro reactors for organic synthesis. *Chemical Society reviews* **2005**, *34*, 235-46.
- (15) Haswell, S. J.; Middleton, R. J.; O'Sullivan, B.; Skelton, V.; Watts, P.; Styring, P. The application of micro reactors to synthetic chemistry. *Chemical Communications* **2001**, 391-398.
- (16) Commenge, J. M.; Falk, L.; Corriou, J. P.; Matlosz, M. Optimal design for flow uniformity in microchannel reactors. *AIChE Journal* **2002**, *48*, 345-358.
- (17) Amador, C. Flow distribution in different microreactor scale-out geometries and the effect of manufacturing tolerances and channel blockage. *Chemical Engineering Journal* **2004**, *101*, 379-390.
- (18) Wada, Y.; Schmidt, M. a.; Jensen, K. F. Flow distribution and ozonolysis in gas-liquid multichannel microreactors. *Industrial & Engineering Chemistry Research* **2006**, *45*, 8036-8042.
- (19) Hasebe, S. Design and operation of micro-chemical plants—bridging the gap between nano, micro and macro technologies. *Computers & Chemical Engineering* **2004**, *29*, 57-64.
- (20) Iwasaki, T.; Kawano, N.; Yoshida, J.-ichi Radical polymerization using microflow system: numbering-up of microreactors and continuous operation. *Organic Process Research & Development* **2006**, *10*, 1126-1131.
- (21) Hornung, C. H.; Mackley, M. R.; Baxendale, I. R.; Ley, S. V. A microcapillary flow disc reactor for organic synthesis. *Organic Process Research & Development* **2007**, *11*, 399-405.
- (22) Schenk, R. Numbering-up of micro devices: a first liquid-flow splitting unit. *Chemical Engineering Journal* **2004**, *101*, 421-429.
- (23) Calabrese, G. S.; Park, S.; Pissavini, S. From batch to continuous flow processing in chemicals manufacturing. *AIChE Journal* **2011**, *57*, 828-834.
- (24) Zhao, Y.; Chen, G.; Yuan, Q. Liquid-liquid two-phase flow patterns in a rectangular microchannel. *AIChE Journal* **2006**, *52*, 4052-4060.
- (25) Dessimoz, a; Cavin, L.; Renken, a; Kiwiminsker, L. Liquid-liquid two-phase flow patterns and mass transfer characteristics in rectangular glass microreactors. *Chemical Engineering Science* **2008**, *63*, 4035-4044.

- (26) Cherlo, S. K. R.; Kariveti, S.; Pushpavanam, S. Experimental and numerical investigations of two-phase (liquid–liquid) flow behavior in rectangular microchannels. *Industrial & Engineering Chemistry Research* **2010**, *49*, 893-899.
- (27) Serizawa, A.; Feng, Z.; Kawara, Z. Two-phase flow in microchannels. *Experimental Thermal and Fluid Science* **2002**, *26*, 703-714.
- (28) Kashid, M. N.; Gupta, A.; Renken, A.; Kiwi-Minsker, L. Numbering-up and mass transfer studies of liquid–liquid two-phase microstructured reactors. *Chemical Engineering Journal* **2010**, *158*, 233-240.
- (29) Kashid, M. N.; Gerlach, I.; Goetz, S.; Franzke, J.; Acker, J. F.; Platte, F.; Agar, D. W.; Turek, S. Internal circulation within the liquid slugs of a liquid–liquid slug-flow capillary microreactor. *Industrial & Engineering Chemistry Research* **2005**, *44*, 5003-5010.
- (30) Tice, J. D.; Song, H.; Lyon, A. D.; Ismagilov, R. F. Formation of droplets and mixing in multiphase microfluidics at low values of the Reynolds and the Capillary numbers. *Langmuir* **2003**, *19*, 9127-9133.
- (31) Song, H.; Chen, D. L.; Ismagilov, R. F. Reactions in droplets in microfluidic channels. *Angewandte Chemie (International ed. in English)* **2006**, *45*, 7336-56.
- (32) Nere, N. K.; Patwardhan, A. W.; Joshi, J. B. Liquid-phase mixing in stirred vessels: turbulent flow regime. *Industrial Chemical Engineering Research* **2003**, *42*, 2661–2698.
- (33) Mitrinovic, D. M.; Zhang, Z.; Williams, S. M.; Huang, Z.; Schlossman, M. L. X-ray reflectivity study of the water–hexane interface. *The Journal of Physical Chemistry B* **1999**, *103*, 1779-1782.
- (34) Lockhart, R. W.; Martinelli, R. C. Proposed correlation of data for isothermal, two-phase, two-component flow in pipes. *Chemical Engineering Progress* **1949**, *45*, 39-48.
- (35) Gennes, P. G.; Wyart, F. B.; Quere, D. Capillarity and Wetting Phenomena: Drops, Bubbles, Pearls, Waves; *Springer*: Berlin Heidelberg, **2003**.
- (36) Tabeling, P. Investigating slippage, droplet breakup, and synthesizing microcapsules in microfluidic systems. *Phys. Fluids* **2010**, *22*, 1-7.
- (37) Clift, R., Grace, J.R., Weber, M. E. Bubbles, drops and particles; *Academic Press*: New York, **1978**.
- (38) Vananroye, A.; Puyvelde, P. V.; Moldenaers, P. Morphology development during microconfined flow of viscous emulsions. *Applied Rheology* **2006**, *16*, 242-247.
- (39) Tsouris, C.; Lizama, H. M.; Spurrier, M. a.; Takeuchi, T. L.; Scott, T. C. Hydrodynamics of bioreactor systems for liquid-liquid contacting. *Applied Biochemistry and Biotechnology* **1996**, *57-58*, 581-592.
- (40) Jovanović, J.; Rebrov, E. V.; Nijhuis, T. a. (Xander); Hessel, V.; Schouten, J. C. Phase-transfer catalysis in segmented flow in a microchannel: fluidic control of selectivity and productivity. *Industrial & Engineering Chemistry Research* **2010**, *49*, 2681-2687.
- (41) Lemenand, T. Droplets formation in turbulent mixing of two immiscible fluids in a new type of static mixer. *International Journal of Multiphase Flow* **2003**, *29*, 813-840.
- (42) Calderbank, P. H.; Lochiel, A. C. Mass transfer coefficients, velocities and shapes of carbon dioxide bubbles in free rise through distilled water. *Chemical Engineering Science* **1964**, *19*, 485-503.
- (43) Higbie, R. The rate of absorption of a pure gas into a still liquid during short periods of exposure. *Transactions of the American Institute of Chemical Engineers* **1935**, 365-389.
- (44) Timson, W.; Dunn, C. Mechanism of gas absorption from bubbles under shear. *Industrial & Engineering Chemistry* **1960**, *52*, 799-802.

- (45) Deindoerfer, F.; Humphrey, A. Mass transfer from individual gas bubbles. *Industrial & Engineering Chemistry* **1961**, *53*, 755-759.
- (46) Lapidus, L.; Elgin, J. C. Mechanics of vertical-moving fluidized systems. *AIChE Journal* **1957**, *3*, 63-68.
- (47) Lockett, M. J.; Kirkpatrick, R. D. Ideal bubbly flow and actual flow in bubble columns. *Transactions of the Institution of Chemical Engineers* **1975**, *53*, 267-273.
- (48) Laurenzi, F.; Coroneo, M.; Montante, G.; Paglianti, A.; Magelli, F. Hydrodynamics of immiscible liquid-liquid dispersions in stirred vessels. *13th European Conference on Mixing*, London **2009**, 14-17.
- (49) Kamienski, J.; Wojtowicz, R. Dispersion of liquid-liquid systems in a mixer with a reciprocating agitator. *Chemical Engineering and Processing* **2003**, *42*, 1007-1017.
- (50) Zhou, G.; Kresta, S. M. Correlation of mean drop size and minimum drop size with the turbulence energy dissipation and the flow in an agitated tank. *Chemical Engineering Science* **1998**, *53*, 2063-2079.
- (51) Buchs, J.; Bernd, Z. Evaluation of maximum to specific power consumption ratio in shaking bioreactors. *Journal of Chemical Engineering of Japan* **2001**, *34*, 647-653.
- (52) Kashid, M.; Agar, D. Hydrodynamics of liquid-liquid slug flow capillary microreactor: Flow regimes, slug size and pressure drop. *Chemical Engineering Journal* **2007**, *131*, 1-13.
- (53) A. M. Al Taweel; C. Li; Goma, H. G.; Yuet, P. Intensifying mass transfer between immiscible liquids using screen-type static mixers. *Trans IChemE, Part A, Chemical Engineering Research and Design* **2007**, *85*, 760-765.
- (54) Lemenand, T.; Dupont, P.; Della Valle, D.; Peerhossaini, H. Turbulent mixing of two immiscible fluids. *Journal of Fluids Engineering* **2005**, *127*, 1132.
- (55) Kashid, M. N.; Renken, A.; Kiwi-Minsker, L. Gas-liquid and liquid-liquid mass transfer in microstructured reactors. *Chemical Engineering Science* **2011**, *66*, 3876-3897.
- (56) Merchuk, J. C. Experimental study of dispersion and separation of phases in liquid-liquid extraction of copper by LIX 64N in various types of mixers. *Ind. Eng. Chem. Process Des. Dev.* **1980**, *19*, 522-526.
- (57) Su, Y.; Zhao, Y.; Chen, G.; Yuan, Q. Liquid-liquid two-phase flow and mass transfer characteristics in packed microchannels. *Chemical Engineering Science* **2010**, *65*, 3947-3956.

4 Experimental determination of residence time distribution in the Advanced-Flow Reactor

4.1 Abstract

Determination of the residence time distribution (RTD) to characterize the hydrodynamics of a reactor is essential for reactor development, scale-up, design, and optimization purposes. Here the RTD for single-phase flow in the Advanced-Flow Reactor (AFR) Gen 1 is determined experimentally covering flow rates from 10 mL/min to 80 mL/min at ambient temperature and atmospheric outlet pressure. Comparison with conventional RTD models (tanks in series and dispersion models) and a two-zone model that accounts for dynamic/static zones with mass transfer between them is also included. From the analysis, it is concluded that the two-zone model with no axial dispersion describes with best accuracy the RTD in the AFR. Percentage reductions of 78 – 88 % for sum of errors with respect to the tanks in series and dispersion models are achieved with the two-zone model.

4.2 Introduction

Understanding and characterizing the hydrodynamics of a reactor is essential in every scale-up, reactor design, and optimization process. Not only the kinetics of the reaction may be affected by residence time distribution (RTD), but also comparison of the different RTDs for different reactor sizes provides insight about the challenges that can be encountered during the scale-up process.

Residence time distribution studies are frequently used to determine the “mixing” characteristics of a vessel or continuous flow device. Each fluid particle stays a different amount of time inside the reactor and thus, the entire fluid system is characterized by a distribution function of residence times for fluid particles. The function $F(t)$ is defined as the fraction of particles whose residence time is “ t ” or less, whereas the complementary function, $F^*(t)$, is the fraction of particles possessing a residence time greater than “ t ”, as given by eq 4.1. ^{1, 2}

$$F^*(t) = 1 - F(t) \quad (4.1)$$

Both $F(t)$ and $F^*(t)$ functions are seen as probability functions: $F(t)$, the probability of a single fluid particle staying in the system for a time “ t ” or less; $F^*(t)$, the probability of a single particle possessing a residence time greater than “ t ”. The density function $E(t)$ is defined as the derivative of the function $F(t)$ and is given by eq 4.2. The amount “ $E(t)dt$ ” represents the probability of a fluid particle having a residence time between “ t ” and “ $t + dt$ ”.^{1,2}

$$E(t) = dF(t)/dt \quad (4.2)$$

The first (μ_1) and second (μ_2) statistical moments of the density function $E(t)$ provide information about the mean residence time (τ) and the variance of the distribution (σ^2), respectively.

$$\mu_n = \int_0^{\infty} t^n E(t) dt \quad (4.3)$$

There are two methods mainly used to measure experimentally the residence time distributions: a) introducing an impulse of tracer within a very short time (resembling a delta function) at the entrance of the reactor and measuring the concentration at the outlet. This outlet concentration is proportional to the density function $E(t)$; b) introducing a step change of tracer concentration at the entrance of the reactor and monitoring the concentration at the outlet until a constant value is reached. The $F(t)$ function is then given by the ratio $C(t)/C_{\text{final}}$, and $E(t)$ by the temporal derivative of $F(t)$. In both cases, the system must be at steady state.

There are two ideal cases considered when studying RTDs:

- a) *Plug flow reactor (PFR)*: there is no axial mixing and each element of fluid is completely mixed in the radial direction at each axial position. All fluid elements leave the reactor at time τ (residence time of the PFR) if they entered the reactor at time zero. The RTD of a PFR is a Dirac delta function at τ (eq 4.4) and its variance is zero.

$$E(t) = \delta(t - \tau) \quad (4.4)$$

- b) *Complete stirred tank reactor (CSTR)*: the fluid particles are instantaneously mixed once they enter the reactor so that the outlet has a homogeneous composition. The RTD is decreasingly exponential, as given by eq 4.5.

$$E(t) = \frac{e^{-t/\tau}}{\tau} \quad (4.5)$$

Deviations from the PFR are very common in real reactors and non-zero variances are encountered, normally due to the presence of dispersion, diffusion, non-uniform velocity profiles, or turbulence. Stagnant zones cause deviations from the ideal PFR or CSTR, with an earlier arrival of the fluid at the outlet, whereas channeling and strong internal circulations may cause the presence of more than one peak in the E(t) curve.

Simple models have been developed to account for non-idealities in the flow. One-parameter models include the “tanks in series” and “dispersion” models. A more complex model called “two-zone model” accounts for dynamic and static zones within the reactor with mass transfer between them. These three models are explained in detail in sections 4.2.1-3.

4.2.1 Tanks in series model

The “tanks in series” model is one of the conventional models used to model real reactors. The single parameter to determine is the number of tanks in series which best describes the RTD compared with the experimental data. The RTD E(t) and E(θ) are given by eqs 4.6 and 4.7, respectively³. The number of tanks can be either obtained from the dimensionless variance (eq 4.8) or by fitting the experimental data to the predicted RTD by the model. For cases when the variance is very sensitive to the experimental data, the second approach is preferable.

$$E(t) = \frac{t^{n-1}}{(n-1)!\tau_i^n} e^{-t/\tau_i} \quad (4.6)$$

$$E(\theta) = \frac{n(n\theta)^{n-1}}{(n-1)!} e^{-n\theta} \quad (4.7)$$

$$n = \frac{1}{\sigma_{\theta}^2} \quad (4.8)$$

4.2.2 Dispersion model

Non ideal reactors can be described by a “dispersion model” in which the single parameter to determine is the Peclet number (Pe), defined by eq 4.9. Pe is a dimensionless number that measures the degree of dispersion in the vessel. For low degrees of dispersion, $Pe > 100$, eqs 4.10 and 4.11 describe the dimensionless residence time distribution curve $E(\theta)$ and variance, respectively ⁴:

$$Pe = \frac{UL}{D} \quad (4.9)$$

$$E(\theta) = \frac{1}{2\sqrt{\pi Pe}} \exp\left[-\frac{(1-\theta)^2}{4Pe}\right] \quad (4.10)$$

$$\sigma_{\theta}^2 = \frac{2}{Pe} \quad (4.11)$$

For higher degrees of dispersion, $Pe < 100$, only when the boundary conditions for the inlet and outlet are open (there is dispersion both upstream and downstream), an analytical solution can be obtained. Here the non-dimensional concentration of tracer, mean residence time, and dimensionless variance, are given by eqs 4.12 – 14, respectively:

$$E(\theta) = \frac{1}{2\sqrt{\pi/Pe_r}} \exp\left(\frac{-(1-\theta)^2}{4\theta/Pe_r}\right) \quad (4.12)$$

$$\bar{t} = \left(1 + \frac{2}{Pe_r}\right) \tau \quad (4.13)$$

$$\sigma_{\theta}^2 = \frac{2}{Pe_r} + \frac{8}{Pe_r^2} \quad (4.14)$$

4.2.3 Two-zone model

The “two-zone model” considers the presence of stagnant zones in the reactor by dividing the liquid flow into a dynamic zone, modeled as plug flow with axial dispersion, and a static zone, with mass transfer

between both zones (Figure 4.1) ^{5, 6}. The model incorporates the contribution of stagnant holdup and dynamic holdup through the parameters $\epsilon_{L,st}$ and $\epsilon_{L,d}$, respectively, and the mass transfer between them by incorporating the number of mass transfer units, N . The Peclet number (Pe) is a measurement of the amount of axial dispersion in the dynamic zone.

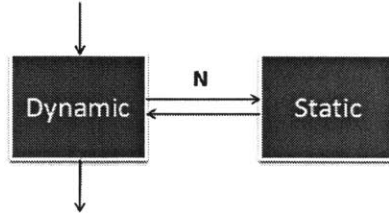


Figure 4.1: Schematic of two-zone RTD model. This model incorporates contributions from a static zone and an axially dispersed dynamic zone, with mass transfer between them.

The mass balances for the tracer in the dynamic and the static zones are described by eq 4.15 and eq 4.16, respectively ^{5, 6}:

$$\epsilon_{L,d} \frac{\partial C_d}{\partial t} + \frac{v_{sL}}{L} \frac{\partial C_d}{\partial x} + N \frac{v_{sL}}{L} (C_d - C_{st}) = \frac{1}{Pe} \frac{v_{sL}}{L} \frac{\partial^2 C_d}{\partial x^2} \quad (4.15)$$

$$\epsilon_{L,st} \frac{\partial C_{st}}{\partial t} + N \frac{v_{sL}}{L} (C_{st} - C_d) = 0 \quad (4.16)$$

The boundary and initial conditions considered are given by eqs 4.17 – 4.19.

$$x = 0, \quad C_d|_{x=0^-} = C_d|_{x=0^+} - \frac{1}{Pe} \frac{\partial C_d}{\partial x} \quad (4.17)$$

$$x = 1, \quad \frac{\partial C_d}{\partial x} = 0 \quad (4.18)$$

$$t = 0, \quad C_d = 0; C_{st} = 0 \quad (4.19)$$

4.3 Experimental

The measurements of the residence time distribution (RTD) in the AFR were performed following the tracer injection method. The variation in the UV absorbance of the liquid phase at the outlet of the

microreactor was monitored. An online UV spectro photometer (Ocean Optics with multi-wavelength UV source) was used to measure the tracer concentration in terms of absorbance at a sampling frequency of 70 Hz. In these experiments, a DH-200 Mikropack UV-VIS – NIR deuterium and halogen light source was used. The experimental setup is shown in Figure 4.2.

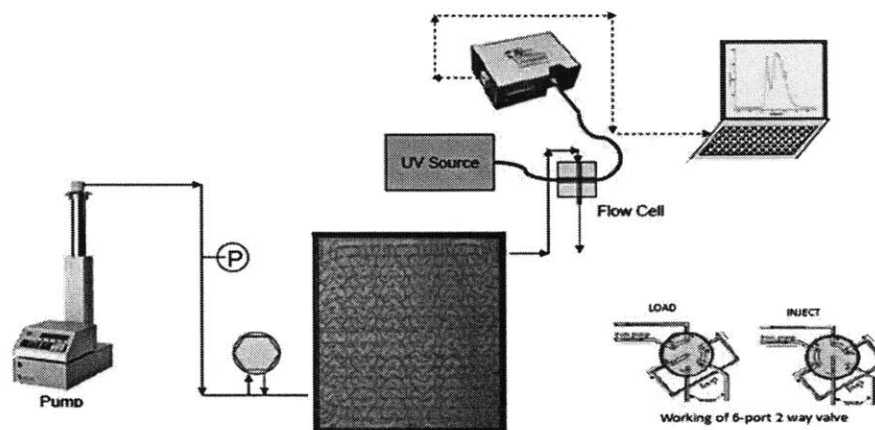


Figure 4.2: Experimental set-up for RTD measurements. Liquid is introduced in the Advanced-Flow reactor through an ISCO pump; a six-way valve is used to introduce a pulse of tracer into the liquid phase; a flow cell at the outlet measures UV absorbance and results are monitored in a computer

Water was used as the liquid phase and the tracer was an aqueous solution of acetone with concentration 20% vol./vol. The water was pumped at constant flow rate using an ISCO syringe pump, and a six-way two-position valve operated manually was used to introduce a small amount of tracer as a pulse at time $t = 0$ into the liquid phase that flows into the AFR. The volume injected by the valve into the system was 50 μL . Downstream of the reactor, the spreading of the tracer pulse was measured by UV absorbance of the outlet stream (linearly related to the tracer concentration) through a flow cell of 0.2 mL volume, giving a discrete data for the impulse response of the system. The signal was integrated for wavelengths ranging from 200 to 300 nm, which comprises the wavelengths of maximum absorbance of acetone. The data acquisition time was varied for case-to-case depending on the complete exit of the tracer from the plate. The RTD was

measured at ambient conditions (22 °C and atmospheric pressure at the outlet) for 10, 20, 60, and 80 mL/min of water, injecting the tracer three times for each flow rate.

4.3.1 Analysis of experimental data

The raw data are processed by computing moving average to reduce the noise. The mean residence time and variance were then determined for each experiment using the experimental discrete data of UV absorbance, $A(t)$, as given by eq 4.20 and eq 4.21, respectively:

$$\bar{t} = \frac{\int_{t_0}^{t_f} A(t) dt}{\int_{t_0}^{t_f} A(t) dt} \quad (4.20)$$

$$\sigma_t^2 = \frac{\int_{t_0}^{t_f} A(t)(t-\bar{t})^2 dt}{\int_{t_0}^{t_f} A(t) dt} = \frac{\int_{t_0}^{t_f} A(t)t^2 dt}{\int_{t_0}^{t_f} A(t) dt} - \bar{t}^2 \quad (4.21)$$

The integration of the discrete data was performed numerically by the trapezoidal integration method using Matlab 7.8.0. The $E(t)$ curve was determined from the processed discrete data by eq 4.22.

$$E(t) = \frac{A(t)}{\int_{t_0}^{t_f} A(t) dt} \quad (4.22)$$

The dimensionless $E(\theta)$ curve was determined from the mean residence time and the $E(t)$ curve, as given by eq 4.23.

$$E(\theta) = E(t)\bar{t} \quad (4.23)$$

The dimensionless residence time and variance are determined by eq 4.24 and eq 4.25, respectively.

$$\theta = \frac{t}{\bar{t}} \quad (4.24)$$

$$\sigma_\theta^2 = \frac{\sigma_t^2}{\bar{t}^2} \quad (4.25)$$

There are two methods used to fit the model to the experimental data: Method A relies on finding the parameter that best matches the experimental and predicted dimensionless variance, whereas Method B finds the parameter that minimizes the sum of the square of errors between the experimental data and the model.

In our experiments, it was found that the dimensionless variance was very sensitive to the noise in the experimental data and the criteria used in data processing, such as the decision of the start and end points characterizing the RTD curve. Thus, the criterion for the selection of the parameter that fit best the experimental data is to minimize the sum of the squares of the errors between the experimental $E(t)$ vs. t and the one predicted by the model, as given by eq 4.26.

$$\text{Minimization function} = \sum_{i=0}^N (Y_{exp,i} - Y_{model,i})^2 \quad (4.26)$$

4.4 Results and discussion

4.4.1 Experimental Data

In this section, the residence time distribution curves (RTD) obtained at ambient conditions are presented at different liquid flow rates. The collected raw data (absorbance) corresponding to the response of the system to a pulse injection of tracer was normalized to obtain the residence time distribution, $E(\theta)$. The experimentally obtained $E(\theta)$ versus the dimensionless time, θ , are shown in Figure 4.3, for the different liquid flow rates. The mean residence times (\bar{t}), variance (σ^2), and dimensionless variance (σ_θ^2) calculated for 10, 20, 60, and 80 mL/min residence time distribution $E(t)$ curves are shown in Table 4.1.

Table 4.1: Experimental mean residence time and variance

Q_L (mL/min)	\bar{t} (s)	σ^2 (s ²)	σ_θ^2 (-)
10	55.83	82.42	0.0264
	55.79	89.57	0.0288
20	27.55	19.59	0.0258
	27.71	21.89	0.0285
60	9.31	1.68	0.0194
	9.39	2.07	0.0235
80	6.94	1.01	0.0210
	6.85	0.98	0.0209

In a plug flow reactor, all the tracer arrives at the outlet of the tube at time τ (reactor residence time) yielding a Dirac delta function for $E(\theta)$ centered at 1 and with zero variance. However, from the experimental

RTD it is seen that the $E(\theta)$ curve is centered around $\theta = 1$ but there is some dispersion that broadens the distribution: some fluid particles arrive at the outlet earlier than most part of the fluid particles that arrive close to the mean residence time, and there is also a fraction of particles that arrives later than the average. Thus, the RTD characteristic of the AFR is PFR with dispersion. Here it should be noticed that the recommended operating conditions for the AFR are flow rates above 30 mL/min, and thus, the AFR will perform with a more symmetric RTD than what is observed at 10 mL/min, which can be seen as an atypical case and not the commonly observed behavior of the AFR.

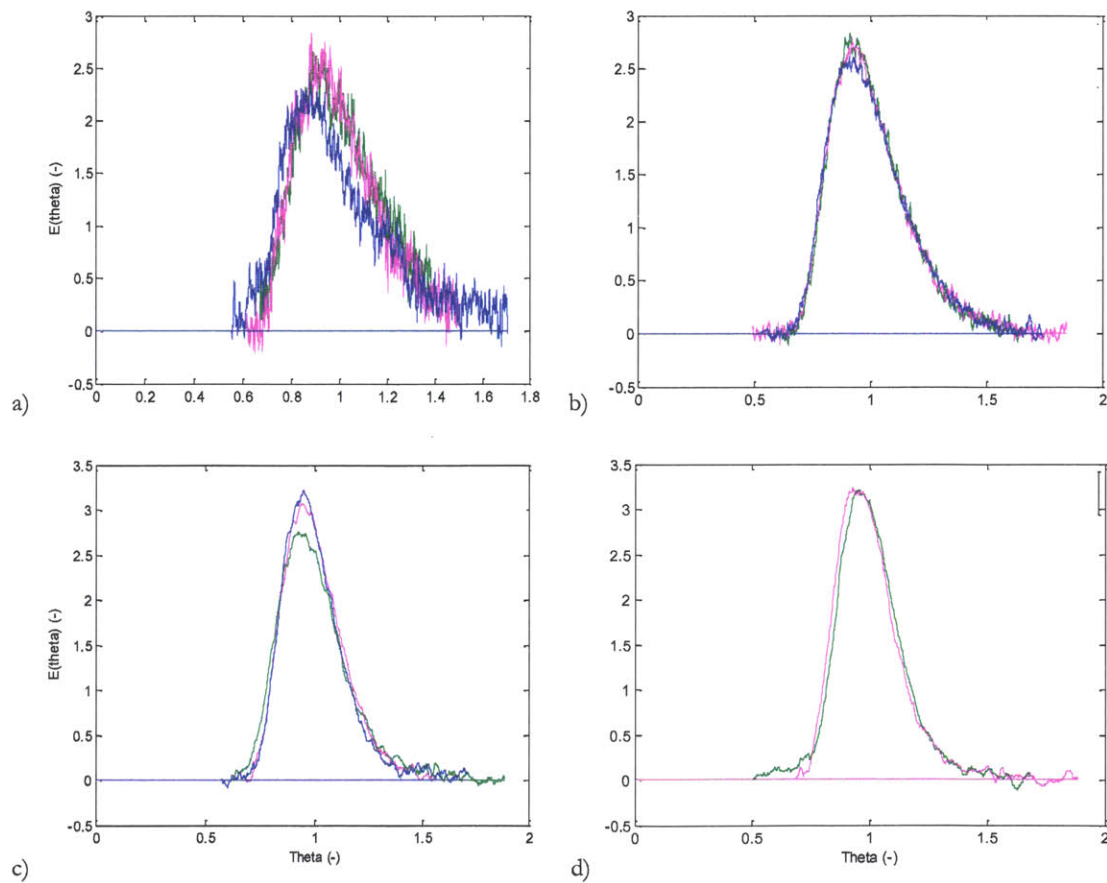


Figure 4.3: Experimental residence time distribution $E(\theta)$ versus θ for different water flow rates (mL/min): a) 10; b) 20; c) 60; d) 80. Legend: ---, experiment 1; ----, experiment 2; -.-, experiment 3

4.4.2 Models

4.4.2.1 Tanks in series model

The results obtained for the tanks in series model are shown Table 4.2. The number of tanks was first calculated from the experimental dimensionless variance. A better agreement was found when the sum of the square of errors was chosen as the criterion to decide the number of tanks in series. The reason why for some experiments there is a significant difference between both methods is caused by the uncertainty in the determination of the experimental variance. The experimental data itself, and the initial and end points selected to compute the variance affect directly the result obtained. The parameters that characterize the RTD curve predicted by the tanks in series model for both methods are shown in Table 4.2. The results show that as the flow rate increases the number of tanks in series increases, which means that the Peclet number or mixing in the reactor is smaller at larger flow rates therefore resembling a plug flow behavior with small degree of dispersion.

Table 4.2: Number of tanks in tanks in series model

Q_L (mL/min)	N_{tanks} based on σ_{θ}^2	N_{tanks} based on sum of square of errors
10	38	30
	35	31
20	38	39
	34	37
60	52	52
	43	53
80	50	62
	60	62

The predicted curves by the tanks in series model using different number of tanks for different flow rates are shown in Figure 4.4. It is observed that none of the number of tanks is able to predict with excellent accuracy the RTD, especially at the lowest flow rates. Better agreement with the experimental results is seen at the highest flow rates, 60 and 80 mL/min, for which the number of tanks is 52 and 62, respectively. A more complex RTD model that introduces more parameters may be necessary to predict more accurately the RTD in the AFR for all flow rates.

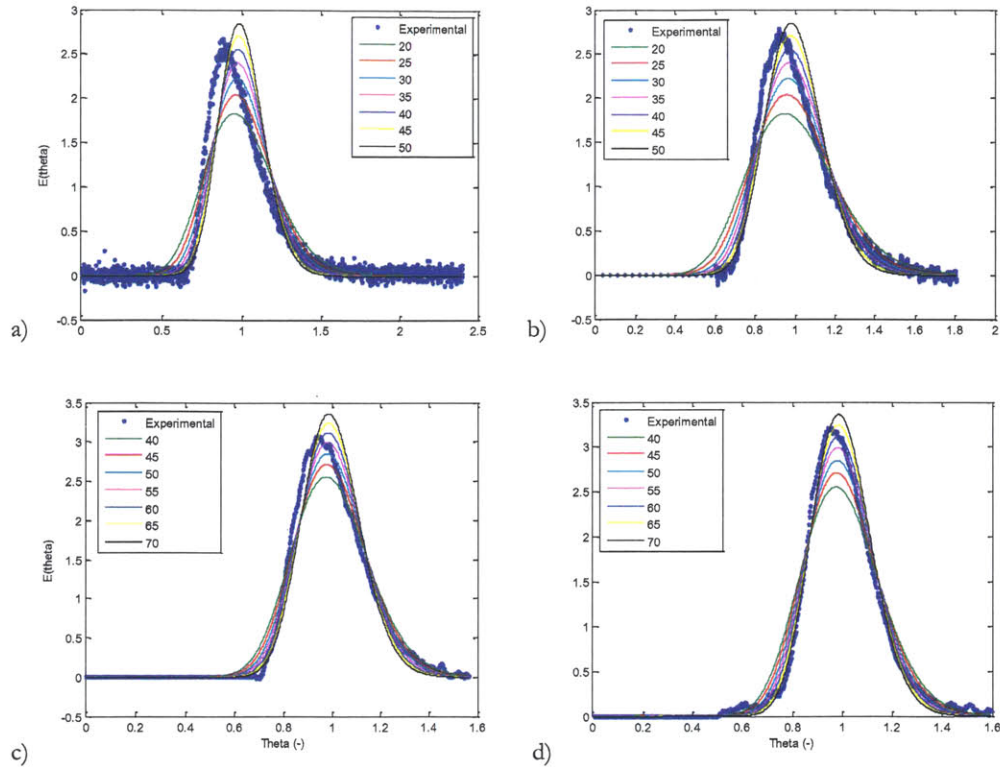


Figure 4.4: Predicted RTD by tanks in series model at different flow rates (mL/min): a) 10, b) 20, c) 60, d) 80

A device whose RTD can be described with a large number of tanks in series resembles a plug flow reactor with dispersion. In the limit of a number of tanks equal to infinite, the behavior of the reactor is close to PFR. The AFR is composed by 51 hearts in series which are designed to provide good mixing performance. Based on the reactor design, one would expect the RTD to be similar to 51 CSTRs in series, each CSTR having the volume of a single heart cell. We cannot obtain further information about this hypothesis here, because the experimental measurement of RTD requires additional tubing and measuring system that affect the overall RTD. However, further computational fluid dynamic simulations have been performed in order to obtain isolated RTDs for the AFR module for different flow rates. The results are included in Chapter 5.

4.4.2.2 Dispersion model

The dispersion model for large and small degrees of dispersion is used to predict the experimental RTD data. The dimensionless RTD curves $E(\theta)$ are calculated using eq 4.10 and 4.12 for $Pe > 100$ and $Pe < 100$, respectively. Table 4.3 includes the results using both dispersion models for both approaches of: a) matching the dimensionless variance; b) minimizing the sum of the square of errors between experiments and model, similarly to the tanks in series model analysis. It is seen from the results that a better agreement with the experiments is obtained when the analysis is performed in base of the minimization of errors due to the increased uncertainty in the determination of the dimensionless variance of the RTD from the experiments. Focusing now on the calculated parameters, it is clearly seen that larger Peclet numbers are obtained for higher flow rates. Peclet numbers are a measurement of the degree of dispersion, being smaller for higher degrees of dispersion. Infinite values of Pe correspond to a PFR RTD. Thus, increasing the flow rate reduces the axial dispersion. Figure 4.5 includes the Peclet numbers in terms of flow rates. It is observed that the slope Pe versus Q_L changes from the lowest flow rates to the largest flow rates, which may be due to a change in the flow regime in the reactor. This observation needs further investigation and a more detail explanation is included in Chapter 5.

Table 4.3: Peclet number for dispersion model

Q_L (mL/min)	Pe based on σ_θ^2		Pe based on sum of square of errors		Derived variables from Peclet	
	Dispersion I	Dispersion II	Dispersion I	Dispersion II	Dispersion module	Dispersion coefficient
10	76	80	60	57	0.0175	0.0029
	69	73	65	63	0.0159	0.0026
20	77	81	79	76	0.0132	0.0044
	69	81	75	81	0.0123	0.0041
60	104	107	105	101	0.0095	0.0095
	85	89	111	104	0.0090	0.0090
80	99	103	125	125	0.0080	0.0107
	120	124	126	122	0.0079	0.0106

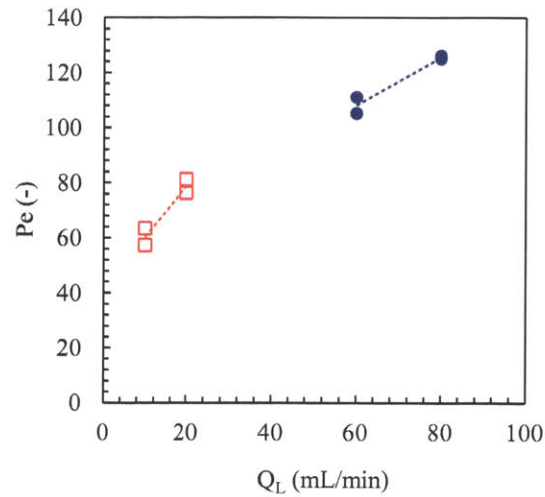


Figure 4.5: Pelet number versus liquid flow rate for dispersion model. Two flow regimes are observed based on the Pelet numbers with different behavior at the lowest flow rates with respect to the largest flow rates.

A comparison of the results obtained with the dispersion model and the tanks in series models together with the experimental RTDs are presented in Figure 4.6 for different water flow rates. Similar agreement is seen for both the tanks in series and the dispersion models. While the least agreement is seen at the lowest flow rates, the best agreement is obtained at 60 and 80 mL/min, where the behavior is closer to plug flow with certain degree of axial dispersion. In particular, for 80 mL/min, $Pe = 123$. The AFR has an overall length of 2.2 meters if the flow is treated as if it was split between the two sides of the hearts traveling at half speed (half flow rate flows through each side of the heart channel). Considering that $Pe = UL/D$, where D is the dispersion coefficient, the dispersion module ($1/Pe$) for 80 mL/min is 0.008 and D is 0.011 m^2/s . The remaining values for all flow rates are also included in Table 4.3. According to Levenspiel ⁶, it is considered that the dispersion is large when the dispersion module is on the order of 0.1, intermediate when it is 0.01 and small when it is on the order of 0.001. At the limit of plug flow, the dispersion module is zero, and for complete mixing (CSTR), the dispersion module is infinite. Based on these general rules, the dispersion in the AFR ranges from small to intermediate when operating at the largest flow rates or at the smallest flow rates, respectively.

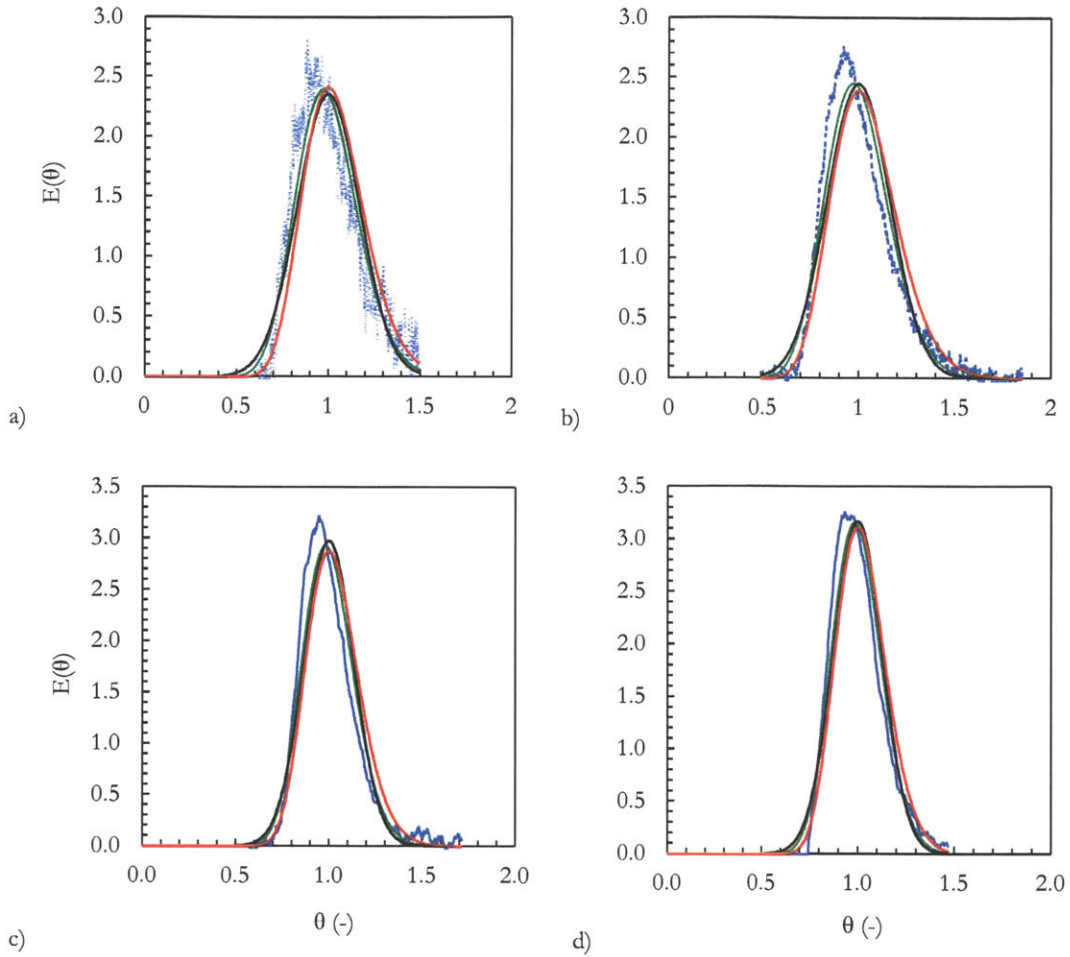


Figure 4.6: Comparison of tanks in series model with dispersion model for different water flow rates (mL/min): a) 10, b) 20, c) 60, d) 80; Legend: — (blue), Experimental; — (green), Tanks in series; — (red), Dispersion model $Pe < 100$; — (black) Dispersion model $Pe > 100$;

4.4.2.3 Two zone model

A more complex model with more than one parameter is presented here. This model considers the presence of a static zone connected to a dynamic zone with mass transfer between them. The Peclet number (Pe), static holdup ($\varepsilon_{L,st}$), number of mass transfer units (N), and reactor length (L) are four parameters that need to be known for the correct application of this two-zone model. In order to examine the effect of each parameter, a sensitivity analysis of the parameters is performed. The response variables to monitor are: a) mean residence time (\bar{t}); b) variance ($\sigma^2, \sigma_{\theta}^2$). Here we present only a few examples showing the main trends

in Figures 4.7 and 4.8. It was observed that increasing the number of mass transfer units and the static holdup the variance increases, with the effect of the static holdup stronger at low N (slow mass transfer between static and dynamic zones). On the other side, increasing Pe reduces the axial dispersion and thus, the variance. The Peclet number, N , and static holdup do not have a strong effect on the mean residence time. The main parameter affecting the mean residence time is the flow path length, L .

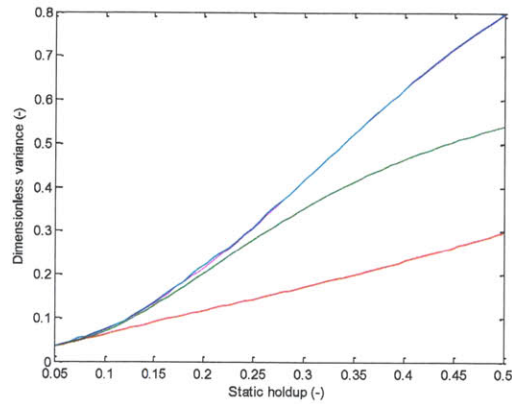


Figure 4.7: Effect of static holdup on dimensionless variance. $Pe = 150$, $L = 2.15$ m, $N = 0.5$. Legend: — (red), 10; — (green), 20; — (pink), 60; — (blue), 80 (mL/min water)

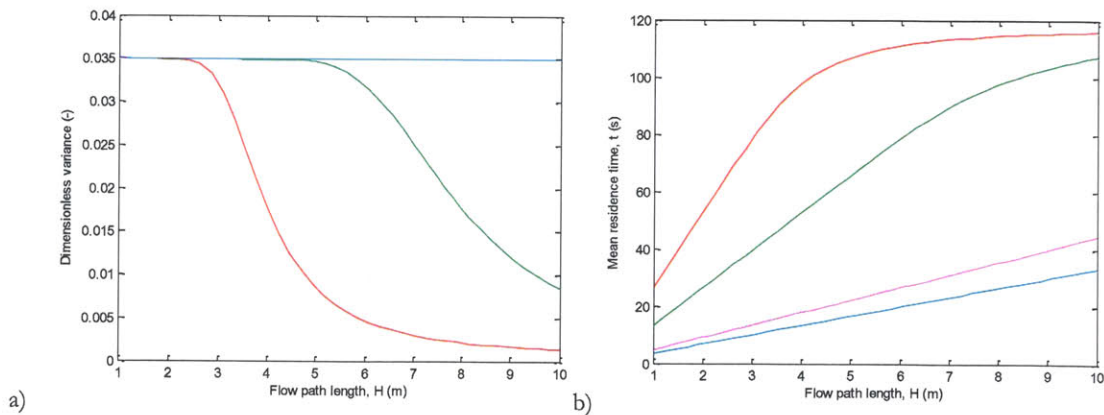


Figure 4.8: Effect of flow path length on a) dimensionless variance, and b) mean residence time. $Pe = 150$, $L = 2.15$ m, $N = 3$, for different water flow rates (mL/min): — (red) 10, — (green) 20, — (pink) 60, — (blue) 80

The best fitting parameters of the two-zone model were obtained using Matlab 7.8.0. The code imports the processed experimental data from a *.xls* file, calculates relevant parameters and finds the Peclet number (Pe), number of transfer units (N), flow path length (L), and static holdup ($\epsilon_{L,st}$) that fit best the experimental data. The RTD model was implemented by discretization of the spatial derivatives, selecting upwind differencing mode for one order differential equations to reduce numerical oscillations, and solving the differential equations for the independent variable time. In this way, the problem is to find the solution to a system of algebraic and one-order differential equations.

Before trying to find four parameters that best fit the experimental data, it is best to find physical meaning to each one of them and try to estimate them based on prior knowledge of the system. The *flow path length* is a parameter that has a significant influence on the mean residence time. The value obtained based on the dimensions of the additional tubing (29 cm 1/8" OD and 17 cm 1/4" OD) and the flow path length of the AFR considering that the flow splits into two streams flowing near the walls at half speed is 2.2 m.

A dimensional analysis provides information about what terms are important in the equations describing the two zone model (Section 4.2.3). The dispersion term is negligible as compared to other terms in our system (as seen in Table 4.4) and, as a first approximation, will be neglected in the simulations. This is also in accordance with the results obtained with the axial dispersion models, where the Peclet numbers correspond to a small dispersion in the system.

Table 4.4: Dimensional analysis of two-zone model equations

Q_L (mL/min)	Dispersion	Transient	Convection	Dispersion/transient	Dispersion/convection
10	0.0006	0.0161	0.0344	0.0375	0.0175
	0.0005	0.0161	0.0344	0.0339	0.0159
20	0.0009	0.0327	0.0689	0.0277	0.0132
	0.0009	0.0325	0.0689	0.0262	0.0123
60	0.0020	0.0967	0.2066	0.0212	0.0099
	0.0020	0.0958	0.2066	0.0207	0.0096
80	0.0022	0.1297	0.2755	0.0170	0.0080
	0.0023	0.1314	0.2755	0.0172	0.0082

The number of mass transfer units, static holdup, and flow path length were obtained by adjusting the experimental data to the model based on a minimization of the sum of square of errors. The results are presented in Table 4.5. For all experiments, the resulting flow path length L was approximately 2.1 m, very close to the estimated value of 2.2 m based on the physical measurement of the reactor length and tubing. It is important to notice here that the two-zone model is a simplified model that assumes a constant velocity V_{st} . In reality, the velocity is different at each point along the width, the height and the reactor length. Calculating the cross section average velocity at different positions along the heart cell and averaging them gives an averaged velocity (U) that represents well the system.

Table 4.5: Model parameters for two-zone dynamic-static model.

Q_L (mL/min)	$k_{L,a}$ (1/s)	$\epsilon_{st,L}$ (-)	L (m)	Σ (Exp. - Model) ² (-)
10	0.034	0.19	2.21	0.014
	0.039	0.17	2.15	0.022
20	0.063	0.13	2.11	0.0086
	0.068	0.14	2.12	0.0068
60	0.168	0.094	2.13	0.0189
	0.114	0.076	2.14	0.0252
80	0.128	0.064	2.14	0.0399
	0.133	0.063	2.08	0.0319

A comparison between the RTD's obtained using the two-zone model and the experiments is shown in Figure 4.9. It is seen that the prediction using the two-zone model is in better agreement with the experiments than using the one-parameter "tanks in series" and "dispersion" models.

The relative error in predicting the mean residence time and variance is presented in Table 4.6. It is noticed here that the mean residence time is predicted with excellent accuracy with this model. However, there is a larger disagreement when predicting the variance. The reason for this discrepancy is derived from the noise in the experimental data more than the variance itself. In order to discriminate between different RTD models, the sum of square of errors between the experiments and the model is used as a better metric for comparison.

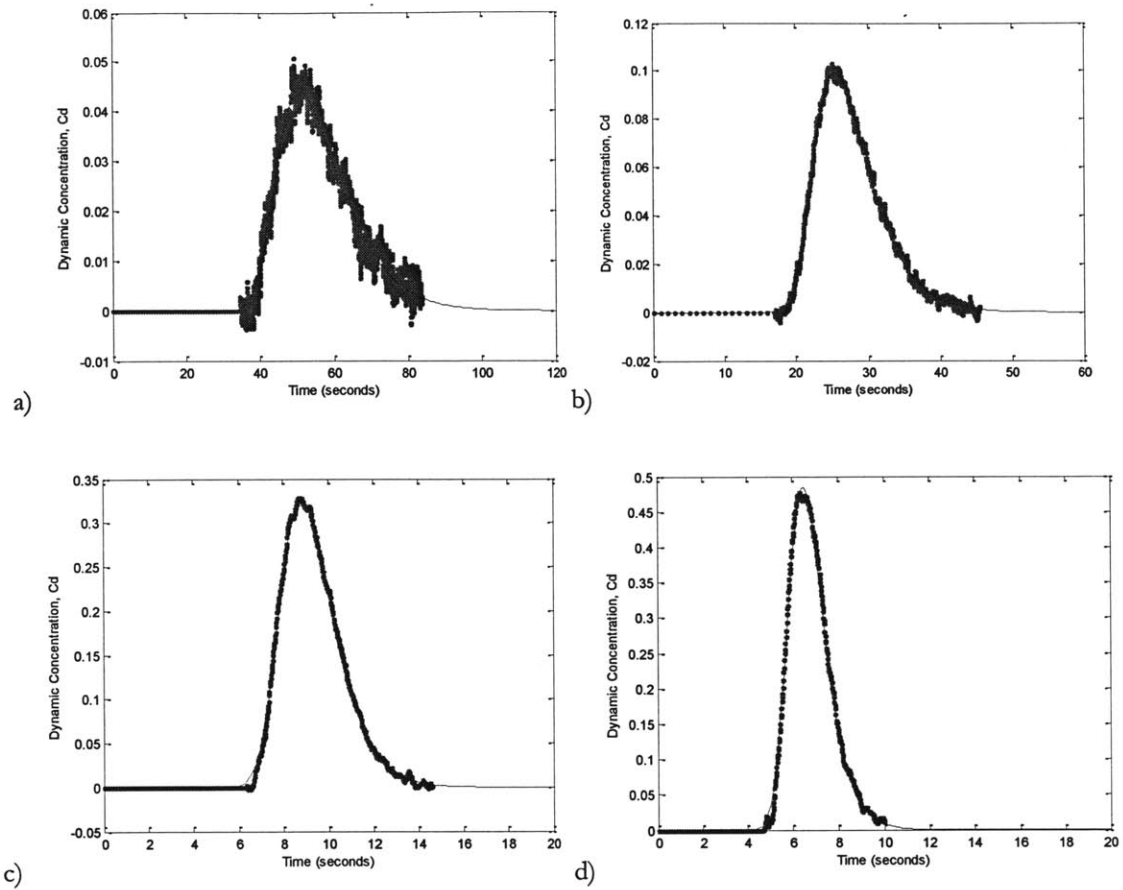


Figure 4.9: $E(t)$ predicted by two-zone model for different flow rates (mL/min): a) 10, b) 20, c) 60, d) 80; Model yields excellent agreement with experimental residence time distribution.

Table 4.6: Relative error (%) in mean residence time and variance in prediction by two-zone model.

Q_L (mL/min)	Mean residence time			Variance		
	Experimental	Model	Error (%)	Experimental	Model	Error (%)
10	55.83	57.95	3.80	82.42	175.19	112.56
	55.79	56.23	0.79	89.56	129.57	44.67
20	27.54	27.56	0.07	19.6	26.06	32.96
	27.71	27.70	0.00	21.41	27.23	27.18
60	9.31	9.31	0.00	1.68	2.17	28.99
	9.39	9.33	-0.64	2.07	2.29	10.72
80	6.94	7.00	0.86	1.03	1.20	16.12
	6.85	6.80	0.00	0.98	1.10	12.24

4.4.3 Comparison among models

It has been shown that there are many factors affecting the RTD variance, and, in consequence, the obtained model parameters. Such factors include ones that affect the direct measurement, and ones that come from the signal processing. The former include the oscillations/variability in the measured absorbance of the tracer, and the later, the decision of the start and end point in the recorded absorbance with time, in addition to the method used to smooth the signal. For this reason, a comparison of the suitability of the models was established in base of the sum of the squares of the errors between the predicted and the experimental data points. A summary of these results is presented in Table 4.7.

It is seen that the two-zone model is able to predict the RTD for different flow rates with the smallest sum of square of errors. The largest sum of square of errors is obtained for 10 mL/min for all models. This is due to the presence of noise in the data at this flow rate. With the two-zone model, reductions of the total error for all predictions from 10 to 80 mL/min of 78%, 88%, and 87% with respect to the tanks in series, dispersion I, and dispersion II models respectively, are achieved. The percentage of reduction in the total errors is even larger when not considering the lowest flow rate (for which the errors are larger in all models): 92%, 96%, and 96% for the tanks in series, dispersion model I, and dispersion model II, respectively.

Table 4.7: Comparison between models based on sum of square of errors

Q_L (mL/min)	Tanks in series	Dispersion I	Dispersion II	Two-zone static-dynamic
10	136.3	301.2	215.6	46.5
	201.0	362.4	343.7	68.8
20	82.6	161.5	149.9	6.7
	85.2	169.7	153.8	5.4
60	18.8	41.1	37.4	1.7
	33.8	75.0	63.7	2.3
80	6.8	24.3	18.5	2.2
	18.8	34.4	37.1	1.6
Total	583.26	1169.57	1019.74	135.09

Thus, accounting for the presence of static zones and mass transfer between dynamic/static regions is important and one-parameter models such as the tanks in series and dispersion models are not as accurate as the two-zone model because they do not consider additional phenomena present in the system. For very large

flow rates (60 and 80 mL/min) the difference between the three models is smaller, probably due to the smaller contribution of mass transfer and static volume. At these flow rates, the system behaves closer to plug flow with small axial dispersion.

4.5 Conclusions

Residence time distributions have been measured in the Advanced-Flow reactor (AFR) for water flow rates of 10, 20, 60, and 80 mL/min. Comparison with single-parameter models such as tanks in series and dispersion models gave fair agreement with experimental results. The number of tanks that best fit the experimental data are 30, 38, 52, and 62 tanks, and the Peclet number (Pe) characteristic of the dispersion model are 60, 79, 105, and 124, for the flow rates tested, respectively. The high Pe numbers informs us about the small axial dispersion present in the system. The AFR presents a plug-flow behavior with small axial dispersion for a wide range of flow rates, especially at the flow rates for which the device is recommended to operate (above 30 mL/min). To further improve the accuracy of the model, a two-zone dynamic-static zone model is seen to improve the accuracy with respect to the one-parameter models by at least 78%.

4.6 Notation

a	Specific interfacial area (m^2/m^3)
$A(t)$	UV Absorbance (arbitrary units)
$C(t)$	Concentration of tracer (mol/L)
C_{final}	Concentration of tracer at final time (mol/L)
C_d	Concentration in dynamic zone (mol/L)
C_{st}	Concentration in static zone (mol/L)
D	Effective diffusion coefficient (m^2/s)
$E(t)$	Residence time distribution (s^{-1})

$E(\theta)$	Dimensionless residence time distribution (-)
$F(t)$	Probability function for particle residence time in reactor (-)
$F^*(t)$	Probability function complementary to $F(t)$ (-)
k_L	Individual mass transfer coefficient (m/s)
$k_{L\bar{a}}$	Overall mass transfer coefficient (1/s)
N	Mass transfer units between static and dynamic zones (-)
n	Number of tanks in series (-)
Q_L	Liquid flow rate (mL/min)
t	Time (s)
t_0	Time of injection of tracer at reactor inlet (s)
t_f	Final time at which no more tracer is seen at reactor outlet (s)
\bar{t}	Mean residence time (s)
U	Average velocity (m/s)
L	Reactor length (m)
V_{sl}	Liquid superficial velocity (m/s)
x	Dimensionless distance in x coordinate (-)
$Y_{exp,i}$	Data point corresponding to experiment
$Y_{model,i}$	Data point corresponding to model

Dimensionless numbers

$\frac{D}{UL}$	Dispersion number (-)
Pe	Peclet number (-)

Pe_τ Peclet number based on the diameter of the tube (-)

Greek letters

θ Dimensionless time (-)

$\varepsilon_{L,st}$ Liquid holdup in static zone (-)

$\varepsilon_{L,d}$ Liquid holdup in dynamic zone (-)

σ_t^2 Variance (s^2)

σ_θ^2 Dimensionless variance (-)

τ Expected residence time (-)

τ_1 Expected residence time of a single tank (s)

μ_n n^{th} moment of the distribution function $E(t)$ (s^n)

4.7 References

- (1) Naor, P; Shinnar, R. Representation and evaluation of residence time distributions. *IEC Fundamentals*, **1963**, 278 – 285
- (2) Martin, A. D. Interpretation of residence time distribution data. *Chem. Eng. Sci.*, **2000**, *55*, 5907 – 5917
- (3) Fogler, H. Scott. Elements of Chemical Reaction Engineering. *Prentice Hall Professional Technical Reference*, 4th Edition, **2006**
- (4) Levenspiel, O. Chemical Reaction Engineering. 3rd Edition. *John Wiley & Sons*, **1999**, New York
- (5) Stegeman, D.; van Rooijen, F. E.; Kamperman, A. A.; Weijer, S.; Westerterp, K. R. Residence time distribution in the liquid phase in a cocurrent gas-liquid trickle bed reactor. *Ind. Eng. Chem. Res.*, **1996**, *35*, 2, 379
- (6) Iliuta, I.; Larachi, F.; Grandjean, B. P. A. Residence time, mass transfer and back-mixing of the liquid in trickle flow reactors containing porous particles. *Chem. Eng. Sci.*, **1999**, *54*, 4099 – 4109

5 Computational fluid dynamic simulations: single-phase flow

5.1 Abstract

Computational fluid dynamic (CFD) simulations are performed for single-phase flow in the Advanced-Flow Reactor (AFR) using the open source software OpenFOAM¹. Streamlines, stagnant zones, velocity profiles, and pressure fields are obtained at different flow rates ranging from 5 mL/min to 100 mL/min. A change in the flow regime with presence of recirculation zones is observed at 40 mL/min flow rate. The extent of the recirculation zones increases with increasing flow rate from 40 to 60 mL/min and is limited further by the presence of a second cylindrical post inside the heart cell, remaining almost constant for the flow rate range 60 – 100 mL/min.

The residence time distribution (RTD) is also determined for all flow rates and a comparison between different reactor designs (two – posts, single – post, Low – Flow reactor – like single – post) is presented. The AFR shows a plug-flow behavior with a small degree of dispersion, which broadens the RTD. Symmetric RTD curves are obtained for the single – post designs, while the Gen 1 AFR design experiences asymmetry in the RTD at flow rates in the transition between 20 and 60 mL/min.

5.2 Introduction

Knowledge of the hydrodynamic characteristics of a reactor is essential for reactor design, development, and optimization. The traditional approach for process development is experimentally based. However, experiments provide limited information about the behavior inside the reactor. Computational Fluid Dynamics (CFD) is a useful tool that allows the prediction of the hydrodynamics without the need of performing experiments once the model has been validated. In particular, the complex geometry of the AFR and its design makes difficult to obtain information locally from experiments. The availability of local information helps understand how the system works and make decisions about how to modify the reactor design to improve its performance by overcoming the limitations of the existing devices. Moreover, CFD

simulations can be used to study the effect of the fluid properties on the flow characteristics and its influence on reactor performance. In this way, the CFD tool can be further used to optimize reaction conditions and maximize yields, minimize energy requirements, and identify safety concerns.

In this section CFD simulations are limited to single-phase incompressible flow, using water as the model fluid. The response variables analyzed are: pressure drop, velocity profiles, streamlines, stagnant zones, and swirling strength, as function of flow rate. CFD simulations are performed using the Open Source CFD Toolbox “OpenFOAM” (Field Operation And Manipulation) ¹. CFD results are compared with experimental measurements of pressure drop and residence time distributions.

5.2.1 Basic physical equations

The governing equations for single-phase flow of an incompressible Newtonian fluid in isothermal conditions with only gravity as body force are given by the continuity equation (eq 5.1) and the conservation of linear momentum equation (eq 5.2).

$$\nabla \cdot \vec{v} = 0 \quad (5.1)$$

$$\rho \left(\frac{\partial \vec{v}}{\partial t} + \vec{v} \cdot \nabla \vec{v} \right) = -\nabla \bar{P} + \rho \vec{g} + \mu \nabla^2 \vec{v} \quad (5.2)$$

For an incompressible fluid of known density (ρ) and viscosity (μ) there are four equations (eq 5.2 has three components) and four unknowns (P, v_x, v_y, v_z). The boundary conditions for these variables and the initial condition are needed to fully specify the problem.

These equations are sufficient to describe laminar flow. To include turbulence, additional equations for the Reynolds stress or turbulent stress ($\overline{\vec{v}'\vec{v}'}$) that provide closure to the Reynolds-averaged Navier-Stokes equations are needed. ²⁻⁶

$$\nabla \cdot \bar{\vec{v}} = 0 \quad (5.3)$$

$$\rho \frac{D\bar{v}}{Dt} = \rho \left(\frac{\partial \bar{v}}{\partial t} + \bar{v} \cdot \nabla \bar{v} \right) = -\nabla \bar{P} + \rho \bar{g} + \mu \nabla^2 \bar{v} + \overline{v'v'} \quad (5.4)$$

Where the over-bar indicates time averaged values, and v' , fluctuating velocity. An eddy viscosity (μ_T), is defined by eq 5.5 in analogy to molecular motions and does not depend on fluid properties, but rather on the local turbulence of the flow.

$$-\overline{\rho u_i u_j} = \mu_T \left(\frac{\partial U_i}{\partial x_j} + \frac{\partial U_j}{\partial x_i} \right) - \frac{2}{3} \delta_{ij} \left(\mu_T \frac{\partial U_k}{\partial x_k} + \rho k \right) \quad (5.5)$$

Combination of eq 5.4 and eq 5.5 leads to a closed set of equations provided the turbulent viscosity is known. The form of the Reynolds averaged momentum equation is analog to the momentum conservation equation for laminar flow having the molecular viscosity (μ) replaced by an effective viscosity (μ_{eff}), given by eq 5.6.

$$\mu_{eff} = \mu + \mu_T \quad (5.6)$$

Different turbulent models that describe the turbulent viscosity in different ways have been developed over the years, each one being more convenient depending on the flow characteristics. These allow for the calculation of the mean flow without the need to calculate the full – time dependent flow field. Although there are zero – equation (mixing length) and one – equation (Spalart-Allmaras) turbulence models, the two – equation models are the most used due its relative simplicity and suitability. In these models, two additional partial differential equations need to be solved. Here we present the standard $k - \epsilon$, $k - \epsilon$ RNG, realizable $k - \epsilon$, and $k - \omega$ turbulent models. The $k - \epsilon$ turbulence models incorporate two additional equations for the turbulent kinetic energy (k) and dissipation rate of turbulent kinetic energy (ϵ), while the $k - \omega$ model uses a transport equation for the specific dissipation energy (ω) and the turbulent kinetic energy (k).²⁻⁶

The standard $k - \epsilon$ model leads to stable calculations with relatively fast convergence, predicting reasonably the flow in many situations. However, it introduces a very simplistic equation for ϵ , generally leading to poor predictions for flows that present swirling, rotation, strong separation, axisymmetric jets,

unconfined flows, and fully developed flows in non-circular ducts, and it is only valid for fully developed flows. In the RNG model the Renormalization Group Method is applied to the instantaneous Navier – Stokes equations to account for the effects of smaller scales of motion. It also includes an additional term in the ε – equation to account for the interaction between turbulence dissipation and mean shear. This model improves the prediction of swirls and transitional flows, but still does not predict well the spreading of a round jet correctly. The realizable k – ε model is based on the same turbulent kinetic energy as the standard k – ε model, but includes an improved equation for ε and variable parameters, which helps improve the performance of the model for planar and round jets, flow separation, rotation, recirculation, and strong streamline curvature. ^{2,7} In OpenFOAM®, these models are specified in the “constant/RASProperties” file in RASModel by kEpsilon, RNGkEpsilon, realizableKE, kOmega, and kOmegaSST. ¹

The CFD simulations shown here are performed at steady – state for single – phase flow for different inlet flow rates. Determination of the residence time distribution (RTD) is implemented using a convection – diffusion equation for the tracer (C_T = tracer concentration), which is treated as a passive scalar based on the velocity profiles obtained at steady – state (\vec{v}). The transport equation is shown in eq 5.7 where D_T is the diffusion coefficient of the tracer, assumed constant.

$$\frac{\partial C_T}{\partial t} + \nabla \cdot (\vec{v} C_T) - \nabla^2 (D_T C_T) = 0 \quad (5.7)$$

5.2.2 Numerical approach

OpenFOAM® is based on a finite volume discretization method applied to arbitrary shaped cells and uses a segregated iterative solution (separate matrix equations for each equation instead of a single matrix for the entire system of equations). ¹ Inter – equation coupling is treated in the explicit manner and non-linear equations are linearized before discretized. The space is divided into a finite number of discrete regions (control volumes) and the finite volume equation discretization is based on the integral form of the equation

over the control volume. For transient problems, time is a parabolic coordinate and it is sufficient to specify explicitly the time step or implicitly through the Courant number.

The OpenFOAM solver used for our simulations to study the flow is *simpleFoam*, implemented for incompressible steady – state single – phase flow. Once the flow field is known, the RTD is determined using the *scalarTransportFoam* solver, which solves a transport equation for a passive scalar, which in this case is the tracer injected at the reactor inlet. In order to solve the equations for velocity and pressure, these solvers use the Pressure – Implicit with Splitting of Operators (PISO) algorithm, for transient problems, or semi – implicit method for pressure – linked equations (SIMPLE) algorithm, for steady – state problems. Both algorithms in OpenFOAM can introduce non – orthogonality correctors (“0” for an orthogonal mesh, and “20” for the most non – orthogonal mesh).^{1,8}

OpenFOAM has several options available to solve velocity, pressure, and turbulent variables, depending on the symmetry of the matrices to solve. Velocity and turbulent variables are solved with preconditioned bi – conjugate gradient (PBiCG) and the preconditioner DILU. For pressure, a preconditioned conjugate gradient (PCG) solver with the preconditioner DIC is used (Tables 5.1 and 5.2). Tolerances and maximum number of iterations can also be specified here. Relaxation factors are used to stabilize the computation, especially for steady state problems. They work limiting the amount by which the variable changes between iteration steps. Small values enhance stability, but make the computation slower. Maximum and minimum values for relaxation factors are 0.2 and 0.9. Based on CFD experience, relaxation factors have been set to 0.3 for the pressure field and 0.7 for the velocity and other turbulent variables.

Table 5.1: Linear solvers¹

Solver	Keyword
Preconditioned bi-conjugate gradient	PCG (symmetric)/PBiCG (asymmetric)
Solver using a smoother	smoothSolver
Generalized geometric algebraic multi-grid	GAMG
Diagonal solver for explicit systems	Diagonal

Table 5.2: Preconditioner options ¹

Preconditioner	Keyword
Diagonal incomplete-Cholesky (symmetric)	DIC
Faster diagonal incomplete-Cholesky	FDIC
Diagonal incomplete-LU (assymmetric)	DILU
Diagonal	diagonal
Geometric-algebraic multi-grid	GAMG
No preconditioner	none

The numerical schemes used in this work are: ‘Gauss linear corrected’ scheme for laplacian calculations, and ‘Gauss upwind/linear’ for gradient and divergence calculations. For steady – state simulations the time derivative is not solved and the keyword “steadystate” within the ddtSchemes is used. ¹

The evolution of residuals for the main variables (pressure and velocity for laminar regime, additional variables – k , ε , ω – for turbulent cases) and velocity and pressure at a fixed point in the domain located at the inlet of the third heart cell was monitored until convergence was achieved. In addition, validation of the predictions is performed comparing CFD results with experimental data of pressure drop and residence time distribution.

5.2.3 Mesh

The computational domain of the portion of the AFR of study is discretized in cells forming an unstructured mesh and the dependency of CFD results with grid resolution is studied. In addition, effect of 2D and 3D mesh is also studied in order to determine if the presence of walls at such small scales is significant. All meshes are constructed using the software Pointwise ®. Additional simulations are performed using a structured mesh and the results are compared with the unstructured mesh (Figure 5.1). For multiphase simulations based on the volume – of – fluid method, the use of structured meshes is highly recommended. Further details for two – phase CFD simulation are included in Chapter 6.

Table 5.3: Resolution (in number of cells) of 2D and 3D unstructured mesh

Mesh type	Resolution 1	Resolution 2	Resolution 3
2D	79,972	57,170	29,793
3D	1,599,440	857,550	446,895

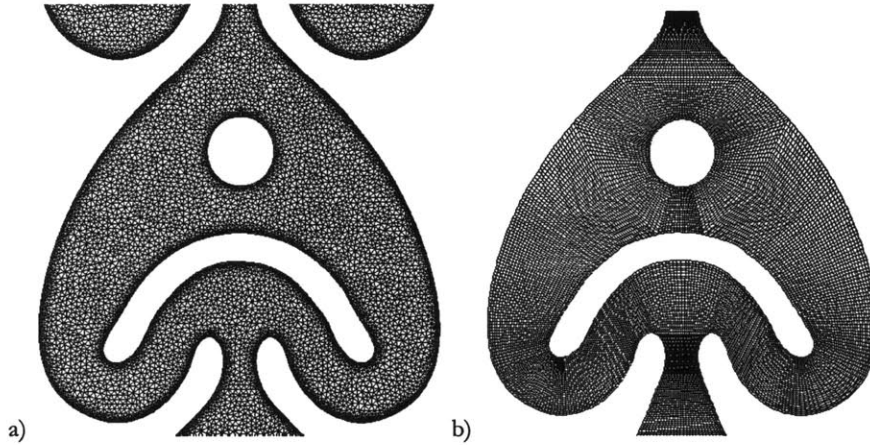


Figure 5.1: Detail of mesh for single-phase CFD simulations with simpleFoam: a) unstructured; b) structured

5.2.4 Boundary conditions

All simulations share the following boundary conditions: the velocity is fixed at the reactor inlet with a flat profile, non – slip condition at the walls, and zero gradient velocity at the outlet. The pressure is fixed at the outlet (zero, reactor outlet opened to the atmosphere), whereas the gradient pressure at the inlet and at the walls is zero.

The turbulent models require the specification of additional variables: dissipation rate of turbulent kinetic energy (ε), turbulent kinetic energy (k), and specific dissipation of turbulent kinetic energy (ω). An estimated fixed value for these variables based on the characteristic length and velocities for each case is specified at the inlet, while the gradient is set to zero at the outlet, and a wall function is used at the walls. The turbulence model variables (k , ε , ω) are estimated based on other better known parameters, such as the turbulent intensity, turbulent viscosity ratio, and turbulence length scale. The turbulent intensity (I) for internal flows at the inlet can vary from 1 to 10%. Another parameter is the turbulence length scale (l), which

represents the size of the large eddies in turbulent flows. An empirical relationship between the characteristic length (L) and the size of the eddy (l) can be used to estimate the turbulent length scale, according to eq 5.8. The characteristic length L can be the width or hydraulic diameter of the channel.

$$l = 0.07L \quad (5.8)$$

These turbulence variables are related to the turbulent kinetic energy (k), turbulent dissipation rate (ϵ), and specific dissipation rate (ω), and can be estimated using equations 5.9 – 5.12 for RANS models.

For the $k - \epsilon$ model:

$$k = \frac{3}{2} (\overline{U}l)^2 \quad (5.9)$$

$$\epsilon = \frac{0.1643k^{1.5}}{l} \quad (5.10)$$

For the Spalart – Allmaras model:

$$v_t = \sqrt{\frac{3}{2}} \overline{U}l \quad (5.11)$$

For the $k - \omega$ and Menter SST Models:

$$\omega = \frac{\epsilon}{k} \quad (5.12)$$

Different wall function models available in OpenFOAM can be applied at the boundaries and are specified within the “0” folder for incompressible RAS. The low – Reynolds turbulence models, such as Spalart – Allmaras and $k - \omega$ SST, describe both sublayer and log – law wall turbulence and they can be used both in high Reynolds (needing wall functions) and low Reynolds regimes.

5.2.5 Analysis of results

Steady – state simulations for single-phase flow using water as incompressible fluid for flow rates ranging from 5 to 100 mL/min were performed. A laminar flow model for flow rates smaller than 20 mL/min and turbulent Reynolds – Averaged – Stress (RAS) model for flow rates larger than 20 mL/min is

used. A detailed study of the flow for 2D and 3D meshes in a portion of the AFR including the straight inlet portion and four heart-shaped cells were first performed. After this preliminary study, simulations for the entire reactor were performed based on the experience obtained in the simulations of the portion of the domain. This enabled obtaining pressure drop for the entire AFR and velocity profiles that are later used to obtain the residence time distribution and compare both with experimental results.

Analysis of the results includes post – processing of velocity fields to obtain streamlines and swirling strength. It is known that swirling strength is useful to identify stagnant zones and eddies, and calculating reliable vortex statistics that are not identified by velocity decompositions.⁹ The strength of any local swirling motion or “vortex swirling strength” is quantified by the imaginary part of the complex eigenvalue (λ_{ci}) of the local velocity gradient tensor. For a 2D case, the velocity gradient tensor (D^{2D}) is represented by eq 5.13 and it has either two real eigenvalues (λ_r) or two complex conjugate eigenvalues ($\lambda_{cr} \pm i \lambda_{ci}$). Vortices are identified by plotting iso-regions of imaginary part of the complex conjugate, λ_{ci} .⁹

$$D^{2D} = \begin{vmatrix} \frac{\partial u_1}{\partial x_1} & \frac{\partial u_1}{\partial x_2} \\ \frac{\partial u_2}{\partial x_1} & \frac{\partial u_2}{\partial x_2} \end{vmatrix} \quad (5.13)$$

The results are validated comparing pressure drop and residence time distributions with experimental data. The relative error is calculated with respect to the experimental value (eq 5.14). For the RTD measurements the sum of square of errors is calculated (eq 5.15).

$$\text{error} = \frac{P_{sim,i} - P_{exp,i}}{P_{exp,i}} 100 \quad (5.14)$$

$$E = \sum_i |P_{sim,i} - P_{exp,i}|^2 \quad (5.15)$$

5.3 Results and discussion

In this section, the CFD simulations results are presented for each flow rate. Comparison between 2D and 3D meshes is also shown. Velocity, pressure fields are presented, in addition to streamlines, stagnant zones, and swirls after post – processing using the softwares Tecplot® and paraView®.

5.3.1 Velocity fields, streamlines, and swirling strength

The velocity profiles within each heart – shaped cell are shown in Figure 5.2 for different flow rates, ranging from 5 to 100 mL/min, comparing the results between 2D and 3D meshes. Reynolds numbers for these flow rates calculated at the inlet of the heart are 79 – 1,580. Significant differences are observed between 2D and 3D meshes, being these differences stronger below 40 mL/min of flow rate. In all cases, the maximum velocity is achieved at the inlet of each heart – shaped cell. The fluid encounters the first obstacle and splits into two streams, each one traveling at approximately half speed next to the walls, leading to a low velocity region between the two obstacles. Recirculation zones are formed between these two obstacles, increasing the amplitude with increasing flow rates, as shown by the streamlines.

The 2D mesh is equivalent to having the top and bottom walls of the reactor far from each other, as if the walls did not have any effect on the flow patterns. However, at these small characteristic lengths, the effect of having two walls very close to each other (1.1 mm height) is significant and cannot be ignored. The recirculation zones present between the two obstacles within the heart are suppressed by the walls, and while in the 2D mesh for flow rates from 5 to 40 mL/min recirculation zones are present, this effect is suppressed in the 3D mesh. The suppression effect is captured in 3D simulations for different heights of the reactor, as shown in Figure 5.3.

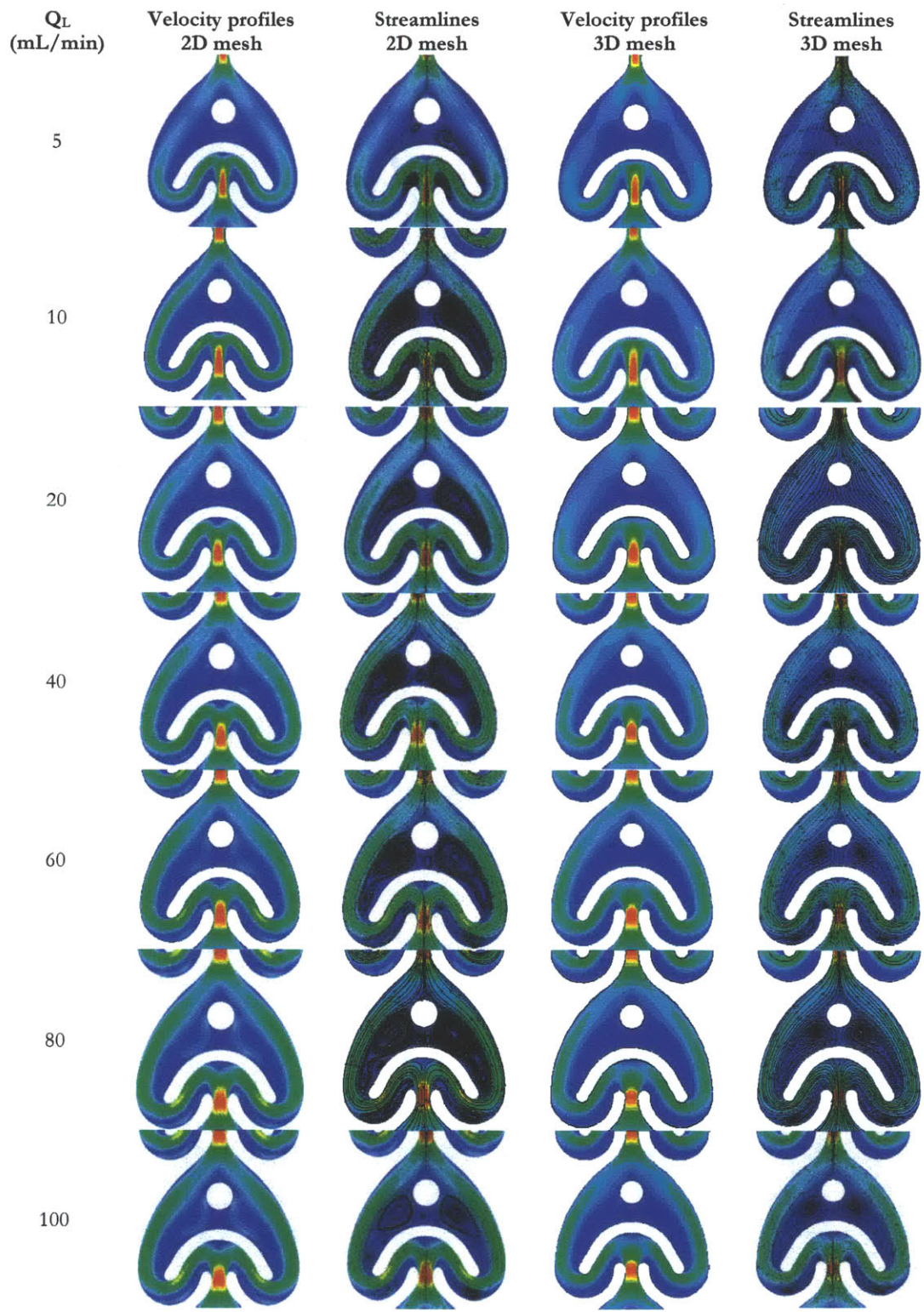


Figure 5.2: Velocity profiles and streamlines for 2D and 3D meshes in Advanced-Flow Reactor. Velocity profiles are non-dimensionalized by the maximum velocity (■). Minimum velocity represented by: ■. Computations using simpleFoam; post-processing in Tecplot.

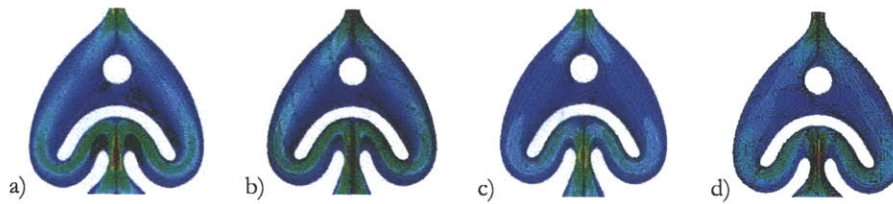


Figure 5.3: Streamlines of 3D mesh for different Advanced-Flow Reactor heights at 5 mL/min: a) $H = \infty$; b) $H = 5$ mm; c) $H = 2$ mm; d) $H = 1.1$ mm. Computations using simpleFoam; post-processing in Tecplot.

As already mentioned previously, the computation of the swirling strength from the velocity profiles can help identify stagnant zones within the heart – cell that otherwise would be difficult to detect. The swirling strength has been computed for different flow rates in a 3D mesh and the results are shown in Figure 5.4. The amount of swirling strength increases with flow rate and creates stagnation points in those regions where the swirling strength is higher. These stagnation points are located right before the flow encounters the first obstacle within the heart and also at the edges of the long post. It should be noticed here that these CFD simulations correspond to single – phase flow, and thus, although these stagnation points can affect the residence time distribution for single – phase, the results for two-phase flow may be different and require further study. However, it was observed in two – phase visualization experiments that bubbles were trapped in the stagnation points already detected in single – phase flow CFD simulations. These bubbles are observed when the pump flow is set at very high flow rates. Bubbles disappear if the pump flow is set first to low flow rates and the flow is progressively increased until the desired high flow rate is achieved.

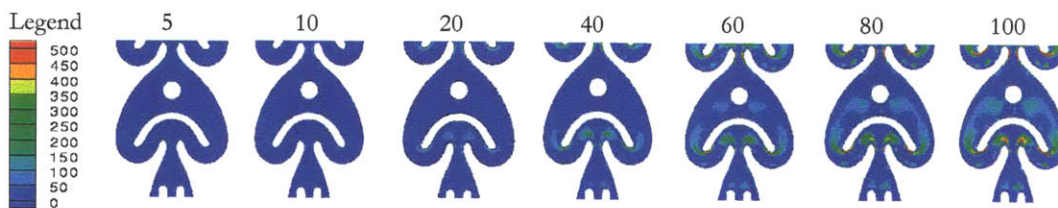


Figure 5.4: Swirling strength for different water flow rates (mL/min). Computed from simpleFoam velocity profiles in 3D mesh. Post-processed in Tecplot. Swirling strength identifies stagnant spots and recirculation zones non-detected by other methods.

Additionally, the effect of turbulent flow model for 80 mL/min is shown in Figure 5.5. It can be observed that there are no significant differences among the standard and realizable $k - \epsilon$, Launder – Sharma $k - \epsilon$, RNG, and $k - \omega$ SST models. Not only no significant differences are observed in the velocity fields, but also the total pressure drop across the entire AFR is less than 4% different, a percentage that falls within the relative error range with respect to the experimental results (as seen in Section 5.7.2).

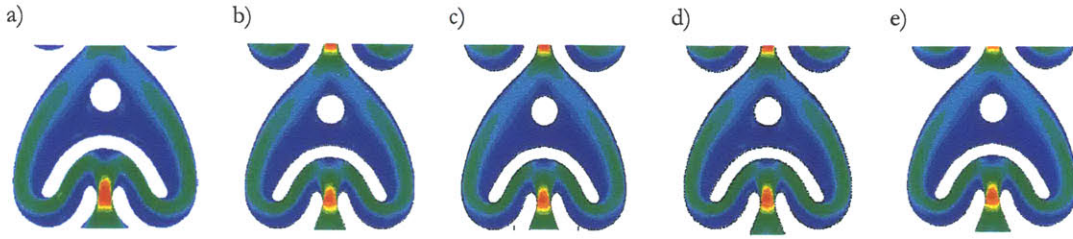


Figure 5.5: Velocity profiles for different turbulent flow models at 80 mL/min water using a 3D mesh: a) realizable $k - \epsilon$; b) RNG; c) standard $k - \epsilon$; d) Launder-Sharma $k - \epsilon$; e) $k - \omega$ SST. Post-processing in Tecplot.

Additional CFD simulations have been performed for the entire AFR using a mesh composed by 378,460 hexahedral cells reducing the computation time while keeping enough accuracy in the results. The objectives of these simulations are: a) determine velocity field along the reactor and the position at which the flow becomes fully developed; b) determine total pressure drops in the AFR and compare them with experimental results (Section 5.3.2); c) use the velocity fields to obtain the residence time distribution and compare them with experiments (Section 5.3.3).

The velocity profiles in the middle plane of the Z coordinate (at $z = 0.00055$ m) along the cross section at one side of the center of the heart cells and at the center of the heart cells are shown in Figures 5.6 and 5.7, respectively. It is observed that in both cases the velocity profiles are periodic along the row of hearts. The maximum velocities for both locations of the cross sections (side and center) fall under the same parallel lines, only with slight differences encountered in the first heart. This shows us that almost a fully developed flow is already reached within the first heart of the reactor and all heart cells behave in the same way regarding the single – phase flow.

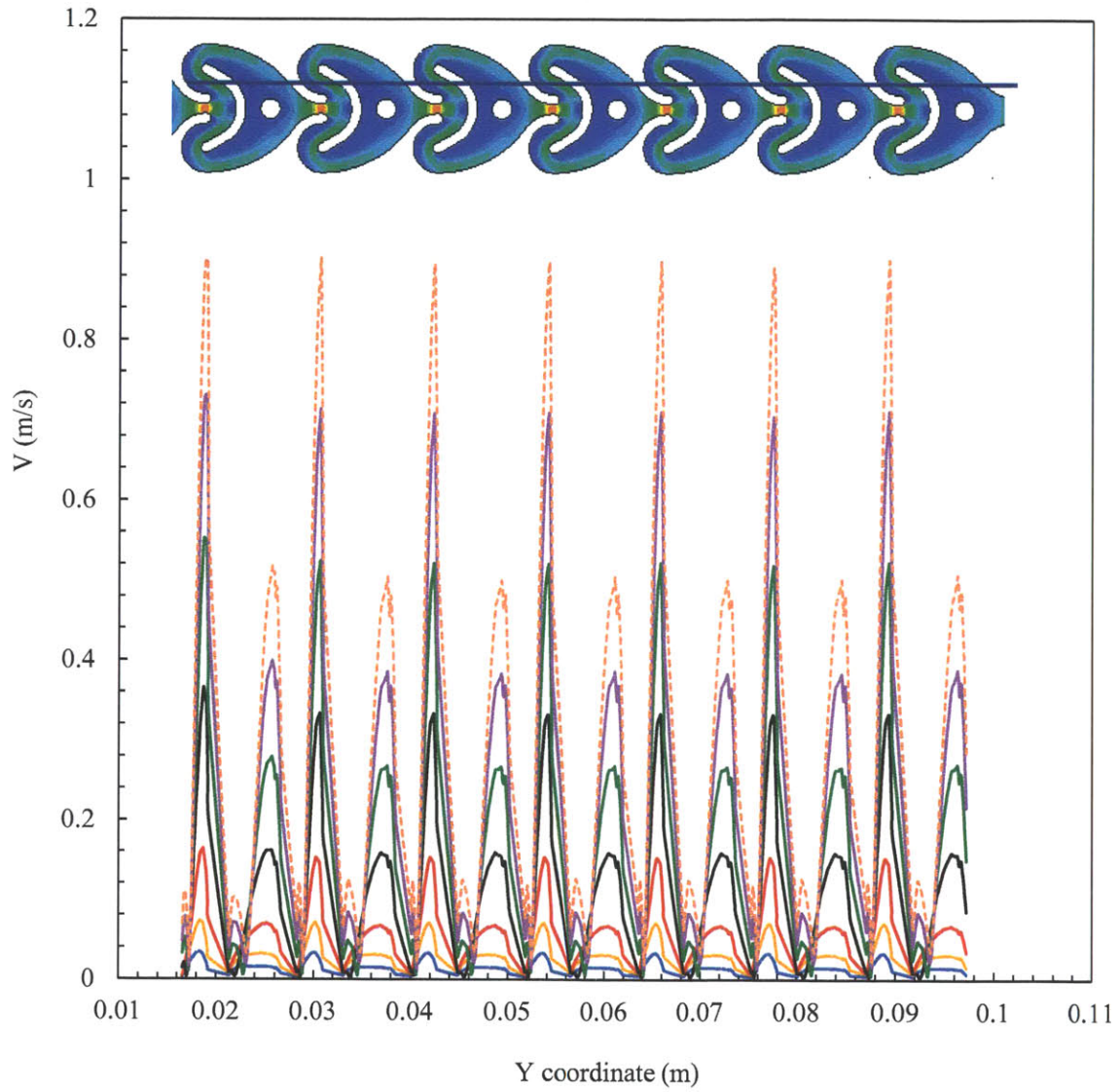


Figure 5.6: Velocity profile along cross-section on side of heart cell (represented by black line crossing above) in first row of AFR. Water flow rate (mL/min): —, 5; —, 10; —, 20; —, 40; —, 60; —, 80; - - -, 100;

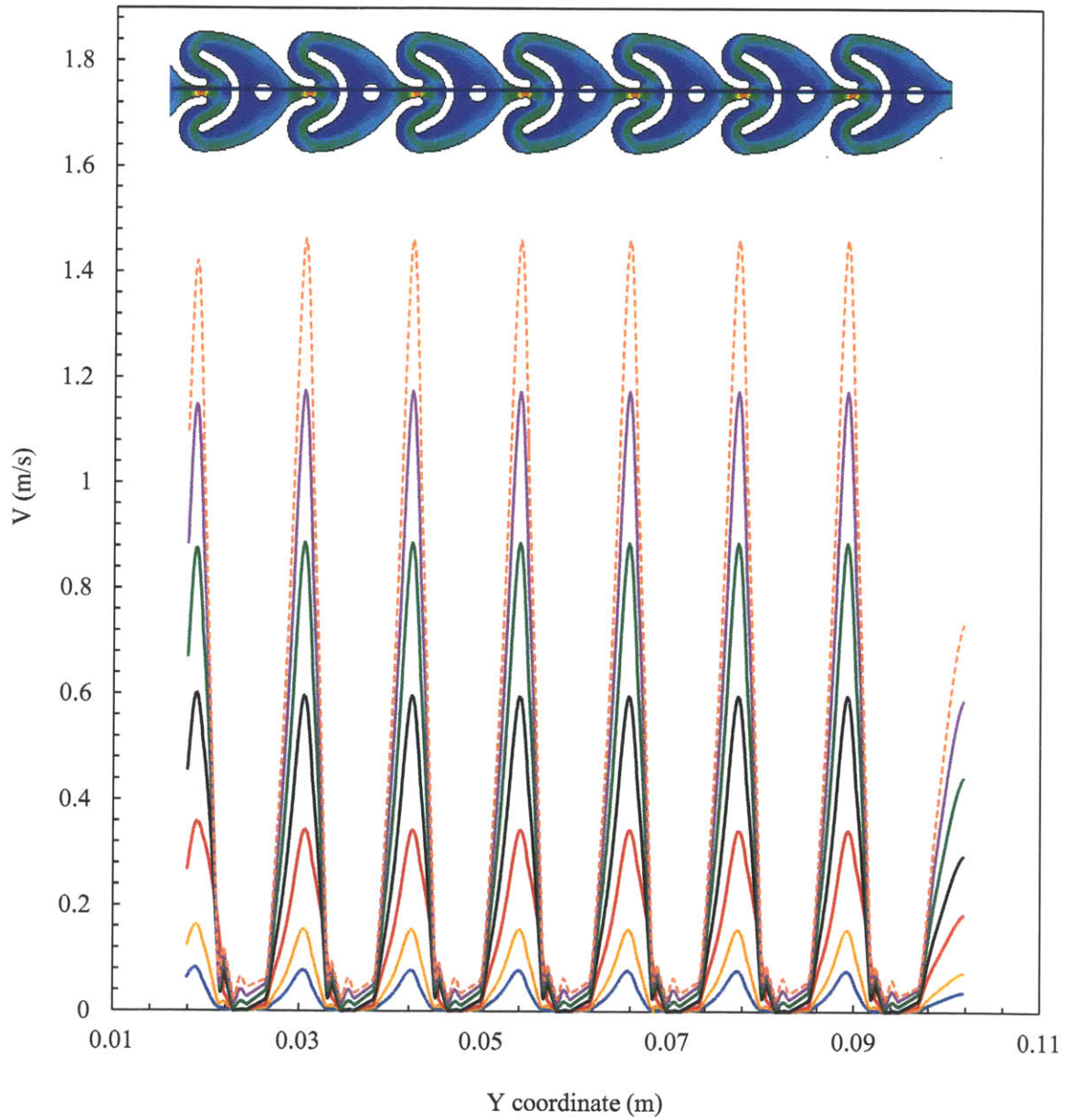


Figure 5.7: Velocity profile along cross-section at center of heart cell (represented by black line crossing above) in first row of AFR. Water flow rate (mL/min): —, 5; —, 10; —, 20; ---, 40; —, 60; —, 80; - - -, 100;

5.3.2 Pressure fields

A typical pressure field is shown in Figure 5.8. A confined annular configuration yields a co – flow followed by a converging/diverging section that generates a low – pressure zone followed by a pressure recovery. This series of converging/diverging sections help break the flow and increase the specific interfacial area in multiphase flows. Similar results for the pressure field are obtained for the different flow rates, with the total pressure drop being different.

Table 5.3 includes results for pressure drop in each heart – cell and the entire AFR for different flow rates. The CFD results obtained with OpenFOAM are validated by comparison with experimental results between 20 mL/min and 80 mL/min. As it is shown in Table 5.3, the CFD results are in very good agreement with the experiments, with relative errors below 4% in absolute value, which is the same order of magnitude for relative errors in pressure drop predictions among the different turbulent flow models.

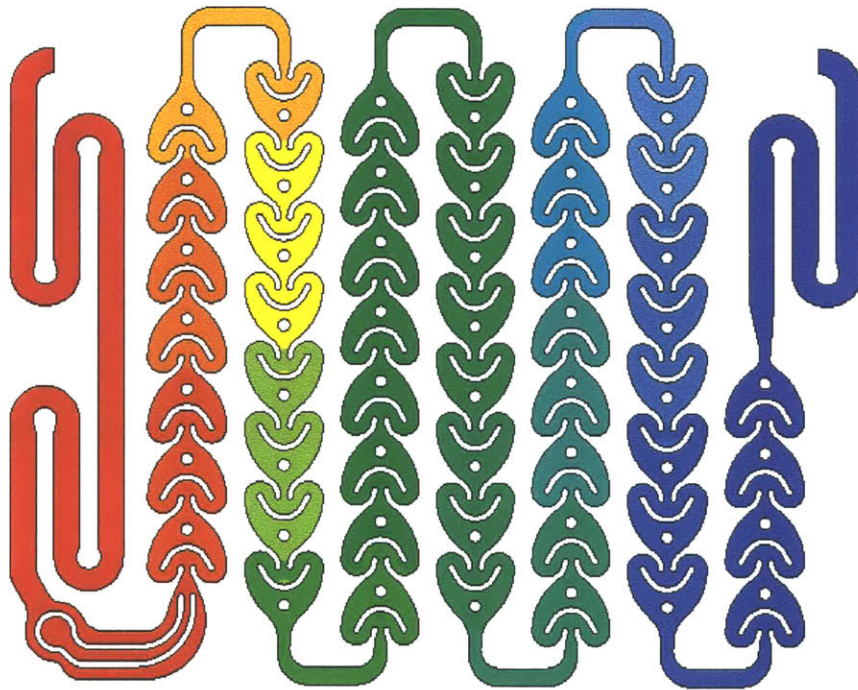


Figure 5.8: Non-dimensional pressure field for incompressible water in structured 3D mesh. Atmospheric outlet pressure. Maximum (■) and minimum (■) pressure. Simulation in simpleFoam, post-processing in Tecplot.

Table 5.3: Comparison of experimental and CFD results for pressure drop in AFR. Total pressure drop includes additional tubing at the inlet and outlet

Q_L (mL/min)	Reynolds (-)	$U_{\text{inlet heart}}$ (m/s)	U_{max} (m/s)	ΔP_{AFR} (kPa)	ΔP_{total} (kPa)	$\Delta P_{\text{experimental}}$ (kPa)
5	79	0.076	0.108	0.7	0.81	N/A
10	158	0.152	0.197	1.6	1.9	N/A
20	317	0.303	0.360	4.1	5.0	4.82
40	634	0.606	0.677	11.4	14.0	13.8
60	951	0.909	0.998	21.7	26.8	26.2
80	1268	1.212	1.362	35.0	43.2	44.8
100	1584	1.515	1.710	51.1	63.1	N/A

It is known that in classical theory, a liquid flowing in laminar flow regime through a pipe has a pressure drop that is linearly proportional to the flow rate or Reynolds number as shown by Hagen – Poiseuille ¹⁰ equation 5.16.

$$\Delta P = \frac{8\mu L Q}{\pi r^4} \quad (5.16)$$

For a fully turbulent fluid, the pressure drop can be estimated using the Darcy – Weisbach ¹¹ equation (eq 5.17), in which the friction factor is calculated using eq 5.18. In this flow regime, the pressure drop is proportional to the square of the flow rate or the Reynolds number, instead of being linearly proportional as in laminar flow regime.

$$\Delta P = f \frac{L}{D} \rho \frac{v^2}{2} \quad (5.17)$$

$$\frac{1}{\sqrt{f}} = -2 \log \left(\frac{\varepsilon_r}{3.7D_h} + \frac{2.51}{Re\sqrt{f}} \right) \quad (5.18)$$

The maximum Reynolds numbers at the inlet of the heart – cells in the AFR range from 79 to 1,584 and thus, a laminar flow behavior would be expected a priori. However, the non – linear dependence of pressure drop with the Reynolds number, shown in Figure 5.9, with a power law $\Delta P \sim Re^{1.44}$ suggests that the flow within the AFR is in the transition regime for the operating conditions tested. This early transition may

be due to higher friction at small scales linked to surface roughness or/and presence of obstacles along the flow path. It is reported in the literature the critical Reynolds numbers (Re_c) at which the transition occurs can range from 300 to 2,000 ¹². In addition, several authors have reported in the literature deviations in the predictions of pressure drop in microchannels from the classical theory. This is probably due to the effects of surface roughness at the walls that becomes very significant at such small scales, causing an earlier transition from laminar to turbulent regime. Several authors that obtained experimental values of the Poiseuille number fRe larger than the conventional theory, such as Harley et al. ¹³, Rahman and Gui ¹⁴, Wilding et al. ¹⁵, Peng et al. ^{16, 17}, Jiang et al. ¹⁸, Mala and Li (0 – 40 %) ¹⁹, Papautsky et al. (10 – 20 %) ²⁰, Qu et al. ²¹, Ding et al. ²², Pfund et al. ²³, Ren et al. ²⁴, Kandlikar et al. ²⁵, Li et al. ²⁶, and Urbanek et al. (5 – 30 %) ²⁷. In other cases, this value was lower than the expected fRe using the classical theory. This was found by Pfalher et al (0 – 30 %) ²⁸, Yu et al. (19 %) ²⁹, Jiang et al. (50 – 100 %) ¹⁸, Xu et al. ²⁹, and Judy et al. ³⁰. In other cases, no significant differences were found with respect to the classical theory: Harms et al. ³¹, Pfund et al. ²³, Webb and Zhang ³².

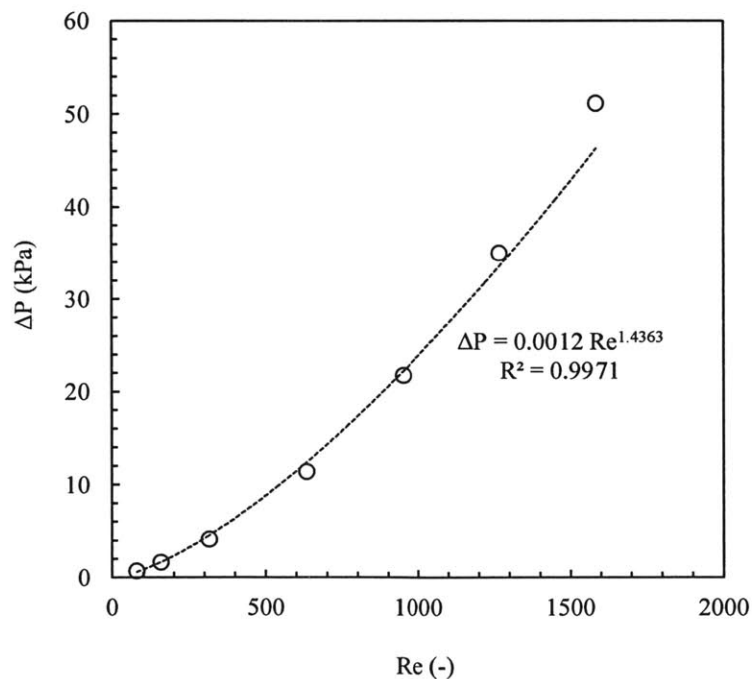


Figure 5.9: Pressure drop in AFR for incompressible water at different Reynolds numbers using simpleFoam. The non-linear behavior indicates that the flow is in the transition regime, as opposed to the laminar regime where the pressure drop is linear (Hagen-Poiseuille). Presence of obstacles within the flow causes an earlier transition to turbulent regime.

Table 5.4 includes critical Reynolds numbers reported in the literature by several authors to determine the transition regime for different materials, geometries, and channel sizes. Wu and Little reported values for Re_c between 350 and 900³³, Peng et al. ($Re_c = 200 - 700$)^{16, 17}, Mala and Li ($Re_c = 300 - 900$)³⁴. Higher ranges were observed by Choi et al ($Re_c = 2,300$)³⁵, Yu et al. ($Re_c = 2,000$)²⁹, Pfund et al. ($Re_c = 1,700 - 2,200$)²³, and Wu and Cheng ($Re_c = 1,500 - 2,000$)³⁶. In 2004, Morini³⁷ experimentally investigated the pressure drop through microchannels and observed deviations from conventional behavior for hydraulic diameters less than 1 mm. The transition from laminar to turbulent occurs at lower Reynolds numbers than conventional channels and is explained in base of the Obot – Jones model and the increase in the surface roughness. Morini also concluded that the fluid flow in microchannels still remains a topic of future research for a full understanding of this phenomenon.

Table 5.4: Transition regime for different microchannel geometry, hydraulic diameters, and materials.³⁷

Reference	Geometry	D_h (μm)	Material	Re range	Re critical	Fluid
Wu and Little (1983)	Trapezoidal	55.8 – 83.1	Silicon, glass	100 – 15,000	350 – 900	N_2 , H_2 , Ar
Peng et al. (1994)	Rectangular	133 – 367	SS	50 – 4,000	200 – 700	Water
Choi et al. (1991)	Circular	3.0 – 81.2	Silica	30 – 20,000	2,300	N_2
Yu et al. (1995)	Circular	19 – 102	Silica	250 – 20,000	2,000	N_2 , water
Flockhart and Dhariwal (1998)	Trapezoidal	50 – 120	Silicon	< 600	N/A	Water
Mala and Li (1999)	Circular	50 – 254	Fused silica, SS	80 – 2,100	300 – 900	Water
Qu et al. (2000)	Trapezoidal	51 – 169	Silicon	0 – 1,500	N/A	Water
Pfund et al. (2000)	Rectangular	252 – 973	Polycarbonate/polyimide	40 – 4,000	1,700 – 2,200	Water
Judy et al. (2002)	Round, square	15 – 150	Fused silica, SS	8 – 2,300	N/A	Water, methanol, isopropanol
Wu and Cheng (2003)	Trapezoidal	25.9 – 291	Silicon	10 – 3,000	1,500 – 2,000	Water

5.3.3 Residence time distribution

One of the essential steps in the scale-up of reactors is the determination of the residence time distributions (RTD). In previous sections, differences between simulations using 2D and 3D meshes are observed. Velocity fields and streamlines are different, and this is found to have a significant effect on the residence time distribution. For single-phase simulations at steady – state, the velocity fields are steady over time, and thus, the scalarTransportFoam solver can be used to compute the RTD of a tracer for the two different meshes.

First, the RTD for 10 mL/min water at the outlet of the second heart – shaped cell is shown in Figure 5.10 for 2D and 3D meshes. A step of tracer concentration is introduced at the inlet, and the concentration is monitored at the outlet of the second heart cell over time. Calculating the derivative of each signal $C(t)$ versus time yields the residence time distribution curve for both cases, $E(t)$. Typical tracer concentration profiles at two different times for 2D and 3D meshes (D2DU1 and D3DU1) are presented in Figure 5.10. It is observed that the presence of recirculation zones in the velocity field predicted by the 2D model affects the RTD making the tracer bypass the recirculation zones, reach the outlet earlier, and leave the reactor later than in the 3D mesh, resulting in a broader $E(t)$ curve. This demonstrates the importance of using validated CFD methods before predicting flow behaviors. In addition, 3D meshes tend to represent better the real device, especially when working at small scales when wall effects are important. In this specific case, a 3D mesh is required for an accurate prediction of the flow and RTD in the AFR. It was observed how recirculation zones are suppressed from 2D simulations (upper and bottom walls of the AFR are located at an infinite distance from each other) to 3D simulations (upper and bottom walls are located 1.1 mm far from each other), affecting the RTD.

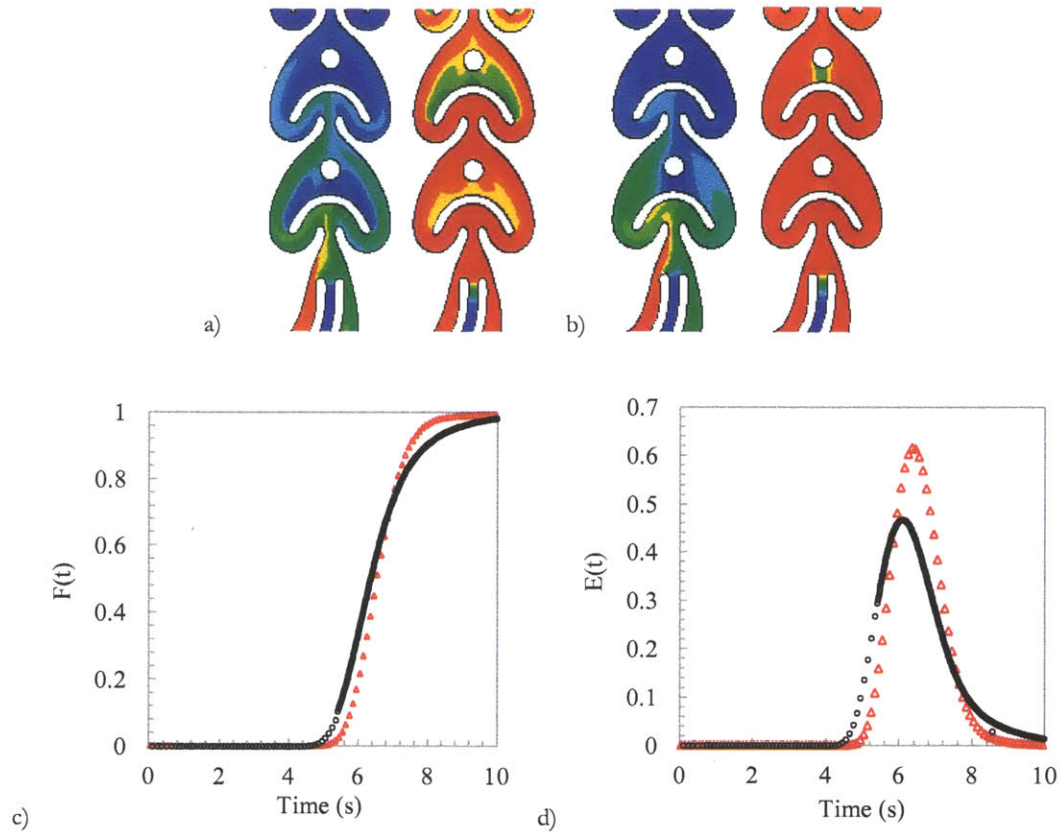


Figure 5.10: Comparison of RTD simulation for a) 2D mesh vs. b) 3D mesh at two different times (5.4 s and 7.5 s); c) $F(t)$ curve; d) $E(t)$ curve. The tracer is introduced at the inlet in a step pulse and its concentration at the outlet is monitored. Legend a) and b) for tracer concentration (mol/m^3): ■, 1; ■, 0; c) and d): ○, 2D mesh; △, 3D mesh

The RTD simulations for the entire AFR (not including the measuring system and additional tubing) use a structured mesh composed by 378,460 hexahedral cells in order to reduce the computation time while keeping enough accuracy in the results. The dimensionless RTD curves are shown in Figure 5.11. Here it can be clearly seen a different regime at the lowest (10 and 20 mL/min) and the largest (60 and 80 mL/min) flow rates, with a transition regime at 40 mL/min. At the lowest flow rates, the RTD is sharper than at the highest flow rates, while the intermediate flow rate causes a non – symmetric RTD curve. This reflects the complexity of the geometry and thus, of the flow in the AFR.

In a single tube one expects that larger flow rates increase the Peclet number and reduce the axial dispersion, with the result of a narrower $E(\theta)$ curve³⁸. This is not what is observed in the AFR according to the CFD simulations. An explanation is found based on the streamlines obtained and how they change for the different flow rates. Looking back at Figure 5.2, flow rates from 5 to 20 mL/min do not show any recirculation zone, which yields a narrow RTD. Increasing the flow rate to 60 and 80 mL/min broadens the RTD. This is due to two main contributions: a) the recirculation zones that occupy the region between the two obstacles make the tracer bypass these regions and arrive at the outlet of the reactor earlier than if no recirculation zones are present; b) the mass transfer between the recirculation zones and the main flow stream makes the tracer to be transported first from the main stream to the recirculation zones, and then to leave the recirculation zones and follow the main stream towards the outlet of the reactor. This causes a delayed arrival of the tracer and, together with the bypass effect, broadens the RTD symmetrically.

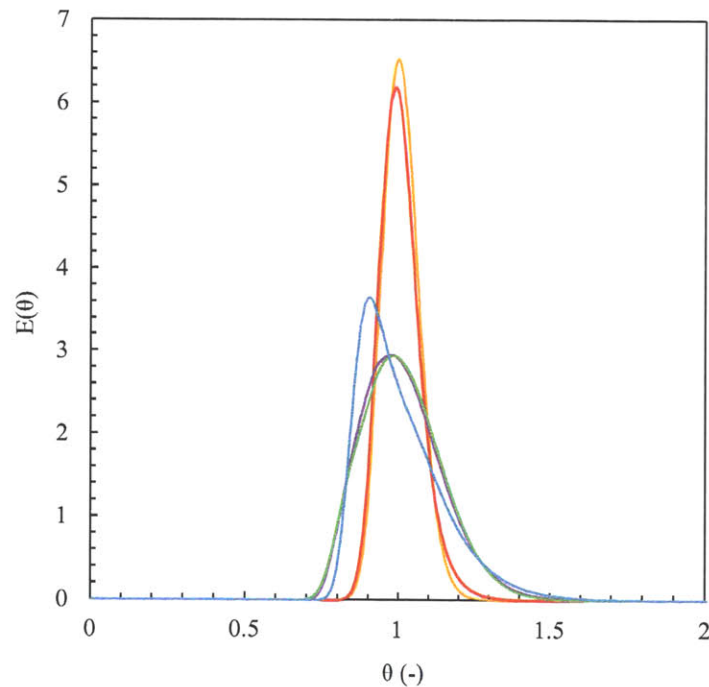
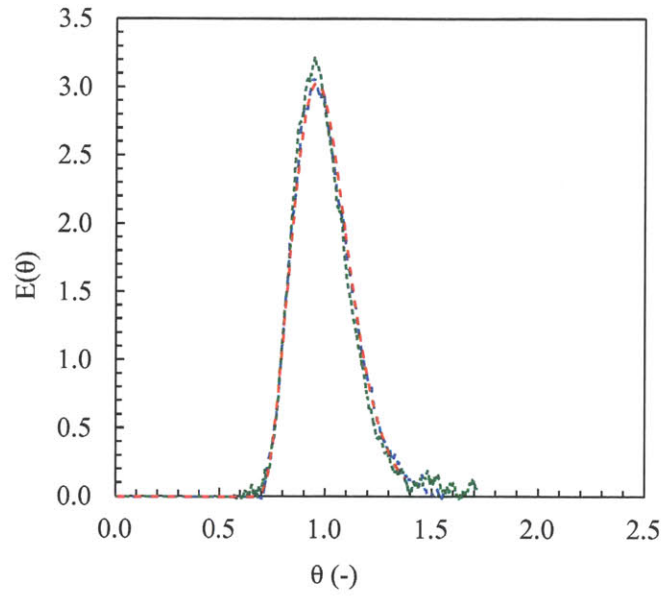


Figure 5.11: Dimensionless residence time distribution $E(\theta)$ for different flow rates. Water flow rate (mL/min): —, 10; —, 20; —, 40; —, 60; —, 80; A plug flow behavior with certain degree of dispersion is observed, with a change of regime above 40 mL/min where recirculation zones are present.

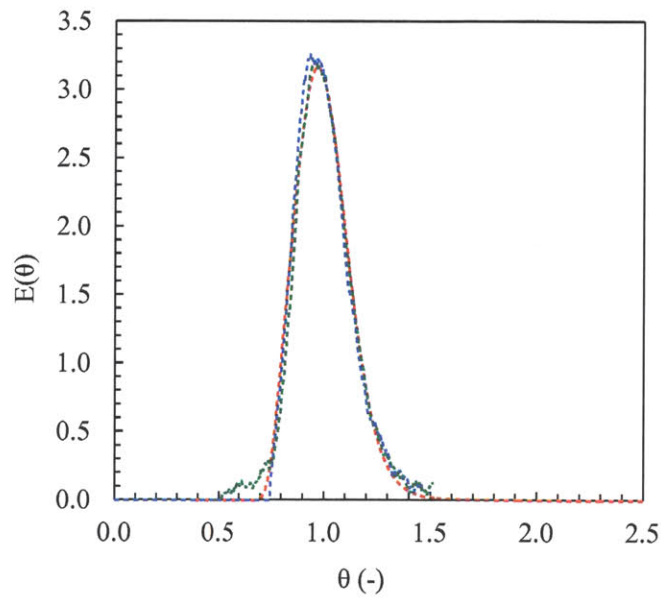
A different behavior is observed for 40 mL/min. Here, recirculation zones are also present, but there are two smaller recirculation zones enclosed into a larger one. First, the tracer arrives earlier to the outlet of the reactor due to the bypass effect, but later than for 60 and 80 mL/min, since the extent of the recirculation zones is smaller (and thus, the effective volume, larger). The RTD curve is not symmetric, and this is due to the enclosed recirculation zones. Not only the tracer is transported from the main stream into the recirculation zones, but also it takes more time to get out because the resistance to the transport is higher due to the enclosed double recirculation zones.

In practice, it is desirable to have a reactor with well – defined or easily predictable RTD curves. This is not the case for the AFR, in which there are two different behaviors with symmetric RTDs at the lowest (10 and 20 mL/min) and highest flow rates (60 and 80 mL/min), and a transition region with non-symmetric RTD's for intermediate flow rates (40 mL/min). A detailed study of the influence of reactor design on the velocity profiles and RTD is described in Section 5.3.4.

The next step is to compare the RTD obtained from CFD simulations with experimental results. The CFD overall RTD is obtained by convolution of the RTD of the AFR and the RTD of the tubing at the inlet (17cm 1/16" O.D.) and the outlet (13 cm 1/8" O.D.; 16 cm 1/16" O.D.) of the reactor with the measuring system similar to the experimental setup. The dimensionless RTD curves for different flow rates are shown in Figure 5.12. As is it observed, the convoluted RTD obtained with CFD is in agreement to the experimental RTD.



a)



b)

Figure 5.12: Comparison of CFD and experimental residence time distribution, $E(\theta)$. Simulation results obtained for 3D mesh using scalarTransportFoam and differentiation of signal obtained at the outlet using a step function for the inlet concentration. Flow rates (mL/min): a) 60; b) 80; Legend: ---, Experimental 1; ----, Experimental 2; -.-.-, CFD

5.3.4 Effect of reactor design

There are different versions of the Advanced-Flow Reactor (AFR) that Corning Inc. has created with slightly different designs. The Generation 1 (design 1) includes two posts inside each heart – cell. A second design removed the post – dot, which was first introduced for simplicity in the manufacturing process of the AFR. The Low-Flow Reactor (LFR), a smaller version of the Gen 1 AFR with a volume of 0.45 mL per module, removes the entire region of low velocity between the two posts, as shown in Figure 5.13. Modifications in the reactor design can have a significant impact on the reactor performance and thus, determination of the hydrodynamic characteristics and comparison between designs can provide insightful information on this matter. Here we analyze velocity fields and pressure drops for the three different designs and determine through CFD simulations residence time distributions (RTD) for single – phase flow. Simulations are performed in 3D meshes for the entire AFR reactors.

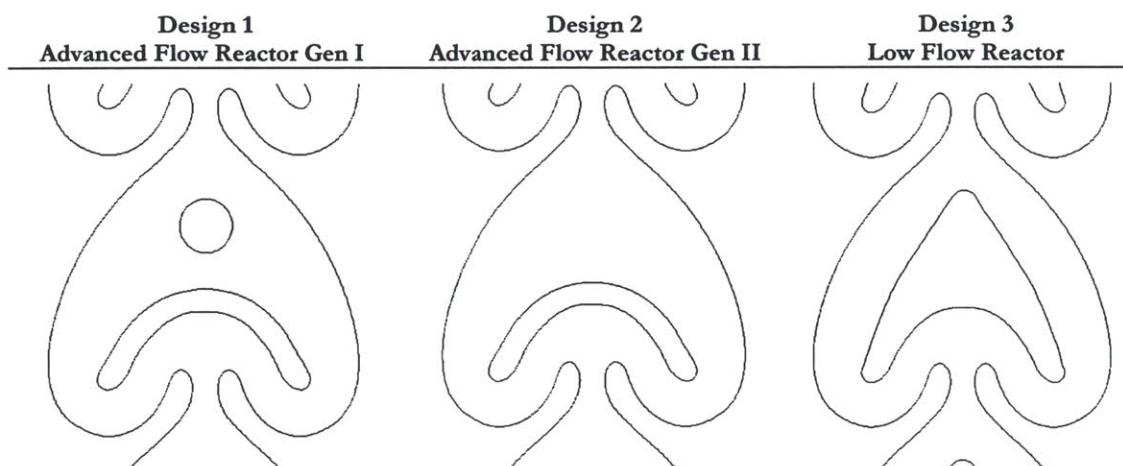


Figure 5.13: Geometry for three AFR designs studied

The velocity profiles and streamlines for the three different reactor designs at 10, 20, 40, 60, and 80 mL/min are included in Figure 5.14. A common characteristic at low flow rates is the absence of recirculation zones for the three designs. The largest difference appears at 40 mL/min, when recirculation zones start to be present in design 1 and design 2, while they are almost absent in design 3. The design 1 has two enclosures of

recirculation zones, while design 2 only has two single recirculation zones at both sides of the heart cell. Thus, one would expect the RTD to be more symmetric for the design 2 as compared to design 1. Regarding design 3, the RTD is expected to be narrower since no significant recirculation zones are present. The residence time distributions for the three designs are shown in Figure 5.13.

The extent of recirculation zones increases significantly from 40 to 60 mL/min for all designs. A further increase in the flow rate increases the recirculation strength in design 2. However, the second obstacle in design 1 prevents the wake to extend further downstream and makes the streamlines to be very similar to all flow rates above 60 mL/min. This causes the RTD to be the same for design 1 at flow rates above this flow rate. In design 2, however, the extent of recirculation zone still increases with flow rate. This causes the tracer first to bypass these zones of increasing volume (and thus, reduced effective reactor volume), causing the tracer to arrive earlier at the outlet of the reactor as the flow rate increases. At the same time, the tracer takes longer time to arrive at the outlet as the extension of recirculation zones increase. The overall effect is to broaden symmetrically the RTD as the Re increases for design 2.

In design 3, increasing the flow rate from 60 to 80 mL/min does not increase the extent of recirculation zones; it has the contrary effect instead. This causes a narrower RTD: the effective volume is larger, the tracer takes more time to arrive at the outlet, and leaves sooner because mass transfer process from a smaller recirculation zone is faster overall.

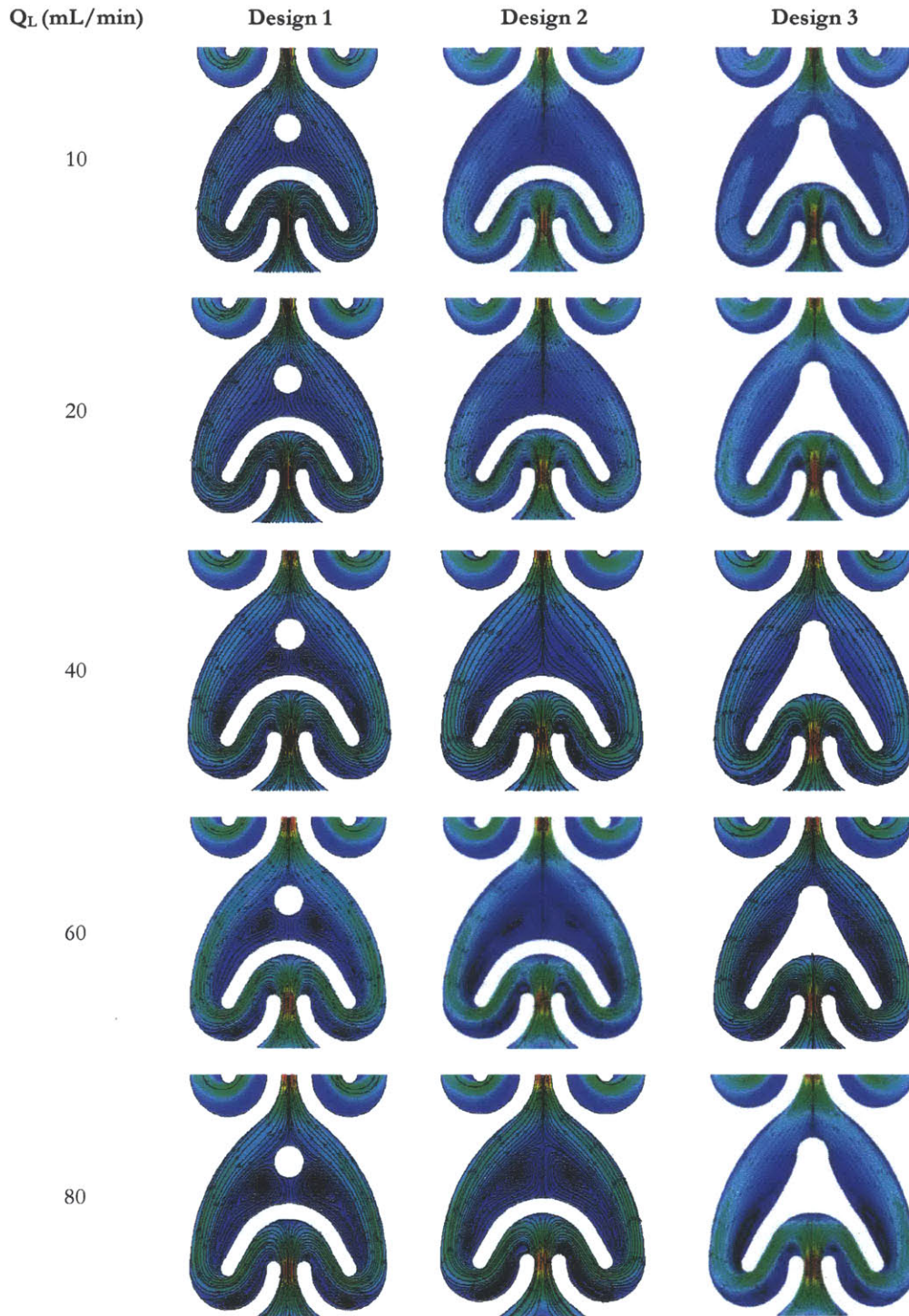
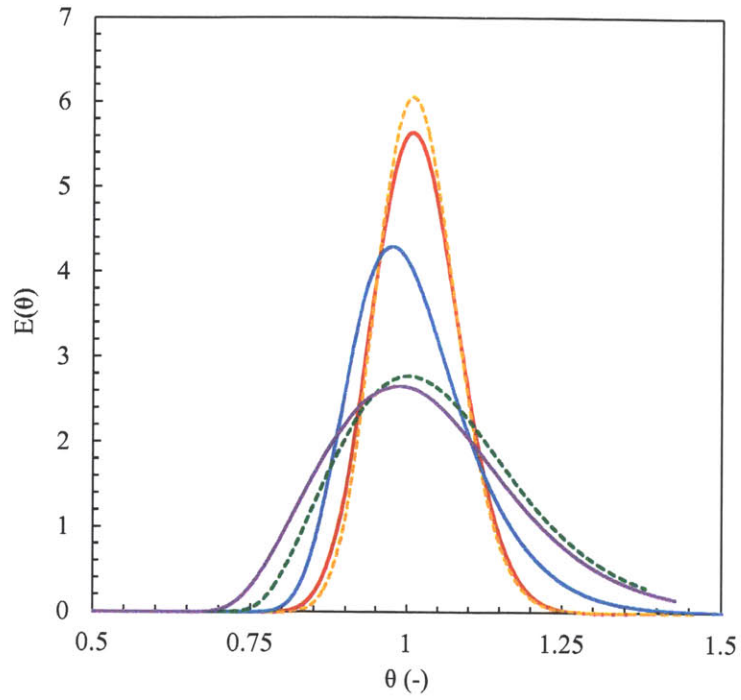
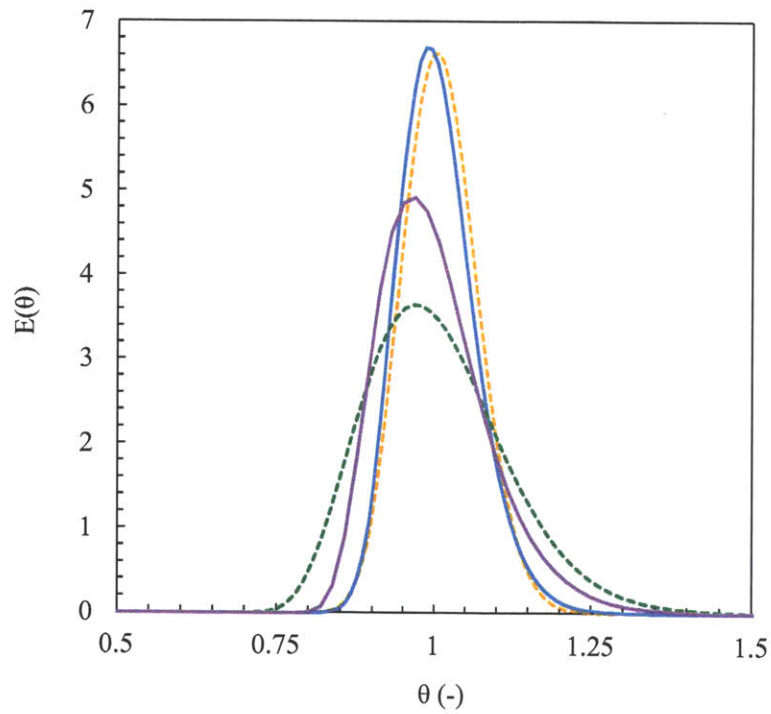


Figure 5.14: Comparison of velocity fields and streamlines among three different AFR designs (dot, no dot, low-flow reactor-like) for incompressible flow using simpleFoam and a 3D mesh. Non-dimensionalized velocity fields with maximum velocity (■). Post-processing in Tecplot.



a)



b)

Figure 5.15: Dimensionless residence time distributions $E(\theta)$ for different AFR designs: a) design 2; b) design 3. Simulation results obtained for 3D mesh using `scalarTransportFoam` and differentiation of signal obtained at the outlet using a step function for the inlet concentration. Water flow rate (mL/min): —, 10; - - -, 20; —, 40; - - -, 60; —, 80;

The pressure drop across the entire reactor for the three designs is shown versus the Reynolds number at the inlet of the heart cell in Figure 5.16. It is observed that the three designs have similar pressure drops, especially at the lowest Re, but differences start to increase at larger Re. Design 3 has an average channel width smaller than designs 1 and 2, and this may be the reason why pressure drops for this reactor design are higher. If we compare the AFR with the LFR of 0.45 mL volume, the total pressure drops are even larger (Figure 5.17). This is due to the smaller reactor height and width. The height dimension for the AFR of 8.7 mL volume is 1.1 mm, whereas the LFR has a height dimension of 0.35 mm. the maximum recommended operating flow rate for the LFR is 10 mL/min, for which the pressure drop almost equals the pressure drop in the AFR at 100 mL/min.

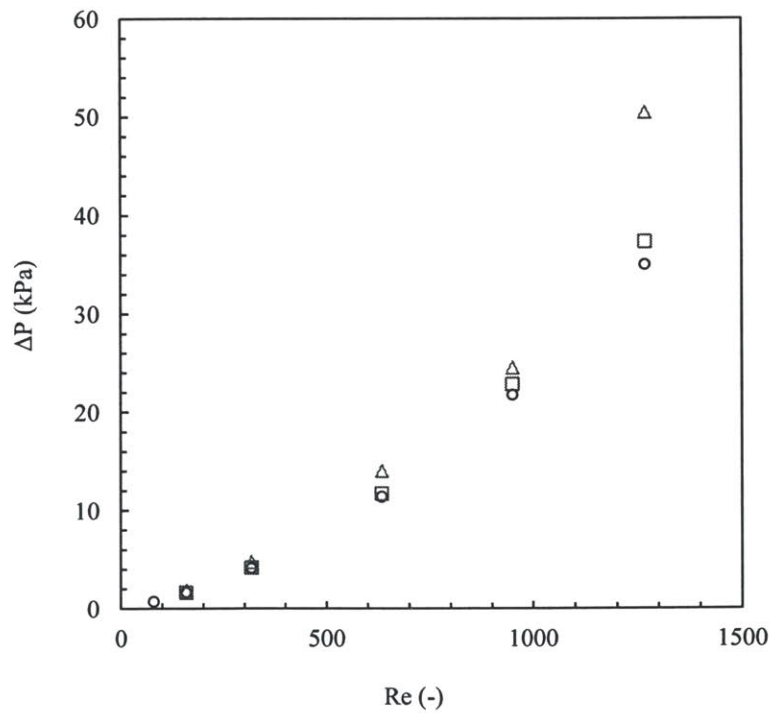


Figure 5.16: Effect of reactor design on pressure drop. Results obtained with simpleFoam using a 3D mesh. Legend: ○, design 1; □, design 2; △, design 3.

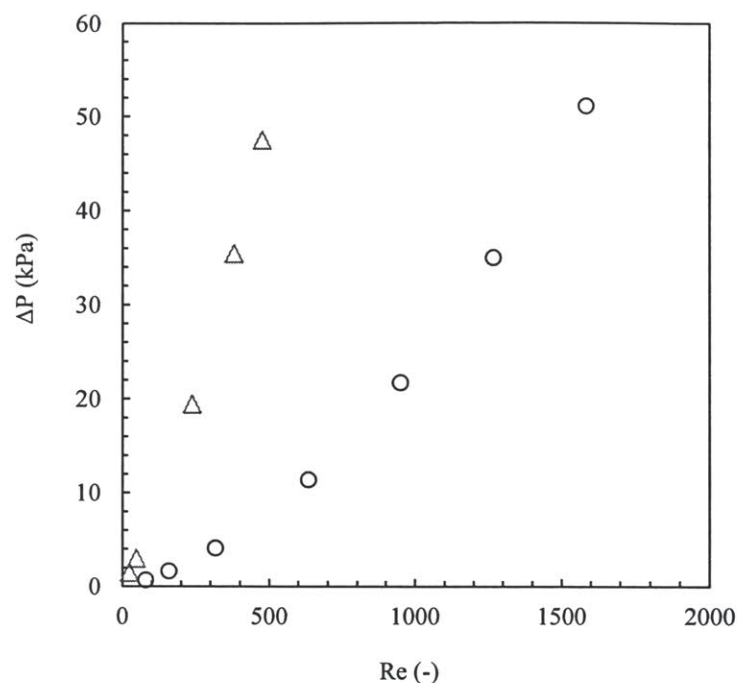


Figure 5.17: Pressure drop for LFR and comparison with AFR. Results obtained with simpleFoam for 3D mesh. Legend: ○, AFR (8.7 mL); △, LFR (0.45 mL). Larger pressure drops are observed for same Reynolds number in the LFR than in the AFR, which limits the recommended maximum flow rate in the LFR.

An improvement in the design has been made in the LFR, with removal of the space between the two posts in the original AFR design, using a single post. As shown in Figure 5.18, this design removes the formation of large recirculation zones for the recommended flow rates, between 0.5 and 10 mL/min. It is expected that the residence time distribution for this reactor design will be shaper and closer to plug flow behavior with less axial dispersion, especially at the largest flow rates. This is shown in Figure 5.19, where it is seen also that the RTDs are symmetric, as expected from the streamlines in the LFR. A small tail in the RTD is observed at the largest flow rate. This is due to the appearance of small recirculation zones, which makes the tracer bypass these zones while mass transfer occurs from the main stream. Later on, mass transfer transports the tracer from the recirculation zones to the main stream, taking more time to arrive at the outlet of the reactor. Due to the very small extent of recirculation zones, this effect is not as important as in the AFR design.

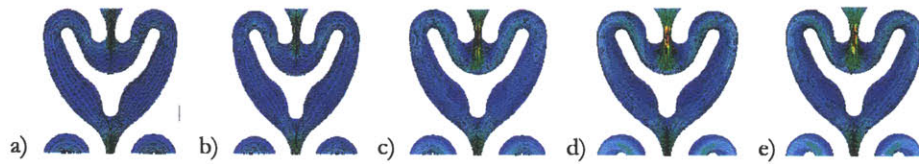


Figure 5.18: Velocity profiles and streamlines in LFR. Results obtained with simpleFoam for 3D mesh. Velocity profiles are non-dimensionalized with respect to maximum velocity. Water flow rates (mL/min): a) 0.5; b) 1; c) 5; d) 8; e) 10;

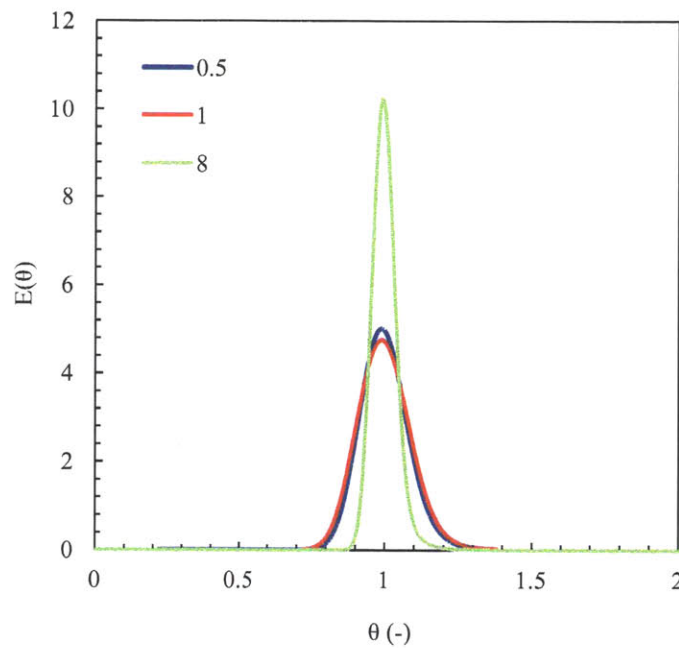


Figure 5.19: Residence time distribution in LFR. Simulation results obtained for 3D mesh using scalarTransportFoam and differentiation of signal obtained at the outlet using a step function for the inlet concentration.

One important thing to consider here is the ease of scalability of the different Corning reactors. The best case scenario would be to have the same RTD for the same Reynolds numbers (or other variable of reference for scale-up) at the different Corning scales. In this way, the overall reaction kinetics would be affected in the same way at the different scales and the scalability between different sizes would be straightforward. However, this is not the case for the designs shown in this work. Although the reactors have

plug-flow behavior with certain degree of dispersion, bypass, and mass transfer effects, the degree of each phenomenon is different depending on the flow rates and the design.

In order to quantify the importance of the differences between designs in the actual performance of the reactor when reaction is occurring, the average reagent concentration is calculated from the residence time distribution and compared with two ideal cases: a) plug flow (PFR); b) single stirred tank (CSTR). The results are shown in Figure 5.20 and Table 5.5 for different Damköhler numbers and designs. The model reaction to study is an irreversible reaction $A + B \rightarrow C$, with first order kinetics: $r = kC_A$. The Damköhler number is calculated as given by eq 5.19.

$$Da = \tau k \quad (5.19)$$

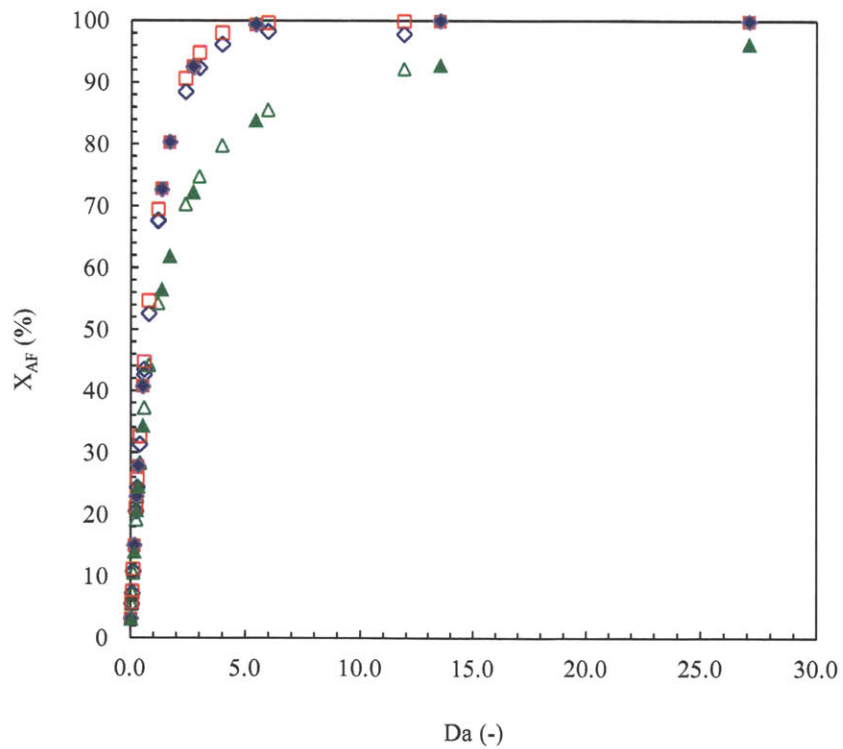


Figure 5.20: Conversion of reagent A in first order kinetics ($r = kC_A$) irreversible reaction $A + B \rightarrow C$. Legend: ■, Plug flow 0.45 mL; ◆, LFR 0.45 mL; ▲, CSTR 0.45 mL; □, Plug flow 8 mL; ◇, AFR 8 mL; △, CSTR 8 mL

From the results, it can be seen that the conversion for all reactor designs is not significantly different, and all of them are very close to the plug flow conversions. A single CSTR gives the minimum conversion that can be achieved in the system and is below the actual conversion achieved in the AFR (8 mL volume) and the LFR (0.45 mL). A slight better performance is achieved in the LFR, which has sharper RTD curves and this reflects a closer conversion to PFR. However, the difference is not significant, especially at the smallest Da numbers (high flow rates, small residence time, narrower RTD). This shows once more that the different generations of AFR have been designed to provide a sharp RTD regardless of the flow rates and slight different designs. This behavior might not be the same for two-phase flow, where mass transfer effects are also important and compete with the intrinsic reaction kinetics. Chapter 6 is devoted to modeling two-phase flow and will study this matter in more detail.

Table 5.5: Comparison of conversion (%) between different reactor designs

Q_L (mL/min)	Da (-)	X_{AF} design 1	X_{AF} design 2	X_{AF} design 3
80	3.04	92.4	93.2	92.9
	0.61	42.6	44.3	41.5
	0.30	24.4	25.5	23.5
	0.06	5.6	5.7	5.3
60	4.05	96.2	96.5	97.0
	0.81	52.6	54.2	52.3
	0.41	31.3	32.5	31.0
	0.08	7.3	7.6	7.2
40	6.08	98.3	98.3	99.1
	1.22	67.6	69.0	66.3
	0.61	43.5	44.7	42.1
	0.12	10.9	11.2	10.4
20	12.15	97.9	97.6	99.0
	2.43	88.5	88.9	88.7
	1.22	67.7	68.6	67.1
	0.24	20.6	21.1	20.1

5.4 Conclusions

Computational fluid dynamic (CFD) simulations were performed in the Advanced-Flow Reactor (AFR) for single-phase incompressible flow using the open source software OpenFOAM. Results showed a very good agreement with experimental results of pressure drop and residence time distribution (RTD). The velocity profiles reveal the presence of stagnant zones between the two obstacles within the heart-shaped Gen 1 reactor and recirculation zones starting at 40 mL/min. The RTDs for the AFR are plug flow with certain degree of back mixing, with two different flow regimes. The extent of recirculation zones, which increases with flow rates, broadens the residence time distribution above 40 mL/min. Introduction of slight differences in the design in the zone between the two obstacles changes slightly the flow patterns and recirculation zones, therefore having an effect on the RTD. However, predictions for a first order irreversible reaction in all designs yielded conversions that were not significantly different.

The Low-Flow Reactor (LFR) of volume 0.45 mL was also simulated. Results showed a higher pressure drop for the same Reynolds numbers than the Gen 1 AFR, which limits the operating flow rate to a maximum of 10 mL/min. On the other hand, sharper RTD curves are obtained in the LFR with respect to the AFR, yielding conversions slightly larger for large Damkhöler numbers. Whereas the AFR is able to achieve 95 – 99 % times the PFR conversion, conversions above 99 % the PFR conversion is achieved in the LFR. However, the LFR has the limitation of low throughput, whereas the AFR can handle flow rates on the order of 100 mL/min.

5.5 Notation

C_A	Concentration of reagent A (mol/L)
C_T	Tracer concentration (mol/L)
D_h	Hydraulic diameter (m)
D_T	Tracer diffusion coefficient (m ² /s)
D^{2D}	Determinant to determine vortices from velocity field

E	Sum of square of errors between simulated and experimental results
$E(t)$	Residence time distribution from pulse experiment (s^{-1})
$E(\theta)$	Dimensionless residence time distribution of $E(t)$ (-)
$F(t)$	Residence time distribution from step experiment (-)
f	Darcy's friction factor (-)
\vec{g}	Gravity vector (m/s^2)
I	Turbulence intensity (-)
l	Turbulence length scale (m)
L	Characteristic length (m)
k	Kinetic constant (s^{-1})
P	Pressure (Pa)
ΔP	Pressure drop (Pa)
$P_{sim,i}$	Result from simulation
$P_{exp,i}$	Result from experiment
Q	Flow rate (mL/min)
Q_L	Liquid flow rate (mL/min)
t	Time (s)
$U_{inlet\ heart}$	Average velocity at inlet of heart (m)
U_{max}	Maximum velocity at inlet of heart (m)
\vec{v}	Velocity vector (m/s)
v'	Velocity fluctuation (m/s)
\bar{v}	Averaged velocity (m/s)
V	Velocity magnitude (m/s)
r	Channel radius (m)
x_{AF}	Reagent concentration (%)
z	Coordinate in Z axis

Dimensionless numbers

Da	Damkhöler number (-)
D/UL	Dispersion module (-)
Pe	Peclet number (-)
Re	Reynolds number (-)
Re _c	Critical Reynolds number (-)

Greek letters

ρ	Fluid density (kg/m ³)
ε	Turbulence dissipation rate (m ² /s ³)
λ_r	Real eigenvalue
λ_{cr}	Real part of complex conjugate eigenvalue $\lambda_{cr} + i\lambda_{ci}$
λ_{ci}	Imaginary part of complex conjugate eigenvalue $\lambda_{cr} + i\lambda_{ci}$
k	Turbulence kinetic energy (m ² /s ²)
ω	Specific turbulence dissipation rate (s ⁻¹)
ν_t	Turbulence dynamic viscosity (m ² /s)
ε_r	Material rugosity (m)
θ	Dimensionless time (-)
μ	Fluid viscosity (Pa s)

5.6 References

- (1) Open source CFD Software OpenFOAM, England. Web: www.openfoam.org. Accessed on 03/15/2014
- (2) Pope, S. B. Turbulent flows. *Cambridge University Press*, 2000 ISBN-10: 0521598869
- (3) Bardina, J.E.; Huang, P.G.; Coakley, T.J. Turbulence modeling validation, testing, and development. *NASA Technical Memorandum* 110446, 1997, Moffett Field, CA 94035-1000
- (4) Lam, C. K. G.; Bremhorst, K. A modified form of the k-epsilon model for predicting wall turbulence ASME, Transactions, *J. Fluids Eng.*, 1981, 103(3), 456 – 460. DOI:10.1115/1.3240815

- (5) Nagano, Y.; Hishida, M. Improved form of the k- ϵ model for wall turbulent shear flows. *J. Fluids Eng.*, **1987**, *109*(2), 156-160. DOI:10.1115/1.3242636
- (6) Myong, H. K.; Kasagi, N. A new approach to the improvement of k-epsilon turbulence model for wall-bounded shear flows. *JSME International Journal, Series II*, **1990**, *33*, 63 – 72 (ISSN 0914-8817)
- (7) Bakker, A. The colorful fluid mixing gallery. Turbulence modeling. *Dartmouth College*, **2012**. Web: <http://www.bakker.org/cfm>. Accessed on 03/15/2014
- (8) Jasak, H. Error analysis and estimation for the finite volume method with applications to fluid flows, *PbD. Thesis*, **1996**, Imperial College, University of London
- (9) Adrian, R. J.; Christensen, K. T.; Liu, Z. C. Analysis and interpretation of instantaneous turbulent velocity fields. *Experiments in Fluids*, **2000**, *29*, 275 – 290
- (10) Brown, G. The history of the Darcy-Weisbach equation for pipe flow resistance. *Environmental and Water Resources History*, **2003**, *4*, 34 – 43
- (11) Deen, W. M. Analysis of transport phenomena. *Oxford University Press*, **1998**, New York
- (12) Morini, G. L. Laminar to turbulent flow transition in microchannels. **2002**, Università degli Studi di Ferrara. MECT-02 Abstract, web: <http://www.ichmt.org/abstracts/MECT-02/Abstracts/2-2.pdf>
- (13) Harley, J.; Huang, Y.; Bau, H.H.; Zemel, J.N. Gas flow in microchannels, *J. Fluid Mech.*, **1995**, *284*, 257 – 274
- (14) Rahman, M.M.; Gui, F.J. Experimental measurements of fluid flow and heat transfer in microchannel cooling passages in a chip substrate, in: *Advances in Electronic Packaging, ASME EEP*, **1993**, *199*, 685 – 692
- (15) Wilding, P.; Pfalher, J.; Zemel, J.N.; Bau, H.H.; Kricka, L.J. Manipulation and flow of biological fluids in straight channels micromachined in silicon, *Clin. Chem.*, **1994**, *40*, 43 – 47
- (16) Peng, X.F.; Peterson, G.P. Convective heat transfer and flow friction for water flow in microchannel structures, *Int. J. Heat Transfer Mass Transfer*, **1996**, *39*, 2599 – 2608
- (17) Peng, X.F.; Peterson, G.P.; Wang, B.X. Frictional flow characteristics of water flowing through rectangular microchannels, *Exp. Heat Transfer*, **1994**, *7*, 249 – 265
- (18) Jiang, X.N.; Zhou, Z.Y.; Huang, X.Y.; Liu, C.Y. Laminar flow through microchannels used for microscale cooling systems, in: *IEEE/CPMT Electronic Packaging Technology Conference*, **1997**, 119 – 122
- (19) Mala, G.M.; Li, D.; Dale, J.D. Heat transfer and fluid flow in microchannels, *Int. J. Heat Mass Transfer*, **1997**, *40*, 3079 – 3088
- (20) Papautsky, I.; Gale, B.K.; Mohanty, S.; Ameen, T.A.; Frazier, A.B. Effects of rectangular microchannel aspect ratio on laminar friction constant, in: *Proceedings of SPIE – The International Society for Optical Engineering Proceedings of the 1999 Microfluidic Devices and Systems II*, Santa Clara, **1999**, *3877*, 147 – 158
- (21) Qu, W.; Mala, M.; Li, D. Pressure-driven water flows in trapezoidal silicon microchannels, *Internat. J. Heat Mass Transfer*, **2000**, *43*, 353 – 364
- (22) Ding, L. S.; Sun, H.; Sheng, X.L.; Lee, B.D. Measurement of friction factors for R134a and R12 through microchannels, in: *Proceedings of Symposium on Energy Engineering in the 21st Century*, **2000**, *2*, 650 – 657

- (23) Pfund, D.; Shekarriz, A.; Popescu, A.; Welty, J.R. Pressure drop measurements in a microchannel, in: *Proceedings of the 1998 ASME International Mechanical Engineering Congress and Exposition: DSC Micro-Electro-Mechanical-Systems*, 1998, 66, 193 – 198
- (24) Ren, L.; Qu, W.; Li, D. Interfacial electrokinetic effects on liquid flow in microchannels, *Internat. J. Heat Mass Transfer*, 2001, 44, 3125 – 3134
- (25) Kandlikar, S. G.; Joshi, S.; Tian, S. Effect of channel roughness on heat transfer and fluid flow characteristics at low Reynolds numbers in small diameter tubes, in: *Proc. of 35th National Heat Transfer Conference*, Anaheim CA, USA, 2001, paper 12134
- (26) Li, Z. X. Du, D. X. Guo, Z.Y. Experimental study on flow characteristics of liquid in circular microtubes, in: G.P. Celata, et al. (Eds.), *Proceedings of International Conference on Heat Transfer and Transport Phenomena in Microscale*, Begell House, New York, USA, 2000, 162 – 168.
- (27) Urbanek, W.; Zemel, J.N.; Bau, H. An investigation of the temperature dependence of Poiseuille numbers in microchannel flow, *J. Micromech. Microeng.: Struct. Dev. Syst.*, 1993, 3, 206 – 208
- (28) Pfahler, J.; Harley, J.; Bau, H.; Zemel, J.N. Gas and liquid flow in small channels, *Micromech. Sensors, Actuators, Syst.* 1991, 32, 49 – 58
- (29) Yu, D.; Warrington, R.; Barron, R.; Ameal, T. Experimental and theoretical investigation of fluid flow and heat transfer in microtubes, in: *Proceedings of the 1995 ASME/JSME Thermal Engineering Joint Conference*, Maui, Hawaii, 1995, 1, 523 – 530
- (30) Judy, J.; Maynes, D.; Webb, B. W. Characterization of frictional pressure drop for liquid flows through microchannels. *International Journal of Heat and Mass Transfer*, 2002, 45, 17, 3477 – 3489
- (31) Harms, T.M.; Kazmierczak, M.; Gerner, F.M.; Holke, A.; Henderson, H.T.; Pilchowski, J.; Baker, K. Experimental investigation of heat transfer and pressure drop through deep microchannels in a (110) silicon substrate, in: *Proceedings of the ASME Heat Transfer Division*, 1997, 1, 347 – 357
- (32) Webb, R. L.; Zhang, M. Heat transfer and friction in small diameter channels, *Microscale Thermophys. Eng.*, 1998, 2, 189 – 200
- (33) Wu, P.Y.; Little, W.A.. Measurement of friction factors for the flow of gases in very fine channels used for microminiaturize Joule–Thomson refrigerators. *Cryogenics*, 1983, 24 (8), 273 – 277
- (34) Mala, Gh. M.; Li, D. Flow characteristics of water in microtubes. *International Journal of Heat and Fluid Flow*, 1999, 20, 2, 142 – 148
- (35) Choi, S. B.; Barron, R.F.; Warrington, R.O. Fluid flow and heat transfer in microtubes, in: *Micromechanical Sensors, Actuators and Systems, ASME DSC*, 1991, 32, Atlanta, GA, 123 – 134
- (36) Wu, H.Y.; Cheng, P. Friction factors in smooth trapezoidal silicon microchannels with different aspect ratios, *Internat. J. Heat Mass Transfer*, 2003, 46, 2519 – 2525
- (37) Hrnjaka, P.; Tub, X. Single phase pressure drop in microchannels. *International Journal of Heat and Fluid Flow*, 2007, 28, 1, 2 – 14
- (38) Levenspiel, O. Chemical Reaction Engineering. 3rd Edition. *John Wiley & Sons*, 1999, New York

6 Computational fluid dynamic simulations: two-phase flow

6.1 Abstract

This Chapter focuses on modeling two-phase flow in microchannels and the Advanced-Flow Reactor using the volume-of-fluid method and OpenFOAM. After describing the main equations and numerical schemes, several test cases are used in order to validate the model with simple geometries and conditions. These serve to realize the challenges of this modeling approach for this particular application and the existing alternatives to overcome these difficulties. After validation with test cases, it is applied to the Advanced-Flow Reactor (AFR) to predict flow patterns for carbon dioxide/water and hexane/water systems. The results are in good agreement with experimental results from visualization experiments, with larger discrepancies observed at the largest flow rates.

6.2 Introduction

There has been a strong effort over the years directed towards the simulation of multiphase flow with the aim of capturing dynamic events observed experimentally. Capturing detachment, deformation, breakup, and coalescence of bubbles and drops becomes a challenging task. An additional challenge is to capture accurately capillary effects important at small scales. Accuracy is a desired characteristic in simulations, but achieving high accuracy normally requires very large computation times. Over time, different approaches have been developed, each one providing specific features and advantages. Figure 6.1 includes different approaches reported in the literature to simulate multiphase flows ².

The continuum methods for computation of two-fluid flows are based on macroscopic conservation equations for mass and momentum, and an additional equation that expresses the conservation of each phase mass for the description of the phase evolution. Coupling with the main conservation equations is required to achieve a full description of the multiphase system. ² The continuum methods can be classified into two groups, depending on how the interface is described:

a) **Sharp interface methods:** physical properties experience an abrupt jump at the interface. There are two subgroups depending on the nature of the mesh:

- (1) *Moving unstructured grid*, interface as boundary (Lagrangian movement): the mesh is adapted by local coarsening and refining to capture the interface deformation and curvature. This method is not appropriate when the system undergoes strong topological changes because of the very complex algorithms needed to capture the evolution in topology. The advantage of this method is that sharp interfaces can be achieved.
- (2) *Fixed structured grid*: within this subgroup, there are *front-capturing* methods^{3,4}, where the interface is embedded in a scalar field, and the *front-tracking* methods^{2,5,6}, in which the interface is represented by Lagrangian particles or markers that move with the interface.

The *front-capturing* methods include the volume-of-fluid (VOF) method and the level set (LS) method. The VOF method uses an indicator function to describe the interface. In most cases, the indicator function (α) is the volume fraction of a reference phase. All grid cells that are fully occupied by phase 1 adopt a value of α equal to 1, and those cells fully occupied by phase 2 have a value of α equal to 0. Those cells that contain the interface possess a value between 0 and 1, depending on the relative phase volume fraction occupied in the cell. The LS method, however, uses a distance function, with a value of zero at the interface, a positive value for phase 1, and a negative value for phase 2. The absolute value for the distance function determines how far each fluid point is from the interface.

In the *front-tracking* methods, the interface position is described by the motion of Lagrangian particles or markers in the structured mesh. The disadvantage is the complexity of the method. Additional markers need to be added when the interface stretches or eliminated when the interface grows. Other problems arise in three-dimensional computations and merging of interfaces within one grid cell.

b) **Diffusive interface methods:** physical properties vary continuously along the interface. In the Color-function volume-of-fluid (CF-VOF) ⁷ and Conservative level-set (C-LS) ⁸ methods, the diffusive interface is result of a numerical approach. In the phase-field method ⁹, the diffusive interface is based on a physical approach.

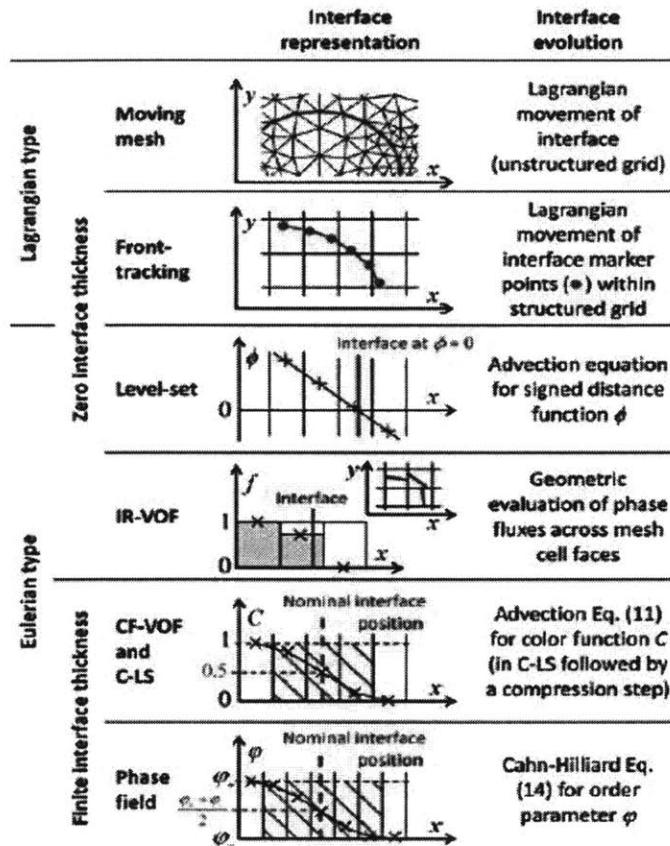


Figure 6.1: Illustration of the different continuum methods for describing the evolution of deforming interfaces. ² Lagrangian approach includes moving mesh and front-tracking methods; Eulerian type, Level-set, VOF with interface reconstruction, color function - VOF and conservative level-set

6.3 Modeling two-phase flow using OpenFOAM

The flow visualization experiments for carbon dioxide/water and hexane/water revealed the dynamic nature of the multiphase flow within the Advanced-Flow Reactor (AFR). The observations showed that many

events of detachment, deformation, breakup, and coalescence of dispersed phase are continuously present at all times along the reactor, and need to be captured by the simulation method.

The OpenFOAM solver developed for modeling two-phase flows called `interFoam`¹⁰⁻¹² is based on the color function volume-of-fluid (CF-VOF) method. Its implementation is based on an Eulerian description of each phase on a fixed mesh (eq 6.1) and description of the interface between the two phases using a transport equation for an indicator function (eq 6.2), which in OpenFOAM implementation is the local volume fraction of one phase, α . This code uses the multidimensional universal limiter with explicit solution (MULES) algorithm to solve the advection equation for the volume fraction.

$$\rho \left(\frac{\partial \vec{v}}{\partial t} + \vec{v} \cdot \nabla \vec{v} \right) = -\nabla \bar{P} + \rho \vec{g} + \mu \nabla^2 \vec{v} \quad (6.1)$$

$$\frac{\partial \alpha}{\partial t} + \nabla \cdot (\vec{v} \alpha) = 0 \quad (6.2)$$

With this definition, each grid cell is described by a velocity vector, pressure, and volume fraction. Those cells fully occupied by phase 1 have a value of $\alpha = 1$, while cells fully occupied by phase 2 adopt a value of $\alpha = 0$. Cells that contain the interface have a value of α between 0 and 1, depending on the volume fraction of each phase.

The approach of the VOF method is to describe the entire domain with a single momentum conservation equation with volume averaged values for the fluid properties at the interface: density (eq 6.3) and viscosity (eq 6.4).

$$\rho = \rho_1 \alpha + \rho_2 (1 - \alpha) \quad (6.3)$$

$$\mu = \mu_1 \alpha + \mu_2 (1 - \alpha) \quad (6.4)$$

The surface tension is a two-dimensional (2D) effect that in a classical problem formulation appears in the stress boundary condition at the interface, both in the normal and tangential components, as described in eq 6.5.

$$(p_1 - p_2 + \sigma\kappa)\vec{n}_i = (\tau_{1ik} - \tau_{2ik})\vec{n}_k + \nabla_s \sigma \quad (6.5)$$

However, in the VOF approach the exact position of the interface is not known, and it is described by a number of cells with finite volume. Thus, the surface tension effect (2D) needs to be converted into a volume effect (3D) that can be incorporated into the main momentum equation valid for the entire domain (eq 6.6).

$$\rho \left(\frac{\partial \vec{v}}{\partial t} + \vec{v} \cdot \nabla \vec{v} \right) = -\nabla \bar{P} + \rho \vec{g} + \mu \nabla^2 \vec{v} + F_{sv} \quad (6.6)$$

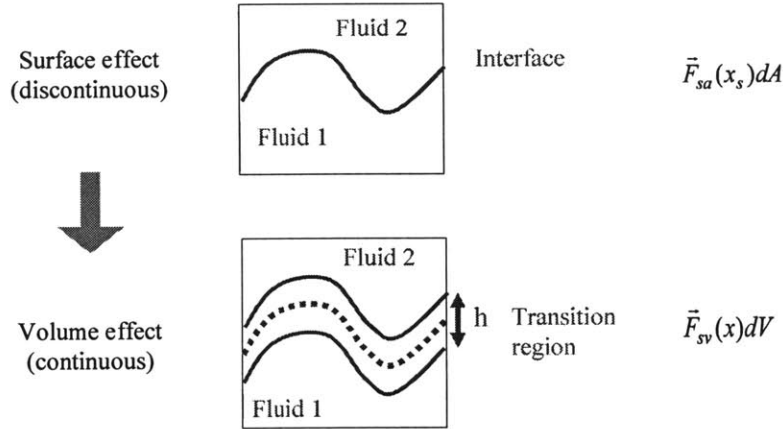


Figure 6.2: Schematic of the Continuum Surface Force (CSF) approach. The surface tension two-dimensional effect is converted into a three-dimensional approach to be inserted into the main momentum conservation equation.

The OpenFOAM solver designed to solve two-phase flows of incompressible fluids with no phase change called 'interFoam' follows the approach described by Brackbill et al.¹³ for the surface tension force. The Continuum Surface Force (CSF) interprets surface tension as a continuous, three-dimensional effect across an interface. For a volume force $F_{sv}(x)$ that provides the correct surface tension force per unit interfacial area, $F_{sa}(x_s)$, for an interface thickness approaching zero, and being zero outside of the interface:

$$\lim_{h \rightarrow 0} \int_{\Delta V} F_{sv}(x) dV = \int_{\Delta A} F_{sa}(x_s) dA \quad (6.7)$$

where the area integral over the portion ΔA of the interface within the small volume of integration ΔV . The original discontinuous indicator function is defined by $c(x)$ using eq 6.8:

$$c(x) = \begin{cases} \text{phase 1} & c(x) = c_1 \\ \text{interface} & c(x) = (c_1 + c_2)/2 \\ \text{phase 2} & c(x) = c_2 \end{cases} \quad (6.8)$$

Within the thickness of the interface (h), called transition region, an indicator function that varies smoothly from phase 1 to phase 2 is defined, $\tilde{c}(x)$. For very small interface thickness, the two equations are equivalent:

$$\lim_{h \rightarrow 0} \tilde{c}(x) = c(x) \quad (6.9)$$

$$\lim_{h \rightarrow 0} \nabla \tilde{c}(x) = \nabla c(x) \quad (6.10)$$

And, for very small interface thickness ($h \rightarrow 0$):

$$\int_A F_{sa}(x_s) dA = \lim_{h \rightarrow 0} \int_V \sigma \kappa(x) \frac{\nabla \tilde{c}(x)}{c_2 - c_1} dV \quad (6.11)$$

Thus, by comparison with the volume force, $F_{sv}(x)$, it is demonstrated that for small interface thickness, the expression given by eq 6.12 can be used to approximate the surface tension effect as a body force which can be inserted in the momentum conservation equation (eq 6.6).

$$F_{sv}(x) = \sigma \kappa(x) \frac{\nabla \tilde{c}(x)}{c_2 - c_1} \quad (6.12)$$

As mentioned previously, the indicator function in `interFoam` is defined as the phase fraction (α) and an additional advection equation for the transport of α is defined. However, the advection equation for the volume fraction suffers from numerical diffusion, and an additional compression term that compensates for this artificial diffusion of the interface is added to the original eq 6.2 to yield eq 6.13:

$$\frac{\partial \alpha}{\partial t} + \nabla \cdot (\alpha \vec{v}) + \nabla \cdot (\vec{v}_r (\alpha(1 - \alpha))) = 0 \quad (6.13)$$

Where \vec{v}_r is the relative velocity between phases and is calculated using eq 6.14:

$$\vec{v}_r = n_f \min \left[\frac{c_r |\varphi|}{|s_f|}, \max \left(\frac{|\varphi|}{|s_f|} \right) \right] \quad (6.14)$$

This compression factor is only active at the interface and vanishes at those cells that are fully occupied by phase 1 or phase 2. The amount of compression can be adjusted by specifying the *alpha* value, C_r (usually ranges from 0 to 4) in the “*system/fvSolution*” file.

The local surface curvature (κ) is calculated using eq 6.15, where \hat{n} is the normal vector perpendicular to the interface, calculated with eq 6.16.

$$\kappa = \nabla \cdot \hat{n} \quad (6.15)$$

$$\hat{n} = \nabla \alpha / |\nabla \alpha| \quad (6.16)$$

The wall adhesion force is considered by specifying the three-phase contact angle:

$$\hat{n} = \hat{n}_w \cos(\theta_w) + \hat{t}_w \sin(\theta_w) \quad (6.17)$$

where \hat{n}_w and \hat{t}_w are the normal and tangential vectors to the wall, respectively. In the subsequent simulations, the contact angle is considered to be constant and independent of the velocity and the direction of the contact line movement.

6.3.1 interFoam solver validation

There is a very limited number of publications in the literature regarding two-phase flow modeling in microchannels using OpenFOAM. Most of the work is done using other commercial softwares, such as Fluent, STAR-CCM, or COMSOL. The advantage of the OpenFOAM software is that being open source the original code is available for consultation and modifications to improve the current performance of solvers or create new ones to satisfy specific modeling requirements. Indeed, there are continuous efforts in both the academic and industrial communities to broaden the applicability of OpenFOAM to solve different problems.

The publications that report the use of the `interFoam` solver for two-phase incompressible flow include the work performed by Deshpande et al. (2012)¹⁴, Hoang et al. (2012)¹⁵, Raees et al. (2011)¹⁶ and Raeini et al. (2012)¹⁷. Deshpande et al focused on a detail evaluation of the performance of the `interFoam` solver using a variety of test validation cases trying to cover a wide range of applications: a) pure advection; b) dynamics for inertia dominated flows; c) dynamics for surface tension dominated flows. It is concluded in this work that the performance of `interFoam` is comparable to other VOF existing algorithms, but the geometric reconstruction schemes, such as the one available in Fluent, perform better. It was also shown that for inertia-dominated flows with large density ratios `interFoam` is able to perform with excellent agreement with experimental and analytical values. In the case of surface tension dominated flows, `interFoam` guarantees a consistent formulation of pressure and surface tension. However, 10 % disagreement for the computation of curvature with respect to analytical values is observed. Further improvements need to be done in this regard.

A common problem when simulating two-phase flow at small scales are artificial velocities appearing at the interface. This problem has been reported by many authors using VOF methods^{15 - 27} in their simulations. This is attributed to an imbalance of forces caused by the introduction of surface tension body force as approximation for the surface effects into the single-conservation momentum equation and/or incorrect method for the computation of the interface curvature. This effect is especially important at low or zero velocities and strong capillary forces. The artificial velocities created are often called ‘spurious or parasitic currents’. To overcome the problem of spurious currents in `interFoam`, Deshpande et al. suggest a criterion based on the analysis of Galusinski and Vigneaux²⁴ for the time step which depends on the fluid properties (ρ , σ , μ), as given by eq 6.18:

$$\Delta t \leq \max[10\tau_\mu, 0.1\tau_p] \quad (6.18)$$

$$\tau_\mu = \frac{\mu\Delta x}{\sigma} \quad (6.19)$$

$$\tau_p = \sqrt{\frac{\rho\Delta x^3}{\sigma}} \quad (6.20)$$

However, other authors introduce modifications into the main solver to reduce parasitic currents. For instance, Hoang et al. ²⁸ use a Laplacian smoother for the volume fraction α , as given by eq 6.21, and recommend best selection of parameters, such as the compression factor C_n , for best performance.

$$\tilde{\alpha}_p = \frac{\sum_{f=1}^n \alpha_f S_f}{\sum_{f=1}^n S_f} \quad (6.21)$$

Raeini et al. ¹⁷ follow a more complicated procedure, incorporating a semi-sharp surface model (SSF) to reduce the artificial diffusion of the interface, and two new filtering methods (FSF) to correct for capillary forces and reduce spurious currents. This solver is implemented after reformulation of the Navier-Stokes equation by defining a dynamic pressure p_d according to eq 6.22 and a body force which lumps together the effects of gravity, capillary forces, and capillary pressure gradients, as described by eq 6.23.

$$p_d = p - p_c \quad (6.22)$$

$$f' = \rho g + f_c - \nabla p_c \quad (6.23)$$

The capillary pressure is calculated by eq 6.24.

$$\nabla \cdot \nabla p_c = \nabla \cdot f_c \quad (6.24)$$

The capillary force is sharpened using a modified indicator function, which limits the capillary pressure transition area to one cell. The value for the sharpening factor C_{pc} ranges from 0 to 1. The limit of $C_{pc} = 0$ corresponds to the original CSF formulation, $C_{pc} = 0.98$ is demonstrated to be the best option to remove spurious currents in static problems (SSF), and $C_{pc} = 0.5$ is best used for moving interfaces. More details are described in the literature. ¹⁷

Different test cases of two-phase flow using the OpenFOAM simulation solver interFoam are shown in this section in order to illustrate with examples and discuss the different challenges that are encountered when simulating two-phase flow using this solver. Test cases include: a) static bubble in a stagnant liquid; b) rising bubble in a stagnant liquid; c) flow in T-junctions and microchannels.

6.3.1.1 Static bubble

The “static bubble” test case consists of a transient simulation of a bubble immersed in a stagnant liquid in absence of gravity. Initialization of the domain is done by setting the volume fraction of the dispersed phase in the form of a cube of side L , as shown in Figure 6.3. The simulation runs until the bubble reaches at equilibrium a spherical shape of diameter d_B and the maximum velocity magnitude within the entire domain (v_{max}) is monitored over time. The mesh is 3D, structured, with 8,000 cells, and fixed cell size to 5×10^{-6} m. The model system is water/air, whose properties are included in Table 6.1. The effect of the solver used, bubble size, and compression factors are studied here.

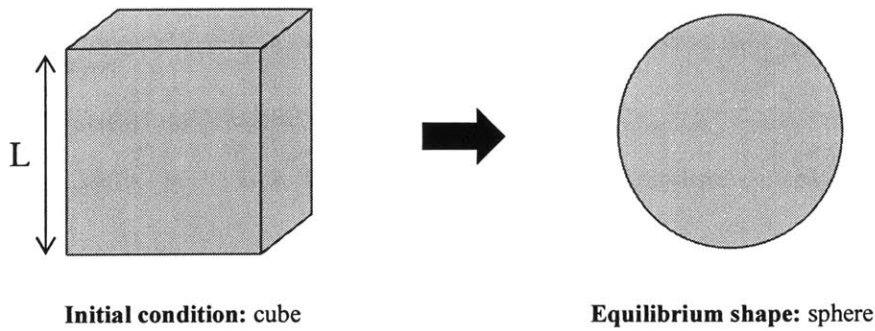


Figure 6.3: Schematic of the static bubble test case. Initial shape of the dispersed phase is in the form of a cube. Relaxation of the cube shape into a sphere occurs while the maximum velocity within the entire domain is monitored.

Table 6.1: Fluid properties of air and water at 25°C.

	ρ (kg/m ³)	μ (Pa s)	σ (N/m)
Air	1.2	$1.983 \cdot 10^{-5}$	0.072
Water	998.2	10^{-3}	

a) Effect of solver

Two different solvers are used for comparison in the simulations: a) *interFoam*, the original formulation of VOF approach in OpenFOAM; and b) *poreFoam*, the modified solver based on *interFoam*, performed by Raeni et al. ¹⁷

A comparison between results obtained with interFoam and poreFoam is shown in Figures 6.4 and 6.5 for a bubble size of 0.4 mm. The maximum velocity over time is shown in Figure 6.4 and the velocity field in the cross section at the center plane of the bubble, in Figure 6.5. The maximum velocity that should be observed for both solvers in an ideal case is zero at the equilibrium state (once the sphere shape has been reached). However, artificial velocities are created at the interface yielding a maximum velocity on the order of 0.0005 m/s when interFoam is used. This velocity is not reduced further over time, but remains constant. The reason behind this behavior is that at such small scales, capillary effects become significant and there is an imbalance created by the surface tension body force embedded in the momentum conservation equation. It is seen from Figure 6.4 that poreFoam is effective in reducing the maximum velocity in 0.4 seconds from 0.0005 m/s to zero. The velocities observed initially in the simulations are caused by the transient transformation of the initialized cube of air achieving the final equilibrium sphere shape.

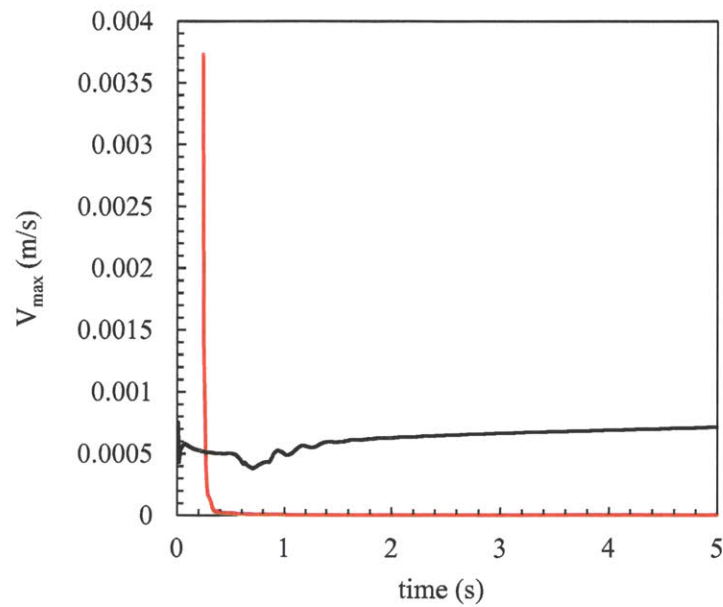


Figure 6.4: Comparison between interFoam and poreFoam solvers for bubble diameter of 0.4 mm. Legend: ---, interFoam; ---, poreFoam; poreFoam solver is effective in reducing the maximum velocity whereas interFoam creates spurious velocities that remain steady over time.

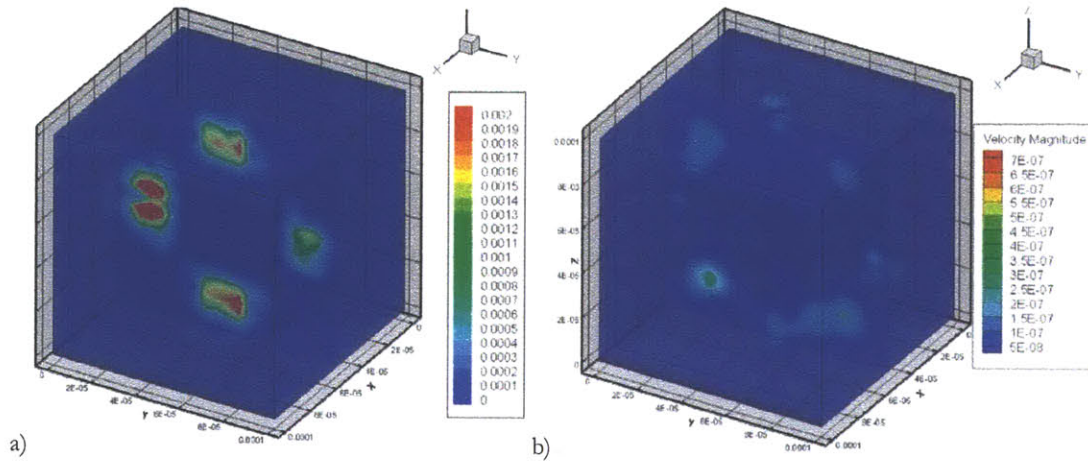


Figure 6.5: Velocity fields showing spurious currents for 0.4 mm bubble size using a) interFoam; b) poreFoam. Spurious velocities are effectively reduced using poreFoam from 0.002 m/s (interFoam) to 10^{-7} m/s.

b) Effect of bubble size

The next example shows the effect of the bubble size on the maximum velocity magnitude encountered during the simulation with interFoam and poreFoam for two different bubble sizes: a) 0.4 mm and b) 0.2 mm. Reducing the bubble size increases the capillary pressure, and thus, it is expected the effect of the spurious currents to be stronger for 0.2 mm than for 0.4 mm. The comparison between solvers and bubble sizes is shown in Figures 6.6 and 6.7. Again, it is very clear how the poreFoam solver is effective in reducing the spurious velocities, while the interFoam solver encounters problems and creates artificial velocities which are more significant at smaller bubbles (0.2 mm) than at larger bubbles (0.4 mm), as expected. Not only the average maximum velocity is about four times larger at 0.2 mm bubble size, but also the oscillations at smaller bubble size become more pronounced.

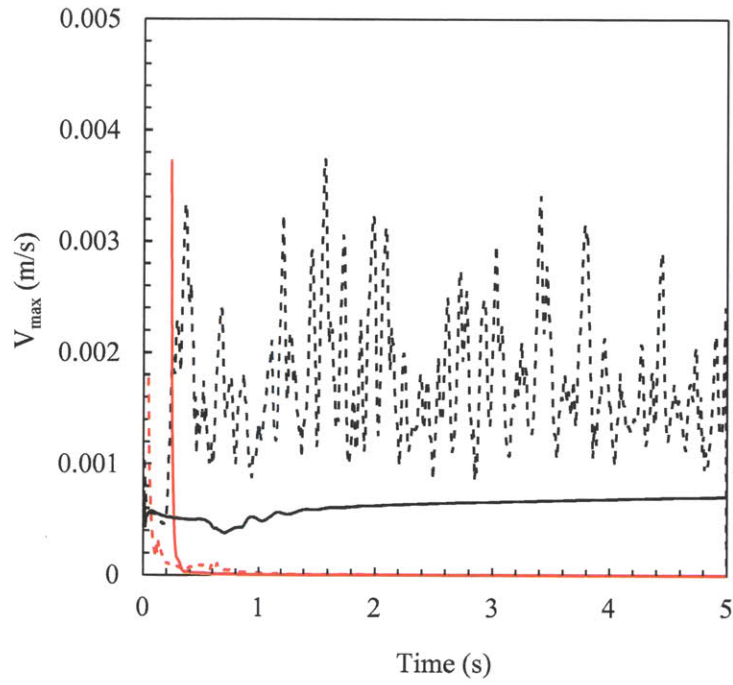


Figure 6.6: Comparison between interFoam and poreFoam solvers for two different bubble diameters. Legend: —, interFoam, $d_B = 0.4$ mm; - - -, interFoam, $d_B = 0.2$ mm; — — —, poreFoam, $d_B = 0.4$ mm; - - - - -, poreFoam, $d_B = 0.2$ mm

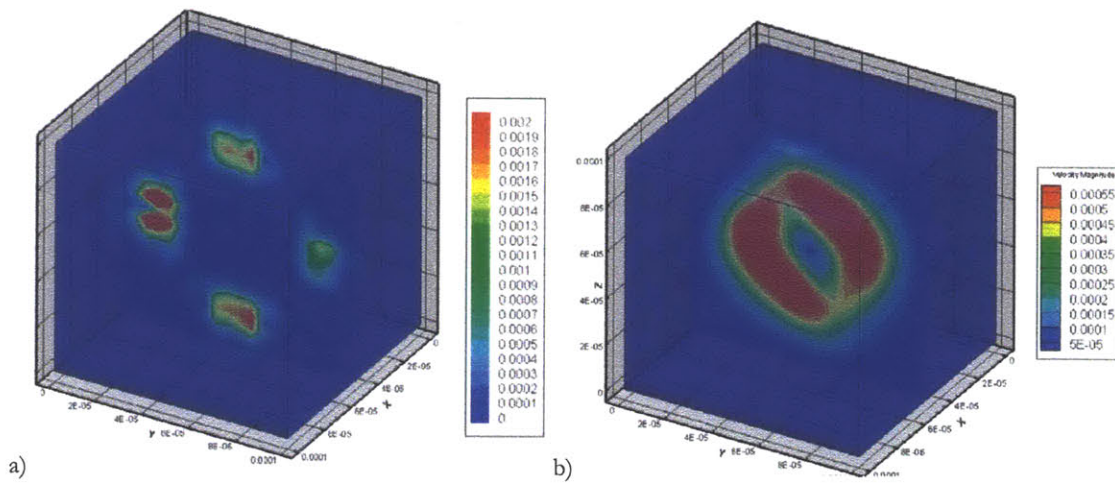


Figure 6.7: Velocity fields showing spurious currents using interFoam for different bubble sizes: a) 0.4 mm; b) 0.2 mm. Spurious currents increase significantly with reduction in droplet size.

c) Effect of compression term

Another variable in the interFoam solver that is defined in the simulation is the compression term through the quantity 'cAlpha'. A comparison between different compression factors in terms of maximum velocity magnitude monitored over time is included in Figure 6.8. It is seen that very large spurious velocities are created for both compression factors and do not decay over time. Interestingly, at short times, the absence of compression factor reduces the spurious velocities ten times, whereas from 0.35 seconds on, the magnitude of the spurious currents increases abruptly reaching over 0.2 m/s of maximum velocity. Increasing the compression term to 2 helps stabilize the spurious velocities whose magnitude remains almost constant over time despite of the instantaneous oscillations.

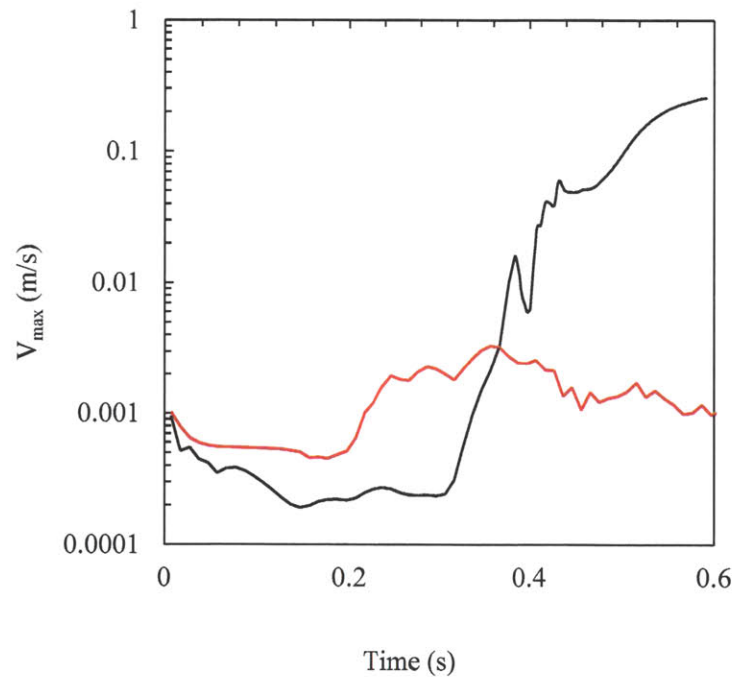


Figure 6.8: Comparison between different compression terms using interFoam for bubble size 0.2 mm. Legend for cAlpha: —, 0; - - -, 2; Increasing compression term does not help reduce spurious currents for this bubble size. Moreover, at low compression terms, higher velocities are observed at longer times.

d) Effect of Courant number

Additional simulations were performed in order to see if the method used to specify the time step in the simulations has an influence on the poreFoam solver performance. The time step can be specified in two ways: a) fixed constant value; b) varying time step to keep Courant number ($Co = V\Delta t/\Delta x$) constant. The later adjusts the time step (Δt) depending on the velocity (V) and the cell size (Δx) in the domain.

Simulation results performed for a bubble size of 0.4 mm are shown in Figure 6.9. Although with both approaches the maximum velocity magnitude is below 10^{-4} m/s, using the Courant number as reference to fix the time step seems to be more stable than fixing the time step directly. It is important to consider this for future simulations, especially when the cell sizes that form the mesh are different.

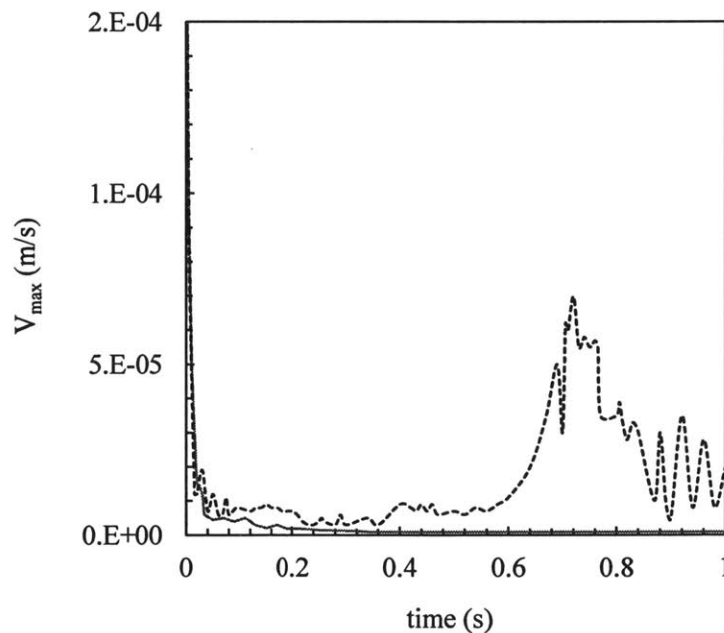


Figure 6.9: Stagnant bubble 0.4 mm, simulation with poreFoam solver. Legend: ----, fixed time step; - - - -, fixed Courant number. Effective reduction in spurious currents is observed with poreFoam using a fixed Courant number. Although maximum velocity is small, oscillations are observed for fixed time steps.

6.3.1.2 Rising bubble

Another common test to validate VOF solvers is to simulate an air bubble moving upwards in a stagnant liquid driven by buoyancy. This is a good way of analyzing how the interFoam solver performs when gravity is present and a way of evaluating the problem of spurious currents for moving interfaces. Terminal rising velocities have been measured experimentally for a number of systems and bubble sizes, and they are available in the literature ^{29,30}. For air/water system, typical representations of the terminal rise velocity versus the equivalent bubble diameter are presented, as shown in Figure 6.10.

Table 6.2: Flow characteristic numbers for air rising bubble in water.

d_B (mm)	40	4	0.4
Re (-)	15971	998	16
Eo (-)	217	2.2	$2.2 \cdot 10^{-2}$
Ca (-)	$5.6 \cdot 10^{-3}$	$3.5 \cdot 10^{-3}$	$5.6 \cdot 10^{-4}$
We (-)	88.7	3.47	$8.9 \cdot 10^{-2}$

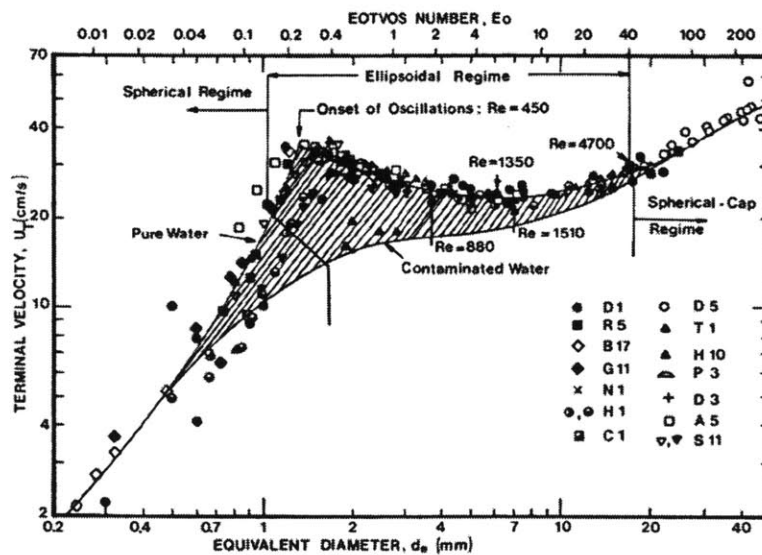


Figure 6.10: Terminal velocity of air bubbles in water at 20 °C. Reprinted from Clift et al ²⁹

The effect of interface compression term for different bubble sizes on the bubble rise velocity is shown in Figure 6.11. It is observed that at 40 mm of equivalent bubble size diameter the bubble moves with a rising velocity of 0.4 m/s. Its terminal rise velocity is predicted within 5% accuracy by the interFoam solver, regardless of the interface compression factor. Here the gravitational forces are significantly more important than surface tension effects. Decreasing the bubble size to 4 mm, the difference among predictions for different compression terms increases, especially at longer times. The prediction of the bubble rising velocity is still in agreement with the experiments, but discrepancies increase when decreasing the bubble size further.

For bubble sizes of 0.4 mm, the effect of the interface compression term is even more drastic. For a 0.4 mm bubble, where capillary forces are important ($Ca = 5.6 \cdot 10^{-4}$), the rising velocity spans from 0.36 to 0.003 m/s for compression factors between 1 and 3, respectively, whereas the experimental terminal rising velocity is 0.04 m/s. This reflects the problem of the spurious velocities which appear in the vicinity of the interface and become important at low capillary numbers, affecting the overall bubble rising velocity. The effect of spurious currents was already observed for the case of a stagnant bubble and studied in detail by Hoang et al^{15, 28}. They provide best practices in selecting the compression term to minimize spurious currents and interface thickness. Increasing the compression term decreases the interface thickness, but increases spurious currents. A compromise between those two variables needs to be achieved. However, they do not study the rising bubble test case. Raees et al¹⁶ evaluated the performance of interFoam in modeling the rising bubble case regarding the compression term available in OpenFOAM. They showed that interFoam is in good agreement for a two-dimensional case of rising bubble due to buoyancy comparing the results with an anti-diffusion scheme. On the other hand, three-dimensional simulations with interFoam under-predict the rising velocity and spurious currents are observed at the interface. further studies in this regard need to be done.

On the positive side, the interFoam solver is more accurate in the prediction of the bubble shape for all bubble sizes. Figure 6.10 includes the different flow regimes in terms of bubble diameter and Eötvös number. A spherical-cap regime is expected for Eo numbers larger than 40, ellipsoidal regime for Eo between 0.15 and 40, and spherical regime below $Eo = 0.15$. From Table 6.2 we can anticipate the shape of the bubble to be

spherical-cap for 40 mm, ellipsoidal for 4 mm, and spherical for 0.4 mm. This is what is observed in our simulations despite of the compression terms used and the disagreement of the modeling results in terms of rising velocities, as shown in Figure 6.12. However, a more detailed study needs to be performed in this regard for a broader number of bubble sizes. It has been reported in the literature that other momentum advection schemes combined with mesh refinement help achieve better performance with the interFoam solver ³¹.

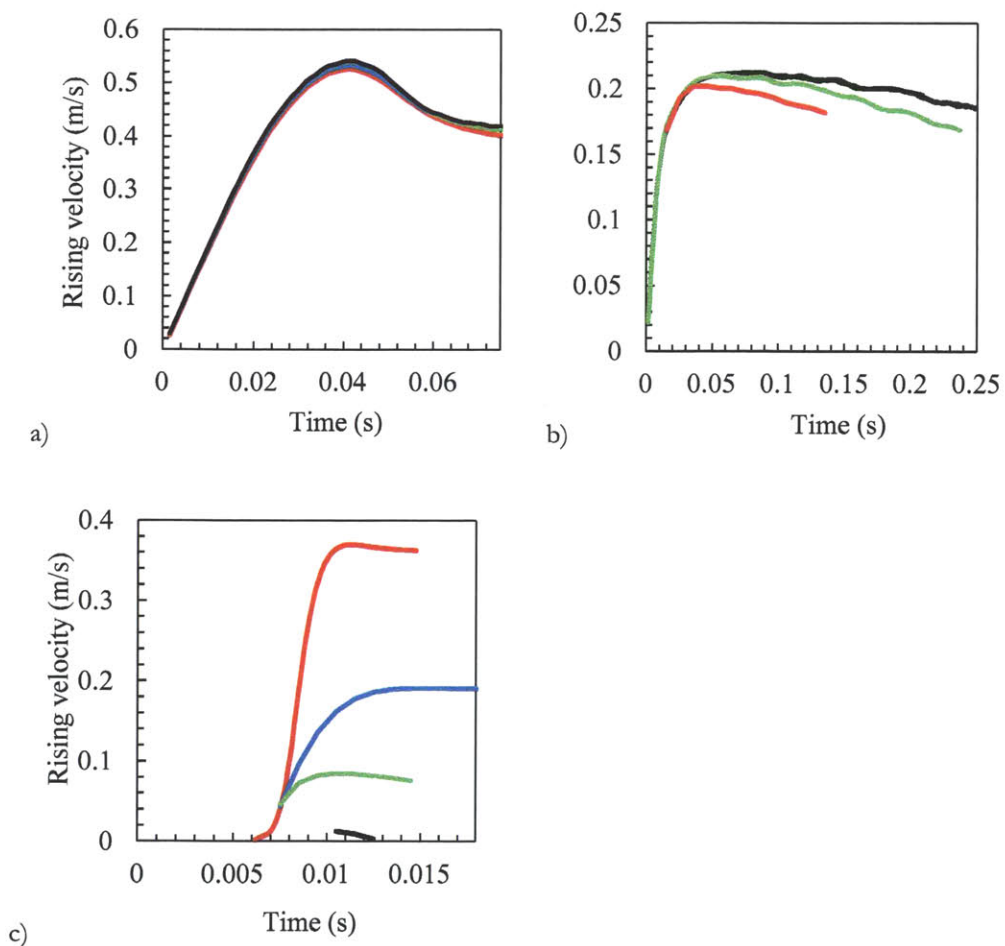


Figure 6.11: Rising velocity for air bubble in water for different bubble sizes: a) 40 mm; b) 4 mm; c) 0.4 mm, as function of compression term $c\alpha$. Legend for $c\alpha$: —, 1; —, 1.5; —, 2; —, 3; Good agreement with experiments is seen at large bubble sizes, but rising velocity highly depends on compression term at lowest bubble sizes.

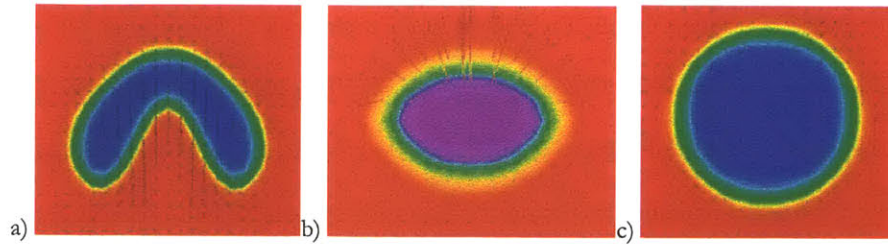


Figure 6.12: Bubble shape for air bubble rising in water for different bubble sizes: a) 40 mm; b) 4 mm; c) 0.4 mm. CFD results are qualitatively in agreement with experiments. Bubble shape is a) spherical-cap; b) ellipsoidal; c) spherical.

6.3.1.3 Microchannels and T-junctions

A test case that increases the complexity of the multiphase simulations with respect to stagnant bubbles in quiescent liquids or the simulation of rising bubbles in water, is modeling two-phase flow in microchannels and T-junctions. This type of flow involves the formation of slugs through deformation and detachment of the dispersed phase at the inlet of the T-junction. The phenomenon of bubble detachment does not occur in either of the two previous cases. The objective is to validate the solver with cases that resemble more closely the two-phase flow in the AFR, although the geometry is different.

Simulations in microchannels have been published by several authors in the literature. Most of them conducted for gas-liquid flows, and very few for liquid-liquid systems. In addition, the most part of them are simulated using commercial softwares such as COMSOL, Fluent, or STAR-CCM, but very few are performed using OpenFOAM. To the best of our knowledge, only Hoang et al. ^{15, 28, 32} investigated droplet breakup in a T-junction, Plouffe et al ³³, the passive mixing in the micro and milliscales, and Semyonov et al ³⁴, the hydrodynamics of a microstructured plate reactor, all using interFoam. Other authors have used CFD commercial softwares to investigate biphasic flow in microchannels. For example, Taha et al (2006) used Fluent to model slug flow inside square capillaries and vertical tubes. ³⁵, Zheng et al. (2007) determined through CFD the hydrodynamics in gas-liquid vertical upward slug flow ³⁶, Kashid et al (2007, 2010) used Fluent to model liquid-liquid slug formation in microreactors ^{37, 38}. Shao et al (2008) used COMSOL Multiphysics to simulate the effect of inlet configuration on slug flow formation ³⁹ as well as mass transfer

with and without chemical reaction during Taylor flow in microchannels ⁴⁰. Gupta et al (2009) used Fluent to model Taylor flow in microchannels with emphasis on capturing the liquid film ⁴¹. Qian et al (2006) performed an extensive study using Fluent to study Taylor flow in microchannels for gas/liquid slugs varying cross-section width at various operating conditions finding good agreement with literature data ⁴². Santos et al (2010) ⁴³ investigated air/water two-phase flow in a microfluidic T-junction with square microchannels both experimentally and using Fluent. Asadolahi et al (2012) investigated the hydrodynamics and heat transfer of Taylor flow with Fluent and compared the results with nitrogen/water and nitrogen/ethylene glycol experimental data ⁴⁴. Raj et al (2010) used Fluent to investigate numerically drop/slug formation for liquid/liquid flow in microchannels studying the effect of flow rates, channel size, flow distributor shape, and fluid properties. ⁴⁵

Here simulations of two-phase flow in microchannels and T-junctions using OpenFOAM for different gas/liquid and liquid/liquid flow rates are compared with simulation results and experiments available in the literature ^{42, 43, 45}.

Two-phase flows studied by Qian and Lawal ⁴²

Qian, D. and Lawal ⁴², A. simulated the formation of slugs of air/water in a T-junction using Fluent. Here the interFoam solver is used to simulate the air/water biphasic flow using the same operating conditions as the authors. The simulations are performed in a 2D structured mesh of a T-junction having a channel width of 0.5 mm, with the geometry shown in Figure 6.13.

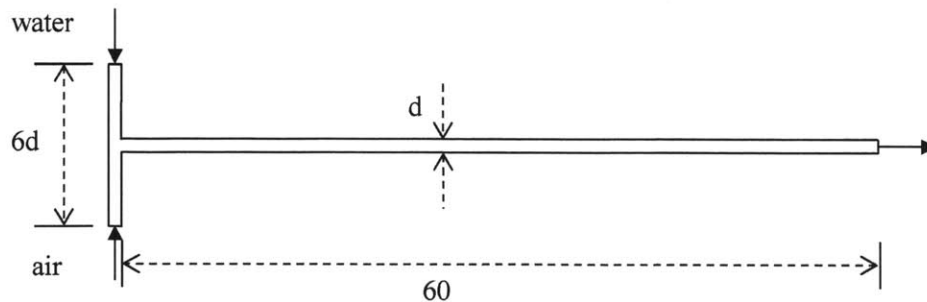


Figure 6.13: Schematic of T-junction with channel size d for two-phase simulations, adapted from Qian and Lawal ⁴²

First, the effect of the mesh resolution is studied and the results are shown in Figure 6.14 for gas and liquid inlet velocities of 0.02 m/s and 0.08 m/s, respectively. Four mesh resolutions are used for comparison, with the following number of cells: a) 1,444; b) 6,534; c) 13,594; d) 27,664. As it is observed in the images of the two-phase flow along the channel, there are significant differences between the coarser mesh (1,444 cells) and the other meshes. The coarser mesh predicts the formation of air slugs followed by smaller satellite slugs, whereas the other three meshes predict the formation of independent air slugs. The slug length for the liquid and gas phases are predicted very similarly by all mesh resolutions, reaching asymptotic values for the larger number of cells. The results are shown in Table 6.3. The corresponding velocity profiles and streamlines for 0.02 m/s and 0.08 m/s of inlet velocity for the gas and liquid phase are shown in Figure 6.15. For the three meshes of higher resolution, the results are very close to each other, with similar velocity profiles and streamlines. A compromise between accuracy and computation time needs to be established for each simulation.

Table 6.3: Effect of mesh resolution on gas and liquid slug lengths for different air and water inlet velocities. L_G : Gas slug length (mm), L_L : liquid slug length (mm)

V_G (m/s)	V_L (m/s)	1,444 cells	6,534 cells	13,594 cells	27,664 cells
0.02	0.08	$L_G = 0.93$	$L_G = 1.02$	$L_G = 1.03$	$L_G = 1.03$
		$L_L = 3.49$	$L_L = 3.29$	$L_L = 3.61$	$L_L = 3.70$
0.08	0.02	$L_G = 3.11$	$L_G = 3.79$	$L_G = 4.13$	$L_G = 4.16$
		$L_L = 0.69$	$L_L = 0.81$	$L_L = 0.88$	$L_L = 0.83$
0.02	0.02	$L_G = 1.57$	$L_G = 1.74$	$L_G = 1.78$	$L_G = 1.81$
		$L_L = 1.37$	$L_L = 1.54$	$L_L = 1.58$	$L_L = 1.60$
0.05	0.05	$L_G = 1.35$	$L_G = 1.54$	$L_G = 1.55$	$L_G = 1.55$
		$L_L = 1.23$	$L_L = 1.35$	$L_L = 1.37$	$L_L = 1.38$

Snapshots of the transient simulation of air and water at one second using the finest mesh at varying inlet velocities of gas and water are shown in Figure 6.16. Here, the effect of varying the inlet velocities of each phase is clearly observed: the slug length of each phase is determined by the flow rates of air and water. For the same inlet velocity, increasing the total flow rate creates slightly smaller slugs. In addition, the slug length of one phase can be increased by increasing the inlet velocity (and thus, the flow rate) of the phase of interest. The ratio of slug length can be roughly estimated by the ratio of inlet velocities. In this particular

example, the slug length of the gas phase is slightly larger than the theoretical ratio based on inlet velocities, probably due to the different fluid properties of air (density, viscosity) against water.

Another interesting feature of CFD simulations is that the effect of introducing changes in the design of the devices can be easily studied. For instance, Qian and Lawal studied the effect of modifying the inlet channel width and configuration on the slug length. Here similar simulations were performed for inlet channel dimensions of 0.5 mm, 1.0 mm, and 0.25 mm, which correspond to “d” (same width as downstream channel), “2d” (double width), and “d/2” (half width). For the same phase inlet velocity (0.02 m/s water, 0.02 m/s air), the slug length increases exponentially with the inlet channel width, as shown in Table 6.4 and Figure 6.17. Another design parameter of study is the configuration of the inlet channels, which also have an effect on the slug length, as shown in Figure 6.18. The trend observed is the same as the described by Qian and Lawal in the literature. However, the actual values of the slug lengths vary, due to several reasons: OpenFOAM and Fluent are different not only in the different numerical schemes they use, but also in the physical representation of the interface effects. In addition, the interFoam solver is modified by the specification of a compression factor cAlpha that also has an influence on the CFD results, as shown in Figure 6.18 and Table 6.5. Both gas and liquid slug lengths decrease with increasing the compression factor. Nevertheless, both simulation methods can provide similar results and trends for the studied system.

Table 6.4: Effect of inlet channel width on slug length for 0.02 m/s air and 0.02 m/s water inlet velocities.

d (mm)	interFoam cAlpha = 4		Qian and Lawal (2006)	
	L _G (mm)	L _L (mm)	L _G (mm)	L _L (mm)
0.25	1.10	0.89	1.40	1.05
0.50	1.91	1.69	2.17	1.78
1.00	4.14	4.07	4.19	3.28

Table 6.5: Effect of cAlpha on slug length for 0.02 m/s air and 0.02 m/s water inlet velocities, configuration C.

cAlpha	L _G (mm)	L _L (mm)
0.5	2.89	2.64
1.0	2.51	2.16
4.0	1.93	1.72

Another factor studied is the effect of the inlet channel length on the slug length. It is observed in Figure 6.19 that the inlet channel length does not have any effect on the slug length and flow development as long as this channel provides enough length to have fully developed flow when the two flow streams meet. This result is in agreement with the observations of Qian and Lawal.

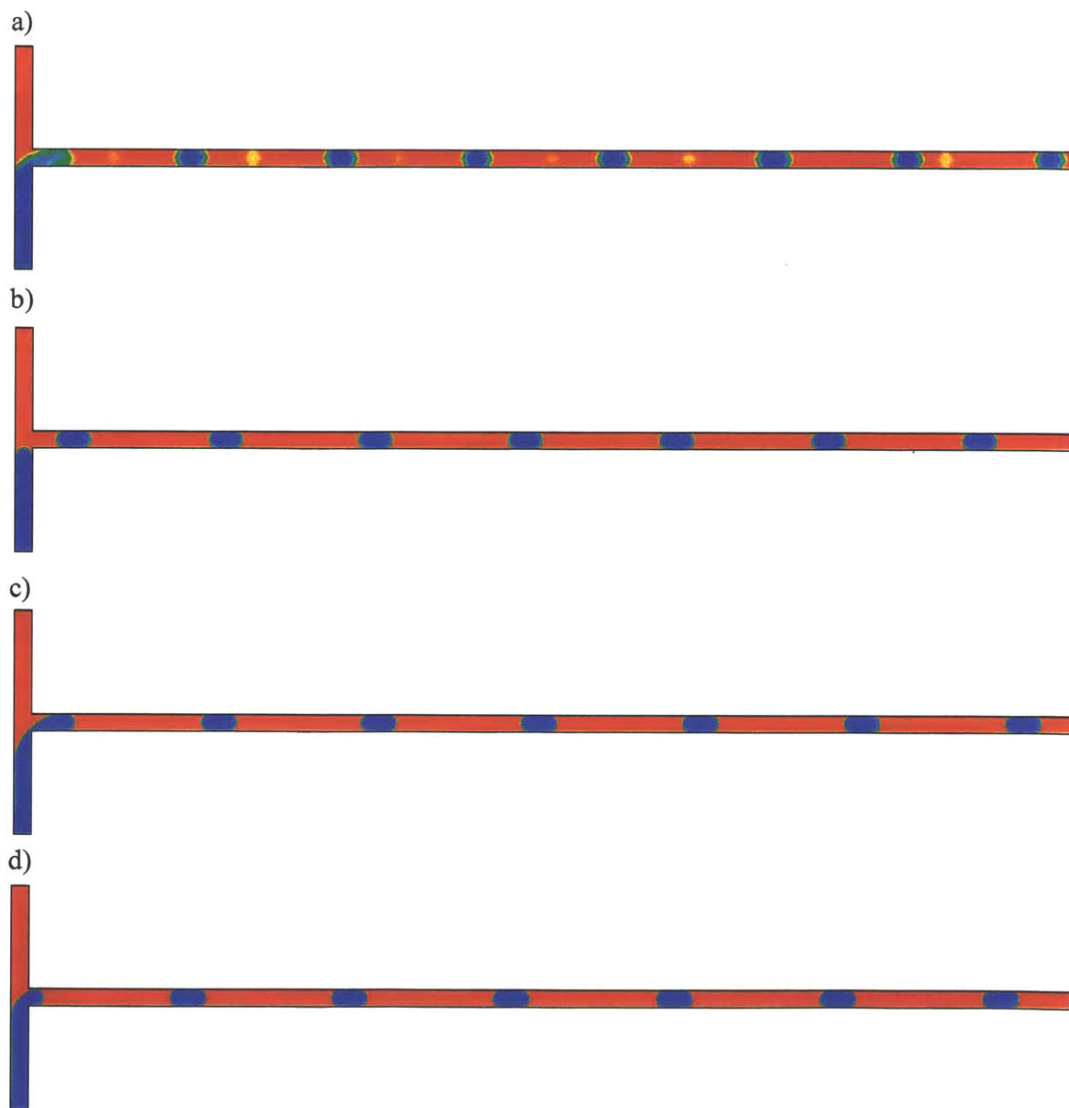


Figure 6.14: $V_G = 0.02$ m/s, $V_L = 0.08$ m/s, snapshot of transient simulation at $t = 1$ s; Number of cells: a) 1,444; b) 6,534; c) 13,594; d) 27,664; $d = 0.5$ mm; phases: red ■, water; blue ■, air;

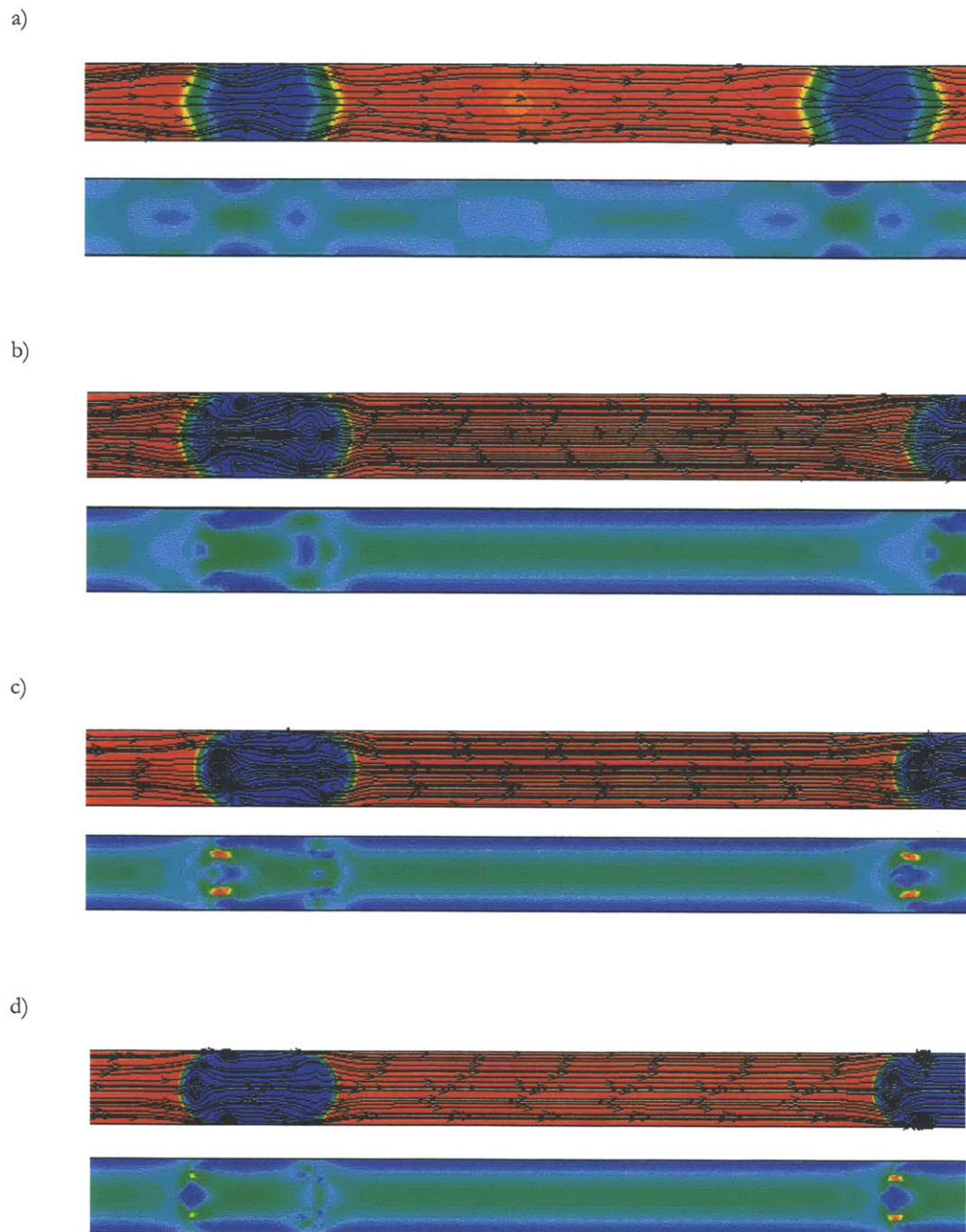


Figure 6.15: Streamlines and velocity profiles for $V_G = 0.02$ m/s, $V_L = 0.08$ m/s, snapshot of transient simulation at $t = 1$ s; Number of cells: a) 1,444; b) 6,534; c) 13,594; d) 27,664; $d = 0.5$ mm; phases: red ■, water; blue ■, air;

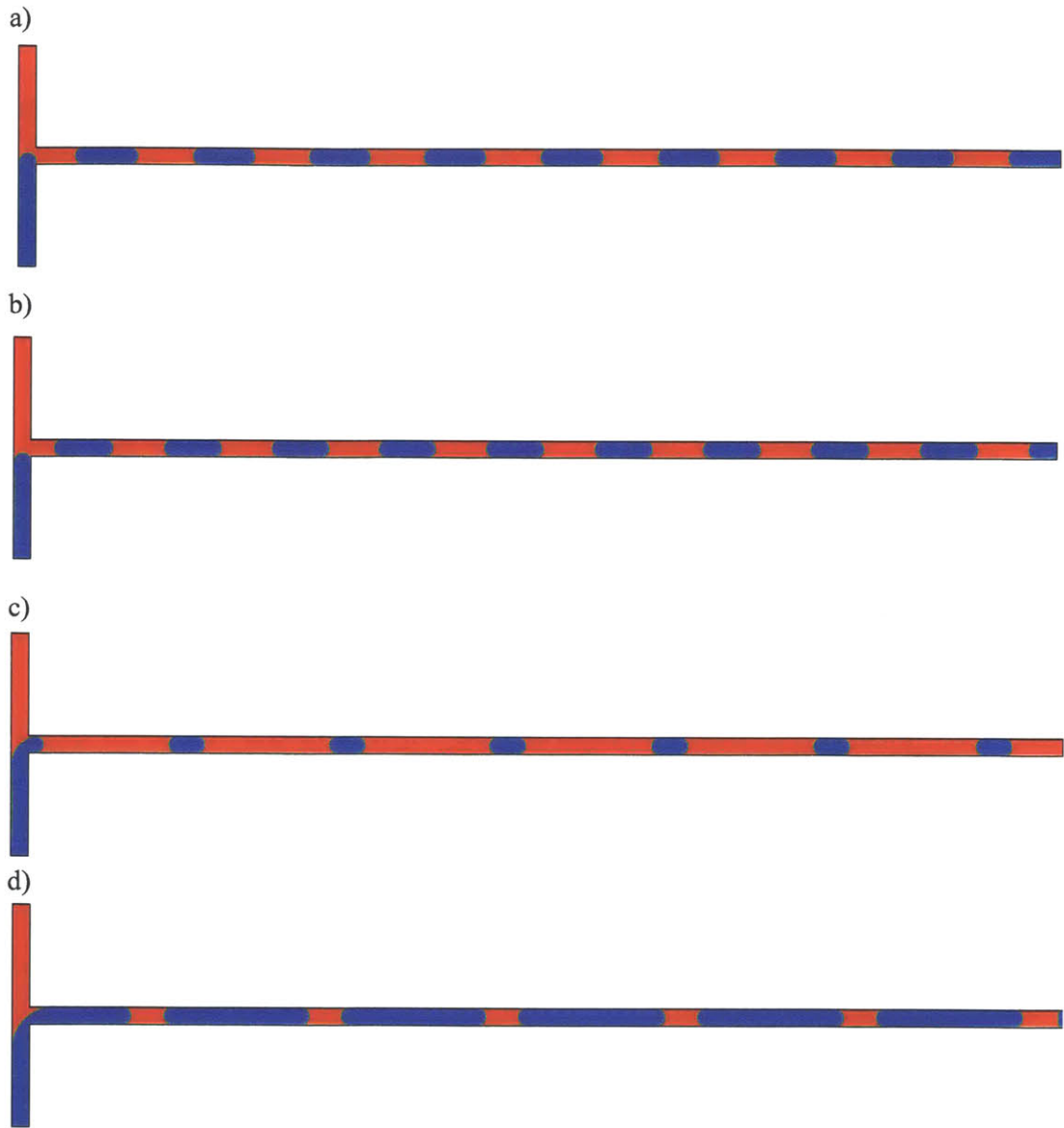


Figure 6.16: Snapshot of transient simulation air/water flow at $t = 1$ s; number of cells: 27,664; a) $V_G = 0.02$ m/s, $V_L = 0.02$ m/s; b) $V_G = 0.05$ m/s, $V_L = 0.05$ m/s; c) $V_G = 0.02$ m/s, $V_L = 0.08$ m/s; d) $V_G = 0.08$ m/s, $V_L = 0.02$ m/s; $d = 0.5$ mm; phases: red ■, water; blue ■, air; Slug size is mainly controlled by the flow rate of each phase. When inlet velocities are 0.08 m/s, the largest slug sizes are obtained. For the same gas and liquid inlet velocities, slugs of similar size are obtained.

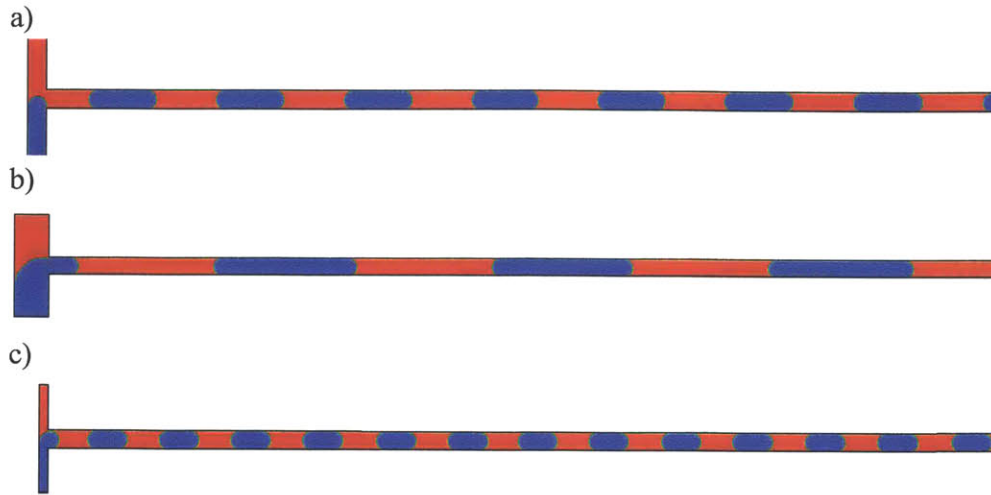


Figure 6.17: Effect of inlet channel width on slug length for $V_G = 0.02$ m/s, $V_L = 0.02$ m/s: a) $W = 0.5$ mm; b) $W = 1$ mm; c) $W = 0.25$ mm; $d = 0.5$ mm; phases: red ■, water; blue ■, air; Inlet channel dimension governs the slug size for constant inlet velocities. Increasing channel size increases the slug sizes of both phases.

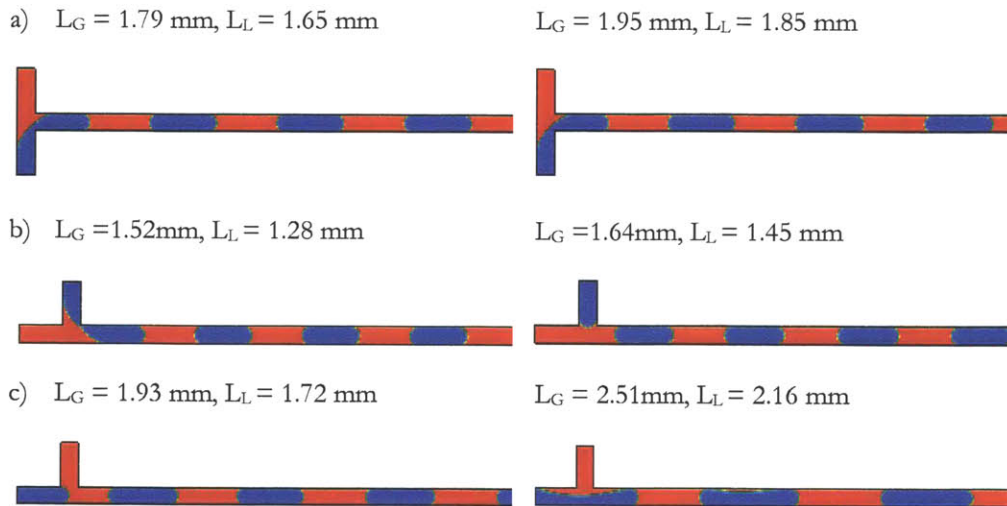


Figure 6.18: Effect of inlet configuration on slug length, simulations with interFoam, $V_G = 0.02$ m/s, $V_L = 0.02$ m/s; left, $cAlpha = 4$; right, $cAlpha = 1$; $d = 0.5$ mm; phases: red ■, water; blue ■, air; the effect of inlet configuration on slug size is not as strong as other factors such as inlet velocity of each phase and inlet channel dimension.

a) $L_G = 1.79 \text{ mm}$; $L_L = 1.65 \text{ mm}$



b) $L_G = 1.75 \text{ mm}$; $L_L = 1.60 \text{ mm}$

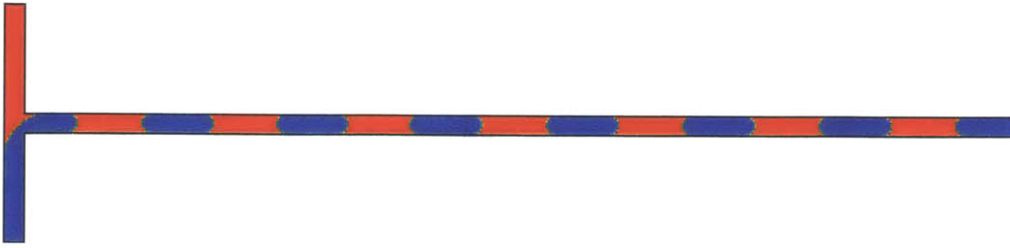
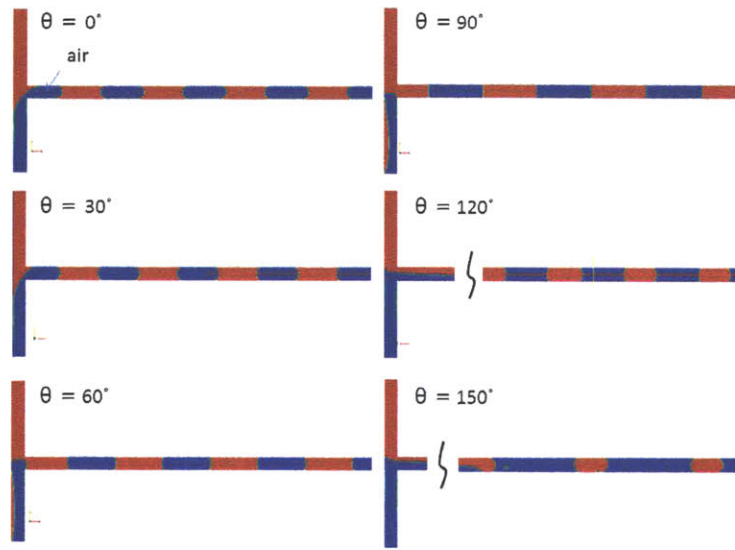


Figure 6.19: Effect of inlet channel length on slug length, simulations with OpenFOAM: a) short inlet channels; b) long inlet channels; interFoam, $c_{\text{Alpha}} = 4$; $d = 0.5 \text{ mm}$; phases: red ■, water; blue ■, air; The slug size is independent of the inlet channel length as long as the flow is fully developed.

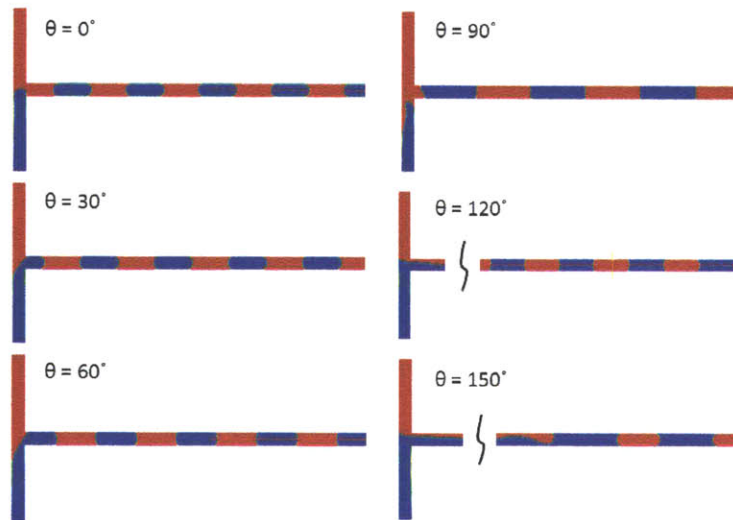
In addition, the effect of fluid properties and wetting characteristics on the slug flow can be easily studied using CFD simulations. Here the effect of contact angle, viscosity, density, and surface tension are studied.

The effect of contact angle is shown in Figure 6.20. Below 90° water wets the walls and air forms the slugs, while above 90° there is an inversion in the wetting phase: in this case, air wets the walls and slugs with convex edges of water are formed.

a)



b)



c)

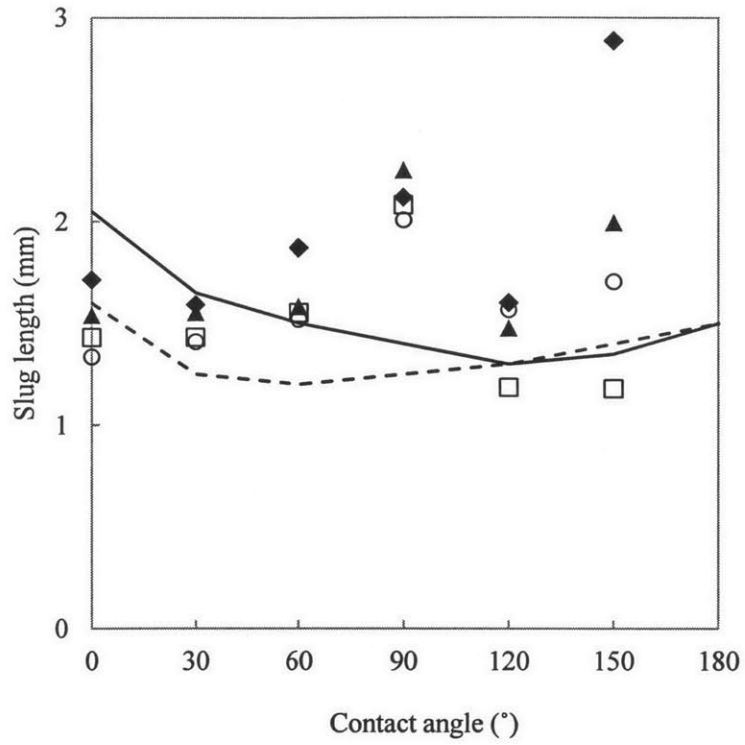
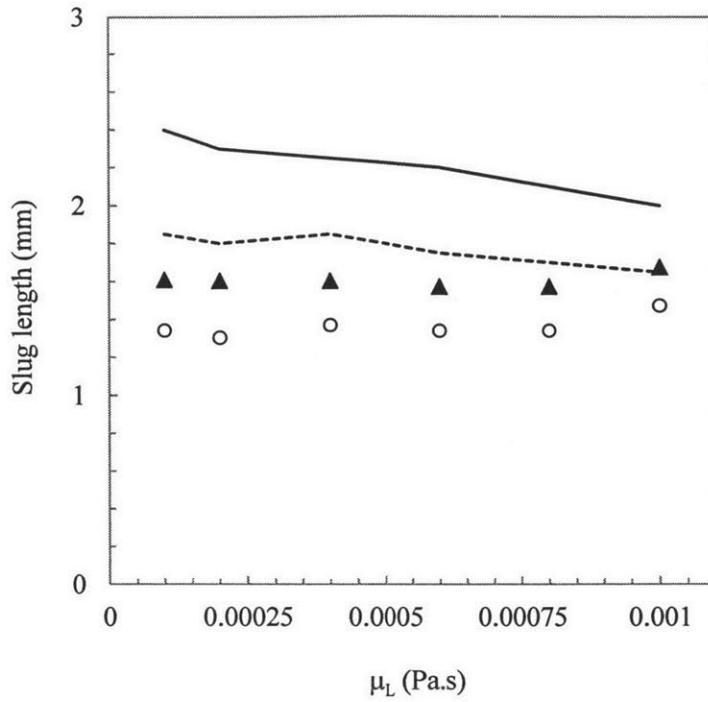
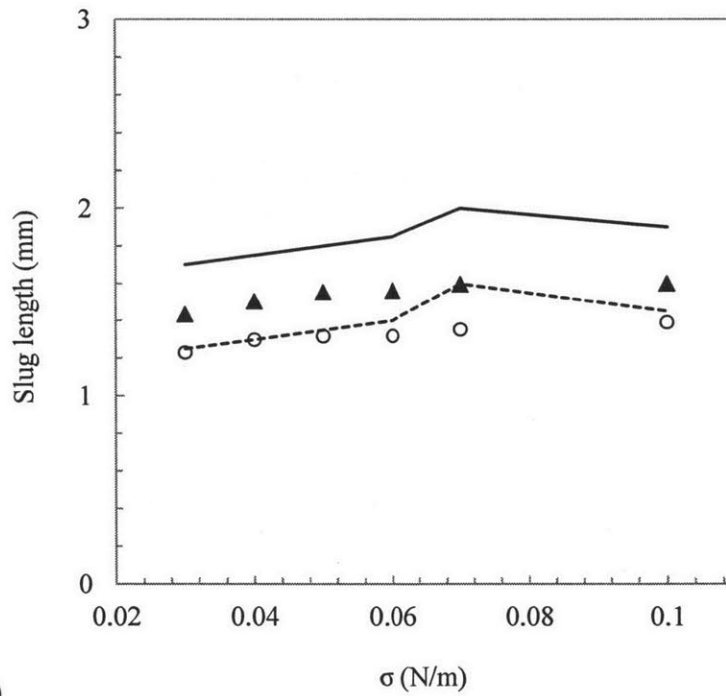


Figure 6.20: Effect of contact angle on slug flow and slug shape: a) interFoam, cAlpha = 1 ; b) interFoam, cAlpha = 4; c) comparison with literature values; legend: ---, liquid slug (Qian and Lawal); --, gas slug (Qian and Lawal); O, liquid slug cAlpha = 4; ▲, gas slug cAlpha = 4; □, liquid slug cAlpha = 1; ◆, gas slug cAlpha = 1;



a)



b)

Figure 6.21: Effect of a) liquid viscosity and b) interfacial tension on liquid and gas slug lengths. Legend: ---, liquid slug (Qian and Lawal); --, gas slug (Qian and Lawal); O, liquid slug $c\alpha = 4$; \blacktriangle , gas slug $c\alpha = 4$; Viscosity and interfacial tension have a negligible effect on the slug size for the interval tested.

According to the simulation results shown in Figure 6.21 a), the effect of liquid viscosity is negligible for this gas/liquid system. This is the same conclusion obtained by Qian and Lawal for the same gas/liquid system. However, other authors in the literature present experimental results and simulation results for different liquid/liquid systems and find that different viscosities can lead to different slug lengths. For instance, Cherlo et al (2010) ⁴⁶ show that the kerosene/water system presents larger water slugs than the coconut oil/water system due to the lower viscosity of kerosene with respect to coconut oil.

The simulation results shown in Figure 6.21 b) demonstrate that both liquid and gas slug lengths do not depend significantly on the surface tension for other fixed conditions (density, viscosity, contact angle, and flow rates were fixed). This is in accordance with results obtained in the literature, such as those presented by Qian and Lawal for gas/liquid systems, or the results presented by Cherlo et al. for a liquid/liquid system of kerosene and water and interfacial tension values ranging from 0.05 to 0.12 N/m.⁴⁶

Two-phase flows studied by Raj, R. et al⁴⁵

Another extensive study of two-phase flow, in this case, liquid-liquid flow, using CFD simulations is performed by Raj et al ⁴⁵ using Fluent. Here OpenFOAM is used to compare results with available ones in the literature, both experimental and computational. The simulations are performed in a structured mesh with the dimensions shown in Figure 6.22.

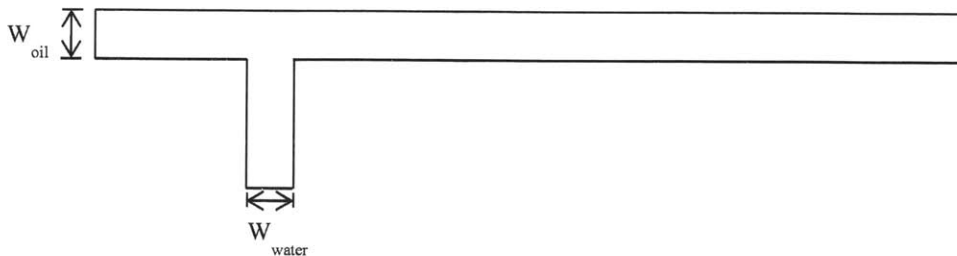


Figure 6.22: Microchannel geometry and computational grid, as shown by Raj et al. ⁴⁵

The simulations with OpenFOAM were first performed in a 2D structured mesh composed by 15,448 cells. Using as reference the geometry A, where $W_{oil} = 100 \mu\text{m}$, $W_{water} = 50 \mu\text{m}$, and $H = 33 \mu\text{m}$, the two-phase flow for oil/water was simulated with interFoam using a cAlpha value of 1. The CFD results are compared in Figure 6.23 with experimental values from Garstecki et al ⁴⁷, and the CFD results using Fluent published by Raj et al. By visual comparison, it is seen that the predictions using OpenFOAM are in agreement with both experiments and CFD results from Fluent, not only in the size and shape of the slugs formed, but also in the slug formation time. CFD results for a 3D mesh are also presented here. As expected, a 3D mesh captures better the interfacial effects, especially the contact angle at the top and the bottom walls of the T-junction. Since the height of the channel is only $33 \mu\text{m}$ the wall effects at small scales are important.

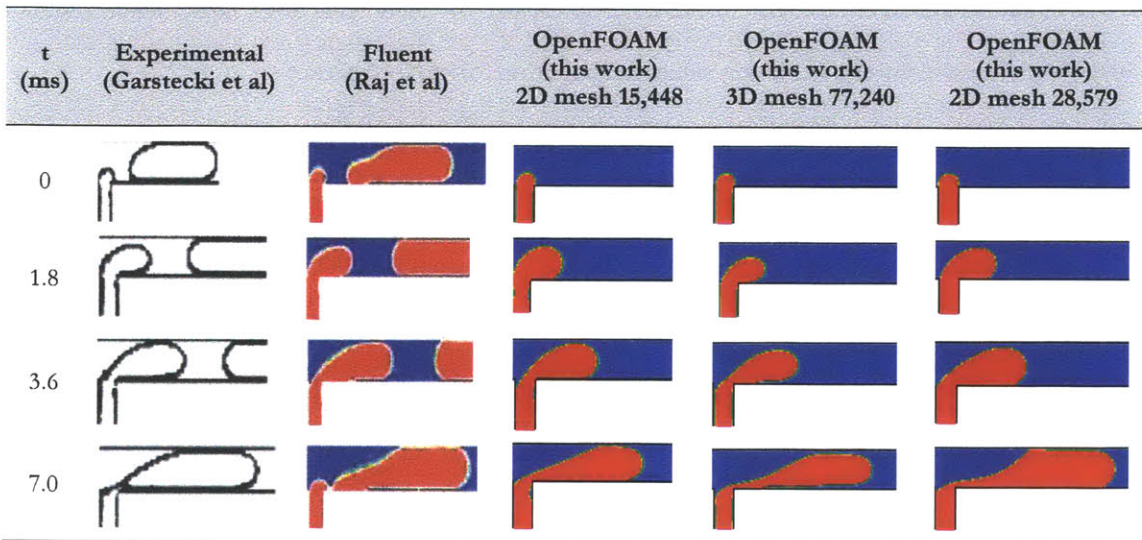


Figure 6.23: Comparison among Fluent (Raj et al ⁴⁵), OpenFOAM, and experimental results (Garstecki et al ⁴⁷) of slug formation for Geometry A, $Q_{water} = 0.14 \mu\text{L/s}$, $Q_{oil} = 0.083 \mu\text{L/s}$

A more detailed analysis is presented here for different combinations of oil and water flow rates. The effect of oil flow rate for a constant water flow rate is shown in Figure 6.24. It is observed that decreasing the oil flow rate changes both water and oil slug lengths: the oil slug length decreases, while the water slug length increases. There are differences in the predictions between Fluent and OpenFoam, although both are fairly

accurate. Note also here that 3D effects are important and differences in the predictions can be seen using a 3D mesh against a 2D mesh.

Q _{oil} (μL/s)	Source of data	Results
0.408	Experimental (Garstecki et al)	
	Fluent (Raj et al)	
	OpenFOAM, 2D mesh	
	OpenFOAM, 3D mesh	
0.124	Experimental (Garstecki et al)	
	Fluent (Raj et al)	
	OpenFOAM, 2D mesh	
	OpenFOAM, 3D mesh	
0.019	Experimental (Garstecki et al)	
	Fluent (Raj et al)	
	OpenFOAM, 2D mesh	
	OpenFOAM, 3D mesh	

Figure 6.24: Effect of oil flow rate on slug formation; comparison among experiments (Garstecki et al⁴⁷), Fluent (Raj et al⁴⁵), and OpenFOAM (this work, 2D mesh 15,448 cells, and 3D mesh 77,240 cells with 5 cells in Z); Geometry A, $Q_{\text{water}} = 0.14 \mu\text{L/s}$; a) $Q_{\text{water}}/Q_{\text{oil}} = 0.343$; b) $Q_{\text{water}}/Q_{\text{oil}} = 1.129$; c) $Q_{\text{water}}/Q_{\text{oil}} = 7.179$;

The effect of water flow rate for a constant water flow rate is shown in Figure 6.25. Increasing the water flow rate grows the water slug size, whereas the oil slug size is decreased significantly. The CFD results provided by Raj et al using Fluent are not accurate enough for the two largest water flow rates, whereas OpenFOAM is able to capture the slug formation with a fair accuracy in slug size prediction for both oil and water phases. However, varying some simulation parameters, such as the Courant number, mesh resolution, or numerical schemes, may improve the results. Indeed, in our simulations, it was observed that decreasing the Courant number from 0.5 to 0.1 for $Q_{\text{water}} = 0.050 \mu\text{L/s}$ and $Q_{\text{oil}} = 0.028 \mu\text{L/s}$, the results are improved and detachment of the droplet occurs as expected, as shown in Figure 6.26.

Q_{water} ($\mu\text{L/s}$)	Experimental (Garstecki et al)	Fluent (Raj et al)	OpenFOAM (this work, 3D mesh)
0.004			
0.050			
0.111			

Figure 6.25: Effect of water flow rate on slug formation; comparison among experiments (Garstecki et al), Fluent (Raj et al), and OpenFOAM (this work, 2D mesh); Geometry A, $Q_{\text{oil}} = 0.028 \mu\text{L/s}$; a) $Q_{\text{water}}/Q_{\text{oil}} = 0.143 \mu\text{L/s}$; b) $Q_{\text{water}}/Q_{\text{oil}} = 1.8 \mu\text{L/s}$; c) $Q_{\text{water}}/Q_{\text{oil}} = 3.96 \mu\text{L/s}$;

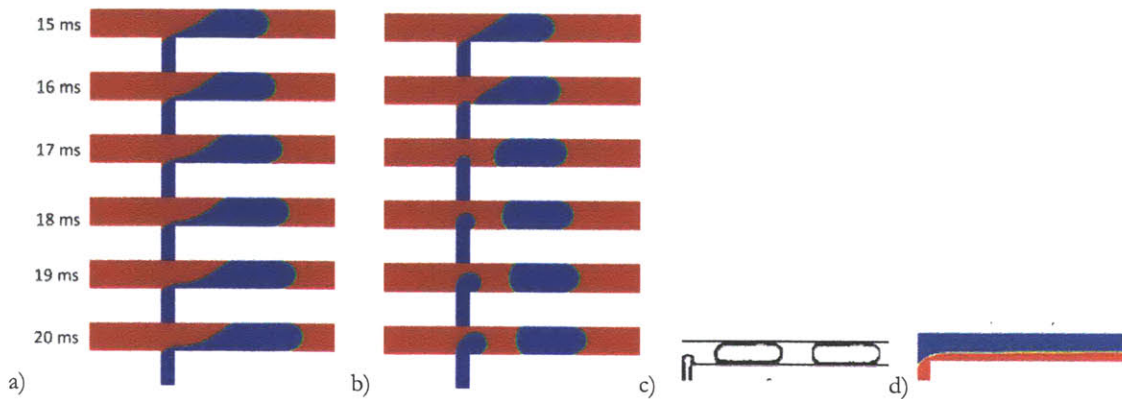


Figure 6.26: Effect of Courant number on slug formation. Geometry A, $Q_{\text{water}} = 0.050 \mu\text{L/s}$ and $Q_{\text{oil}} = 0.028 \mu\text{L/s}$. a) $Co = 0.5$; b) $Co = 0.1$; c) Experimental ⁴⁷; d) Fluent (Raj et al ⁴⁵)

The effect of contact angle (the specified value is the angle formed by the water phase with the wall) for constant water and oil flow rates is shown in Figure 6.27. It is observed that the flow patterns change with the contact angle. While the flow pattern is drop flow for contact angles between 120° and 180° and drop sizes slightly smaller at larger contact angles, for water wetting the walls, the flow patterns are closer to stratified flow. The CFD results obtained with OpenFOAM are very similar to the results shown by Raj et al using Fluent. Here it is shown as well that the simulations need to be 3D, especially for contact angles larger than 140° .

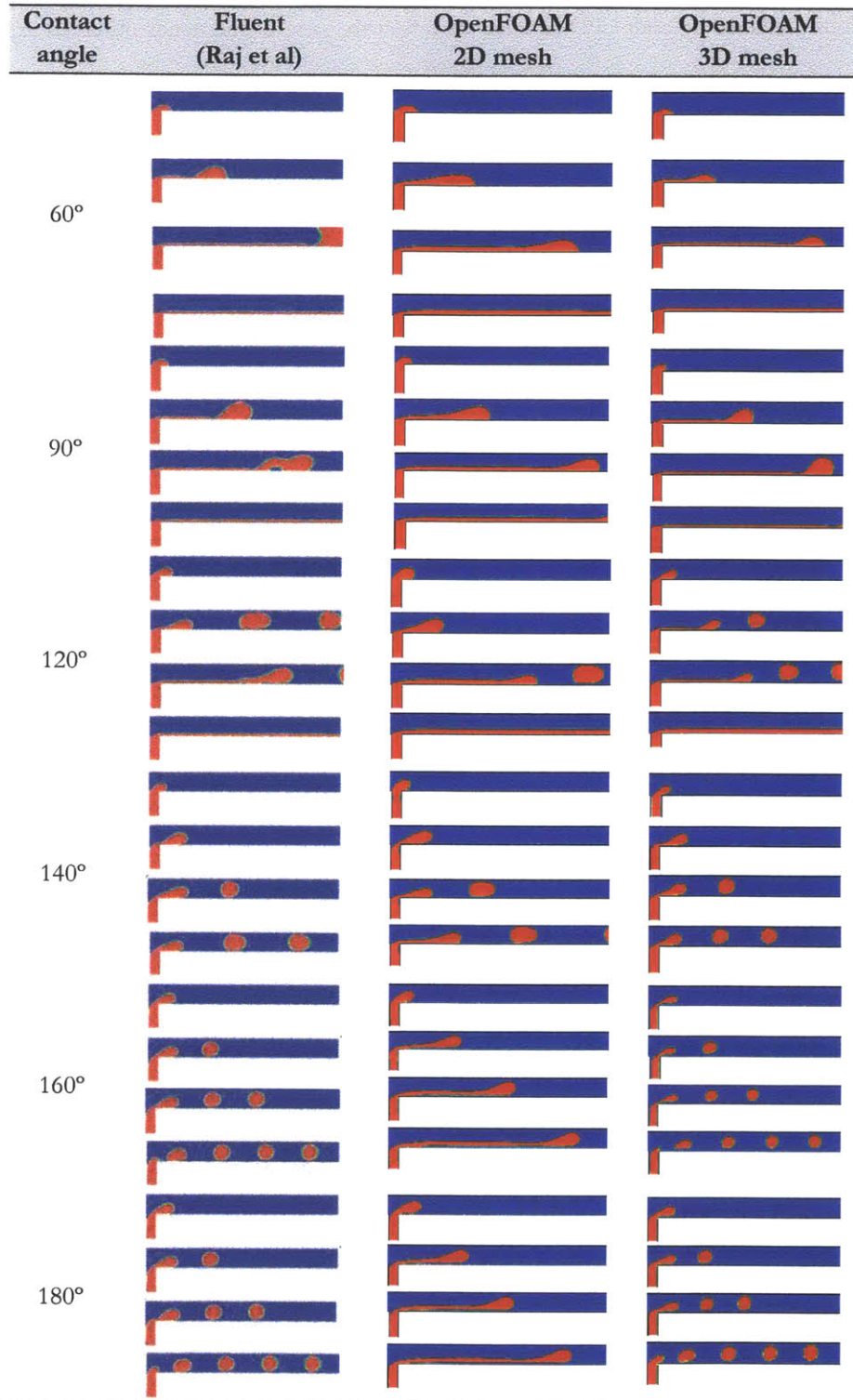


Figure 6.27: Effect of contact angle on slug formation; Geometry A, $Q_{\text{water}} = 0.14 \mu\text{L/s}$, $Q_{\text{oil}} = 0.408 \mu\text{L/s}$, $Q_{\text{water}}/Q_{\text{oil}} = 0.343$

The trends predicted by both CFD simulations reflect the same as the trends observed experimentally. Thus, we can conclude that even if the exact values of the slug sizes are not the same as the experimentally observed, the effect of each variable can be easily studied using computational tools.

Another interesting observation is the liquid film between the slug and the wall. Figure 6.28 shows that increasing the mesh resolution near the wall it is possible to predict the formation of a thin liquid film. In this particular case, increasing the number of cells of the width of the channel from 46 cells to 64 cells was sufficient to account for the liquid film.

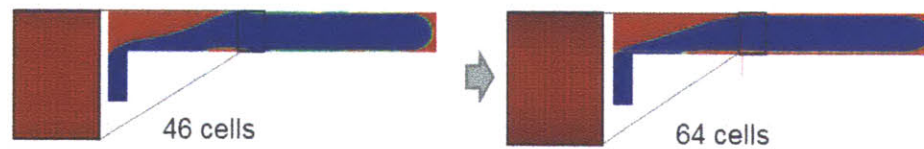


Figure 6.28: Effect of increasing mesh resolution on liquid film

The importance of having a high mesh resolution in order to capture the presence of the liquid film in CFD simulations has been studied by several authors (Taha et al. ³⁵, Qian et al. ⁴², Gupta et al. ⁴¹, Yu et al. ⁴⁸) in the literature. Gupta et al. ⁴¹ came to the conclusion that if the mesh size is $\frac{1}{4}$ of the liquid film thickness, it is possible to capture the liquid film. However, decreasing the cell size further may create artificial pressure jumps and spurious currents, creating non-physical results. For capillary numbers higher than 0.01 the liquid films are thicker and the results are in good agreement with the experiments. Horgue et al. ⁴⁹ performed a parametric study for low capillary numbers using Fluent. They concluded that having more than two cells in the liquid film does not improve the accuracy of the results. In addition, irregular meshes have a small influence on the results provided that the liquid film is covered by at least two cells. Thus, it is good practice to refine the mesh locally near the walls where the liquid film forms, which reduces computation times while increasing the accuracy locally.

Raj et al also studied the effect of changing the distributor configuration for a fixed phase inlet velocity and concluded that the slug length does not depend significantly on the distributor geometry for the flow rates and conditions tested. Here the results obtained with OpenFOAM are shown in Figure 6.29 and compared with the results obtained using Fluent by Raj et al. Similar results are obtained for the cross-flow and co-flow T-junctions, with slug lengths of 80 μm and 81 μm for water and 153 μm and 154 μm for oil. Slightly larger sizes are obtained in the Y-junction (101 μm and 212 μm , for water and oil, respectively).

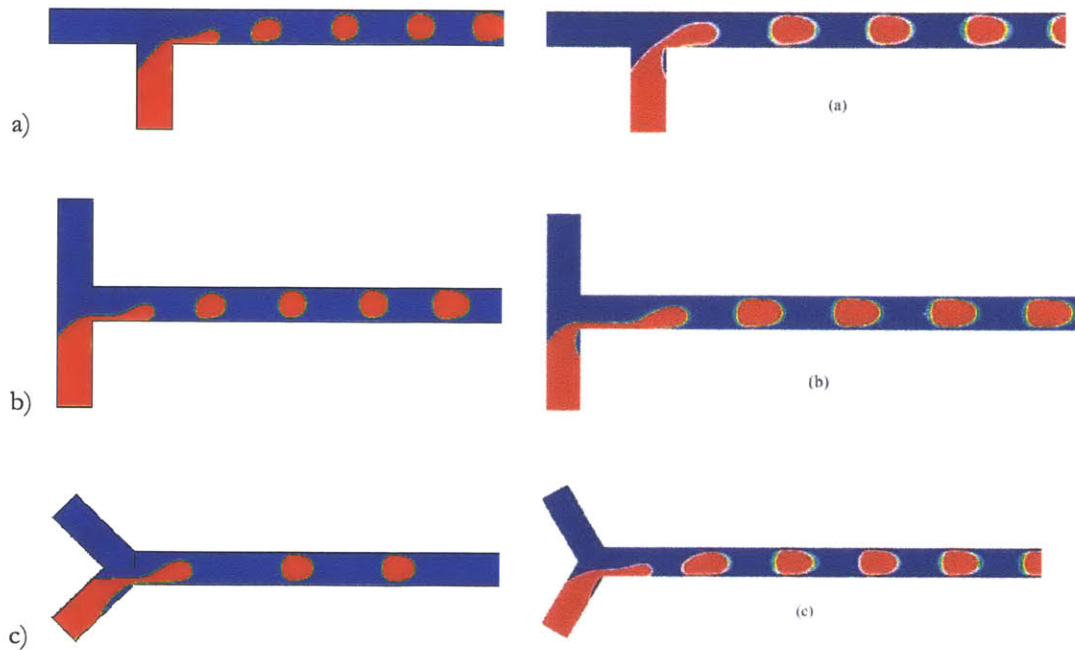


Figure 6.29: Effect of distributor configuration on slug formation, Geometry B, $Q_{\text{water}} = 0.14 \mu\text{L}/\text{s}$, $Q_{\text{oil}} = 0.408 \mu\text{L}/\text{s}$, $Q_{\text{water}}/Q_{\text{oil}} = 0.343$: a) cross-flow T-junction; b) co-flow T-junction; c) Y-junction

6.3.2 Application to the Advanced-Flow Reactor

The interFoam solver has been applied to the Advanced-Flow Reactor (AFR) for different fluid systems and the results of the CFD simulations have been compared with flow visualization images^{50, 51}. The objective for these simulations is to capture the flow patterns and the effects that are seen in the experiments by changing the flow rate of each phase. The mesh is composed by 251,320 hexahedral cells (10 cells in the z

direction) comprising two hearts of the AFR. This was necessary to reduce the computation time. A previous mesh resolution study was performed in order to determine the best grid that captures with accuracy the experimental observations while keeping reasonable computation times. In order to further reduce the computation time, the entrance of the AFR where each phase flows separately, was simulated independently using the simpleFoam solver for incompressible single-phase flow. The outlet of those simulation velocity profiles were used as input for the two-phase simulations with interFoam. In addition, it was necessary to set the boundary conditions for the volume fraction. Water was assigned a value for $\alpha = 1$, and the dispersed phase (carbon dioxide or water), a value of $\alpha = 0$. The boundary condition at the walls was a constant contact angle of 0° (water wetting phase). No-slip condition at the walls for velocity and zero gradient at the outlet were also used. For pressure, zero gradient at the inlet, fixed flux pressure at the walls, and fixed value at the outlet were specified. With all these considerations, the CFD simulations for carbon dioxide/water and hexane/water were performed.

Carbon dioxide/water CFD simulations are shown in Figure 6.30. It is assumed that the effect of reaction of carbon dioxide in water negligible, since the interFoam solver is not capable of accounting for reaction kinetics. This is a reasonable assumption when only simulating two heart cells of the AFR. In Figure 6.30 a), buoyancy effects are observed because of gravity acting towards the left. This effect is captured also in the simulations. Water being the heavier phase and carbon dioxide the lighter phase, have an effect on the flow patterns. Indeed, the Froude number (eq 6.25), which represents the ratio of inertia versus gravitational forces, is less than unity at these flow rates. The gas phase preferentially occupies the top half of the heart with occasional flow of small bubbles at the bottom, whereas if gravitational effects are not present (Figure 6.30 b), the gas phase alternatively flows through both sides.

$$Fr = \sqrt{\frac{v^2}{gH}} \quad (6.25)$$

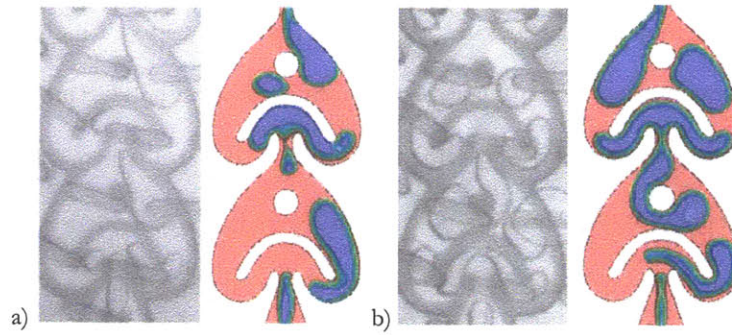


Figure 6.30: CFD simulations of carbon dioxide/water and comparison with experiments ⁵⁰. a) $Q_w = 10$, $Q_{CO_2} = 13.3$, vertical orientation; b) $Q_w = 10$, $Q_{CO_2} = 20.8$, horizontal orientation;

As shown in Figure 6.31, the detachment point is well captured by the CFD simulations, being located between the point at which the two phases get in contact and the inlet to the heart cell. The shape of the bubbles is also well captured by interFoam. The shape is distorted by the presence of obstacles along the path length of the AFR. In addition, both in the simulations and the experimental images, it was observed that carbon dioxide was always the dispersed phase, regardless of the relative flow rates of each phase. This is due to the hydrophilic walls which keep the water wetting them along the entire flow path. The wetting properties of the material are introduced through the contact angle in the simulations, which in this case was set to 0° . It will be shown in later subsections how the properties of the fluids, including the contact angle, affect the flow patterns and, in consequence, the mass transfer rates.

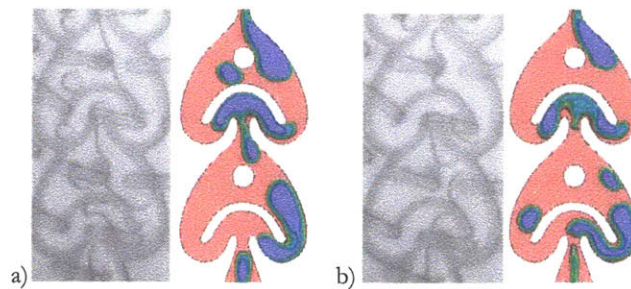


Figure 6.31: Detail of detachment point at different times for carbon dioxide/water system. $Q_w = 10$, $Q_{CO_2} = 13.3$, vertical orientation;

The second system to consider is hexane/water. Characteristic images of the transient flow for CFD simulations and experiments are shown in Figure 6.32 for different water and hexane flow rates. Similarly to the carbon dioxide/water system, water is also the wetting phase due to the hydrophilic walls of the AFR, regardless of the flow rates ($\theta = 0^\circ$). This does not happen always in conventional vessels, where wall effects are not important. An inversion of phases normally occurs at certain phase flow rates, where the continuous phase is no longer continuous and starts to form dispersed droplets.

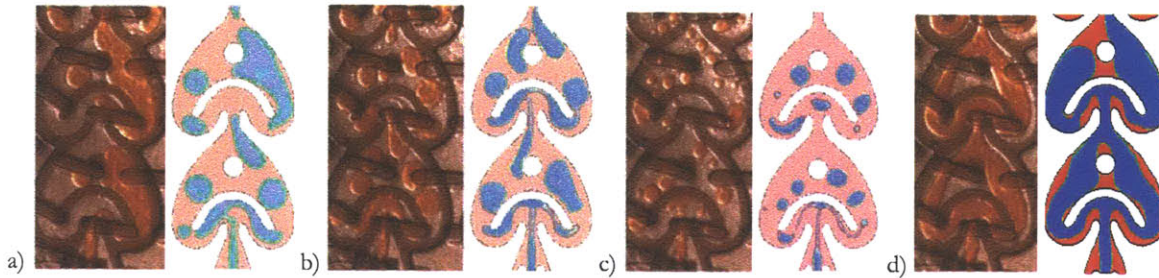


Figure 6.32: CFD simulations of hexane/water and comparison with experiments ⁵¹. Phase flow rate (mL/min): a) $Q_w = 10, Q_h = 10$; b) $Q_w = 20, Q_h = 20$; c) $Q_w = 40, Q_h = 10$

The CFD simulations are in good agreement with the experimental results, as seen in Figure 6.32. It is seen that interFoam is able to capture the effect of flow rates on the droplet size. For instance, increasing the phase flow rate from 10 mL/min to 20 mL/min reduces the droplet size significantly. Increasing the continuous phase flow rate from 10 to 40 mL/min for a fixed hexane flow rate (10 mL/min) reduces the droplet size further and also decreases the hexane holdup. Increasing the flow rate of the hexane phase from 10 to 40 mL/min for a fixed water flow rate (10 mL/min) increases the hexane holdup, what is advantageous from the point of view of having a larger specific interfacial area. However, no breakup occurs and most part of the heart is occupied by the hexane phase, therefore reducing the specific interfacial area with respect to other cases.

More difficulties are observed at higher flow rates (40, 60, and 80 mL/min of each phase), where the degree of breakup seen in the simulations is smaller than in the experiments. There is artificial coalescence of droplets in the simulations due to the proximity of droplets that are within one grid cell distance. This

problem is not observed in the carbon dioxide/water system, where the effect of coalescence is physically observed in the experiments. The current method used in the simulations does not prevent the coalescence between droplets when they are closer than a mesh cell. In principle, increasing the mesh resolution would solve this problem. However, these two-phase simulations are computationally very expensive and decreasing the grid cell size would increase the computation time further becoming an inefficient process. This is one of the disadvantages of VOF methods, which are known to require fine meshes in order to capture all the effects that occur at small scales. Development of a simulation method based on the VOF approach that can handle this problem is out of the scope of this work, but would be a topic of interest for many applications.

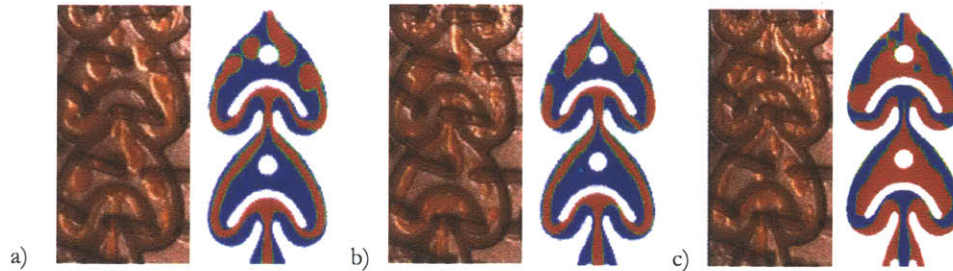


Figure 6.33: CFD simulations of hexane/water and comparison with experiments ⁵¹. Phase flow rate (mL/min): a) $Q_w = 40$, $Q_h = 40$; b) $Q_w = 60$, $Q_h = 60$; c) $Q_w = 80$, $Q_h = 80$

6.4 Conclusions

OpenFOAM has been demonstrated to be a powerful CFD tool capable of predicting two-phase flow in simple and complex geometries using interFoam, a solver based on the volume-of-fluid method (VOF). Validation with standard test cases, such as the stagnant bubble, rising bubble in a stagnant liquid, and flow through T-junctions and microchannels, was performed. Comparison of the predictions was done with existing simulations and experimental results available in the literature. Good performance of the interFoam solver and comparable to other commercial softwares was demonstrated. The challenges of simulating two-phase flow with a VOF approach were also illustrated with examples and best practices to achieve good numerical predictions were presented. Some of this include: sufficiently high mesh resolution, especially near

the walls, to capture the formation of liquid films; low Courant numbers to capture detachment accurately; sufficiently long inlet channels to eliminate entrance effects; selection of proper compression term in interFoam or use of different alternative approaches to reduce spurious currents.

The interFoam solver was applied to simulate two-phase flow in the Advanced-Flow Reactor. Carbon dioxide/water and hexane/water systems were simulated and CFD results were compared with the flow patterns observed using flow visualization techniques. The CFD simulations were in good agreement with the experiments in terms of flow patterns and detachment point at the inlet of the reactor for low flow rates. Larger discrepancies were observed in the prediction of flow patterns for hexane/water system, at the largest flow rates. The differences between CFD results and experiments are attributed to an excess of numerical coalescence of droplets that are closer than one grid cell.

6.5 Notation

a	specific interfacial area (m^2/m^3)
A	area (m^2)
\tilde{c}	color function (-)
c	indicator function (-)
C_{pc}	interface sharpening factor (-)
C_r	compression term (-)
d_B	bubble diameter (m)
d	channel diameter (m)
D_h	hydraulic diameter (m)
F_{sv}	surface tension body force (N/m^2)
F_{sa}	surface tension force (N/m)
f'	modified body force (Pa/m)

f_c	capillary body force (Pa/m)
g	gravity (m/s ²)
h	interface thickness (m)
H	channel height (m)
k_i	kinetic constant of direct reaction in phase i ($i= 1, 2, 12$)
k_{revi}	kinetic constant of reverse reaction in phase i ($i= 1, 2, 12$)
k_L	individual mass transfer coefficient (m/s)
k_{Lg}	individual mass transfer coefficient (m/s)
n_i	normal vector to interface (-)
n_k	tangential vector to interface (-)
n_f	normal vector of the cell surface (-)
\hat{n}_w	normal vector to the wall (-)
P	pressure (Pa)
p_d	dynamic pressure (Pa)
p_c	capillary pressure (Pa)
S_f	cell surface area (m ²)
t	time (s)
\hat{t}_w	tangential vector to the wall (-)
Δt	time step (s)
Δx	cell size (m)
\vec{v}	velocity vector (m/s)
\vec{v}_r	relative velocity (m/s)
v_{max}	maximum velocity (m/s)
V_G	velocity of gas phase (m/s)
V_L	velocity of liquid phase (m/s)

V	volume (m^3)
W_{water}	width of water inlet channel (m)
W_{oil}	width of oil inlet channel (m)

Dimensionless numbers

Re	Reynolds number (-)
Eo	Eötvös number (-)
Ca	Capillary number (-)
We	Weber number (-)
Co	Courant number (-)
Fr	Froude number (-)
Sc	Schmidt number (-)

Greek letters

α	volume fraction (-)
$\tilde{\alpha}_p$	smoothed volume fraction (-)
ρ	density (kg/m^3)
κ	curvature ($1/\text{m}$)
θ_w	contact angle ($^\circ$)
τ_μ	time step limit based on viscous term (s)
τ_ρ	time step limit based on inertial term (s)
φ	mass flux ($\text{mol m}^{-2} \text{s}^{-1}$)
σ	surface tension (N/m)
μ	viscosity (Pa s)

Superscripts

L	Liquid phase
G	Gas phase

Subscripts

1	phase 1
2	phase 2
12	interface
CO ₂	carbon dioxide
f	face index
G	gas
h	hexane
L	liquid
p	cell index
w	water
oil	oil phase

6.6 References

- (1) Danckwerts, P. V. Significance of liquid–film coefficients in gas-absorption. *Ind. Eng. Chem.*, **1951**, *43*, 6, 1460–1467
- (2) Wörner, M. Numerical modeling of multiphase flows in microfluidics and micro process engineering: a review of methods and applications. *Microfluid Nanofluid*, **2012**, *12*, 841–886
- (3) Trontin, P.; Vincent, S.; Estivalezes, J-L.; Caltagirone, J-P. Detailed comparisons of front-capturing methods for turbulent two-phase flow simulations. *Int. J. Num. Meth.Fluids*, **2008**, *56*, 1543–1549
- (4) Changa, Y. C.; Houa, T. Y.; Merriman, B.; Osher, S. Level set formulation of Eulerian interface capturing methods for incompressible fluid flows. *J. Computational Physics*, **1996**, *124*, Issue 2, 449–464

- (5) Unverdi, S. O.; Tryggvason, G. A front-tracking method for viscous, incompressible, multi-fluid flows. *J. Computational Physics*, **1992**, *100*, Issue 1, 25–37
- (6) Anderson, D. M.; McFadden, G. B.; Wheeler, A. A. Diffuse-interface methods in fluid mechanics. *Annu. Rev. Fluid Mech.*, **1998**, *30*, 139–65
- (7) Denis Gueyffier, D.; Li, J.; Nadim, A.; Scardovelli, R.; Zaleski, S. Volume-of-fluid interface tracking with smoothed surface stress methods for three-dimensional flows. *J. Computational Physics*, **1999**, *152*, 423–456
- (8) Olsson, E.; Kreiss, G. A conservative level set method for two phase flow. *Journal of Computational Physics*, **2005**, *210*, 1, 225–246
- (9) Jacqmin, D. Calculation of two-phase Navier–Stokes flows using phase-field modeling. *J. Computational Physics*, **1999**, *155*, Issue 1, 96–127
- (10) Jasak, H.; Weller, H. G. Interface tracking capabilities of the inter-gamma differencing scheme. Department of Mechanical Engineering, *Imperial College*, **1995**, London
- (11) OpenFOAM Website: www.openfoam.org. Accessed on 03/15/2014
- (12) Rusche, H. CFD of dispersed two-phase flows at high phase fractions. PhD Thesis, *Imperial College*, **2002**, London
- (13) Brackbill, J. U.; Kothe, D. B.; Zemach, C. A continuum method for modeling surface tension. *J. Computational Physics*, **1992**, *100*, 335–354
- (14) Deshpande, S. S.; Anumolu, L.; Trujillo, M. F. Evaluating the performance of the two-phase flow solver interFoam. *Computational Science & Discovery*, **2012**, *5*(1), 014016
- (15) Hoang, D. A.; Van Steijn, V.; Portela, L. M.; Kreutzer, M. T.; Kleijn, C. R.; Simos, T. E.; Anastassi, Z. Modeling of low-capillary number segmented flows in microchannels using OpenFOAM. In *AIP Conference Proceedings-American Institute of Physics*, **2012**, *1479*, 1, 86–89
- (16) Raees, F., Van der Heul, D. R.; Vuik, C. Evaluation of the interface-capturing algorithm of OpenFoam for the simulation of incompressible immiscible two-phase flow. *Reports of the Department of Applied Mathematical Analysis*, REPORT 11-07. Delft University of Technology, **2011**, ISSN 1389-6520
- (17) Raeini, A. Q.; Blunt, M. J.; Bijeljic, B. Modelling two-phase flow in porous media at the pore scale using the volume-of-fluid method. *J. Computational Physics*, **2012**, *231*, 17, 5653–5668.
- (18) Meier, M.; Yadigaroglu, G.; Smith, B. L. A novel technique for including surface tension in PLIC-VOF methods. *Eur. J. Mech. B/Fluids*, **2002**, *21*, 61–73
- (19) Francois, M. M.; Cummins, S. J.; Dendy, E. D.; Kothe, D. B.; Sicilian, J. M.; Williams, M. W. A balanced-force algorithm for continuous and sharp interfacial surface tension models within a volume tracking framework. *J. Computational Physics*, **2006**, *213*, 141–173

- (20) Aulisa, E.; Manservigi, S.; Scardovelli, R. A novel representation of the surface tension force for two-phase flow with reduced spurious currents. *Comput. Methods Appl. Mech. Engrg.*, **2006**, *195*, 6239–6257
- (21) Tong, A. Y.; Wang, Z. A numerical method for capillarity-dominant free surface flows. *J. Computational Physics*, **2007**, *221*, 506–523
- (22) Harvie, D. J. E.; Davidson, M.R.; Rudman, M. An analysis of parasitic current generation in Volume of Fluid simulations. *Applied Mathematical Modelling*, **2006**, *30*, 1056–1066
- (23) Gerlach, D.; Tomar, G.; Biswas, G.; Durst, F. Comparison of volume-of-fluid methods for surface tension-dominant two-phase flows. *International Journal of Heat and Mass Transfer*, **2006**, *49*, 740–754
- (24) Galusinski, C.; Vigneaux, P. On stability condition for bifluid flows with surface tension: Application to microfluidics. *Journal of Computational Physics*, **2008**, *227*, 6140–6164
- (25) Liovic, P.; Francois, M.; Murray Rudman, M.; Manasseh, R. Efficient simulation of surface tension-dominated flows through enhanced interface geometry interrogation. *Journal of Computational Physics*, **2010**, *229*, 7520–7544
- (26) Albadawi, A.; Donoghue, D.B.; Robinson, A.J.; Murray, D.B. Delauré, Y.M.C. Influence of surface tension implementation in Volume of Fluid and coupled Volume of Fluid with Level Set methods for bubble growth and detachment. *International Journal of Multiphase Flow*, **2013**, *53*, 11–28
- (27) Renardy, Y.; Renardy, M. PROST: A parabolic reconstruction of surface tension for the Volume-of-Fluid method. *J. Computational Physics*, **2002**, *183*, 400–421
- (28) Hoang, D. A.; van Steijn, V.; Portela, L. M.; Kreutzer, M. T.; Kleijn, C. R. Benchmark numerical simulations of segmented two-phase flows in microchannels using the Volume of Fluid method. *Computers & Fluids*, **2013**, *86*, 28–36
- (29) Clift, R.; Grace, J. R.; Weber, M. E. Bubbles, drops, and particles. *Academic Press*, **1978**, New York, page 172
- (30) Duineveld, P. C. The rise velocity and shape of bubbles in pure water at high Reynolds number. *J. Fluid Mech.*, **1995**, *292*, 325–332
- (31) Cano-Lozano, J. C.; Bohorquez, P.; Martinez-Bazan. Numerical simulation of a bubble rising in still liquids: determination of the instability transition modes. *Numerical Methods for Hyperbolic Equations: Theory and Applications*. An international conference to honour Professor E.F. Toro. University of Santiago de Compostela, 4-8 July **2011**, Spain
- (32) Hoang, D. A.; Portela, L. M.; Kleijn, C. R.; Kreutzer, M. T.; van Steijn, V. Dynamics of droplet breakup in a T-junction. *J. Fluid Mech.*, **2013**, *717*, R4 C. Cambridge University Press 2013 717 R4-1 doi:10.1017/jfm.2013.18
- (33) Plouffe, P.; Macchi, A.; Donaldson, A. A. Enhancement of interphase transport in mini-microscale applications using passive mixing. *Heat Transfer Engineering*, **2013**, *34*, (2–3), 159–168

- (34) Semyonov, D.; Ratchananusorn, W.; Turunen, I. Hydrodynamic model of a microstructured plate reactor. *Computers and Chemical Engineering*, **2013**, *52*, 145–154
- (35) Taha, T.; Cui, Z. F. CFD modelling of slug flow in vertical tubes. *Chem. Eng. Sci.*, **2006**, *61*, 676–687
- (36) Zheng, D.; He, X.; Che, D. CFD simulations of hydrodynamic characteristics in a gas–liquid vertical upward slug flow. *International Journal of Heat and Mass Transfer*, **2007**, *50*, 21–22, 4151–4165
- (37) Kashid, M. N.; Renken, A.; Kiwi-Minsker, L. CFD modelling of liquid–liquid multiphase microstructured reactor: Slug flow generation. *Chem. Eng. Res. Design*, **2010**, *88*, 362–368
- (38) Kashid, M. N.; Agara, D. W.; Turek, S. CFD modelling of mass transfer with and without chemical reaction in the liquid–liquid slug flow microreactor. *Chem. Eng. Sci.*, **2007**, *62*, 5102–5109
- (39) Shao, N.; Salman, W.; Gavrilidis, A.; Angeli, P. CFD simulations of the effect of inlet conditions on Taylor flow formation. *International Journal of Heat and Fluid Flow*, **2008**, *29*, 1603–1611
- (40) Shao, N.; Gavrilidis, A.; Angeli, P. Mass transfer during Taylor flow in microchannels with and without chemical reaction. *Chem. Eng. J.*, **2010**, *160*, 873–881
- (41) Gupta, R.; Fletcher, D. F. Haynes, B. S. On the CFD modelling of Taylor flow in microchannels. *Chem. Eng. Sci.*, **2009**, *64*, 2941–2950
- (42) Qian, D.; Lawal, A. Numerical study on gas and liquid slugs for Taylor flow in a T-junction microchannel. *Chem. Eng. Sci.*, **2006**, *61*, 7609–7625
- (43) Santos, R. M.; Kawaji, M. Numerical modeling and experimental investigation of gas–liquid slug formation in a microchannel T-junction. *International Journal of Multiphase Flow*, **2010**, *36*, 314–323
- (44) Asadolahi, A. N.; Gupta, R.; Leung, S. S.Y.; Fletcher, D. F.; Haynes, B. S. Validation of a CFD model of Taylor flow hydrodynamics and heat transfer. *Chem. Eng. Sci.*, **2012**, *69*, 541–552
- (45) Raj, R.; Mathur, N.; Buwa, V. V. Numerical simulations of liquid-liquid flows in microchannels. *Ind. Eng. Chem. Res.*, **2010**, *49* (21), 10606–10614
- (46) Cherlo, S. K. R.; Kariveti, S.; Pushpavanam, S. Experimental and numerical investigations of two-phase (liquid-liquid) flow behavior in rectangular microchannels. *Ind. Eng. Chem. Res.* Vol., **2010**, *49* (2), 893–899
- (47) Garstecki, P.; Fuerstman, M. J.; Stone, H. A.; Whitesides, G. M. Formation of droplets and bubbles in a microfluidic T-junction-scaling and mechanism of break-up. *Lab Chip*, **2006**, *6*, 437–446.
- (48) Yu, Z., Hemminger, O., and Fan, L.S. Experiment and lattice Boltzmann simulation of two-phase gas–liquid flows in microchannels. *Chem. Eng. Sci.*, **2007**, *62* (24), 7172–7183.

- (49) Horgue, P.; Augier, F.; Quintard, M.; Prata, M. A suitable parametrization to simulate slug flows with the volume-of-fluid method. *C. R. Mecanique*, **2012**, *340* (6), 411–419
- (50) Nieves–Remacha, M. J.; Kulkarni, A. A.; Jensen, K. F. Gas–liquid flow and mass transfer in an Advanced-Flow Reactor. *Ind. Eng. Chem. Res.* **2013**, *52* (26), 8996 – 9010
- (51) Nieves–Remacha, M. J.; Kulkarni, A. A.; Jensen, K. F. Hydrodynamics of liquid–liquid dispersion in an Advanced-Flow Reactor. *Ind. Eng. Chem. Res.* **2012**, *51* (50), 16251–16262

7 Computational fluid dynamic simulations: modeling mass transfer between immiscible phases in the Advanced-Flow Reactor

7.1 Abstract

This chapter is focused on modeling species mass transfer across an interface between immiscible fluids using the volume-of-fluid method and OpenFOAM. Modification of the original `interFoam` solver based on existing models is performed. After successful validation with test cases that can be solved analytically and/or with Matlab, the solver is applied to simulate mass transfer in the Advanced-Flow Reactor at different flow rates and ambient temperature and pressure. The CFD results are shown in terms of bulk concentration in the dispersed phase, average drop size, specific interfacial areas, dispersed phase holdup, and individual and overall mass transfer coefficients. Comparison with the observations in flow visualization experiments showed good agreement between experimental and CFD results, with larger discrepancies present at the largest flow rates. Mass transfer coefficients were compared with semiempirical values based on the surface renewal theory of Danckwerts and the largest discrepancies were attributed to a poor prediction of the specific interfacial areas at the largest flow rates. In addition, study of the influence of fluid properties and reactor design is also performed. It was concluded that the most influencing variable on the flow patterns was the contact angle (wetting properties) and the surface tension had a strong effect on the average drop size. The effect of reactor design for the conditions tested was concluded to be non-significant.

7.2 Introduction

The `interFoam` solver available in OpenFOAM is able to determine flow patterns and streamlines for two-phase flow. However, in most chemical engineering problems, it is important to determine mass transfer of components between two immiscible phases. Thus, in addition to the momentum conservation equation coupled with the advection equation for the volume phase fraction, an additional species conservation equation needs to be solved. In addition, the boundary conditions for concentration jump and flux continuity

at the interface need to be satisfied. The challenge is how to incorporate the boundary conditions which are only effective at the interface (2D effect) within the entire formulation of one-equation for the entire domain (3D effect) in the context of VOF method.

Investigations about modeling mass transfer using the VOF method are very few, and the first ones had the limitation of being applicable only for constant concentrations across the interface. Ohta and Suzuki ¹ first studied mass transfer from a drop in a solvent extraction process. Sato et al ² simulated in 3D the mass transfer process of liquid carbon dioxide single rising droplets in the continuous phase water using a front capturing method, Davidson and Rudman ³ developed a method to simulate in 2D heat and mass transfer between interfaces, and only for continuous equilibrium concentrations between phases; but it was Bothe et al. ⁴ who in 2003 started modeling mass transfer of oxygen from single bubbles and bubble chains rising in aqueous solutions using VOF method and considering equilibrium of concentrations across interfaces based on Henry's law. In 2006, Onca et al.⁵ developed a method based on VOF approach also based in Henry's law to simulate conjugate mass transfer of dilute species accounting for the concentration jump. After validation of the method, application to qualitative investigation of mass transfer in upward bubble train flow within square and rectangular channels is performed. Although their code is not restricted to low Schmidt (Sc) numbers, for large Sc , very fine mesh resolution in order to account for the thin concentration boundary layer need to be used.

Another approach is that followed by Haroun et al. ^{6,7} that combines VOF approach with transport of species across interfaces with application to stable liquid films and structured packing. More recently, Marschall et al. ⁸ developed an algorithm to solve for mass transfer of species across interfaces in free-surface flows using OpenFOAM. In order to capture the concentration jump at the interface, both approaches consider that the solubility is determined by Henry's law with a constant coefficient. Haroun et al. demonstrated that their method is effective and accurate for planar interfaces, however, modifications of the basic algorithm is required in order to diminish the spurious concentration fluxes that arise at curved interfaces. Here we present the implementation of Haroun et al. approach in OpenFOAM and compare it

with the implementation of Marschall et al. using simple validation cases. This solver is later applied to the Advanced-Flow Reactor for determination of mass transfer coefficients.

7.3 Implementation of solver

The implementation of HarounScalarTransportFoam and MarschallScalarTransportFoam are based on the ScalarTransportFoam solver which is already available in OpenFOAM to solve mass transfer of a passive scalar in single-phase flow. This solver solves a species conservation equation in which the velocity profile is fixed over time. The HarounScalarTransportFoam and MarschallScalarTransportFoam solvers are similar to the formulation of ScalarTransportFoam. They consider fixed velocity profiles and phase volume fraction fields (which can be set initially in the specific case or can be solved in a first simulation stage using interFoam).

The species conservation equation that needs to be solved is given by eq 7.1.

$$\frac{\partial C_i}{\partial t} + \nabla \cdot (\vec{v}C_i) = \nabla(D_i \nabla C_i) \quad (7.1)$$

The boundary conditions that need to be satisfied at the interface are described by eq 7.2 and 7.3:

$$He = C_i^L / C_i^G \quad (7.2)$$

$$D_i^L \nabla C_i^L = D_i^G \nabla C_i^G \quad (7.3)$$

The approach followed by Haroun et al. considers one-fluid variables in the interface region for concentration and diffusion coefficients defined by eq 7.4 and 7.5 and a concentration flux defined by eq 7.6.

$$C_i = \alpha C_i^L + (1 - \alpha) C_i^G \quad (7.4)$$

$$D_i = \alpha D_i^L + (1 - \alpha) D_i^G \quad (7.5)$$

$$J_i^L = J_i^G \quad (7.6)$$

The concentration flux expression eq 7.7 is different from the conventional one after the definition of these variables at the interface. As it can be seen, the second term is zero within the domain of each phase separately, and is different from zero only at the interface.

$$J_i = -D_i(\alpha \nabla C_i^L + (1 - \alpha) \nabla C_i^G) = -D_i \nabla C_i + D_i(C_i^L - C_i^G) \nabla \alpha \quad (7.7)$$

Reformulating in terms of the Henry constant, eq 7.8 is obtained. The second term vanishes as well for Henry constant equal to 1.

$$J_i = -D_i \nabla C_i + D_i \left(\frac{C_i (1 - He)}{\alpha + He(1 - \alpha)} \right) \nabla \alpha \quad (7.8)$$

An additional study showed that the harmonic average of the diffusion coefficient (eq 7.9) behaved better than the conventional linear average based on the volume phase fraction α .

$$D_i = \frac{D_i^L D_i^G}{\alpha D_i^L + (1 - \alpha) D_i^G} \quad (7.9)$$

The approach of Marschall et al. (2012) is slightly different. It is based on conditioning and volume-averaging of species conservation equation (eq 7.10) with a definition of molar mixture concentration expressed by eq 7.11.

$$\overline{I_L \frac{\partial C_i}{\partial t}} + \overline{I_L \nabla \cdot (\vec{v} C_i)} = \overline{I_L \nabla (D_i \nabla C_i)} \quad (7.10)$$

$$C_i \approx \frac{D_i^L \alpha C_i^L + D_i^G (1 - \alpha) C_i^G}{D_i^L \alpha + (1 - \alpha) D_i^G} \quad (7.11)$$

The final equation valid within the entire domain containing the interface is described by eq 7.12.

$$\frac{\partial C_i}{\partial t} + \nabla \cdot (C_i \vec{v}) = \nabla \cdot (D_i \nabla C_i) + \nabla \cdot (C_i \nabla D_i) - \nabla \cdot \left[\left(\frac{D_i^G - D_i^L / He}{\alpha + (1 - \alpha) / He} \right) C_i \nabla \alpha \right] \quad (7.12)$$

Both formulations have been implemented in OpenFOAM and here we present a comparison of the performance of both solvers. Table 7.1 includes the code within the main solver and the main differences in

the formulations can be observed. In the 'createFields.H' file, the additional variables required to describe the system are also included (concentration field, diffusion coefficients in each phase, diffusion coefficient at the interface, Henry constant).

Table 7.1: CEqn.H including species conservation equation for solver including mass transfer using approaches of Haroun ^{6,7} and Marschall ⁸

Haroun et al	Marschall et al
<pre> surfaceScalarField phiCi= ((fvc::interpolate(DT))*(1- He)/(fvc::interpolate(alpha1)+(1- fvc::interpolate(alpha1))*He))*fvc::snGrad(alpha1))*mesh.magSf(); solve (fvm::ddt(T) + fvm::div(phi,T) - fvm::laplacian(fvc::interpolate(DT),T) + fvm::div(phiCi,T), mesh.solver("T")); </pre>	<pre> surfaceScalarField phiCi= ((DT1-DT2/He)/(fvc::interpolate(alpha1)+(1- fvc::interpolate(alpha1))/He))*fvc::snGrad(alpha1))*mesh.magSf(); surfaceScalarField phiD= (fvc::snGrad(DT))*mesh.magSf(); solve (fvm::ddt(T) + fvm::div(phi,T) - fvm::laplacian(fvc::interpolate(DT),T) - fvm::div(phiD,T) + fvm::div(phiCi,T), mesh.solver("T")); </pre>
<p><i>T</i> is the species concentration <i>DT1</i>, <i>DT2</i> are the diffusion coefficients of component T in Phase 1 and Phase 2 <i>He</i> is the Henry constant defined as the equilibrium ratio concentration of component in Phase 2 with respect to its concentration in Phase 1 <i>DT</i> is calculated in createFields.H as a weighted average of <i>DT1</i> and <i>DT2</i> or using the harmonic approach</p>	

The solvers shown above are based on static conditions of velocity and volume fraction fields. An additional step is to incorporate velocity, pressure, and volume fraction computations within the main solver. This is performed by combining the already existing interFoam solver in OpenFOAM with a species concentration equation similar to the development followed for the static solvers.

In addition, in most chemical engineering applications, reactions also occur. It is thus essential to modify the above solvers incorporating into the species conservation equations the reaction term. An irreversible reaction is first considered, where A is consumed and B is formed ($A \rightarrow B$). The kinetic constant in phase 1 is k_1 and in phase 2 is k_2 . Normally, reactant A will react only in one phase, but this formulation

considers the more general possibility of A reacting in phase 1 and phase 2. In order to convert the two-phase formulation into a single equation for the entire domain as the VOF formulation, the kinetic constant is calculated as the weight-average. Component B species conservation equation is analog to component A's equation but the sign of the kinetic constant is positive, since B is formed. The piece of code incorporated into the CEqn.H in the solvers is given in Table 7.2.

Table 7.2: Modified species conservation equation in CEqn.H in MarschallInterFoam solver for irreversible reaction $A \rightarrow B$

Component A
<pre>solve (fvm::ddt(A) + fvm::div(phi,A) - fvm::laplacian(DA,A) - fvm::div(phiDA,A) + fvm::div(phiCA,A) == fvm::Sp(k12,A));</pre>
Component B
<pre>solve (fvm::ddt(B) + fvm::div(phi,B) - fvm::laplacian(DB,B) - fvm::div(phiDB,B) + fvm::div(phiCB,B) == - k12*A);</pre>

For an equilibrium reaction $A \leftrightarrow B$ the species conservation equation the reversible reaction needs to be considered. The kinetic constant k_{rev12} is the weight-average of k_{rev1} (kinetic constant of the reverse reaction $B \rightarrow A$ in phase 1) and k_{rev2} (kinetic constant of the reverse reaction $B \rightarrow A$ in phase 2). The kinetic constants need to be defined according to the reaction in the 'transportProperties'. For instance, in this particular example k_{12} is negative for component A and k_{rev12} is positive. The modified equation is shown in Table 7.3.

Table 7.3: Modified species conservation equation in CEqn.H in MarschallInterFoam solver for reversible reaction $A \leftrightarrow B$

Component A
<pre>solve (fvm::ddt(A) + fvm::div(phi,A) - fvm::laplacian(DA,A) - fvm::div(phiDA,A) + fvm::div(phiCA,A) == fvm::Sp(k12,A) + krev12*B);</pre>
Component B
<pre>solve (fvm::ddt(B) + fvm::div(phi,B) - fvm::laplacian(DB,B) - fvm::div(phiDB,B) + fvm::div(phiCB,B) == - k12*A - fvm::Sp(krev12,B));</pre>

7.4 Solver validation

The first simple validation case is the transport of species across a planar interface between two immiscible fluids. The schematic of the system of study is presented in Figure 7.1. Simulation results for different values of diffusion coefficients and Henry constants were performed using the HarounScalarTransportFoam and MarschallScalarTransportFoam solvers. Results were compared with the ones obtained using Matlab by solving the species conservation equation eq 7.13 in one dimension (z coordinate) for each phase, considering the boundary conditions of equal concentration fluxes and jump in concentrations at the interface.

$$\frac{\partial C_i}{\partial t} = D_i \nabla^2 C_i \quad (7.13)$$

One criterion for comparison between solvers is to compare the computed jump in concentration with the theoretical value that should be obtained depending on the Henry constant given as input to the simulation. The boundary conditions for this 1D problem are given in Table 7.4.

Table 7.4: Boundary conditions for 1D validation case.

Time (s)	Position (m)	Boundary Condition	Value
0	z	Fixed value	0
t	0	Fixed value	1
t	0.1	Zero gradient	0

A comparison between solvers for different diffusion coefficients and Henry constants is included in Table 7.5. For cases 1-7 where the diffusion coefficients are equal in both phases to 10^{-5} m²/s, there is no difference in performance between the two different solvers. The jump in concentration at the interface is well captured by both solvers, with errors below 0.5% for Henry constants between 0.01 and 10, and below 5% for Henry constants up to 100. For longer times, even for Henry constant values of 100, the jump in concentration also achieves the correct value. A second set of simulations were performed for different diffusion coefficients, being DT1 = 10^{-5} m²/s and DT2 = 10^{-7} m²/s and different Henry constant values (Table 7.6). It is observed that longer times are needed in order to achieve the correct concentration jump

especially for large Henry constants. However, when comparing the concentration profiles along the entire domain, both solvers provide a good response compared to the value obtained with Matlab (Figures 7.2 and 7.3).

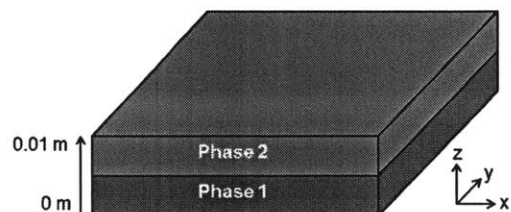


Figure 7.1: Schematic of the system for validation of mass transfer of species under static conditions and constant volume fraction field.

Table 7.5: Solver validation. Jump concentration at interface at 5 s from CFD results as function of Henry constant

Case	DT1 (m ² /s)	DT2 (m ² /s)	He	Jump concentration at interface	Error in jump concentration (%)
1	10 ⁻⁵	10 ⁻⁵	1	0.99945	-0.06
2	10 ⁻⁵	10 ⁻⁵	5	4.98815	-0.24
3	10 ⁻⁵	10 ⁻⁵	10	9.953796	-0.46
4	10 ⁻⁵	10 ⁻⁵	100	95.64985	-4.35
5	10 ⁻⁵	10 ⁻⁵	0.2	0.199963	-0.02
6	10 ⁻⁵	10 ⁻⁵	0.1	0.099986	-0.01
7	10 ⁻⁵	10 ⁻⁵	0.01	0.009999	-0.01

*Same values observed for MarschallScalarTransportFoam and HarounScalarTransportFoam

Table 7.6: Solver validation. Jump concentration at interface from CFD results for different diffusion coefficients as function of Henry constant

Case	He	1 s	5 s	10 s	20 s	50 s	100 s	Error at 1 s (%)	Error at 100 s (%)
8	5	4.761	4.876	4.934	4.973	4.993	4.998	-4.78	-0.04
9	100	52.45	70.10	81.73	91.71	97.80	99.21	-47.55	-0.79

*Same values observed for MarschallScalarTransportFoam and HarounScalarTransportFoam

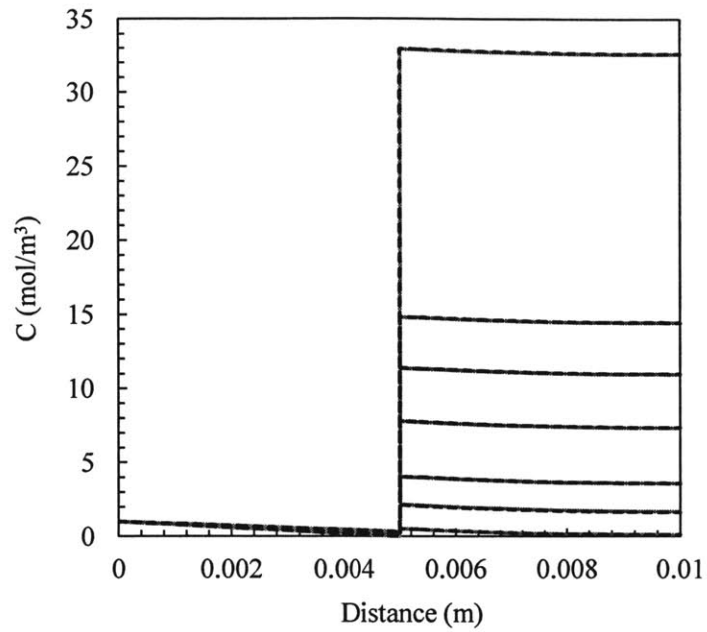


Figure 7.2: Comparison of concentration profiles using Matlab and OpenFOAM for $DT1 = DT2 = 10^{-5} \text{ m}^2/\text{s}$, $He = 100$ for different times = 1 s, 5 s, 10 s, 20 s, 30 s, 40 s, 100 s. Legend: —, OpenFOAM; ----, Matlab

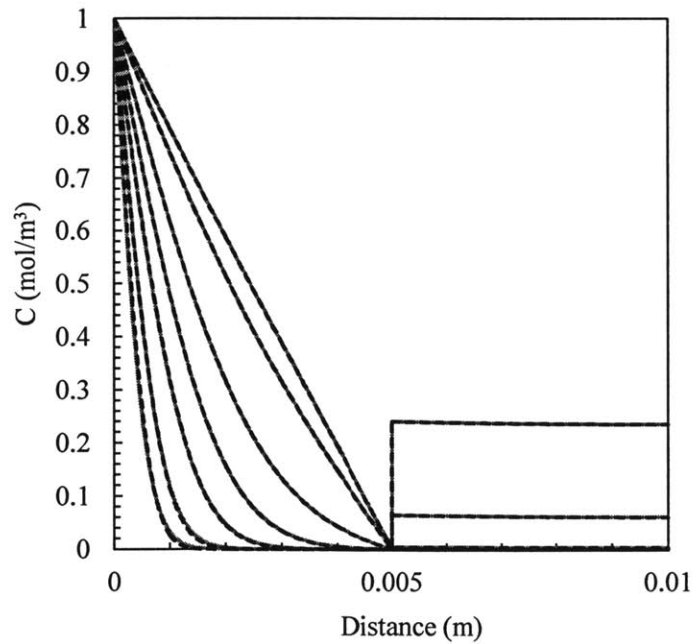


Figure 7.3: Comparison of concentration profiles using Matlab and OpenFOAM for $DT1 = 10^{-5} \text{ m}^2/\text{s}$, $DT2 = 10^{-7} \text{ m}^2/\text{s}$, $He = 100$ for different times = 1 s, 2 s, 5 s, 10 s, 20 s, 50 s, 100 s. Legend: —, OpenFOAM; ----, Matlab

The validation performed above corresponds to static conditions, for zero velocity and a fixed volume fraction field. The next step is to validate the solvers for cases of fixed volume fraction field and constant velocity profiles. One example for this validation is the parallel flow of two immiscible phases between two planar surfaces, as shown in Figure 7.4.

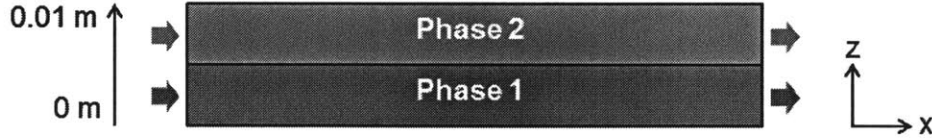


Figure 7.4: Schematic of the system for validation of mass transfer of species under dynamic conditions and constant volume fraction field.

The velocity field is first calculated analytically for 1D dimension and used as an input for the velocity field in the OpenFOAM solvers. Assumptions of steady-state, unidirectional flow (x-component), fully developed flow (x-component of the velocity does not depend on x), no slip at the walls, and no effect of gravity forces:

$$0 = -\frac{\partial P}{\partial x} + \mu \left(\frac{\partial^2 v_x}{\partial z^2} \right) \quad (7.14)$$

With no-slip boundary condition at the walls, and for a fixed pressure drop, the velocity field $v_x(z)$ is given by eq 7.15:

$$v_x(z) = \frac{1}{2\mu_1} \frac{\partial P}{\partial x} z^2 + \alpha_1 z + \beta_1 \quad 0 \text{ m} < z < 0.005 \text{ m} \quad (7.15)$$

$$v_x(z) = \frac{1}{2\mu_2} \frac{\partial P}{\partial x} z^2 + \alpha_2 z + \beta_2 \quad 0.005 \text{ m} < z < 0.01 \text{ m}$$

where $\alpha_1 = \frac{(\frac{\partial P}{\partial x}) \mu_2 H (\frac{3}{4} + \frac{1}{\mu_2 \mu_1})}{\frac{\mu_2}{\mu_1} + 1}$, $\alpha_2 = \alpha_1 \frac{\mu_1}{\mu_2}$, $\beta_1 = 0$ and $\beta_2 = -H \alpha_2 - \frac{H^2}{2\mu_2} \left(\frac{\partial P}{\partial x} \right)$

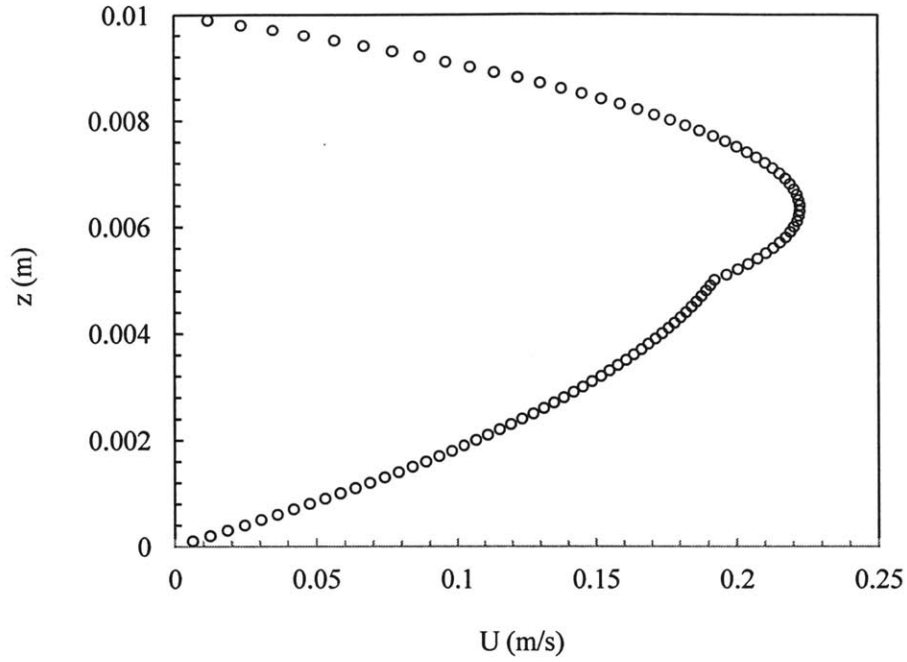


Figure 7.5: Velocity profile for a fully developed flow at steady-state for two immiscible fluids. $dP/dx = -10 \text{ Pa s}$; $\mu_1 = 0.001 \text{ Pa.s}$, $\mu_2 = 0.0003 \text{ Pa.s}$, $\alpha_1 = 63.46$, $\alpha_2 = 211.54$, $\beta_1 = 0$, $\beta_2 = -0.45$

Validation of HarounScalarTransportFoam and MarschallScalarTransportFoam solvers was performed for the same two fluid system with dominance of convection over diffusion ($DT1 = DT2 = 10^{-9} \text{ m}^2/\text{s}$). The CFD results were compared with results obtained with Matlab for a simplified problem, described by eq 7.16 and boundary conditions in Table 7.7.

$$\frac{\partial c}{\partial t} + v_x(z) \frac{\partial c}{\partial x} = 0 \quad (7.16)$$

Table 7.7: Boundary conditions for validation of mass transfer solvers

Time (s)	Position (m)	Boundary condition	Value	Units
t	x = 0	Fixed value	1	mol/m ³
t	x > 0	Fixed value	0	mol/m ³

The concentration profiles obtained using HarounScalarTransportFoam and Matlab are shown in Figures 7.6 and 7.7, respectively. It is observed that the CFD simulations yield the same concentration profiles at different times than the Matlab solution.

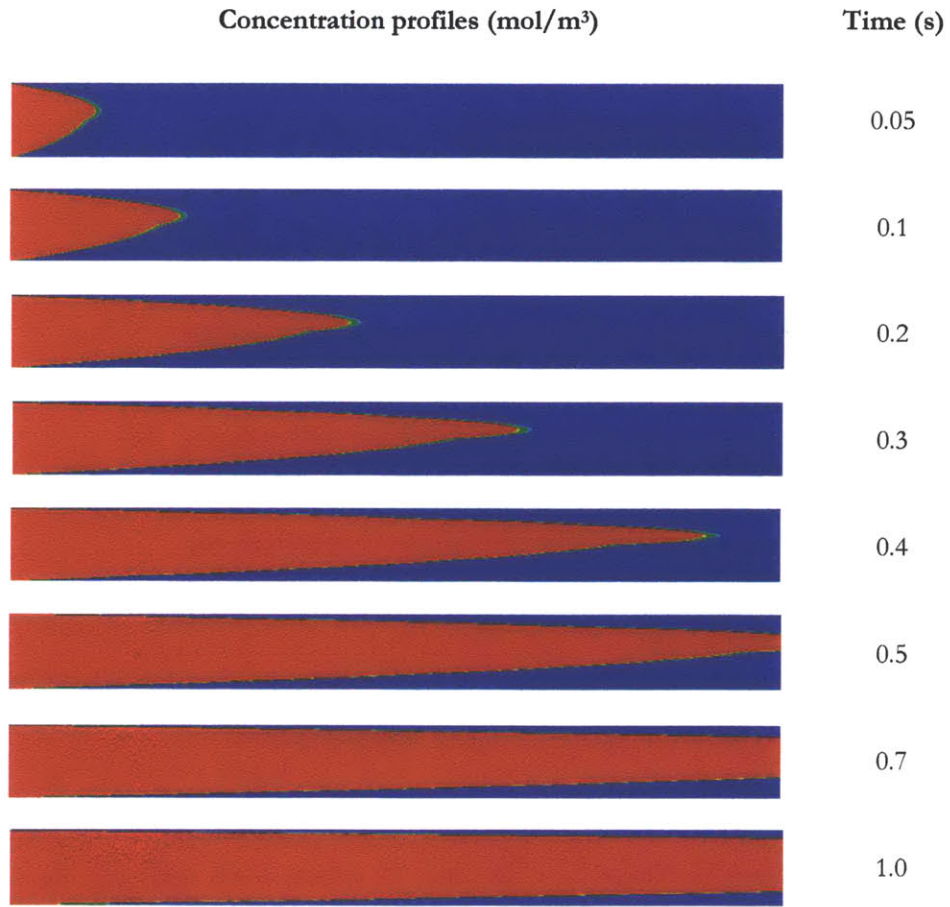


Figure 7.6: Concentration profiles obtained in OpenFOAM using HarounTransportFoam. Concentration is treated as a passive scalar for fixed velocity profiles.

Legend: 0.25 0.5 0.75

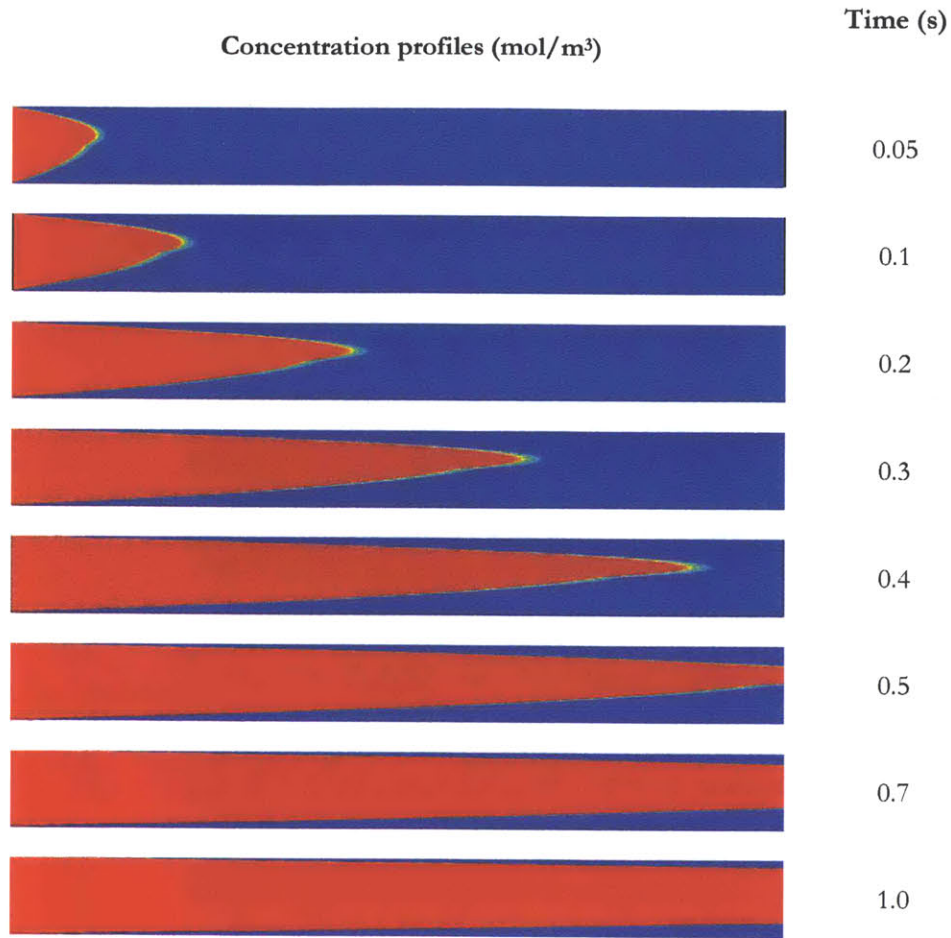



Figure 7.7: Concentration profiles obtained in Matlab using two-fluid formulation with boundary conditions specified at interface. Legend: 

The previous examples were performed for cases where the velocity and α -fields were fixed over time. However, in practical problems, and more specifically applying to the AFR system, there is a continuous break-up and coalescence of bubbles and drops, which modify the velocity and α -fields over time. Thus, the previous solvers have been modified to simultaneously solve for the momentum, α -advection, and species transfer equations. This is performed by applying the same approach followed in `HarounScalarTransportFoam` and `MarschallScalarTransportFoam` (these are based on the single-phase passive scalar solver `ScalarTransportFoam`) to the `interFoam` solver of OpenFOAM. The resulting solvers are

called HarounInterFoam and MarschallInterFoam and are based on the original interFoam solver. Table 7.8 presents the code original from interFoam and the incorporation of the CEqn.H file (#include "CEqn.H"), which is the same used for HarounScalarTransportFoam.

Table 7.8: HarounInterFoam.C. Formulation of coupled species conservation and momentum equations within OpenFOAM solver

<pre> int main(int argc, char *argv[]) { #include "setRootCase.H" #include "createTime.H" #include "createMesh.H" pimpleControl pimple(mesh); #include "initContinuityErrs.H" #include "createFields.H" #include "readTimeControls.H" #include "correctPhi.H" #include "CourantNo.H" #include "setInitialDeltaT.H" // ***** // Info<< "\nStarting time loop\n" << endl; while (runTime.run()) { #include "readTimeControls.H" #include "CourantNo.H" #include "alphaCourantNo.H" #include "setDeltaT.H" runTime++; Info<< "Time = " << runTime.timeName() << nl << endl; twoPhaseProperties.correct(); #include "alphaEqnSubCycle.H" </pre>	<pre> // --- Pressure-velocity PIMPLE corrector loop while (pimple.loop()) { #include "UEqn.H" #include "CEqn.H" // --- Pressure corrector loop while (pimple.correct()) { #include "pEqn.H" } if (pimple.turbCorr()) { turbulence->correct(); } } runTime.write(); Info<< "ExecutionTime = " << runTime.elapsedCpuTime() << " s" << " ClockTime = " << runTime.elapsedClockTime() << " s" << nl << endl; } Info<< "End\n" << endl; return 0;} </pre>
--	---

The solver accounting for simultaneous mass transfer and reaction is validated using two simple test cases. In the first case, the irreversible reaction is tested in a two-phase transient system, and in the second test case, the reversible reaction at steady state is studied. The results are compared with the solution obtained numerically with Matlab in the first case (Figure 7.8), and with the analytical solution in the second case (Figure 7.9). Both figures show that the predictions of OpenFOAM are in good agreement with Matlab, with errors lower than 1% for both cases.

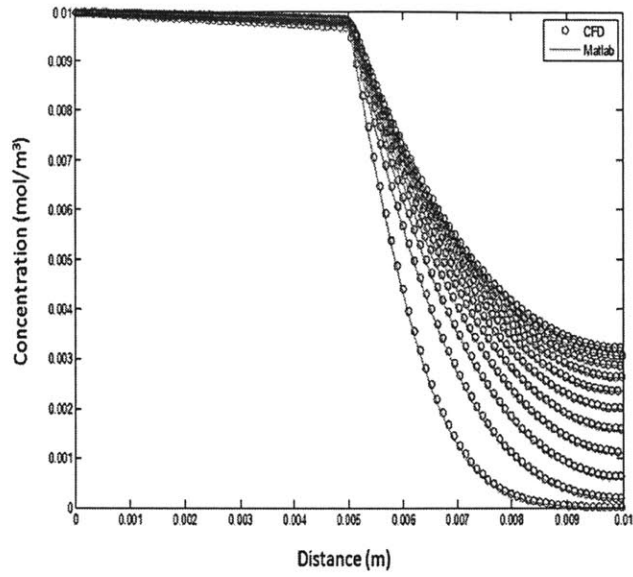


Figure 7.8: Validation of reactInterFoam for a first order reaction in static conditions. $He = 1$ and $k_1 = 0$, $k_2 = -0.01$; Legend: —, Matlab; ○, OpenFOAM

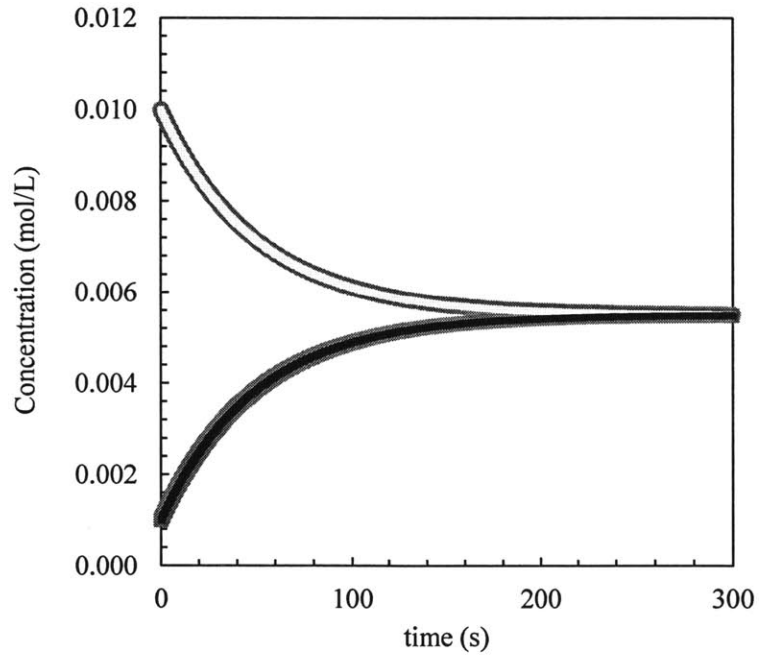


Figure 7.9: Validation of reactInterFoam for first order reversible reaction in static conditions. $k_1 = 0$, $k_2 = -0.01$; $k_{1rev} = 0$, $k_{2rev} = 0.01$; Legend: ■, Concentration of A (analytical); ■, Concentration of B (analytical); , Concentration of A (OpenFOAM); ●, Concentration of B (OpenFOAM)

7.5 Application to the Advanced-Flow Reactor

The motivation for modeling two-phase flow in the AFR is to be able to predict overall mass transfer coefficients ($k_L a$) for different fluid systems prior to experimentation and demonstrate the mass transfer efficiency in the AFR. The overall mass transfer coefficient has two different contributions: a) the individual mass transfer coefficient, k_L ; and b) the specific interfacial area, a . Although there are theoretical approximations to estimate k_L (such as penetration theory ⁹, surface renewal theory ¹⁰), the specific interfacial area remains frequently unknown. For devices such as the Advanced-Flow Reactor (AFR) where the specific interfacial areas highly depend on the operating conditions and cannot be known a priori, a CFD tool such as OpenFOAM can be useful as a preliminary step to predict interfacial areas. For this purpose, just the `interFoam` solver would be sufficient. However, incorporation of mass transfer of species across interfaces, allows also the prediction of mass transfer coefficients, k_L . Furthermore, incorporation of reaction is possible, which increases the potential application of the CFD tool to predict reactor performance for actual reactions coupled with mass transfer occurring in any multiphase reactor.

In this Chapter, the results of applying the `HarounTransportFoam` in the AFR to predict flow patterns, average drop size, specific interfacial areas, dispersed phase holdup, and mass transfer coefficients, are presented and compared with experimental data ^{11, 12}.

Due to constraints in the computation time, only two heart cells of the AFR are modeled. The mesh is structured and three-dimensional, composed of 251,320 cells and 10 cells in the z-direction. In order to save computation time, each portion of the AFR where each fluid flows separately has been modeled using the `simpleFoam` solver, which solves incompressible single-phase steady-state flows. Then, the output of the CFD simulation for single-phase flow for each phase is used as an input for the simulation of two-phase flow.

The estimation of the overall mass transfer coefficient is performed by computation of two variables: k_L and a . Both variables depend on the fluid properties of the system of interest and the operating conditions (temperature, pressure, flow rates). In the simulations performed, the temperature and pressure remain constant and at ambient conditions. The individual mass transfer coefficient, k_L , is computed from the CFD

results according to eq 7.17, from the flux of concentration of component across the interface. Notice here that the concentration of flux given by Fick's law directly does not account for the additional term ϕ (eq 7.18) that should be considered to correct the flux by the presence of jump concentration.

$$k_{L,local} = -\frac{(D\nabla C + \phi)\vec{n}}{\Delta C_{L,local}} \quad (7.17)$$

$$\phi = -D_j \frac{c_j(1-H e_j)}{\alpha + (1-\alpha)H e_j} \nabla \alpha \quad (7.18)$$

In addition, calculation of the individual mass transfer coefficient based on the surface renewal theory¹⁰ is performed and the results are compared with the obtained through CFD.

The specific interfacial area is extracted from the flow patterns obtained in each simulation. A Matlab script was written to measure the contour of the droplets. Depending on the droplet size with respect to the reactor height, the specific area was computed as a sphere or as a planar droplet sandwiched between the two reactor walls. The results were computed from the transient simulation until steady state was reached. Comparison with experimental observations is performed hereafter by comparing average drop size, hexane hold-up, specific interfacial areas, and mass transfer coefficients.

The different flow patterns obtained for different flow rates at constant hexane flow rate and increasing water flow rate are shown in Figure 7.10. Based on the CFD results, the effect of increasing the water flow rate for constant hexane flow rate is to decrease the drop size and hexane holdup. This is also observed experimentally. One factor that allows increasing mass transfer rates is to increase the specific interfacial area. This can be increased by increasing the holdup and decreasing the droplet size. Increasing the holdup is achieved with higher hexane flow rate, whereas smaller droplet size is achieved by increasing both phases flow rates due to the increase in shear rates which enhances droplet breakup.

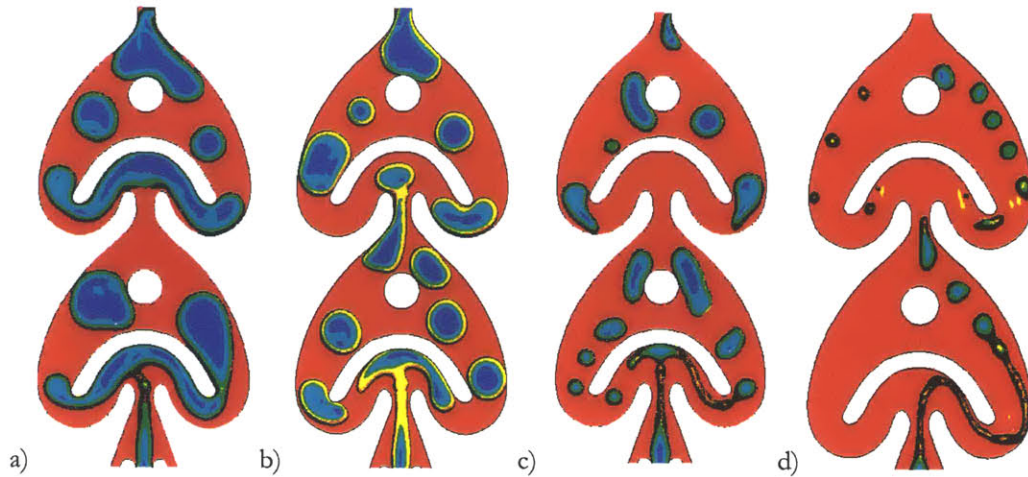


Figure 7.10: Flow patterns for hexane/water system using HarounTransportFoam (OpenFOAM) for different flow rates; a) $Q_w = 10$ mL/min, $Q_h = 10$ mL/min; b) $Q_w = 20$ mL/min, $Q_h = 10$ mL/min; c) $Q_w = 40$ mL/min, $Q_h = 10$ mL/min; d) $Q_w = 80$ mL/min, $Q_h = 10$ mL/min;

Table 7.9 includes a comparison between the hold-up computed from the CFD simulations and the experimental hold-up in the first two hearts of the AFR. It is seen that there is good agreement between the simulations and the experiments. In addition, the bulk concentration of acetone in the dispersed phase (hexane) was monitored over time to see whether a steady-state was achieved. From the final steady-state concentration actually achieved, and the theoretical concentration that could be reached based on the mass balance of component between phases, it is possible to obtain a measurement of the efficiency of the mass transfer process. This variable was computed as the ratio of the actual concentration at steady-state versus the maximum possible concentration achieved. As it is seen from the results, the mass transfer efficiency is comprised in the interval 68 – 84 %, which is a large value considering that only two-hearts have been simulated.

Table 7.9: Mass transfer efficiency, concentration, and hexane hold-up for constant hexane flow rate

Hexane (mL/min)	Water (mL/min)	Experimental hold-up (-)	CFD hold-up (-)	CFD C_{final} (mol/m ³)	CFD C_{max} (mol/m ³)	Efficiency (%)
10	10	0.36	0.43	0.39	0.55	70.9
10	20	0.37	0.36	0.44	0.65	68.3
10	40	0.22	0.22	0.65	0.78	83.3
10	80	0.14	0.09	0.65	0.92	70.7

Regarding the mass transfer coefficients, the values shown in Figure 7.11 e) and f) have been computed based on the surface renewal theory, using the residence time of the dispersed phase as the contact time, for which the CFD hexane hold-up has been used. As shown in the CFD results, the individual mass transfer coefficient increases with the continuous phase flow rate. However, the overall mass transfer coefficient is smaller for higher water flow rates. Although there are differences among the different water flow rates in the individual mass transfer coefficients ($10^{-4} - 2 \cdot 10^{-4} \text{m/s}$), the main contribution to $k_L a$ comes from the interfacial area (varying from 350 to 1,300 m^2/m^3), which was seen to decrease with largest flow rates of water due to the smaller hexane hold-up, despite of the smaller droplets achieved.

A comparison of the CFD individual mass transfer coefficients and specific interfacial areas with experimental results is included in Table 7.10. As it is seen from the results, the k_L values obtained by the different methods (surface renewal theory and from the concentration gradient) are in good agreement with the experimental results also based on surface renewal theory. The largest differences are encountered in the specific interfacial areas. In both simulations and experimental results, it is found that the specific interfacial area decreases when increasing the continuous phase flow rate due to the decrease in hexane holdup, despite of the decrease in droplet size. This shows the importance of having a correct VOF method that is able to capture accurately the formation of droplets and bubbles.

Table 7.10: Comparison of experimental and CFD k_L and a

Hexane (mL/min)	Water (mL/min)	a_{CFD} (m^2/m^3)	$k_{L, \text{CFD I}}$ 10^4 (m/s)	$k_{L, \text{CFD II}}$ 10^4 (m/s)	a_{exp} (m^2/m^3)	$k_{L, \text{exp}}$ 10^4 (m/s)
10	10	1250	1.11	0.84	1028	0.91
10	20	1120	1.07	0.91	1260	1.20
10	40	940	1.11	1.15	1001	1.16
10	80	450	1.75	1.96	930	1.43

$k_{L, \text{CFD I}}$: from concentration gradient

$k_{L, \text{CFD II}}$: from surface renewal theory

Table 7.11 shows that the $k_{L,a}$ values estimated using the surface renewal theory of Danckwerts and from the concentration gradient based on the CFD results are in good agreement. They are also in agreement with the semiempirical values, although there are some discrepancies, especially at the largest flow rates, mainly due to differences in the prediction of the specific interfacial area.

Table 7.11: Comparison of experimental and CFD $k_{L,a}$

Hexane (mL/min)	Water (mL/min)	$k_{L,a}$ CFD I (1/s)	$k_{L,a}$ CFD II (1/s)	$k_{L,a}$ exp (1/s)
10	10	0.139	0.105	0.094
10	20	0.119	0.102	0.152
10	40	0.105	0.093	0.116
10	80	0.092	0.070	0.133

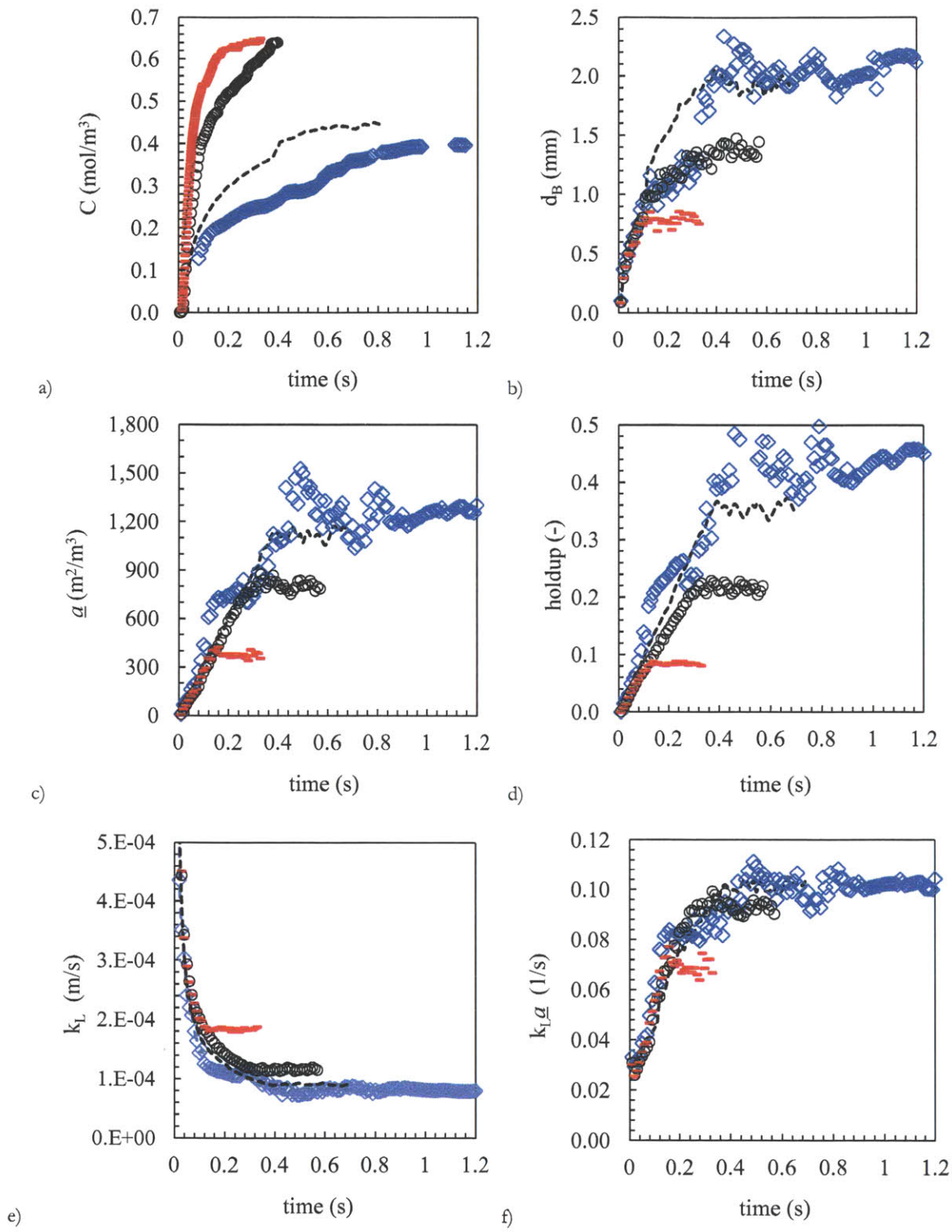


Figure 7.11: Effect of water flow rate at 10 mL/min hexane flow rate on a) concentration in hexane; b) drop size; c) specific interfacial area; d) hexane hold-up; e) individual mass transfer coefficient; f) overall mass transfer coefficient. Water flow rate (mL/min): \diamond , 10; $---$, 20; \circ , 40; $-$, 80

The effect of total flow rate for constant water to hexane ratio is shown in Figure 7.12. While in the experimental work already a breakup is observed in the first heart with formation of small drops, breakup hardly occurs in CFD simulations at 40 and 80 mL/min of each phase. At large flow rates, higher mesh resolution may be needed in order to capture all small drops formed. Since the ratio water-to-hexane is one for these computations, the proximity of drops causes an artificial coalescence effect. In the current VOF methods available there is no method that prevents the numerical coalescence of bubbles/drops that are within one grid cell distance apart. This is a limitation of this method, which requires very fine mesh resolution in order to describe the interface sharpness accurately and avoid coalescence effects that are not present in reality. This is a problem present in liquid-liquid CFD simulations and it is certainly a topic that needs to be further studied, but its implementation is out of the scope of this work.

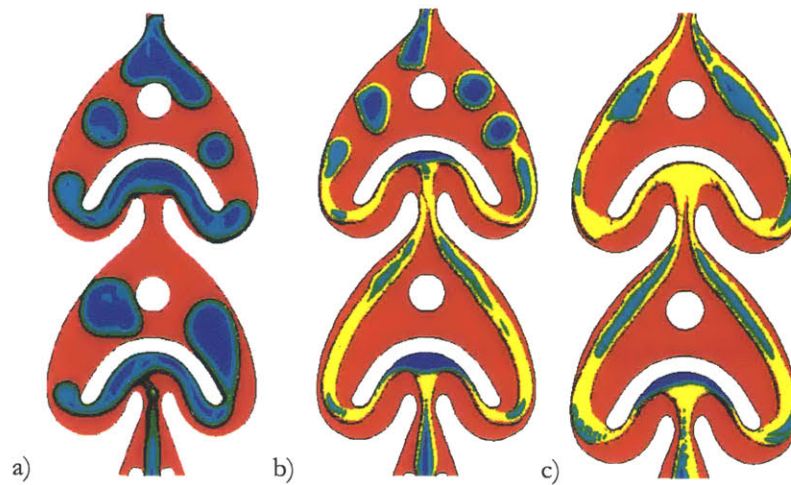


Figure 7.12: Flow patterns for hexane/water system using HarounTransportFoam (OpenFOAM) for different flow rates; a) $Q_w = 10$ mL/min, $Q_h = 10$ mL/min; b) $Q_w = 40$ mL/min, $Q_h = 40$ mL/min; c) $Q_w = 80$ mL/min, $Q_h = 80$ mL/min; Legend: ■, water phase; ■, hexane phase

The bulk component concentration in hexane is shown in Figure 7.13 a). Higher final concentrations are achieved for lower total flow rates. The mass transfer efficiency computed as the ratio between the final concentration and the maximum concentration possible from a mass balance calculated from the hexane holdup falls within the range 46 – 72 %. The smallest efficiencies are observed for the highest total flow rates.

However, this may not be physical result, since it was shown already in Figure 7.12 that there is an artificial coalescence effect caused by the numerical method, which decreases the specific interfacial area with respect to the experimental result. A smaller droplet size would certainly be expected at the largest flow rates (as seen in the experimental results), for the same hexane holdup, thus, increasing the specific interfacial area. This, in turn, increases the mass transfer and the final concentration seen in the bulk of the hexane phase is expected to be larger than the one obtained in the CFD simulations.

Table 7.12: Mass transfer efficiency, concentration, and hexane hold-up for constant hexane flow rate

Hexane (mL/min)	Water (mL/min)	Experimental hold-up (-)	CFD holdup (-)	CFD C_{final} (mol/m ³)	CFD C_{max} (mol/m ³)	Efficiency (%)
10	10	0.36	0.43	0.40	0.56	71.4
20	20	0.37	0.42	0.38	0.56	67.9
40	40	0.36	0.32	0.36	0.69	52.2
80	80	0.31	0.30	0.32	0.69	46.4

Table 7.13 presents a comparison of CFD results and experiments for specific interfacial areas and individual mass transfer coefficients at different total flow rates. Again, there is a good agreement among individual mass transfer coefficients computed either by surface renewal theory or from the CFD concentration gradient. In any case, the largest discrepancies are observed at 80 and 160 mL/min total flow rate, as expected by the poor prediction of flow patterns with the current mesh resolution and the problem of numerical coalescence observed.

Table 7.13: Comparison of experimental and CFD k_L and a for unity flow rate ratio

Hexane (mL/min)	Water (mL/min)	a CFD (m ² /m ³)	$k_{L,CFD I}$ 10 ⁴ (m/s)	$k_{L,CFD II}$ 10 ⁴ (m/s)	a_{exp} (m ² /m ³)	$k_{L,exp}$ 10 ⁴ (m/s)
10	10	1250	1.10	0.84	1028	0.91
20	20	1230	1.09	1.19	1320	1.25
40	40	1170	1.22	1.87	1135	1.81
80	80	850	1.32	2.78	1640	2.21

$k_{L,CFD I}$: from concentration gradient

$k_{L,CFD II}$: from surface renewal theory

A comparison among overall mass transfer coefficients obtained through CFD and experiments is shown in Table 7.14. The results show a reasonable agreement between the three different methods (with the limitations already stated before), with the best agreement observed at the lowest flow rates at which the flow patterns are better predicted.

Table 7.14: Comparison of experimental and CFD $k_{L,a}$ for unity flow rate ratio

Hexane (mL/min)	Water (mL/min)	$k_{L,a}$ CFD I (1/s)	$k_{L,a}$ CFD II (1/s)	$k_{L,a}$ exp (1/s)
10	10	0.138	0.105	0.094
20	20	0.134	0.146	0.165
40	40	0.142	0.219	0.205
80	80	0.112	0.236	0.364

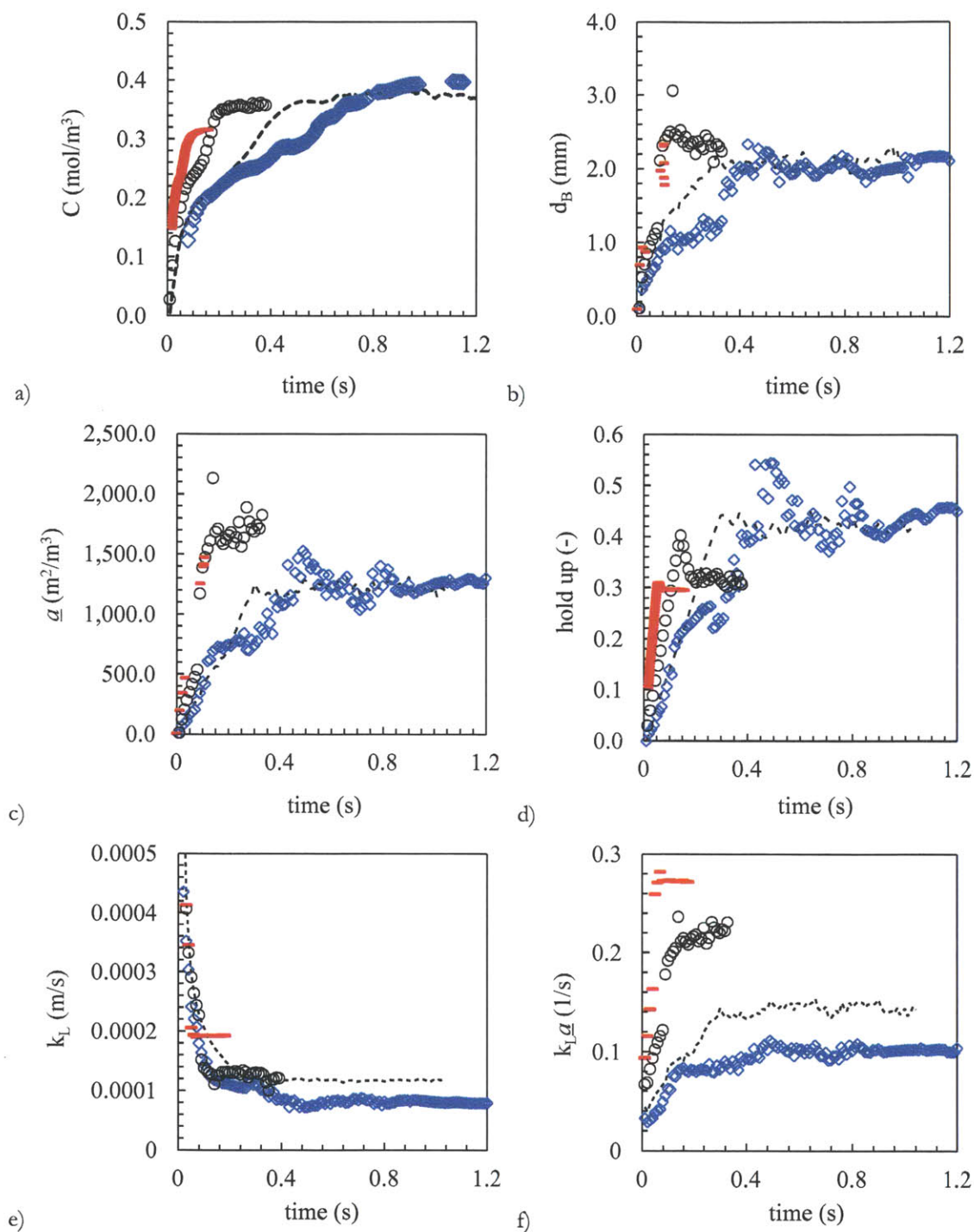


Figure 7.13: Effect of total flow rate at hexane to water flow rate ratio = 1 on a) concentration in hexane; b) average drop size; c) specific interfacial area; d) hexane hold-up; e) individual mass transfer coefficient; f) overall mass transfer coefficient. Total flow rate (mL/min): \diamond , 20; $- -$, 40; \circ , 80; $-$, 160

7.5.1 Effect of fluid properties

Being able to predict the reactor behavior with a computational tool that can avoid or reduce the need of performing experiments is especially important when working with dangerous or very expensive materials. Simulations can help us decide what materials are more appropriate if different alternatives are available depending on the specific requirements of the system. In previous sections it was concluded that, for fixed material properties, the inlet phase flow rates determined the drop size distribution, specific interfacial areas, and mass transfer coefficients. Here, a comparison between simulations for different fluid properties is presented, based on flow patterns, specific interfacial areas, and mass transfer coefficients.

7.5.1.1 Effect of viscosity

It was already shown in the CFD simulation of two-phase flow in T-junctions that viscosity does not have a strong effect on the slug size. The effect, however, may be different in the AFR and therefore, is studied here. Here we present the results for constant surface tension, contact angle, and density of the fluids, but variable viscosity of the continuous phase (water) in the water/hexane system. The results of the flow patterns are shown in Figure 7.14 and variation of concentration in hexane, average drop size, specific interfacial areas, hold-up, and mass transfer coefficients, over time, in Figure 7.15. It can be observed that increasing the viscosity of the continuous phase affects negatively on the mass transfer process. First, the average drop size is decreased by about 0.3 mm, which, together with a decrease in hexane holdup, decreases the specific interfacial area from 805 to 700 m²/m³. This makes the final concentration achieved in the case of highest viscosity to be smaller than in the original case (0.55 versus 0.65 mol/m³), which represents 67% efficiency in mass transfer with respect to the maximum concentration possible. In consequence, the overall mass transfer coefficient is also slightly smaller for the higher fluid viscosity. However, the difference is not significant for such a change in viscosity.

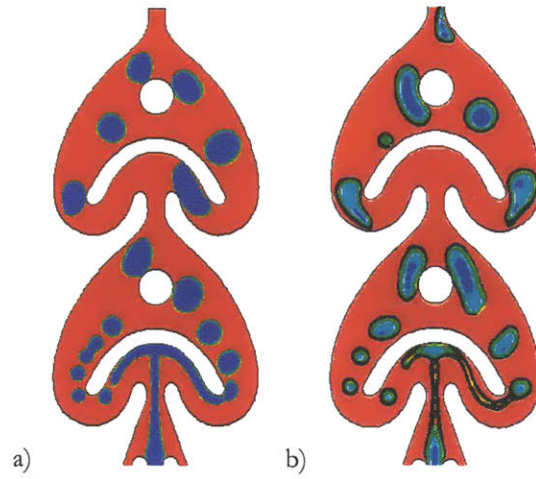


Figure 7.14: Effect of viscosity on flow patterns at 40 mL/min water and 10 mL/min hexane, for a) $\mu/\rho=10^{-5} \text{ m}^2/\text{s}$; b) $\mu/\rho=10^{-6} \text{ m}^2/\text{s}$;

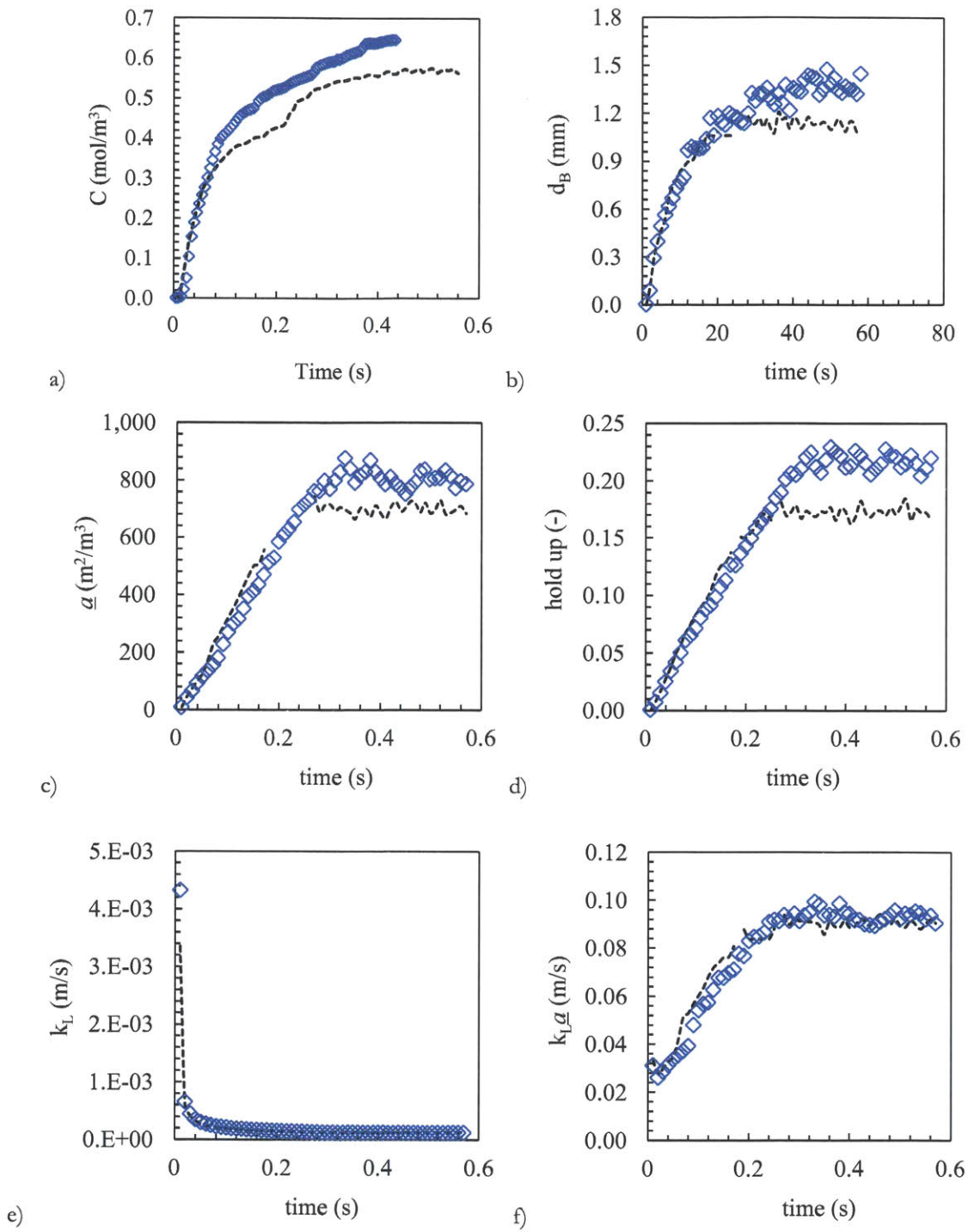


Figure 7.15: Effect of viscosity on a) concentration in hexane phase; b) droplet size; c) specific interfacial area; d) hold-up; e) individual mass transfer coefficient; f) overall mass transfer coefficient. Legend: \diamond , 0.001 Pa s; ---, 0.01 Pa s

7.5.1.2 Effect of surface tension

The surface tension is another variable important in two-phase flow that affects flow patterns. As it can be observed from Figure 7.16, the main effect of surface tension is to decrease the average drop size for decreasing surface tension. However, the decrease in drop size is accompanied by a decrease in hexane hold up as well. This affects negatively to the specific interfacial area, which also decreases with decreasing surface area.

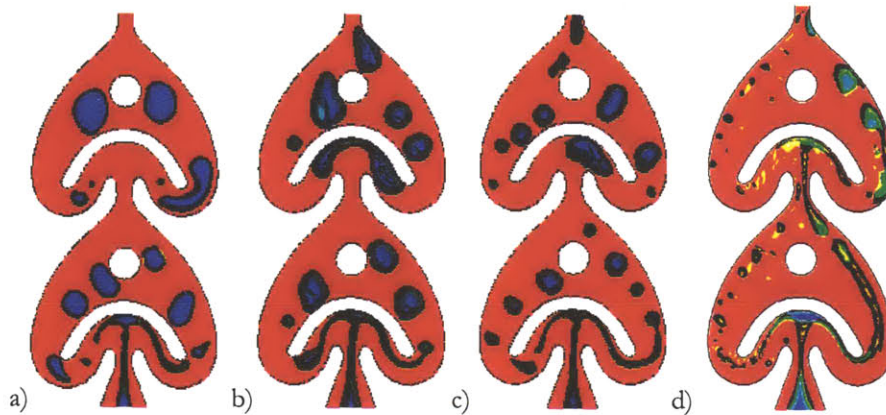


Figure 7.16: Effect of surface tension on flow patterns at 40 mL/min water and 10 mL/min hexane, for σ (N/m): a) 0.052; b) 0.043; c) 0.035; d) 0.0068

Figure 7.17 includes the effect of surface tension on the bulk concentration of component in hexane, the average droplet size, the specific interfacial area, the hexane holdup, and mass transfer coefficients. It is observed that lower surface tension decreases the mass transfer efficiency. First, the bulk concentration of acetone in hexane is lower and the maximum concentration possible is higher, therefore, decreasing the efficiency from 83 % to 60 %. In addition, the specific interfacial area is smaller, and, although the individual mass transfer coefficient is slightly larger for the lower surface tension, the overall effect is to decrease the overall mass transfer coefficient. Therefore, although having lower surface tension is advantageous to achieve smaller droplets sizes (more breakup), in order to have a better performance, it would be necessary to increase the hexane flow rate so that the hexane holdup increases and the total interfacial area also increases (a), contributing to an overall larger mass transfer rate.

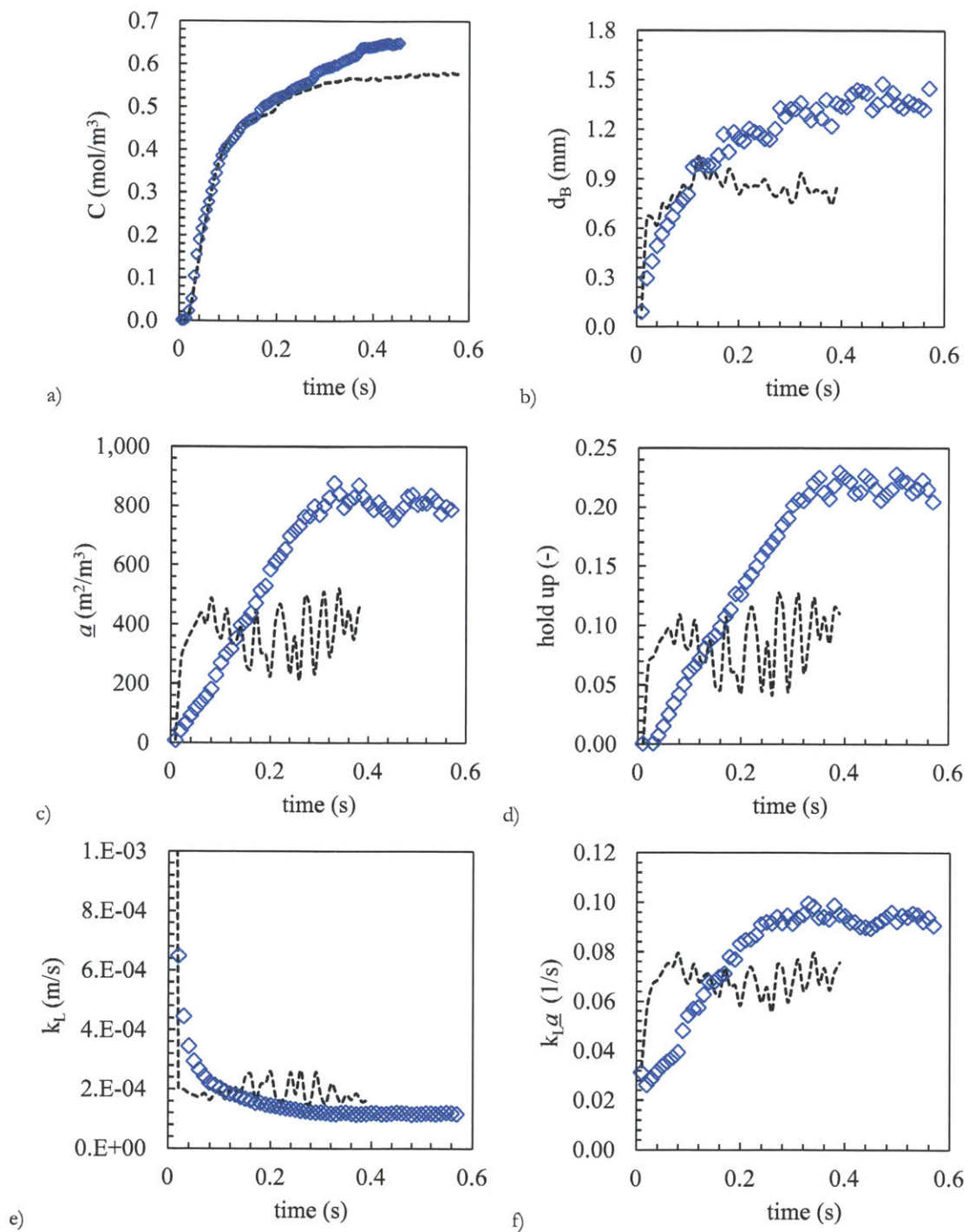


Figure 7.17: Effect of surface tension at 40 mL/min water and 10 mL/min hexane on a) concentration in hexane phase; b) average drop size; c) specific interfacial area; d) hexane holdup; e) individual mass transfer coefficient; f) overall mass transfer coefficient. Legend, σ (N/m): \diamond , 0.052; $---$, 0.0068

7.5.1.3 Effect of contact angle

The effect of contact angle on the flow patterns for 40 mL/min water and 10 mL/min hexane is shown in Figure 7.18. It is observed that the shape and size of the droplets are completely determined by the contact angle. For 75°, water partially wets the reactor walls, while at a contact angle of 0°, water wets completely the wall. When comparing the images from the visualization experiments and the simulation, it is seen that contact angles of 0° provide droplet shapes and sizes that are in agreement with the experimental results, as would be expected since the AFR material is known to be hydrophilic.

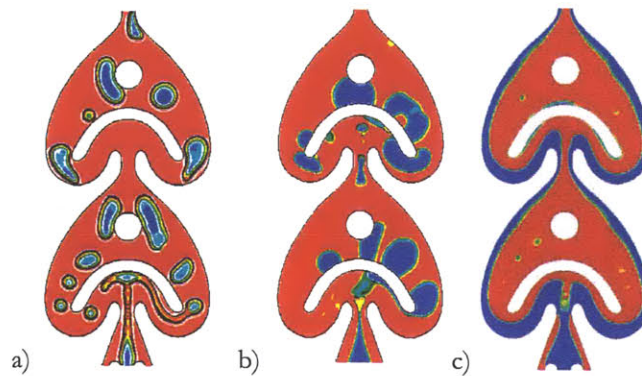


Figure 7.18: Effect of contact angle on flow patterns at 40 mL/min water and 10 mL/min hexane, for a) $\theta = 0^\circ$; b) $\theta = 75^\circ$; c) 150°

The contact angle completely changes the flow patterns, as opposed to other variables. In other simulations it was demonstrated that the effect of viscosity or surface tension was mainly on the droplet size, but the main characteristics of the flow patterns remain unchanged. It can be seen from Figure 7.19 that, although k_L values remain approximately the same, the main effect of the contact angle is on the specific interfacial area. The largest $k_L a$ values are obtained for a contact angle of 0° (water wets the walls totally), whereas in the two other cases, due to the no complete wettability of the walls, the interfacial area is smaller and the overall mass transfer coefficients are lower. In conclusion, for better mass transfer efficiency, the best scenario is to have bubbly flow with smaller bubbles and very high holdup. This is achieved with a hydrophilic phase wetting the walls of the reactor, high continuous phase flow rate to decrease the overall droplet size, and high dispersed phase flow rate to increase holdup.

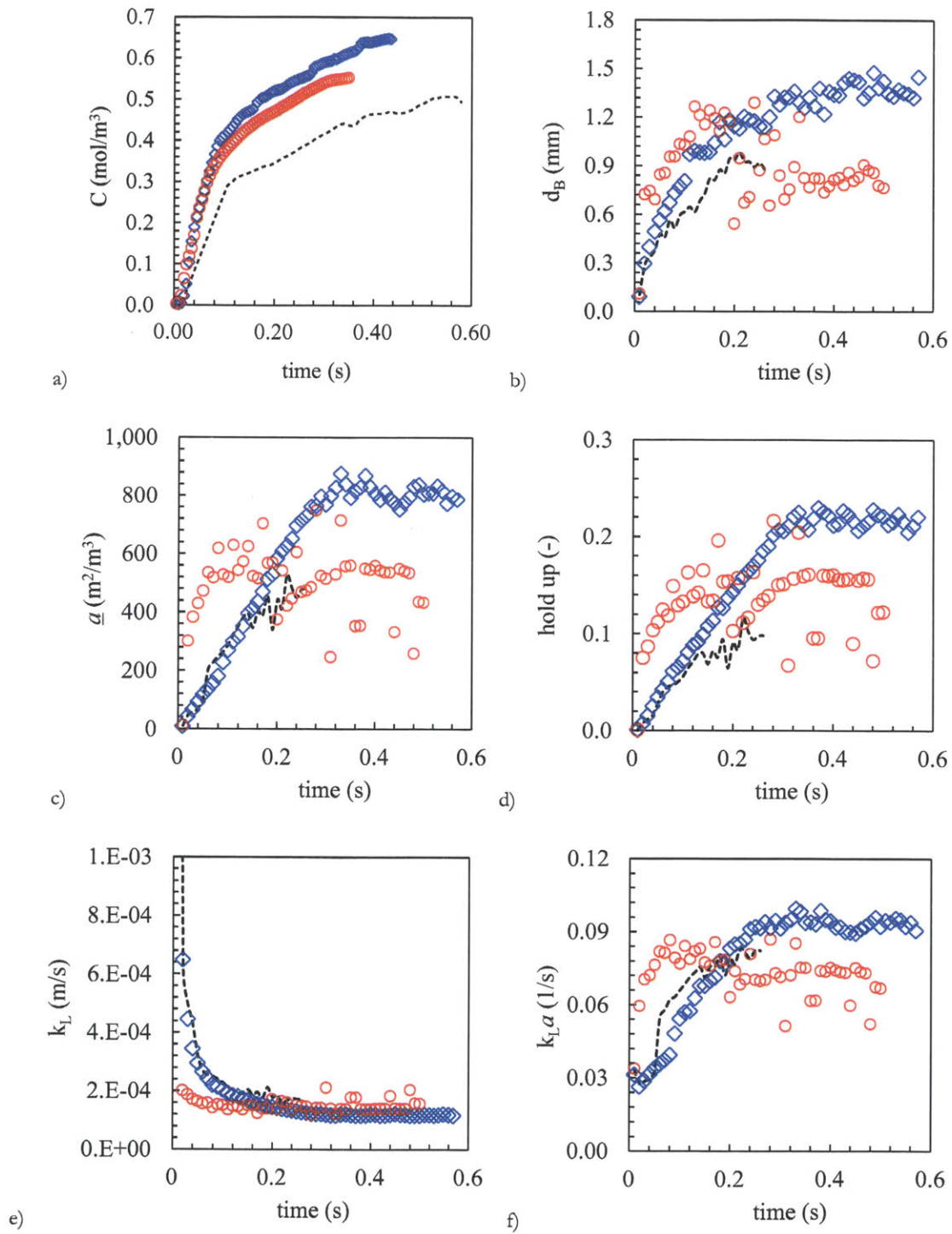


Figure 7.19: Effect of contact angle at 40 mL/min water and 10 mL/min hexane on a) bulk concentration in hexane; b) average drop size; c) specific interfacial area; d) hexane holdup; e) individual mass transfer coefficient; f) overall mass transfer coefficient Legend: \diamond , 0°; ---, 75°; \circ , 150°

7.5.2 Effect of reactor design

In Chapter 4, the influence of reactor design on the velocity profiles and residence time distribution for single-phase flow was studied at different flow rates. Some differences were encountered between the different designs, although all of them behaved essentially as plug flow with a very small degree of dispersion, and the overall effect on the total conversion for a first order reaction was negligible. Since two-phase flow may behave differently, it is necessary to study also the effect of the reactor design.

The results of flow patterns are shown in Figure 7.20 for the original reactor design (AFR, with dot), the modified version ‘no dot’, and the ‘LFR’-like design. The main flow pattern remains unchanged (‘bubbly’ flow type), but the droplet size is different among the different designs.

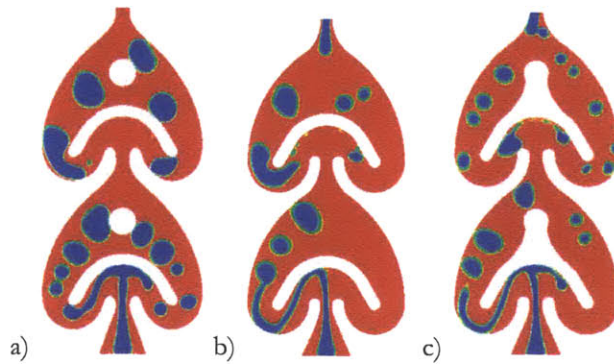


Figure 7.20: Effect of contact angle at 40 mL/min water and 10 mL/min hexane on flow patterns

Measurement of component concentration in hexane, average drop size, specific interfacial area, and mass transfer coefficients are monitored over time. The associated variables to each reactor design and comparison among them are shown in Figure 7.21. The larger drop size is observed for the AFR, followed by the ‘no dot’ and the ‘LFR’ – like designs. While the AFR and the ‘no dot’ designs have similar specific interfacial areas and larger than the ‘LFR’ design, all overall mass transfer coefficients fall within the range $0.075 - 0.09 \text{ s}^{-1}$, being in the upper limit for the AFR design.

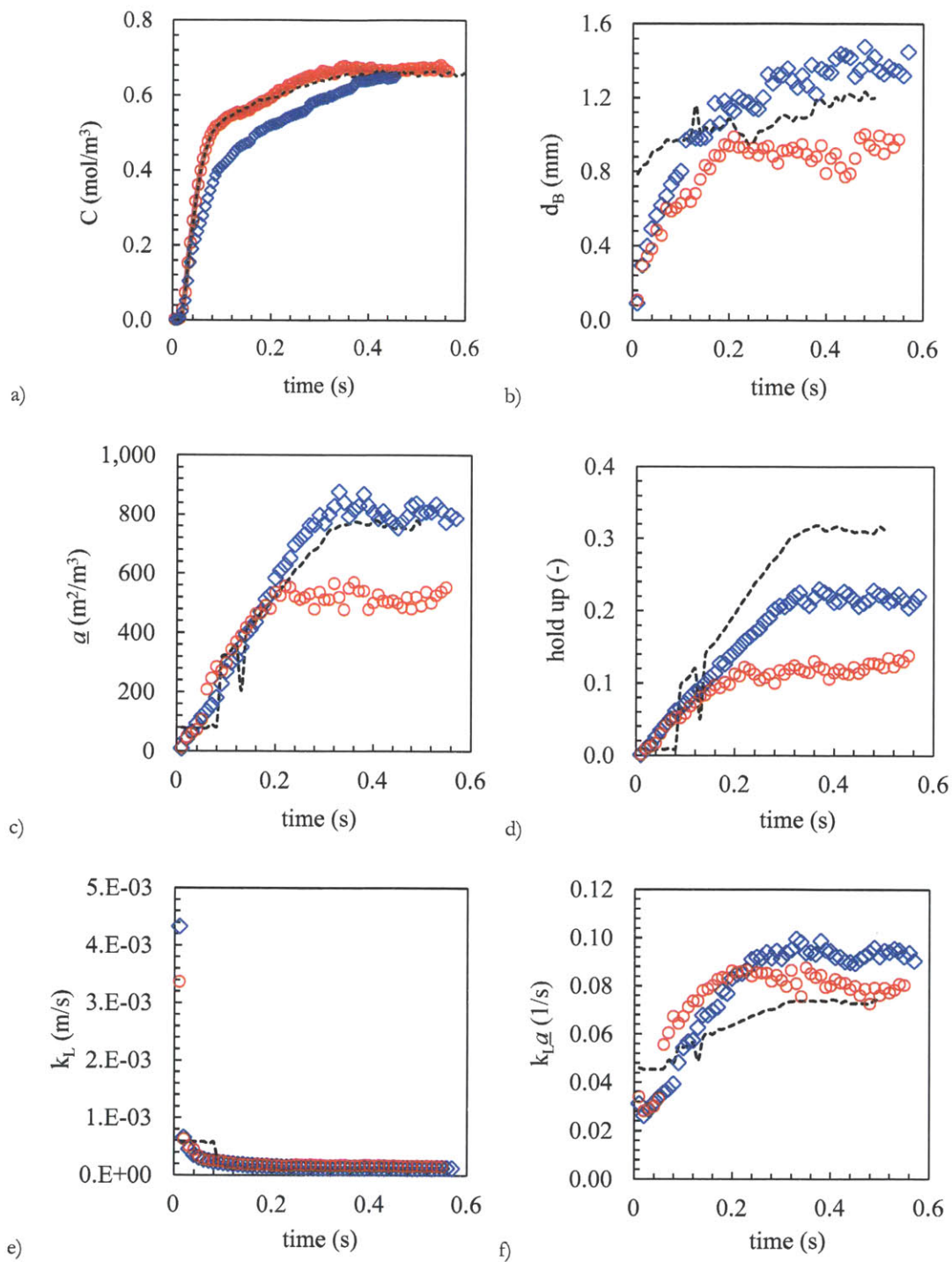


Figure 7.21: Effect of contact angle at 40 mL/min water and 10 mL/min hexane on a) bulk concentration in hexane; b) average drop size; c) specific interfacial area; d) hexane holdup; e) individual mass transfer coefficient; f) overall mass transfer coefficient Legend: \diamond , AFR; ----, No Dot; \circ , LFR

7.6 Conclusions

A modified version of the interFoam solver has been developed based on the approaches of Haroun and Marschall incorporating mass transfer of species across immiscible interfaces. With this solver, flow patterns for hexane/water have been predicted and are in good agreement with the experimental results at low phase flow rates. Larger discrepancies were encountered for flow rates above 40 mL/min due to artificial numerical coalescence observed in the simulations. This effect was seen to be more important in liquid/liquid than in gas/liquid systems, where the degree of coalescence in experiments is significantly large. Although refining the mesh could potentially solve this problem, the increase in computation time limits this possibility. An alternative solution is to develop an algorithm that is able to prevent numerical coalescence while keeping reasonable computation times.

Despite of the mentioned difficulties encountered, the modified solver is able to predict with reasonable accuracy the specific interfacial areas, individual mass transfer coefficients, and overall mass transfer coefficients ($k_{L,d}$) in the AFR, being in good agreement with semi empirical results based on the surface renewal theory of Danckwerts and visualization experiments. Based on these results, a study of the influence of fluid properties on the mass transfer efficiency was performed. It was concluded that the variable that affected the flow patterns the most (and more specially, the specific interfacial area) was the contact angle: by changing the wetting properties of the material, the flow regime can change from bubbly to stratified. Another important variable to consider was the interfacial tension between phases. It was seen that decreasing surface tension decreased droplet size. However, in order to achieve large specific interfacial areas and have a positive impact on the mass transfer process, increase in the dispersed phase flow rate to increase holdup is required. On the other hand, it was seen that viscosity of the continuous phase did not have a significant effect on mass transfer. The effect of reactor design was also seen to be non – significant for the flow rates tested. Although slight differences were observed in the flow characteristics, the overall mass transfer coefficients were seen to be within 17% difference.

All the studies performed in this work were based on two heart cells. From the visualization experiments performed for hexane/water and carbon dioxide/water, it is known that the droplet/bubble size decreases from the inlet towards the outlet of the reactor. Thus, a larger interfacial area is expected downstream as a consequence of smaller droplet size, and therefore, larger values for $k_L a$ assuming that k_L remains constant along the reactor flow path.

7.7 Notation

a	specific interfacial area ($\text{m}^2 \text{m}^{-3}$)
C_i	concentration of i (mol m^{-3})
C_{max}	maximum concentration (mol m^{-3})
D_i	diffusion coefficient of species i ($\text{m}^2 \text{s}^{-1}$)
He	Henry constant (-)
J_i	flux of species concentration ($\text{mol m}^{-2} \text{s}^{-1}$)
k_L	individual mass transfer coefficient (m s^{-1})
$k_L a$	overall mass transfer coefficient (s^{-1})
\vec{n}	normal vector to interface (-)
P	pressure (Pa)
Q_i	flow rate of phase i (mL/min)
t	time (s)
\vec{v}	velocity vector (m s^{-1})

Dimensionless numbers

Co	Courant number (-)
Sc	Schmidt number (-)

Greek letters

α	volume fraction (-)
$\tilde{\alpha}_p$	smoothed volume fraction (-)
$\alpha_1, \alpha_2, \beta_1, \beta_2$	constants (-)
ρ	density (kg/m ³)
θ_w	contact angle (°)
φ	mass flux (mol m ⁻² s ⁻¹)
σ	surface tension (N/m)
μ	viscosity (Pa s)

Superscripts

L	Liquid phase
G	Gas phase

Subscripts

1	phase 1
2	phase 2
12	interface
h	hexane
w	water

7.8 References

- (1) Ohta, M.; Suzuki, M. Numerical analysis of mass transfer from a free motion drop in a solvent extraction process. *Solvent Extr. Res. Dev.*, **1996**, *3*, 138–149
- (2) Sato, T.; Jung, R-T.; Abe, S. Direct simulation of droplet flow with mass transfer at interface. *Trans. ASME*, **2000**, *122*, 510-536

- (3) Davidson, M. R.; Rudman, M. Volume of fluid calculation of heat or mass transfer across deforming interfaces in two-fluid flow. *Numerical Heat Transfer, Part B: Fundamentals: An International Journal of Computation and Methodology*, **2002**, *41*, Issue 3-4, 291–308
- (4) Bothe, D.; Koebe, M.; Wielage, K.; Warnecke, H-J. VOF-simulations of mass transfer from single bubbles and bubble chains rising in aqueous solutions. *ASME/JSME 4th Joint Fluids Summer Engineering Conference*, Honolulu, Hawaii, **2003**. Paper No. FEDSM2003-45155, Vol. 2, 423-429; doi:10.1115/FEDSM2003-45155
- (5) Onea, A.; Worner, M.; Cacucib, D. G. A qualitative computational study of mass transfer in upward bubble train flow through square and rectangular mini-channels. *Chem. Eng. Sci.*, **2009**, *64*, Issue 7, 1416–1435
- (6) Haroun, Y.; Legendre, D.; Raynal, L. Volume of fluid method for interfacial reactive mass transfer: Application to stable liquid film. *Chem. Eng. Sci.*, **2010**, *65*, 2896–2909
- (7) Haroun, Y.; Raynal, L.; Legendre, D. Mass transfer and liquid hold-up determination in structured packing by CFD. *Chem. Eng. Sci.*, **2012**, *75*, 342–348
- (8) Marschall, H.; Hinterberger, K.; Schüler, C.; Habla, F. Hinrichsen, O. Numerical simulation of species transfer across fluid interfaces in free-surface flows using OpenFOAM. *Chem. Eng. Sci.*, **2012**, *78*, 111–127
- (9) Higbie, R. The rate of absorption of a pure gas into a still liquid during a short time of exposure. *Transactions of the American Institute of Chemical Engineers*, **1935**, *31*, 365-389
- (10) Danckwerts, P. V. Significance of liquid-film coefficients in gas-absorption. *Ind. Eng. Chem.*, **1951**, *43*, 6, 1460–1467
- (11) Nieves-Remacha, M. J.; Kulkarni, A. A.; Jensen, K. F. *Gas-Liquid Flow and Mass Transfer in an Advanced-Flow Reactor*” *Ind. Eng. Chem. Res.* **2013**, *52* (26), 8996 – 9010
- (12) Nieves-Remacha, M. J.; Kulkarni, A. A.; Jensen, K. F. *Hydrodynamics of Liquid-Liquid Dispersion in an Advanced-Flow Reactor*. *Ind. Eng. Chem. Res.* **2012**, *51* (50), 16251–16262

8 Ozonolysis

8.1 Abstract

Ozonolysis of alkenes is an exothermic reaction that requires very extreme conditions for heat management in conventional reactors. In addition, with ozone in the gas phase and the substrate in the liquid phase, ozonolysis is a mass transfer limited reaction. These two limitations for ozonolysis in conventional reactors can be overcome using microreactor technology, which has been demonstrated to yield high mass and heat transfer rates thanks to the small characteristic lengths. Few ozonolysis reactions have been demonstrated in microreactors, and fewer have been demonstrated in continuous flow high throughput devices. Here we use the Advanced-Flow Reactor (AFR) technology of Corning Inc. to demonstrate the scale-up of ozonolysis of alkenes from micro to milli scales. It was concluded from the experiments that the mass transfer rates in both the Low Flow Reactor (LFR, 0.45 mL) and the AFR (8.7 mL) are so large that the conversions of alkene are limited only by the amount of ozone available in the gas phase.

8.2 Introduction

The ozonolysis reaction has been studied since 1855 by Schönbein¹ and has been used for decades for water purification and in organic synthesis with direct application in fine chemicals and pharmaceutical industries^{2,3}. Oxidations in the presence of ozone have several advantages over other conventional oxidants, such as permanganate, osmium tetroxide, periodic acid, or peroxides. Using ozone, oxidation of compounds can be done in absence of catalyst, since ozone is a very strong oxidant and thus, the activation energies are usually low. In addition, although ozone by itself is toxic, the byproduct produced in oxidation reactions is oxygen, and thus, makes the ozonolysis reaction environmentally friendly. It is also very efficient reaction from an atom efficiency viewpoint.

There are, however, issues related to safety, due to the low-molecular weight unstable intermediates (ozonides, peroxides) produced during the reaction that can lead to explosions and limit the applicability of

ozonolysis at large scales. In addition, ozonolysis is a very exothermic reaction ($> 50 \text{ kcal/mol}^4$) that requires very extreme conditions of heat management and is normally carried out at $-78 \text{ }^\circ\text{C}^{2-6}$. However, these limitations can be overcome using microreactor technology. First, microreactors have been demonstrated to reduce the accumulation of intermediates reducing the risk of explosion during ozonolysis⁷. In addition, microreactors provide very high mass and heat transfer rates, therefore reducing the need of extreme heat management conditions. Ozonolysis reactions can be thus performed at ambient conditions while achieving high conversions and selectivities, as it was already shown by Wada et al. in 2006 using a multichannel microreactor⁸.

There are other examples of ozonolysis reactions performed in microreactors. In 2007, Jähnisch and collaborators performed the ozonolysis of acetic acid 1-vinyl-hexyl ester in a falling film microreactor designed at the Institut für Mikrotechnik Mainz (IMM, Germany)⁹. In 2009, Jähnisch et al. performed an ozonolysis reduction sequence to synthesize vitamin D analogues in a microplant, using five different microstructured devices for the ozonolysis step. Two of them are falling film microreactors designed by IMM and mikroglass chemtech GmbH (Germany), the third one is a cyclone mixer made by *mikroglass*, and additional five- and one-channel mixers typical for liquid-liquid reactions were tested. The cyclone mixer and 5-channel mixer demonstrated better performance than the falling film approach¹⁰. Steven Ley et al. demonstrated in 2010 the concept of using a semipermeable Teflon-2400 tube (90 cm long and 0.6 mm I.D.) for ozonolysis of several substrates achieving yields from 57 to 95 % for 1 h residence time¹¹. In 2011, Irfan et al. demonstrated the use of a commercially available flow reactor (O-Cube) performing ozonolysis for several substrates from $0 \text{ }^\circ\text{C}$ to ambient temperature and flow rates ranging from 0.2 – 2.0 mL/min achieving isolated yields of 72 – 90 %¹². In 2013 Roydhouse et al. demonstrated the use of Vapourtec technology coupled with an ozone generator to perform ozonolysis of complex organic substrates in flow, observing good conversion (49–99 %) to the corresponding aldehydes and ketones using an inflow quench of triphenylphosphine^{13,14}.

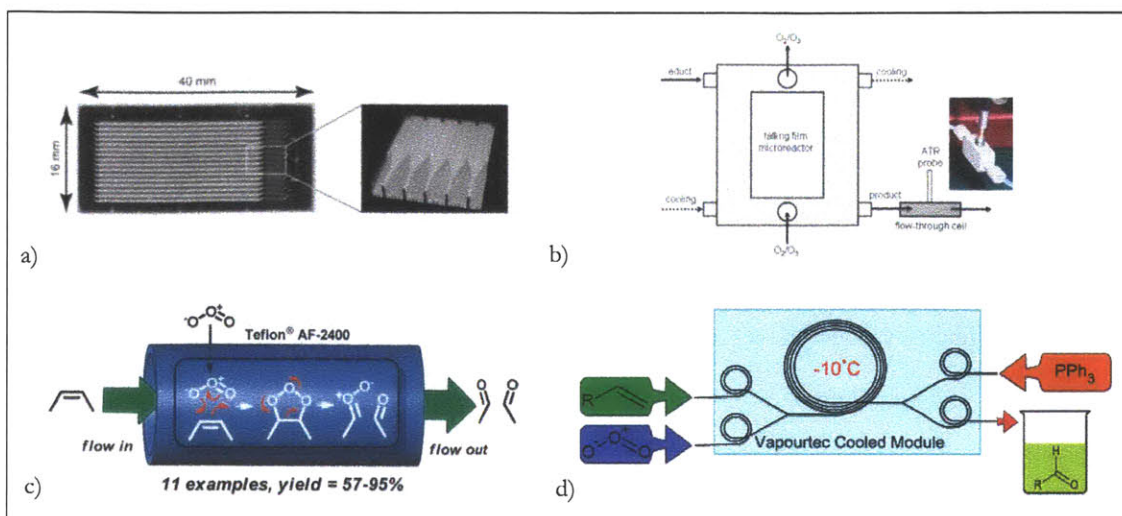


Figure 8.1: Examples of ozonolysis using microreactor technology: a) multichannel microreactor ⁸; b) falling film microreactor ^{9, 10}; c) semipermeable Teflon AF-2400 ¹¹; d) Vapourtec technology ¹³

Due to the instability of the ozone molecule, this gas is normally generated on site, existing different methods to achieve this purpose. The most used is the corona discharge, since the UV light methods provide very low concentrations (0.5 weight % or lower). Concentrations up to 16 % in weight can be achieved for inputs of 95 % volume in oxygen and 5 % nitrogen, which also participates in the generation of ozone through a series of radical reactions.

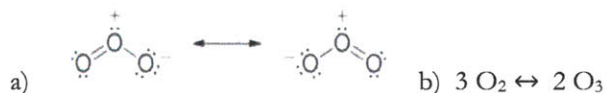


Figure 8.2: Characteristics of the ozone molecule. a) ozone molecule; b) reaction for the generation of ozone.

The reaction mechanism for ozonolysis as described by Criegee ⁶ is comprised by several steps (Figure 8.3):

- a) Formation of a 1,2,3-trioxolane (primary ozonide or molozonide) through the cycloaddition of ozone to the alkene

- b) Decomposition of the short lived primary ozonide into a carbonyl compound and carbonyl oxide (zwitterion). This can react with other zwitterions leading to diperoxide 1,2,3,5-tetraoxalane and polymeric peroxides.
- c) Addition of the carbonyl compound to the carbonyl oxide to produce a 1,2,4-trioxolane (secondary ozonide or ozonide)

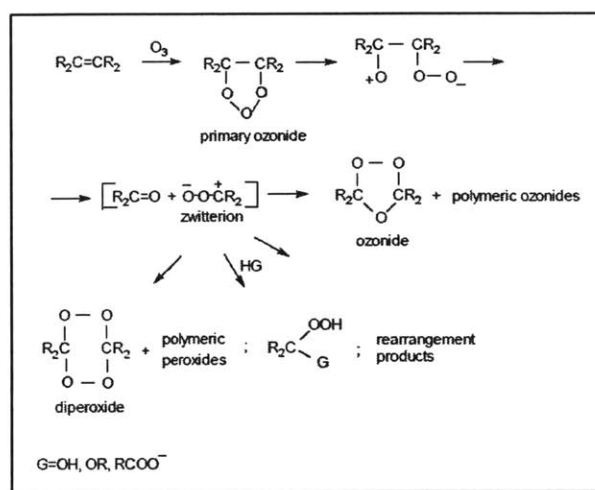


Figure 8.3: Mechanistic steps in ozonolysis reaction according to Criegee ^{4,6}

Depending on the workup procedure, different products can be obtained in the ozonolysis of alkenes:

- a) reducing agents lead to aldehydes or ketones. Strong reducing agents are BH_3 , Pt/H_2 , $Zn/HOAc$, $LiAlH_4$, although they may cause compatibility problems with other functional groups. Other reducing agents frequently used are dimethylsulfide, triethylphosphite, and triphenylphosphine; b) oxidant agents lead to carboxylic acids, such hydrogen peroxide.

While ozonolysis in liquid phase has been demonstrated in microreactors in several occasions, the throughput provided by these devices is very low, on the order of mg/min. Except for the falling film microreactor from IMM ⁹ that can operate at gas flow rates of 100 mL/min and liquid flow rates of 1 – 15

mL/min, microreactors reported in the literature work at very low flow rates (gas flow rate of 20 mL/min in the O-Cube¹² and 10 mL/min in the multichannel microreactor of Wada et al.⁸) or need very long reaction times to provide 100 % conversions¹¹. The Advanced-Flow Reactor (AFR) technology manufactured by Corning Inc. operates at 10 – 300 mL/min flow rate, yielding higher production rates that can increase further when configuring several units in parallel. Since the increase in throughput in the AFR is achieved by increasing the channel size from the micro scale to the milli scale, a question regarding the mass transfer performance in this device arises.

With ozone in the gas phase and the alkene substrate in the liquid phase, the overall reaction rate for the ozonolysis reaction may be determined by either the mass transfer process of ozone from the gas to the liquid phase, either the intrinsic kinetics, or a combination of both competing processes. Regarding the transport process, mass transfer coefficients for gas-liquid have been measured in the multichannel microreactor⁸ and the AFR¹⁶, yielding values of 2.5 and 0.2 – 3 s⁻¹ (depending on the phase flow rates), respectively. These values are at least one order of magnitude larger than the typical value for conventional stirred vessels for the same power consumption. On the other hand, kinetic rate constants for the ozonolysis of olefins with terminal double bonds, such as 1-hexene, 1-octene, and 1-decene, are high and similar (~ 10⁵ M⁻¹s⁻¹).^{4, 8} It is thus expected that the ozonolysis overall reaction rate is controlled by the mass transfer limiting step.

The objective of this study is to demonstrate that ozonolysis can be conducted using the AFR technology at ambient temperature with a good reactor performance. Three reactors are used for this purpose: a) a multichannel microreactor with posts and 54 μ L volume as designed by Wada et al.⁸; b) a low-flow reactor (LFR) with 0.45 mL volume; c) AFR with 8.7 mL volume. Both the LFR and the AFR follow similar reactor designs in the form of heart-shaped cells in series providing a convergent/divergent configuration, which helps increase the specific interfacial area to provide high mass transfer coefficients.

8.3 Experimental

8.3.1 Materials

Chemicals were used as received without prior purification steps. Potassium iodide, 1-decene, ethyl sorbate, triethylphosphite, and triphenylphosphine were purchased from Alfa Aesar, ethylacetate (solvent) from VWR, and the internal standard tridecane and Sudan Red 7B dye, from SigmaAldrich. 1-decene and ethyl sorbate were used as substrates for the ozonolysis reaction with concentrations ranging from 0.05 M to 0.28 M, while tridecane was used as internal standard due to its slow oxidation rate with ozone ⁸. Triethylphosphite and triphenylphosphine 0.28 M in ethyl acetate solutions were used as quench agents ^{8, 14}. Nitrogen and oxygen gas cylinders were purchased from Airgas.

8.3.2 Experimental setup

The schematics of the experimental setup for the ozonolysis reactions are shown in Figure 8.4. Ozone was produced in a water cooled ozone generator OT-5 from OzoneTechnology AB. The inlet composition of the ozone generator was 95 % volume oxygen and 5 % volume nitrogen, as recommended for maximum ozone production. The nitrogen and oxygen flow rates to the ozone generator were delivered using pre-calibrated mass flow controllers (UNIT). The ozone concentration was measured inline right at the outlet of the ozone generator using an ozone monitor (Teledyne Instruments Model 454H). Concentrations can range from 4 to 13 % weight, depending on inlet pressure, temperatures, humidity, and flow rates. A mass flow controller (Aalborg) was used to deliver the ozone/oxygen/nitrogen mixture to the reactor.

The reagent solution was delivered to the microreactor and the Low-Flow Reactor (LFR) using a syringe pump (Harvard Apparatus PHD2000) and to the AFR using a peristaltic pump (Thermo Scientific). The experiments were conducted at ambient temperature and atmospheric pressure at the outlet of the reactor. Samples of the liquid phase were collected at steady-state in glass vials containing the quench solution at 0 °C to prevent evaporation and were analyzed through gas chromatography. The non-consumed ozone at

the outlet of the reactor and the waste stream from the ozone generator was destroyed by bubbling the gas stream through an aqueous solution of potassium iodide 5 % wt.

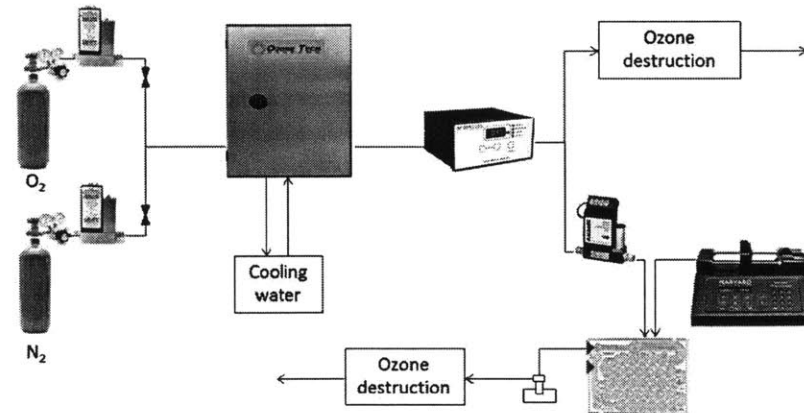


Figure 8.4: Experimental setup for ozonolysis. Oxygen and nitrogen stored in gas cylinders are introduced by mass flow controllers into the ozone generator. Ozone stream containing ~95 % vol. O₂, ~ 5 % vol. N₂, and ~ 5 % vol. O₃ is introduced into the reactor using a mass flow controller. A syringe or peristaltic pump is used for liquid flow. The product is quenched with reducing agent at 0 °C in collecting vial.

Reactions were conducted in three different reactors (Figure 8.5):

- Multichannel microreactor*: design used by Wada et al. in 2006⁸ composed by 16 reaction channels with posts to enhance mass transfer. Its internal volume is 54 μ L.
- Low-Flow Reactor (LFR)*: manufactured by Corning Inc., the LFR has an internal volume of 0.45 mL. Each module is designed by several rows of heart-shaped cells in series, which creates continuous breakup and coalescence of bubbles, enhancing mass transfer rates by creating large specific interfacial areas. Due to the small volume, the LFR is designed to study reactions in the laboratory at small scales. The height of the reactor is 0.35 mm and the operating flow rates range from 1 mL/min to 10 mL/min.
- Advanced-Flow Reactor (AFR)*: similar to the LFR, the AFR has several heart-shaped cells in series, with two posts inside as opposed to the single post present in the LFR. The volume for the AFR is

8.7 mL and operates with flow rates from 10 to 100 mL/min. Thus, it can be used for production purposes in a parallel configuration.

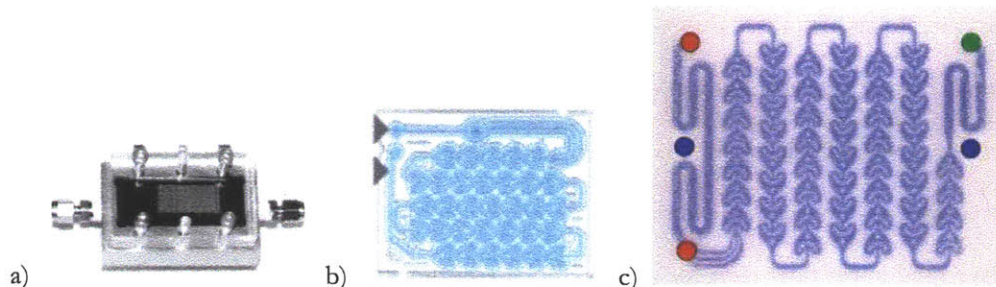


Figure 8.5: Reactors used in the ozonolysis experiments a) multichannel microreactor; b) LFR; c) AFR. Scaling factors are 10x and 200x for the LFR and AFR with respect to the microreactor, respectively.

The ozonolysis experiments in the multichannel microreactor were performed using gas flow rates ranging from 5 to 10 sccm and liquid flow rates from 0.116 to 0.035 mL/min. While the gas flow rate in the LFR was varied from 5 to 10 sccm, the liquid flow rate varied from 0.25 to 2 mL/min. The experiments performed in the AFR were conducted with gas flow rates of 100 sccm and liquid flow rates varying from 5 to 20 mL/min.

In addition, getting advantage from the transparency of the LFR and AFR reactors, which are made of glass, experiments with Sudan Red 7B dye 1 mM in ethyl acetate were also conducted. The original red color of this dye disappears after being oxidized by ozone, as used already by O'Brien et al.¹¹ This experiment is used to determine at which point along the reactor flow path the ozonolysis reaction has been completed. Instead of measuring substrate concentrations using gas chromatography, images of the reactor were taken at different operating conditions.

8.4 Results and discussion

Table 8.1 summarizes the conditions tested in the experiments conducted at ambient temperature and outlet atmospheric pressure for the three reactors using 1-decene as substrate. As it can be seen from the data, the multichannel microreactor can operate with large ratios of gas-to-liquid flow rates ($Q_G/Q_L = 86 - 286$). This helps have available higher amounts of ozone which makes possible to achieve full conversions for higher concentrations of reagent. However, the recommended flow rate range for the LFR is 1 – 10 mL/min. Here we have used lower flow rates for the liquid phase in order to have a larger ozone-to-alkene ratio and see if full conversions are achieved at these conditions. For the largest concentration of reagent (0.28 M), conversions below 21 % were achieved at liquid flow rates below the recommended values (0.35 and 0.58 mL/min). Since the ozone concentration is limited by the ozone generator and the liquid flow rate was already operating below the recommended values, the remaining parameter to change was the reagent concentration. For a 1-decene concentration of 0.07 M it was possible to achieve conversions over 99 % at the lowest liquid flow rates (0.23 and 0.35 mL/min) and largest gas flow rates (above 10 mL/min). Similar results were obtained for the AFR. Only when operating at the largest gas flow rates (100 mL/min), at the minimum liquid flow rate (5 mL/min), and at the lowest concentration (0.05 M), conversions of 99 % can be achieved. It was also observed that selectivity towards the formation of the aldehyde 1-nonanal was only achieved when triphenylphosphine, but not when using triethylphosphite. In this later case, also formation of nonanoic acid was obtained. This is in accordance with the results found by Roydhouse et al.¹³. The same behavior is observed for the ozonolysis of ethyl sorbate, as shown in Table 8.2. It is possible to achieve large conversions for the same operating conditions already discussed.

The question that remains unknown at this moment is whether there are mass transfer limitations in the LFR and AFR that prevent achieving higher conversions. In order to elucidate this, the experimental conversion of reagent for 1-decene and ethylsorbate has been plotted versus the molar ratio of ozone to alkene and are compared with the theoretical maximum conversion in Figure 8.6. As seen from the results, for practically all experiments, the maximum conversion is achieved regardless of the operating conditions

used as long as there is ozone available to react. The deviations from the theoretical maximum conversion are attributed to the associated experimental error and possible slight variations in the ozone concentration while the experiment was conducted. Since it was not possible to determine when the reaction was completed from these results, additional experiments were performed using Sudan Red 7B dye in the LFR and AFR.

Table 8.1: Operating conditions and conversion results for ozonolysis of 1-decene in multichannel microreactor, LFR, and AFR

Reactor	Q_L (mL/min)	C_S (mol/L)	Q_G (mL/min)	C_{O_3} (% wt.)	X_A (%)
Microreactor	0.116	0.28	10	8.5	69.8
Microreactor	0.116	0.28	10	9.6	78.4
Microreactor	0.116	0.28	10	10.4	89.5
Microreactor	0.059	0.28	10	10.5	100
Microreactor	0.059	0.28	10	7.1	100
Microreactor	0.035	0.28	10	7.6	100
Microreactor	0.035	0.28	10	10.6	100
LFR	0.58	0.28	10	7.3	12.4
LFR	0.35	0.28	10	7.4	20.9
LFR	0.23	0.07	10	10.4	99.6
LFR	0.23	0.07	22	10.4	100
LFR	0.35	0.07	10	7.7	77.8
LFR	0.35	0.07	10	10.3	99.2
LFR	0.58	0.07	10	10.5	77.3
LFR	0.84	0.07	5	9.2	26.6
LFR	0.84	0.07	10	9.4	37.5
LFR	0.84	0.07	22	9.6	86.5
LFR	1.68	0.07	4	8.0	7.2
LFR	1.68	0.07	5	9.4	10.6
LFR	1.68	0.07	22	9.6	43.0
LFR	1.68	0.07	8.5	9.1	17.5
LFR	1.68	0.07	22	11.6	53.0
LFR	0.84	0.16	10	8.8	16.4
LFR	0.23	0.16	5	9.3	27.0
LFR	0.23	0.16	10	9.2	62.2
LFR	0.35	0.16	10	9.0	42.2
LFR	0.35	0.16	5	9.2	23.4
LFR	0.58	0.16	10	9.2	27.7
AFR	10	0.05	100	4.5	22.9
AFR	20	0.05	100	4.5	10.6
AFR	5	0.05	100	10.3	99.9
AFR	10	0.05	100	9	62.2
AFR	20	0.05	100	8.5	30.2

Table 8.2: Operating conditions and conversion results for ozonolysis of ethylsorbate in LFR and AFR

Reactor	Q_L (mL/min)	C_s (mol/L)	Q_G (mL/min)	C_{O_3} (% wt.)	X_A (%)
LFR	0.25	0.34	10	8.8	34.7
LFR	0.5	0.34	10	8.7	18.8
LFR	1	0.34	10	8.45	7.6
LFR	0.5	0.34	5	8.74	7.4
LFR	0.25	0.34	10	4.7	20.5
LFR	0.75	0.34	10	4.4	7.6
AFR	5.4	0.06	100	1	12.4
AFR	5.4	0.06	100	7.6	86.6
AFR	11	0.06	100	6.5	34.0
AFR	11	0.06	100	5.8	30.9
AFR	5.4	0.06	100	12.7	98.5
AFR	11	0.06	100	12.7	68.5
AFR	21	0.06	100	12.7	37.1

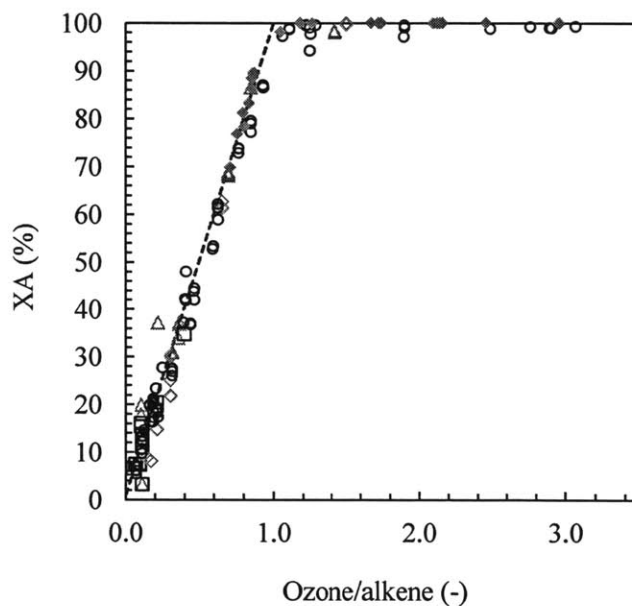


Figure 8.6: Alkene conversion (%) versus molar ratio ozone/alkene. Legend: \blacklozenge , multichannel microreactor; \diamond , 1-decene in AFR; \circ , 1-decene in LFR; \triangle , ethylsorbate in AFR; \square , ethylsorbate in LFR; - - -, theoretical maximum conversion. All reactors provide excellent mass transfer coefficients, which help achieve maximum conversion estimated from the availability of ozone in the gas phase.

The reaction of Sudan Red 7B dye is used to monitor the conversion of substrate along the flow path of the reactor. A concentration of 1 mM is used as comparison with the experiments conducted by O'Brian in a semipermeable Teflon AF – 2400 ¹¹. The images are shown in Figures 8.7 and 8.8 for the AFR at constant gas flow rate and for the LFR at constant liquid flow rate, respectively. As it is seen from the images, at all flow rates complete conversion is achieved within the first row of the AFR. For 1.5 mL/min of liquid flow rate in the LFR, complete conversions are also achieved even at the lowest gas flow rates in three heart cells.


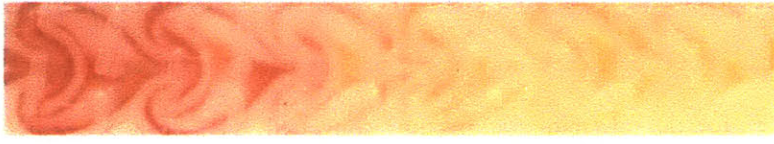

Q_L (mL/min)	Image
5	
10	
20	

Figure 8.7: Images for ozonolysis of Sudan Red 7B dye 1mM in AFR with 100 mL/min gas flow rate at 10 % wt.. The excellent mass transfer rates in the AFR help achieve complete conversion within 1.5, 3, and 5 heart cells for 5, 10, and 20 mL/min liquid flow rate, respectively.

The results of O'Brian et al. show that 2.34 min are required for complete conversion of Sudan Red 7B dye 1 mM in their semipermeable Teflon tube of 0.6 mm I.D and 3 cm long. Here, in 0.5 – 0.6 seconds (depending on the liquid flow rate) complete conversion of the substrate is achieved. Bleaching of the liquid solution is observed at different positions depending on the liquid flow rate: for 5 mL/min, complete decoloration is observed at the 1.5th hearts; for 10 mL/min, at the 3rd heart; and for 20 mL/min, at the 5th heart. The visualization experiments help estimate the mass transfer coefficients for this system. In order to

do this, a reaction model that assumes plug flow (a reasonable assumption after the analysis of residence time distribution for single-phase flow at different flow rates in Chapters 4 and 5) with mass transfer between phases was developed and is described by equations 8.1 – 8.3.

$$\frac{\partial C_{O_3}^G}{\partial z} = -\frac{k_L a}{u_G} (HeC_{O_3}^G - C_{O_3}^L) \quad (8.1)$$

$$\frac{\partial C_{O_3}^L}{\partial z} = \frac{1}{u_L} (k_L a (HeC_{O_3}^G - C_{O_3}^L) - kC_i^L C_{O_3}^L) \quad (8.2)$$

$$\frac{\partial C_i^L}{\partial z} = -\frac{1}{u_L} kC_i^L C_{O_3}^L \quad (8.3)$$

The conditions at $z = 0$ are known. The aim is to predict with the model the same experimental conversion at the end of the first heart. The experimental conversion can be estimated based on the visualization experiments: for a) 5 mL/min, the fraction ‘1 heart/1.5 hearts’, which corresponds to 66 % of the reagent, has been converted; b) for 10 mL/min, the fraction is ‘1 heart/3 hearts’ and corresponds to 33 % conversion; c) for 20 mL/min, the fraction converted is ‘1 heart/5 hearts’, corresponding to 20 % conversion.

Notice here that for the calculation of the phase velocities it was considered that the streams split into two with half flow rates. In addition, as a first approximation for $k_L a$, the correlation in terms of residence time in the AFR that was obtained at horizontal orientation of the AFR module for carbon dioxide/water was used (eq 8.4).

$$k_L a = 8.32 \tau_{AFR}^{-1.27} \quad (8.4)$$

With these values for $k_L a$ at the different residence times, conversions of 87 %, 47 %, and 27 % for the conditions tested were obtained. However, reducing the $k_L a$ values by a factor of 1.36 led to the correct conversions with minimal errors: 66 %, 34 %, and 20 %. The resulting $k_L a$ values were 0.80, 0.86, and 0.96 s⁻¹ for the flow rates tested. For the I.FR, the estimated overall mass transfer coefficients for fixed liquid flow rates to 1.5 mL/min and decreasing gas flow rates (10, 6, and 4 mL/min) were 2.2, 1.7, and 1.4 s⁻¹,

respectively. In all cases, full conversion is achieved within the second or third heart cell. Moreover, conversions for the ozonolysis of 1-decene in the LFR have been predicted using this model and the results are shown in Figure 8.9. In all cases, the maximum conversion is achieved at the outlet of the reactor thanks to the high mass transfer rates provided by this reactor design.

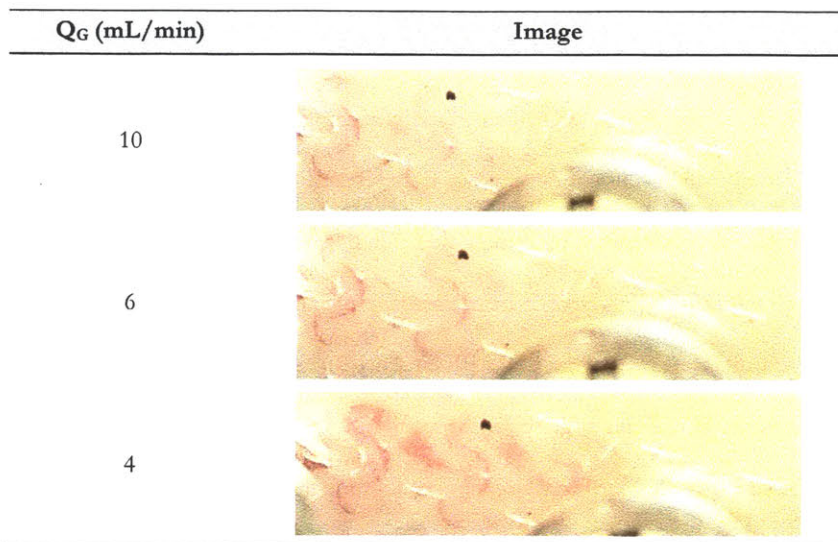


Figure 8.8: Images for ozonolysis of Sudan Red 7B dye 1mM in LFR at 1.5 mL/min and 10 % wt. ozone in the gas phase. Excellent mass transfer rates are also achieved in the LFR. Complete conversions are obtained within the first three hearts for all gas flow rates.

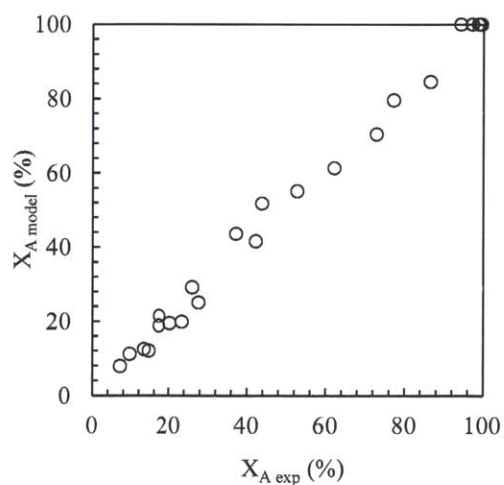


Figure 8.9: Predicted and experimental conversion of alkene. Good agreement is observed between experimental conversions and obtained with the simplified model for the ozonolysis of alkenes.

8.5 Conclusions

Ozonolysis of alkenes has been conducted in a multichannel microreactor, a Low-Flow Reactor (LFR), and an Advanced-Flow Reactor (AFR) to demonstrate the scale-up of multiphase reactions. For this reaction, the kinetic rate constants are very high and thus, the limiting step is the mass transfer process of ozone from the gas to the liquid phase. It was observed that the maximum conversion of alkene from the amount of ozone available in the gas phase was achieved in all reactors, regardless of the operating conditions tested. Therefore, although the overall reaction rate is mass transfer limited, the transport process is also fast. This was also shown through the ozonolysis of Sudan Red 7B dye in both the AFR and the LFR, where the reaction was completed within the first row of hearts in both reactors. Values for k_{LG} were estimated to be in the range 0.80 – 0.96 and 1.4 – 2.2 s⁻¹ in the AFR and LFR, respectively. This shows that the AFR still provides high mass transfer coefficients at large throughputs, which make it useful to conduct multiphase reactions that suffer from mass transfer limitations in conventional contactors.

Regarding the operating parameters of each reactor, the multichannel microreactor operates at flow rate ratios of gas/liquid that can range from 90 to 290 ensuring enough ozone availability. However, the LFR and AFR are able to work at approximate ratios of 10 – 60, which limits the application of these reactors at higher substrate concentrations. Recycling of the product after separation of the gas stream would be an alternative to this issue. On the other hand, the multichannel microreactor with a volume of 0.054 mL provides a very low throughput, whereas the LFR and AFR operate at larger scales: 10 and 200 times larger in comparison with the microreactor. The AFR can operate up to 300 mL/min flow rate, which would increase the potential application for ozonolysis at higher substrate concentrations, increasing the throughput 100 times with respect to the multichannel microreactor. In addition, several modules in parallel can be used to scale-out the reaction and achieve even larger production rates.

8.6 Notation

$C_{O_3}^G$	ozone concentration in the gas phase (mol/L)
$C_{O_3}^L$	ozone concentration in the liquid phase (mol/L)
C_i^L	alkene concentration in the liquid phase (mol/L)
He	Henry constant (-)
k	kinetic rate constant (Lmol ⁻¹ s ⁻¹)
$k_L a$	overall mass transfer coefficient (1/s)
τ_{AFR}	residence time (s)
U_G	gas velocity (m/s)
U_L	liquid velocity (m/s)
X_A	alkene conversion (%)
z	position along reactor path length (m)

8.7 References

- (1) Schönbein, C. F. J. *Prakt. Chem.* **1855**, *66*, 282
- (2) Van Ornum, S. G.; Champeau, R. M.; Pariza, R. Ozonolysis applications for drug synthesis. *Chem. Rev.* **2006**, *106*, 2990–3001
- (3) Caron, S.; Dugger, R. W.; Ruggeri, S. G. Ragan, J. A.; Ripin, D. H. B. Large-scale oxidations in the pharmaceutical industry. *Chem. Rev.* **2006**, *106*, 2943–2989
- (4) Zaikov, G. Rakovsky, S. Ozonation of organic and polymer compounds. Chapter 3: Ozonolysis of alkenes in liquid phase. Smithers Rapra, **2009**, ISBN 978-1-84735-143-2
- (5) Deslongchamps, P.; Moreau, C. Ozonolysis of acetals. (1) ester synthesis, (2) THP ether cleavage, (3) Selective Oxidation of p-Glycoside, (4) Oxidative Removal of benzylidene and ethylidene Protecting Groups. *Canadian Journal of Chemistry*, **1971**, *49*, 2465
- (6) Criegee, R. Mechanism of ozonolysis. *Angew. Chem. Internat. Edit.*, **1975**, *14*, 11

- (7) Steinfeldt, N.; Bentrup, U.; Jähnisch, K. Reaction mechanism and in situ ATR spectroscopic studies of the 1-decene ozonolysis in micro and semibatch reactor. *Ind. Eng. Chem. Res.*, **2010**, *49* (1), 72–80
- (8) Wada, Y.; Schmidt, M. A.; Jensen, K. F. Flow distribution and ozonolysis in gas-liquid multichannel microreactors. *Ind. Eng. Chem. Res.* **2006**, *45*, 8036–8042
- (9) Steinfeldt, N.; Abdallah, R.; Dingerdissen, U.; Jähnisch, K. Ozonolysis of acetic acid 1-vinyl-hexyl ester in a falling film microreactor. *Org. Process Res. Dev.*, **2007**, *11* (6), 1025–1031
- (10) Hübner, S.; Bentrup, U.; Budde, U.; Lovis, K.; Dietrich, T.; Freitag, A.; Küpper, L.; Jähnisch, K. An ozonolysis–reduction sequence for the synthesis of pharmaceutical intermediates in microstructured devices. *Org. Process Res. Dev.*, **2009**, *13* (5), 952–960
- (11) O'Brien, M.; Baxendale, I. R.; Ley, S. V. Flow Ozonolysis using a semipermeable Teflon AF-2400 membrane to effect gas-liquid contact. *Org. Lett.*, **2010**, *12*, 7, 1596–1598
- (12) Irfan, M.; Glasnov, T. N.; Kappe, C. O. Continuous flow ozonolysis in a laboratory scale reactor. *Org. Lett.*, **2011**, *13* (5), 984–987
- (13) Roydhouse, M. D.; Ghaini, A.; Constantinou, A.; Cantu-Perez, A.; Motherwell, W. B.; Gavriilidis, A. Ozonolysis in flow using capillary reactors. *Org. Process Res. Dev.* **2011**, *15*, 989–996
- (14) Roydhouse, M. D.; Motherwell, W. B.; Constantinou, A.; Gavriilidis, A.; Wheeler, R.; Down, K.; Campbell, I. Ozonolysis of some complex organic substrates in flow. *RSC Advances*, **2013**, *3*, 5076
- (15) Schiaffo, C. E.; Dussault, P. H. Ozonolysis in solvent/water mixtures: direct conversion of alkenes to aldehydes and ketones. *J. Org. Chem.* **2008**, *73*, 4688–4690
- (16) Nieves-Remacha, M. J.; Kulkarni, A. A.; Jensen, K. F. Gas–Liquid Flow and Mass Transfer in an Advanced-Flow Reactor. *Ind. Eng. Chem. Res.* **2013**, *52*, 8996–9010

9 Summary, conclusions, and future research direction

9.1 Summary and conclusions

The main contribution of this thesis to the chemical engineering field is to demonstrate the efficiency for multiphase reactions of the Advanced-Flow Reactor (AFR) technology manufactured by Corning Inc. as an alternative that combines scale-up and scale-out concepts to provide large throughputs with potential commercial application.

From microreactor technology, it has been demonstrated in many publications through several years that mass and heat transfer rates are enhanced with respect to conventional contactors thanks to the small diffusion lengths in microdevices. The challenge was how to increase production to levels of kg/min while keeping the good mass and heat transfer performance so that this technology can be not only applied in laboratories for micro scale studies, but also for production purposes. Throughput can be increased by either scale-up procedure (an increase in channel size and/or an increase of the flow rates), or by scale-out (parallelization of units). The AFR technology combines both approaches. While microreactors operate in laminar flow at low Reynolds numbers, the AFR has a broader operating spectrum regime, ranging from laminar to transitional and turbulent regime at the largest flow rates.

The experimental study of the hydrodynamic characteristics for two-phase flow in the AFR for carbon dioxide/water (Chapter 2) and hexane/water (Chapter 3) systems showed that overall mass transfer coefficients in the range $0.1 - 10 \text{ s}^{-1}$ can be achieved in the AFR, depending on the phase flow rates. Large specific interfacial areas are created ($100 - 10,000 \text{ m}^{-1}$) thanks to the reactor design in the form of heart-shaped cells with convergent/divergent configuration in series, which helps break the dispersed phase creating new interfaces. Having simultaneously large dispersed phase holdup (by increasing the dispersed phase flow rate) and small droplet/bubble sizes (increasing continuous phase flow rate) is an indication of the high specific interfacial areas. In summary, the mass transfer efficiency was shown to be superior to other conventional multiphase contactors when comparing mass transfer rates in terms of power consumption.

It was also shown in Chapter 4 through residence time distribution (RTD) experiments for 10 – 80 mL/min water that the AFR behaves as a plug flow with a small degree of dispersion ($Pe = 60 - 124$), which increases at the lowest flow rates and is due mainly to the additional tubing and measurement device associated with the reactor. Comparison with single-parameter models such as tanks in series and dispersion models gave fair agreement with experimental results, but a better agreement with at least 78 % increase in accuracy, was found using a two-zone model accounting for the presence of stagnant zones in the system.

Computational Fluid Dynamic (CFD) simulations using the open source software OpenFOAM were performed to model single-phase flow in the AFR (Chapter 5). An excellent agreement between experimental and predicted pressure drop and residence time distributions was obtained. Velocity profiles and streamlines revealed the presence of low-velocity regions between the two obstacles within the heart-cells in the Gen 1 AFR and recirculation zones above 40 mL/min water flow rate. This finding led to study the effect of reactor design on the flow patterns and RTD. While it was observed that the reactor design ('dot', 'no dot', and 'low-flow reactor') had an effect on flow patterns and RTD, it was concluded that the effect on the final conversion obtained for a first order reaction was not significant and was 95 to 99 % the plug flow conversion for all three designs. The Low-Flow Reactor (LFR) whose use is devoted for laboratory scale studies, showed a narrower RTD, achieving 99 % the plug flow conversion. Therefore, the approximation of both the LFR and AFR as plug flow reactors is shown to be a reasonable assumption for simple calculations.

In addition, the OpenFOAM solver based on the volume-of-fluid (VOF) method has been demonstrated to be capable of predicting two-phase flow in simple geometries and the AFR (Chapter 6). Challenges normally encountered using VOF methods have been illustrated with examples and best practices to achieve good numerical predictions were presented. A modified version of the OpenFOAM solver to account for mass transfer and reaction was developed and validated using simple examples (Chapter 7). Predictions in the AFR were achieved in agreement with semiempirical values in terms of specific interfacial areas, individual and overall mass transfer coefficients. Larger discrepancies were encountered for flow rates above 40 mL/min due to artificial numerical coalescence observed in the simulations for droplets closer than

one cell size. From the study of the influence of fluid properties on the flow patterns, it was concluded that the wetting properties (contact angle) have the greatest effect and can change the pattern from bubbly to stratified flow. Combination of small droplet sizes (which are achieved for low interfacial tensions) and high holdups (achieved by increasing dispersed phase flow rate) helps increase the specific interfacial areas, which in turn, increases the overall mass transfer coefficients. No significant differences among three different designs were encountered.

Experimental ozonolysis of alkenes as example of a mass and heat transfer limited reaction performed in a microreactor, LFR, and AFR, demonstrated once more the excellent mass transfer performance that the microreactor and AFR technologies provide. The throughput was increased by 100 times with respect to the multichannel microreactor while achieving complete conversions, but can be further increased by parallelization of several AFR modules as required by the demand.

This work also shows the impact that the AFR technology can have in the context of process intensification and the current interest of fine chemical and pharmaceutical industries for operating in flow versus the well-established and traditional batch processes. The use of continuous flow technologies can help reduce the time required for process development from the laboratory to the production scale. Issues related to the scale-up process in conventional reactors such as stirred tanks can be alleviated using the different designs provided by Corning Inc.

9.2 Future research direction

The demonstration of the Advanced-Flow technology applied to multiphase systems has been conducted from a fundamentally based viewpoint in this thesis. There are a few practical examples of reactions conducted in the AFR which have been published in the literature, but this technology has not been extensively studied yet. Future investigations should include a wider range of multiphase reactive systems involving two and three phases, different temperature and pressures, and different kinetic behaviors. Scale-up

to AFR reactor designs such as the Gen 3 and Gen 4 reactors, and scale-out by parallelization of units, would demonstrate the applicability of these reactors at commercial scales for a broader range of reaction systems.

Regarding the flow visualization experiments, it would be very useful to investigate the hydrodynamics of two-phase and three-phase flows including a broader range of fluid properties, and temperature and pressure conditions. Flow patterns, evolution of drop/bubble size distributions, holdups, pressure drops, and ultimately, mass transfer coefficients, can be obtained from the visualization images. If the analytical method is automatized, averaged values over time could be obtained and the analysis could be performed faster. In addition, the results obtained could be further used to validate the OpenFOAM calculations.

Two-phase flow CFD simulations have been limited in this thesis to just two heart-shaped cells due to computation time constraints. From the visualization experiments performed for hexane/water and carbon dioxide/water, it is known that the droplet/bubble size decreases from the inlet towards the outlet of the reactor. Thus, a larger interfacial area is expected to be encountered downstream which enhances the mass transfer process. Developing a technique that enables simulating the entire AFR for two-phase flow would be very useful to study mass transfer processes and reactions using CFD for the entire system. Another approach is to develop an algorithm that can prevent the numerical coalescence of interfaces that was observed in our simulations in such a way that coarse meshes can be used to reduce the computation time. Incorporation of volume change for different species and reactions, as well as extension of the solver to three-phase systems, could extend the applicability of the solver further. An additional improvement of the solver is to add energy conservation equations coupled with mass transfer and momentum equations. Careful validation of each step needs to be performed to guarantee a successful outcome for the improved solver. In addition, pressure and temperature have been kept constant at ambient conditions, but further work needs to be performed for a broader range of these variables.

APPENDICES

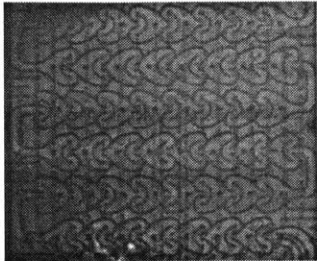
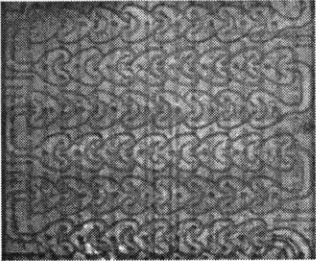
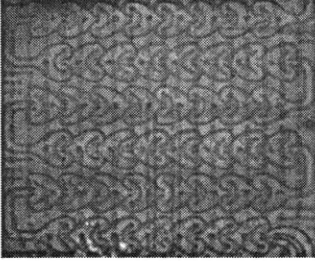
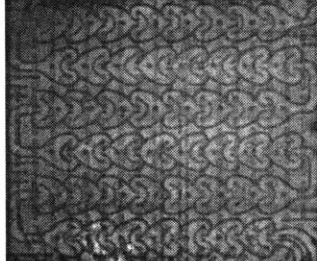
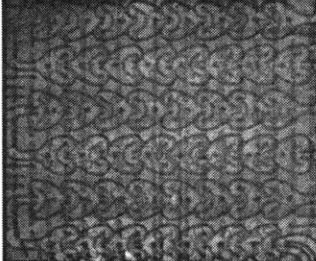
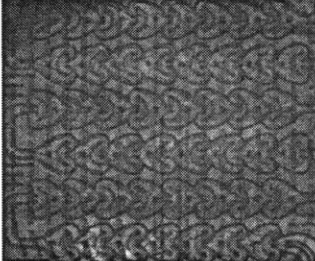
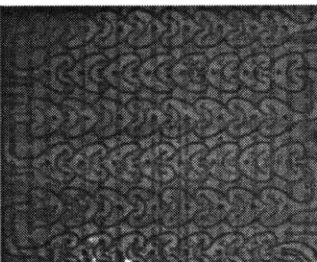
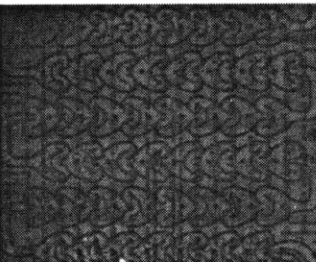
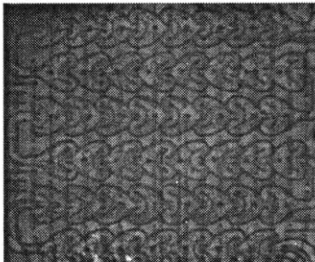
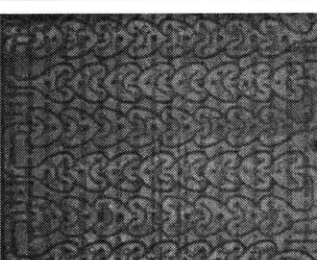
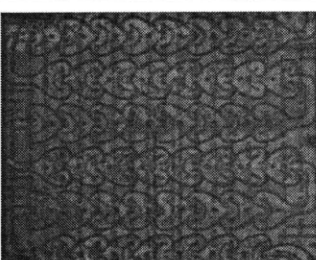
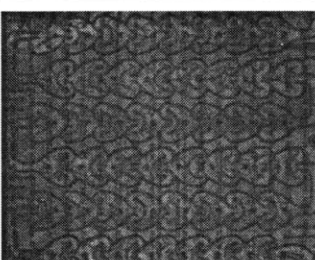
Q _L	Gas flow rates		
10	 <p data-bbox="386 590 501 617">5.6 ml/min</p>	 <p data-bbox="743 590 875 617">20.8 ml/min</p>	 <p data-bbox="1109 590 1240 617">35.8 ml/min</p>
20	 <p data-bbox="386 911 501 938">13.3 ml/min</p>	 <p data-bbox="743 911 875 938">35.8 ml/min</p>	 <p data-bbox="1109 911 1240 938">73.3 ml/min</p>
30	 <p data-bbox="386 1247 501 1274">13.3 ml/min</p>	 <p data-bbox="743 1247 875 1274">35.8 ml/min</p>	 <p data-bbox="1109 1247 1240 1274">73.3 ml/min</p>
40	 <p data-bbox="386 1572 501 1600">26.8 ml/min</p>	 <p data-bbox="743 1572 875 1600">58.3 ml/min</p>	 <p data-bbox="1109 1572 1240 1600">70.3 ml/min</p>

Figure A.1.1: Gas-liquid flow images in AFR module as function of flow rates (mL/min) in horizontal orientation

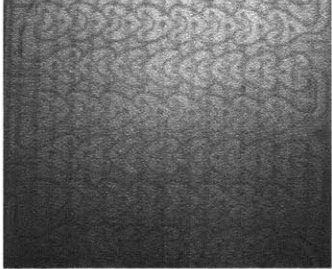
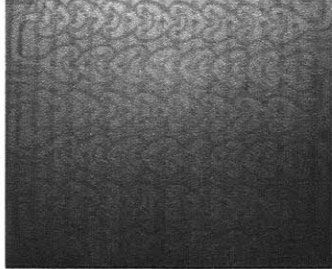
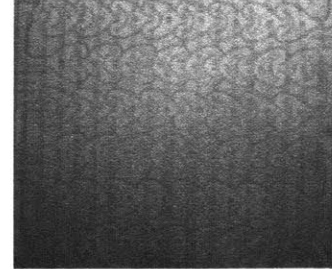
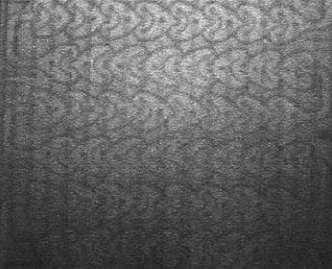
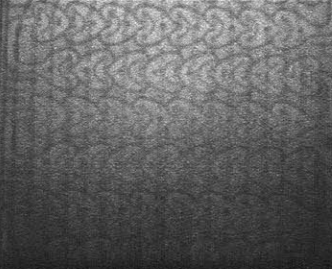
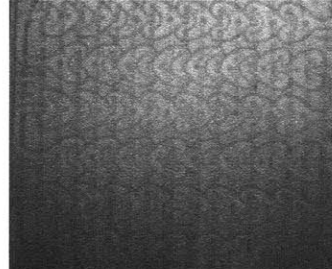
Q _L	Gas flow rates		
60	 <p data-bbox="391 575 516 604">23.8 ml/min</p>	 <p data-bbox="753 575 878 604">35.8 ml/min</p>	 <p data-bbox="1115 575 1240 604">77.8 ml/min</p>
80	 <p data-bbox="391 909 516 938">35.8 ml/min</p>	 <p data-bbox="753 909 878 938">73.3 ml/min</p>	 <p data-bbox="1115 909 1240 938">88.2 ml/min</p>

Figure A.1.1: Gas-liquid flow images in AFR module as function of flow rates (mL/min) in horizontal orientation (Cont.)

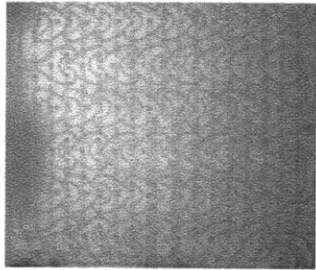
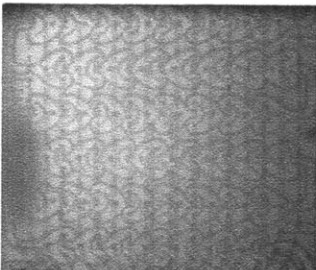
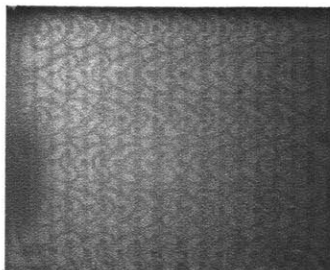
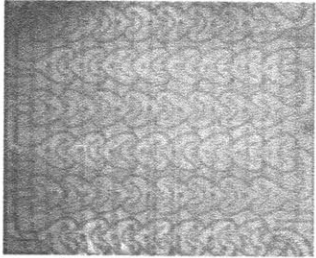
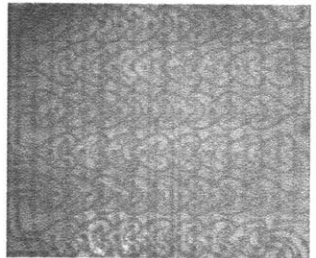
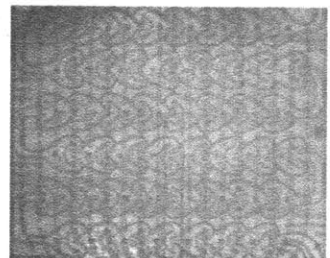
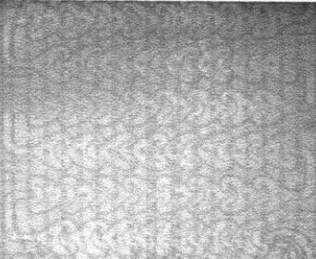
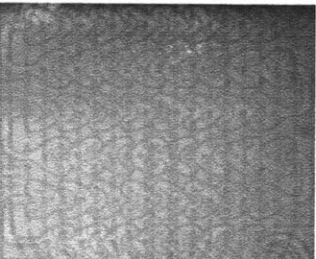
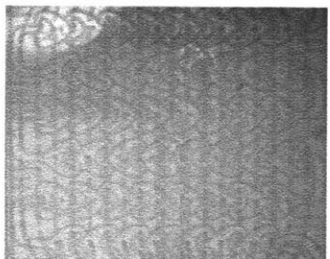
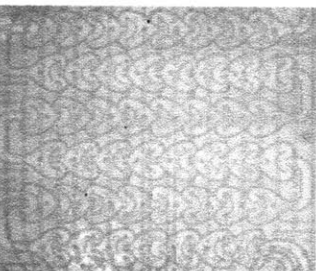
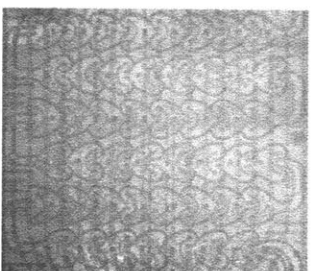
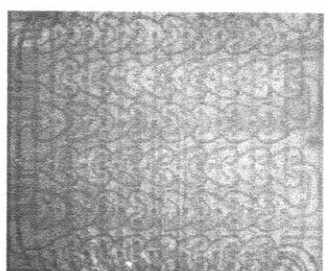
Q _L	Gas flow rates		
10	 <p data-bbox="440 575 565 602">13.3 ml/min</p>	 <p data-bbox="786 575 911 602">35.8 ml/min</p>	 <p data-bbox="1138 575 1263 602">70.3 ml/min</p>
20	 <p data-bbox="440 888 565 915">5.8 ml/min</p>	 <p data-bbox="786 888 911 915">35.8 ml/min</p>	 <p data-bbox="1138 888 1263 915">73.3 ml/min</p>
30	 <p data-bbox="440 1201 565 1228">13.3 ml/min</p>	 <p data-bbox="786 1201 911 1228">35.8 ml/min</p>	 <p data-bbox="1138 1201 1263 1228">65.8 ml/min</p>
40	 <p data-bbox="440 1526 565 1554">26.8 ml/min</p>	 <p data-bbox="786 1526 911 1554">58.3 ml/min</p>	 <p data-bbox="1138 1526 1263 1554">70.3 ml/min</p>

Figure A.1.2: Gas-liquid flow images in AFR module as function of flow rates (mL/min) in vertical orientation

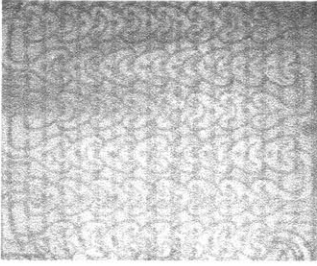
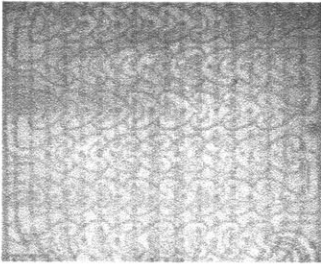
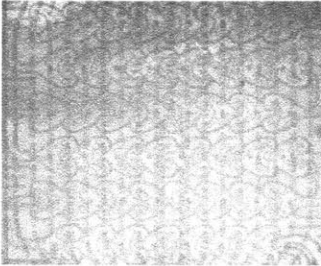
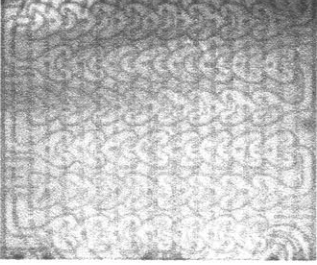
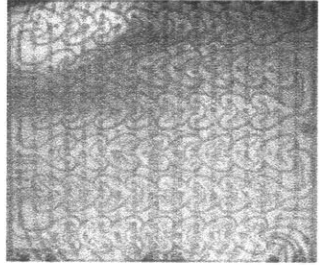
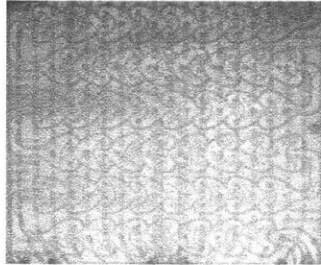
Q_L	Gas flow rates		
60	 <p data-bbox="407 577 521 604">24 ml/min</p>	 <p data-bbox="764 577 870 604">73 ml/min</p>	 <p data-bbox="1122 577 1243 604">106 ml/min</p>
80	 <p data-bbox="407 898 521 926">24 ml/min</p>	 <p data-bbox="764 898 870 926">73 ml/min</p>	 <p data-bbox="1122 898 1243 926">106 ml/min</p>

Figure A.1.2: Gas-liquid flow images in AFR module as function of flow rates (mL/min) in vertical orientation (Cont.)

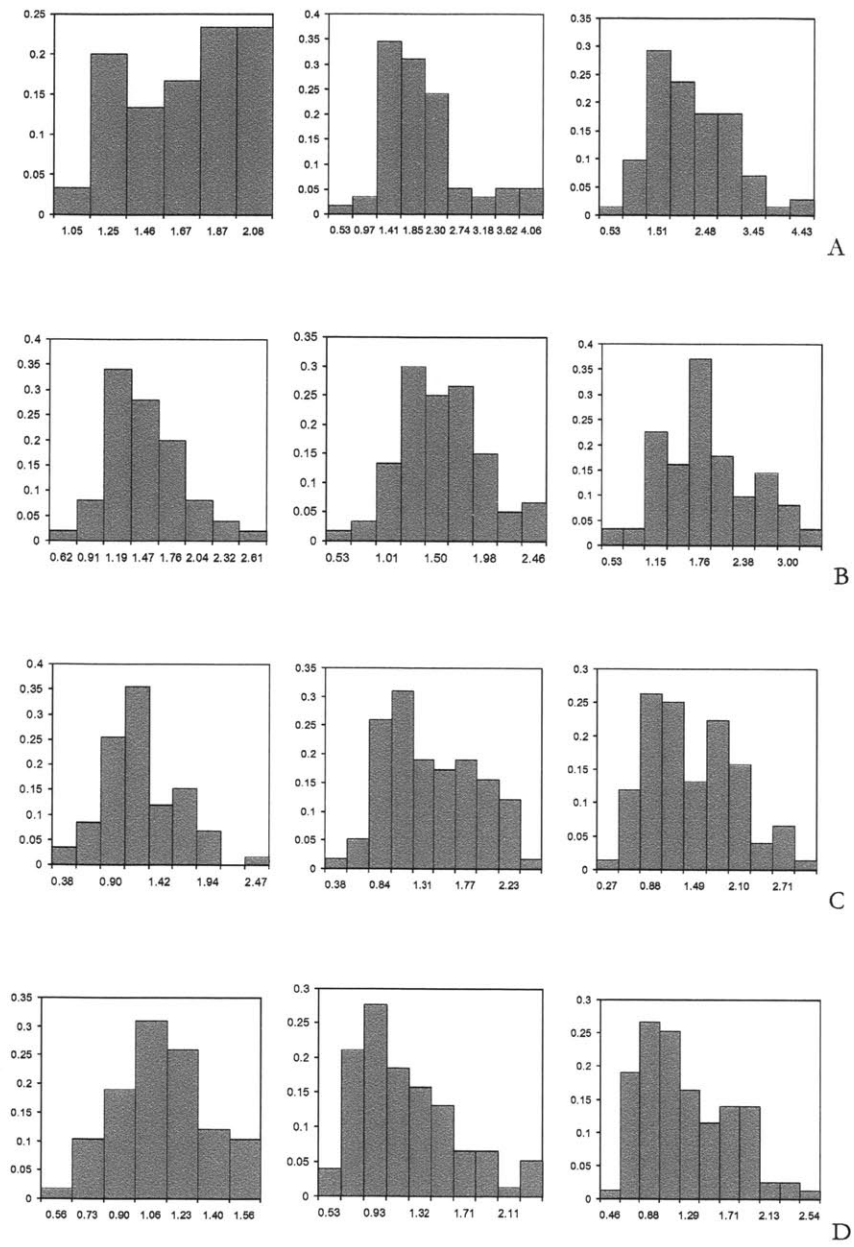


Figure A.2: Bubble size distribution in the AFR at different gas and liquid flow rates for vertical orientation. Gas flow rates are given from left to right for every liquid flow rate. (A) $Q_L = 20$ (ml/min), $Q_G = 13, 36, 66$ ml/min, (B) $Q_L = 30$ (ml/min), $Q_G = 21, 36, 66$ ml/min, (C) $Q_L = 60$ (ml/min), $Q_G = 36, 73, 103$ ml/min, (D) $Q_L = 80$ (ml/min), $Q_G = 36, 79, 103$ ml/min.

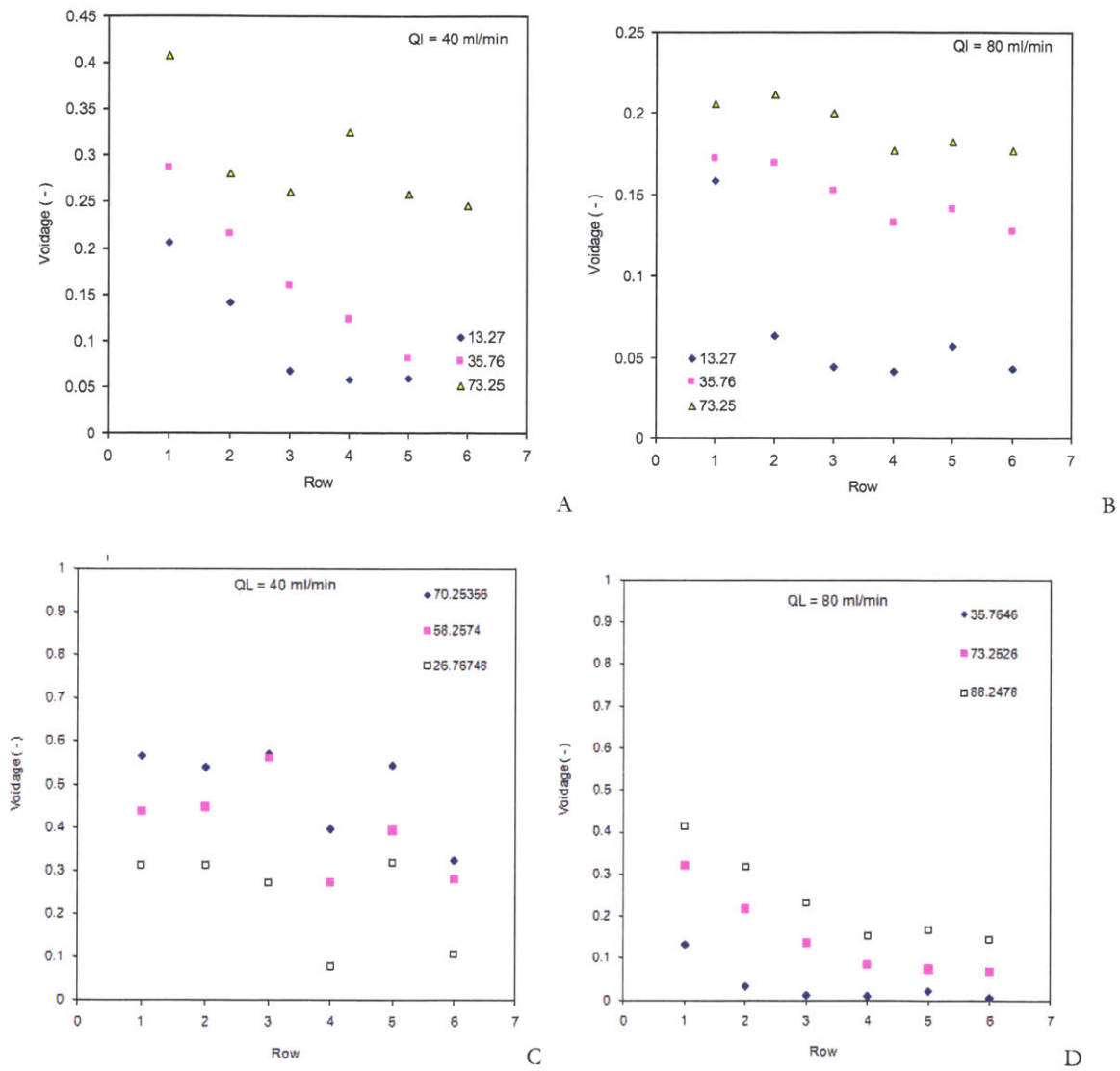


Figure A.3: Change in the fractional gas holdup along the length of the AFR for (A-B) Vertical orientation of module, (C-D) horizontal orientation of module.

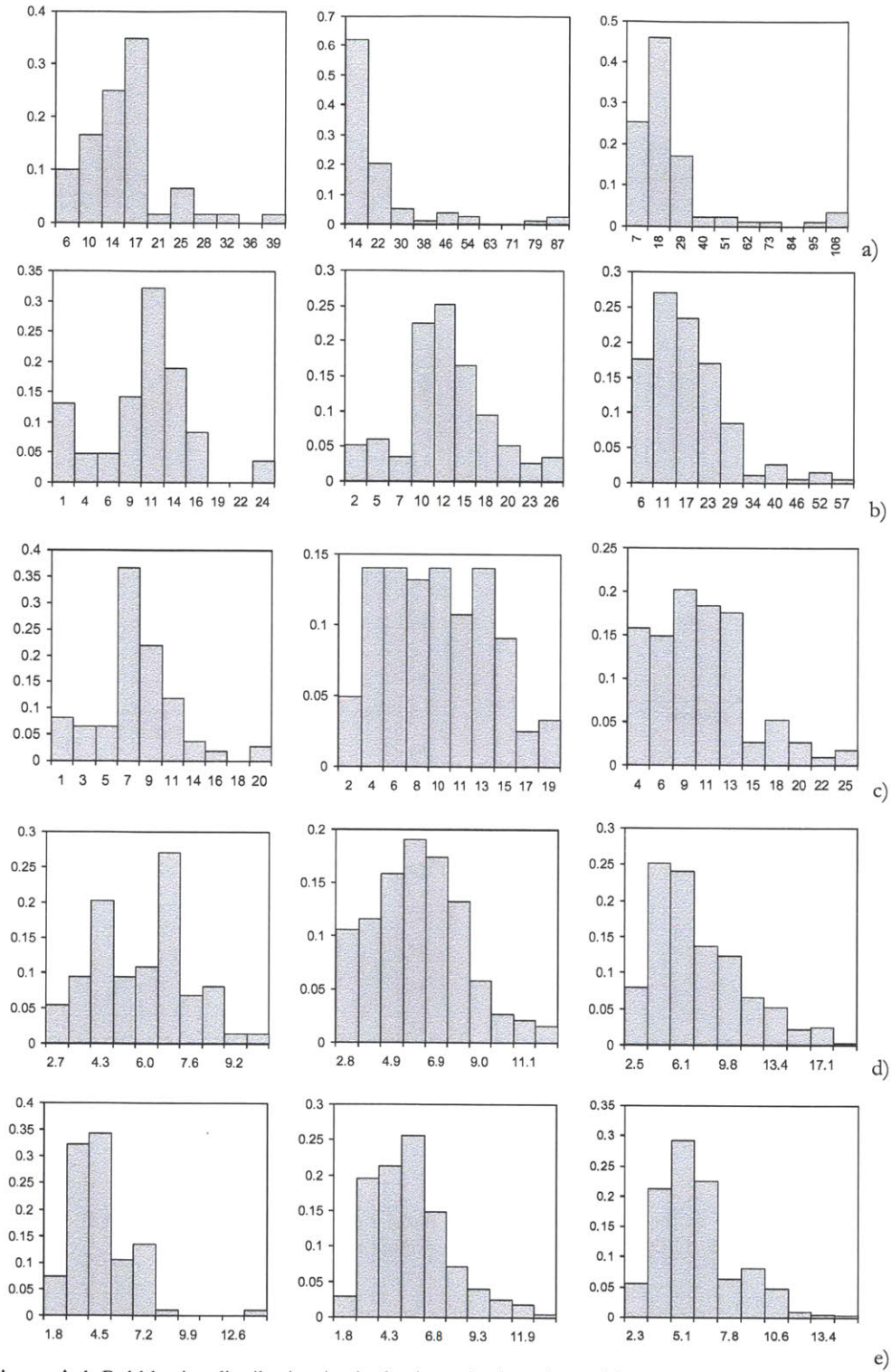


Figure A.4: Bubble size distribution in the horizontal orientation of the AFR. (a) $Q_L = 10$ ml/min, $Q_G = 6, 13, 36$ ml/min, (b) $Q_L = 20$ ml/min, $Q_G = 13, 36, 73$ ml/min, (c) $Q_L = 40$ ml/min, $Q_G = 27, 58, 70$ ml/min, (d) $Q_L = 60$ ml/min, $Q_G = 24, 36, 78$ ml/min, (e) $Q_L = 80$ ml/min, $Q_G = 36, 73, 88$ ml/min.

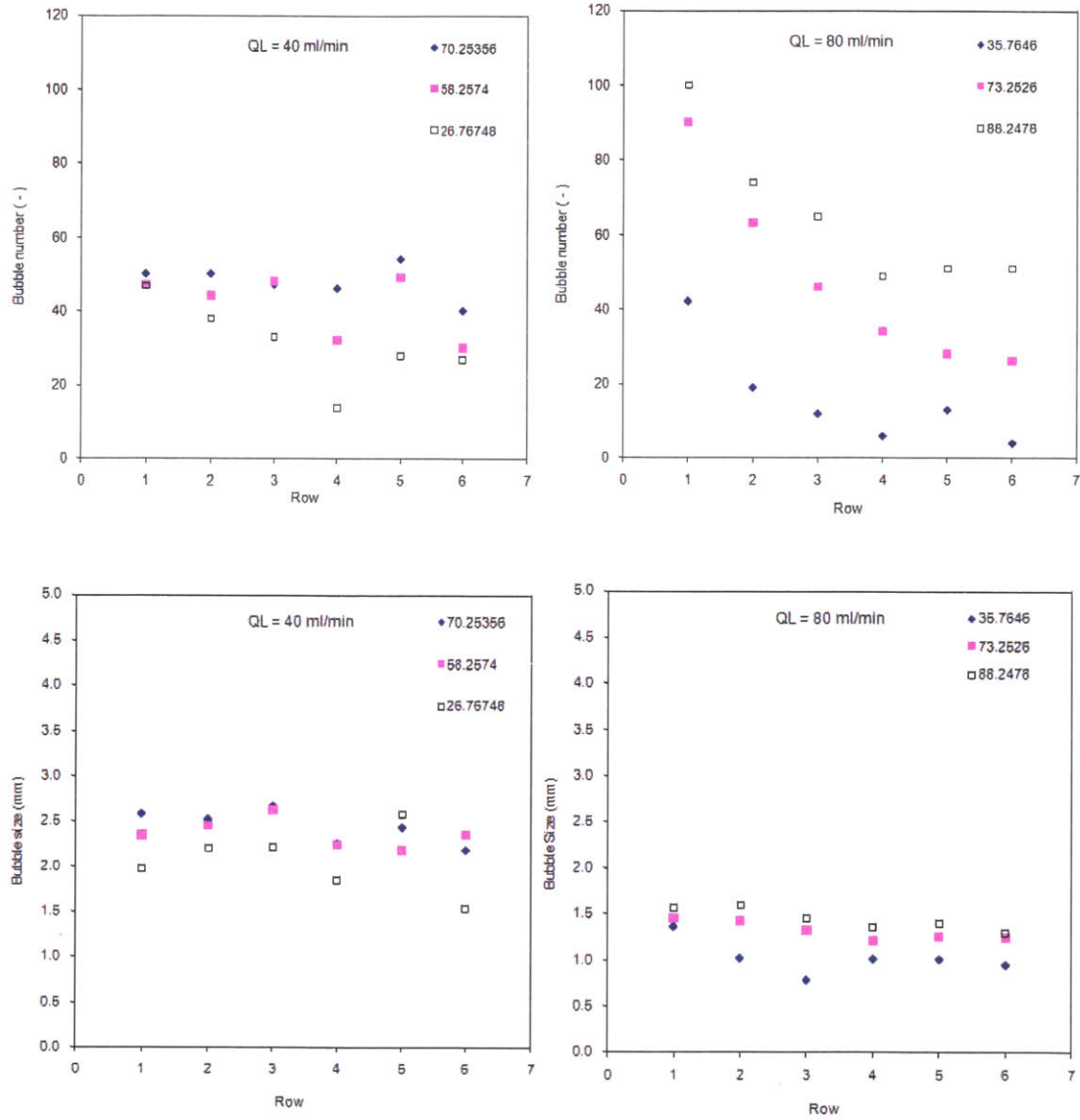


Figure A.5: Variation in the bubble number and bubble size along the length of the AFR in horizontal orientation

Table A.1.1: Reproducibility of measurements. Case a) Single bubble. The perimeter of a single bubble was measured using the software ImageJ three times, the diameter was then calculated from the perimeter, and a confidence interval of 99.5 % using a t_{student} of 9.9925

Measurement	Bubble size (mm)	Average bubble size (mm)	Standard deviation (mm)	Confidence interval (99.5%)
1	1.300			
2	1.400	1.333	0.047	0.27
3	1.300			

Table A.1.2: Reproducibility of measurements. Case b) Single heart cell. Three measurements of all bubbles encountered within one heart cell for a single experiment was performed and a confidence interval of 99.5 % probability for a t_{student} of 9.925 was then calculated. The uncertainty in the experimental measurement of bubble size is taken into account in the error associated in calculation of gas holdup, specific interfacial area, and mass transfer coefficients.

Measurement	Average bubble size in heart (mm)	Average bubble size (mm)	Standard deviation (mm)	Confidence interval (99.5%)
1	1.258			
2	1.300	1.325	0.067	0.38
3	1.427			

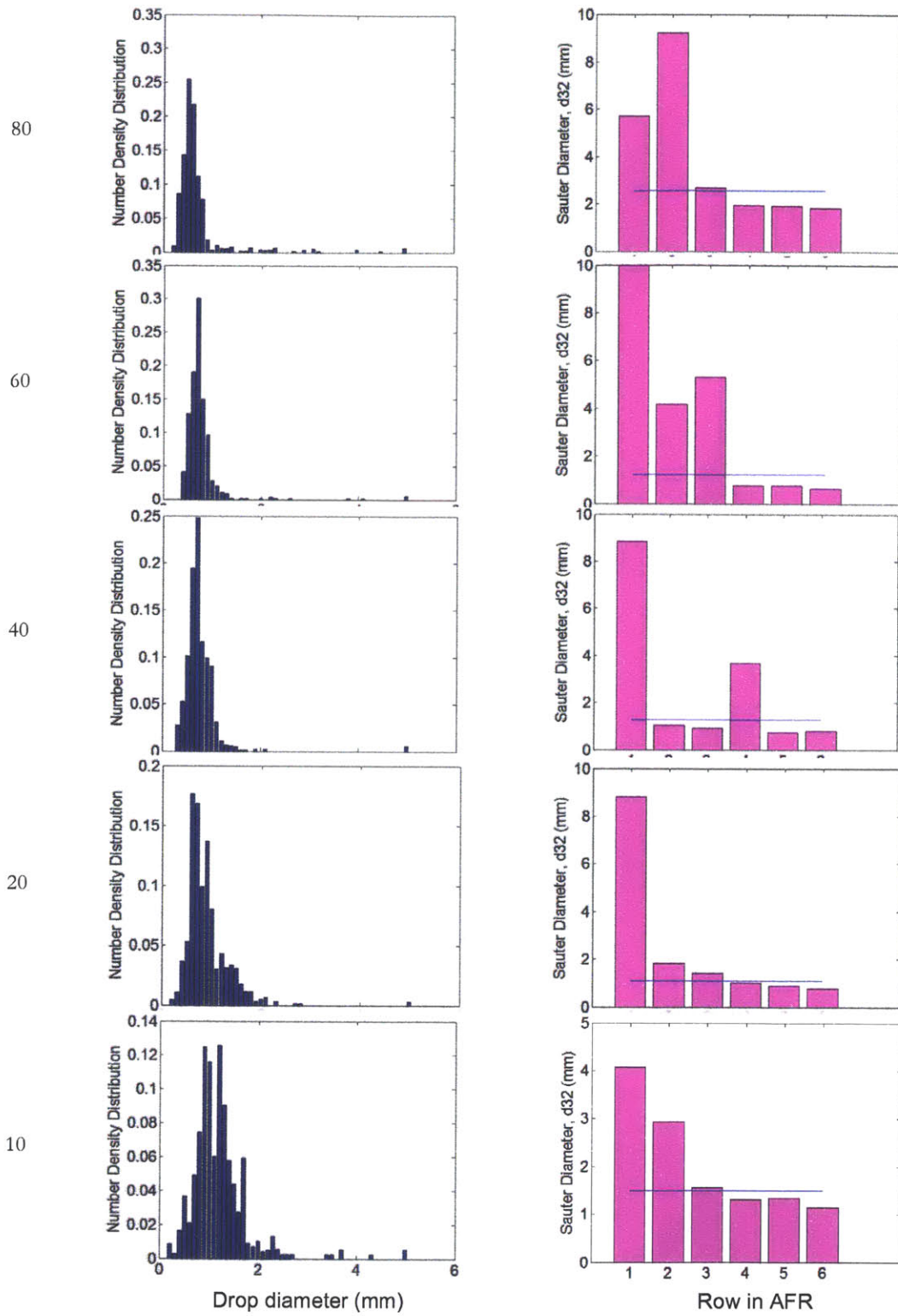


Figure A.6.1: Drop size distribution for hexane/water system in AFR. $Q_w = 10, Q_h = 10, 20, 40, 60, 80$ mL/min.

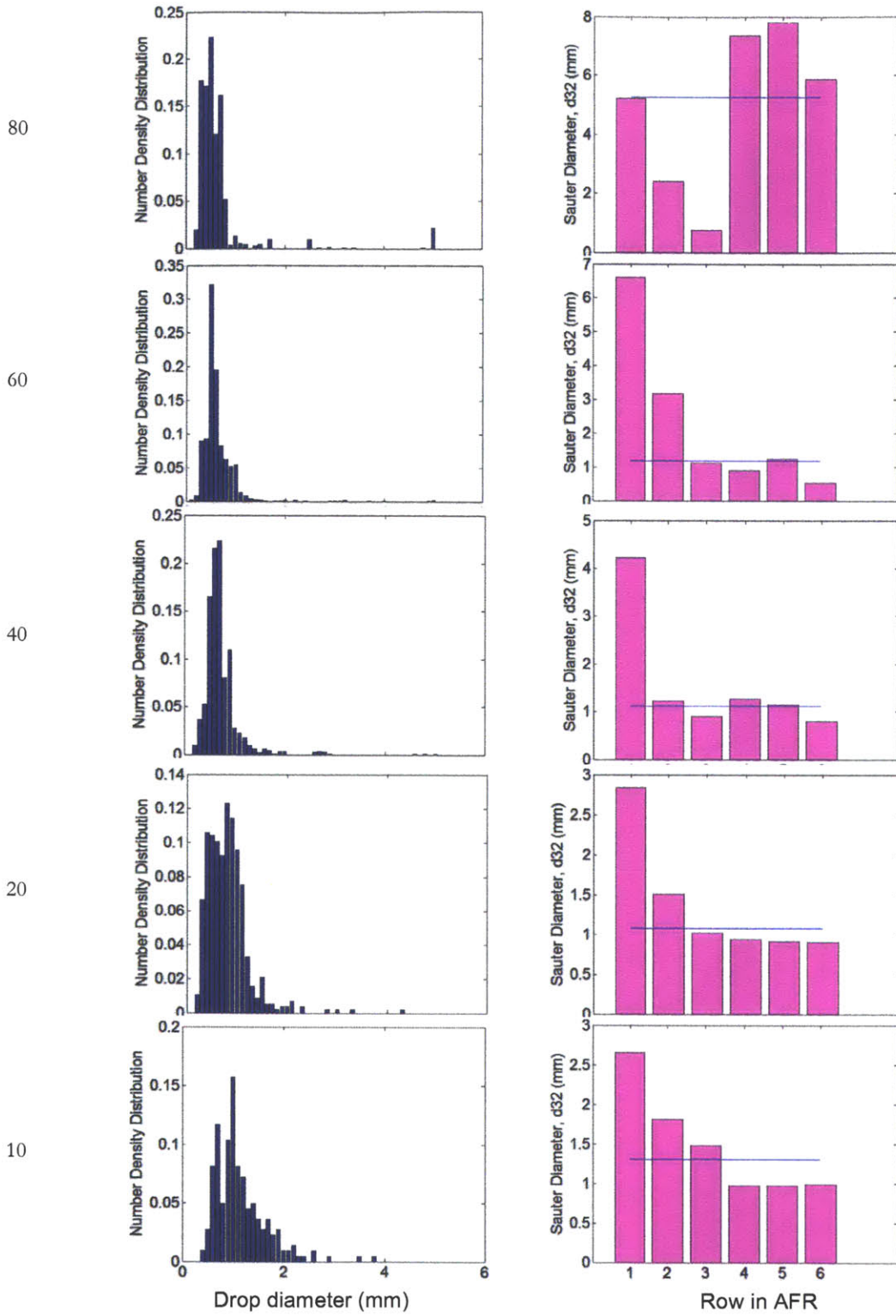


Figure A.6.2: Drop size distribution for hexane/water system in AFR. $Q_w = 20$, $Q_h = 10, 20, 40, 60, 80$ mL/min.

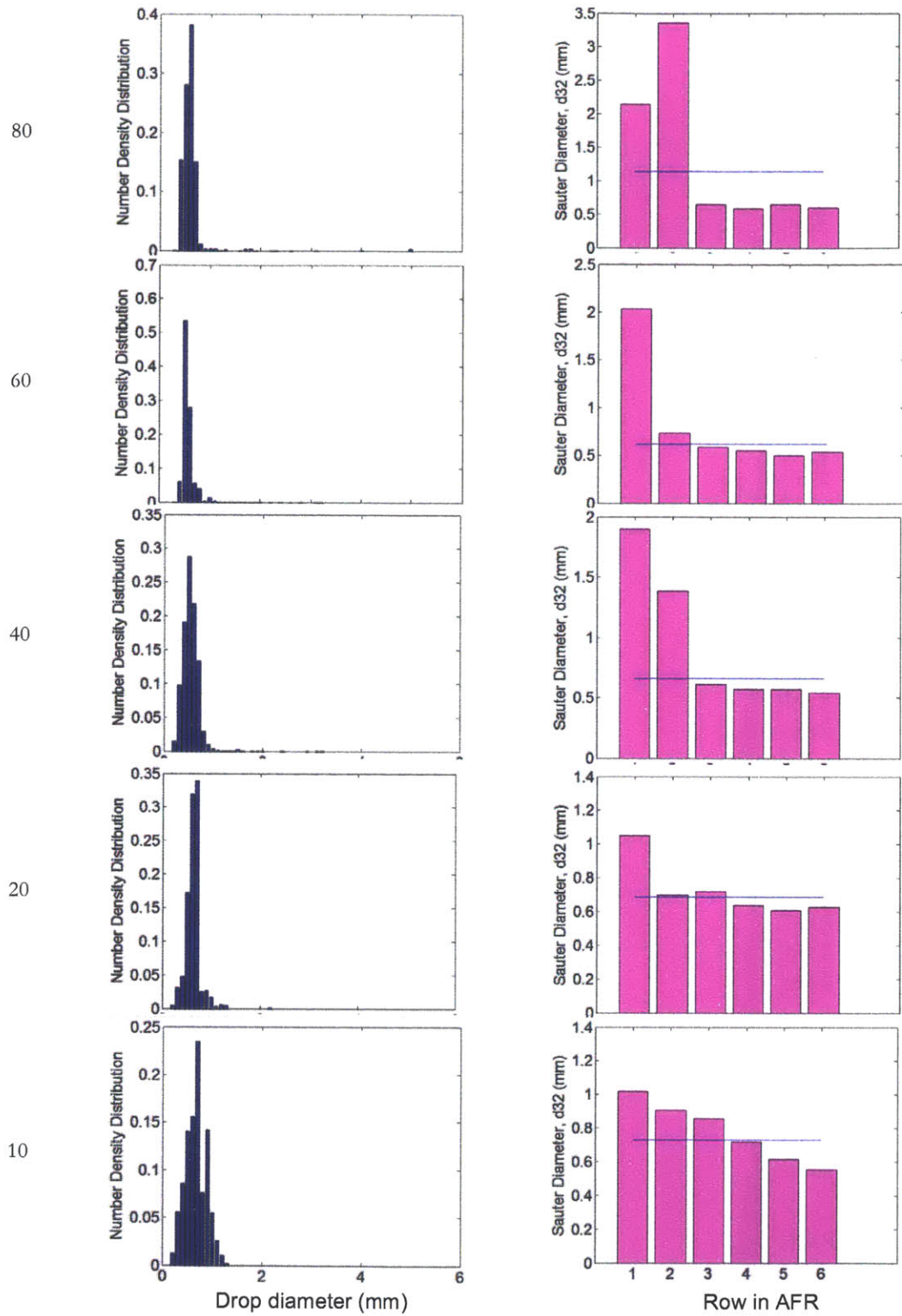


Figure A.6.3: Drop size distribution for hexane/water system in AFR. $Q_w = 40, Q_h = 10, 20, 40, 60, 80$ mL/min.

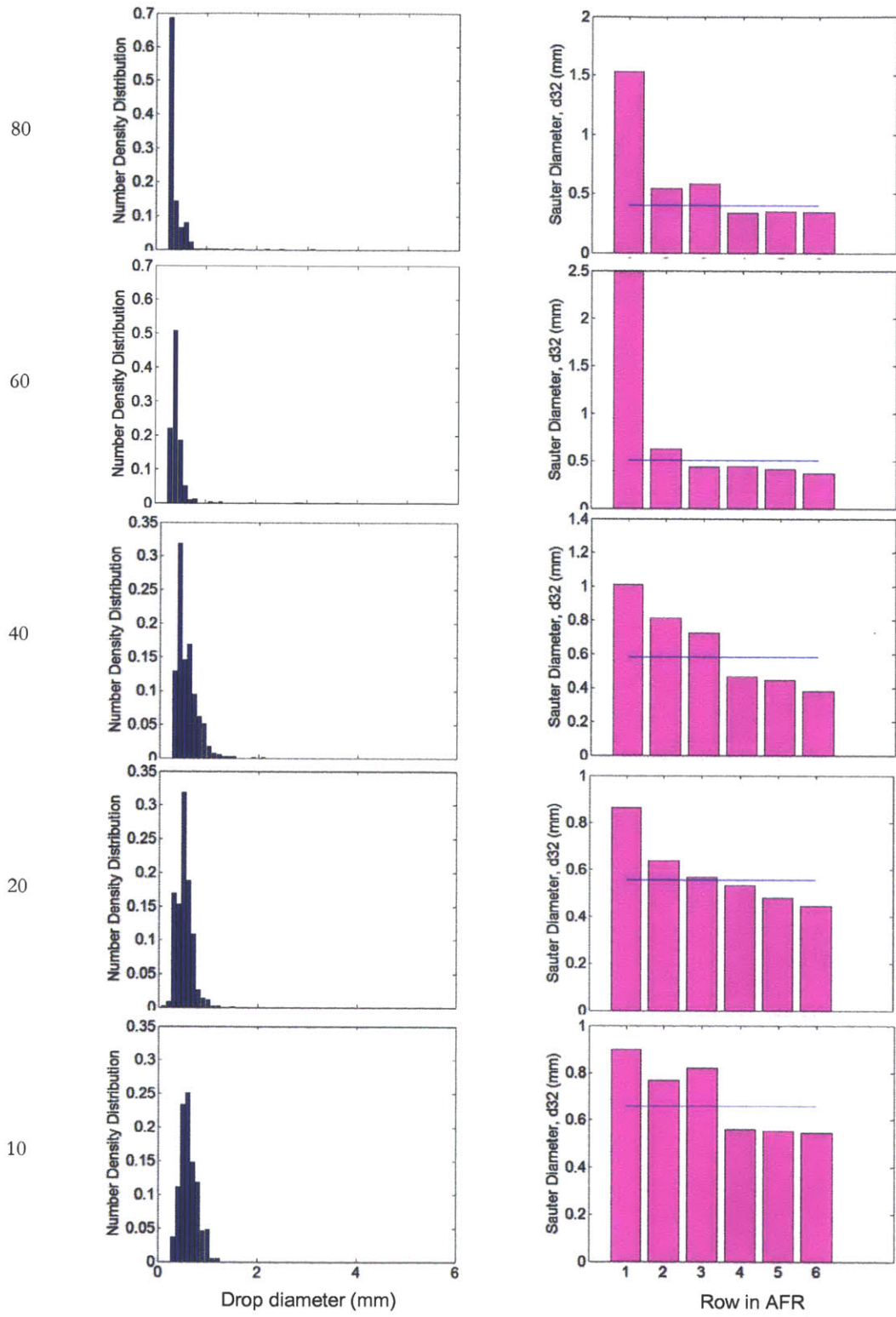


Figure A.6.4: Drop size distribution for hexane/water system in AFR. $Q_w = 60$, $Q_h = 10, 20, 40, 60, 80$ mL/min.

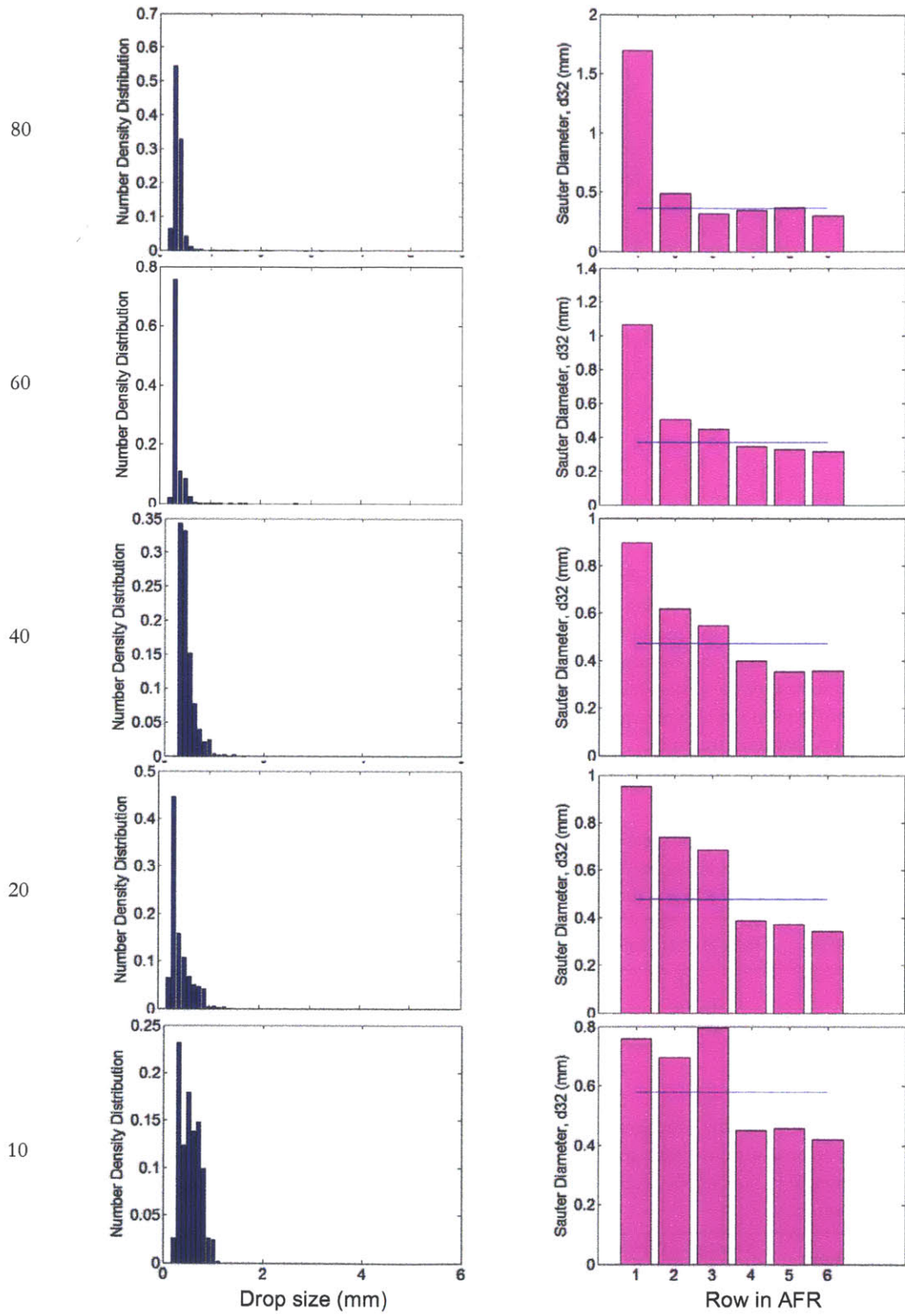


Figure A.6.5: Drop size distribution for hexane/water system in AFR. $Q_w = 80$, $Q_h = 10, 20, 40, 60, 80$ mL/min.

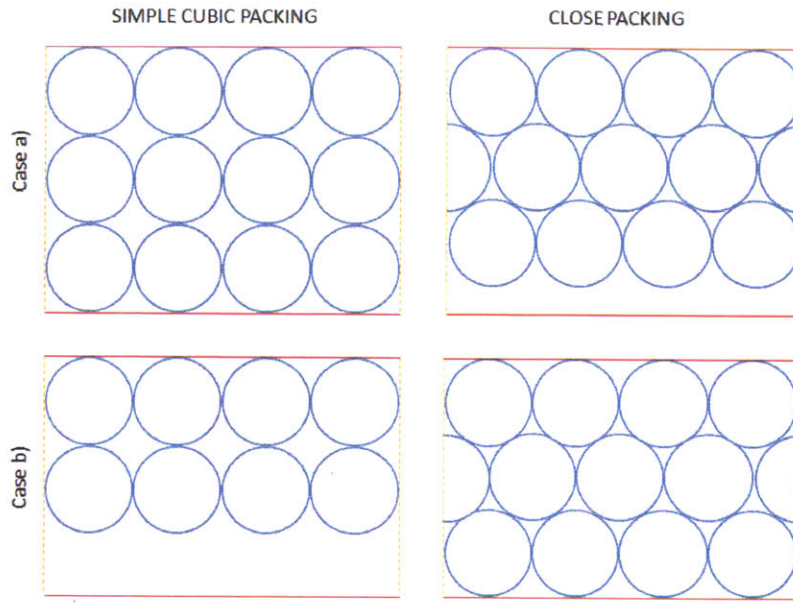


Figure A.7: Hold-up Estimation: Packing Structures in the AFR. There are two main packing structures considered here: simple cubic packing (left) and close packing (right). Besides, depending on the relative size of the drops with respect to the height of the channel, case a) and case b) can be encountered. Neglecting the effects along the width of the channel (i.e. in the X-axis), and focusing on the end effects on the height (it is observed that in case b) the close-packing is able to hold a larger number of drops for one of the contemplated cases (ratio of drops in simple cubic packing / close packing = 0.67), whereas in case a) there is no difference between the two packing structures.

Table A.2.1: Reproducibility of measurements. Case a) Single drop. Three measurements of the size a single drop were conducted by drawing the contour using the software ImageJ. A confidence interval (CI) of 99.5% probability for a t_{student} of 9.925 was then calculated.

Measurement	Drop Size (mm)	Average (mm)	Standard Deviation (mm)	Confidence Interval (99.5%)
1	1.328	1.303	0.023	0.042
2	1.294			
3	1.285			

Table A.2.2: Reproducibility of measurements. Case a) Single heart cell. Three measurements of the size of all droplets encountered within a heart cell were conducted by drawing the contour using the software ImageJ. A confidence interval (CI) of 99.5% probability for a t_{student} of 9.925 was then calculated based on the average and standard deviation.

Measurement	Average in heart drop size (mm)	Average drop size (mm)	Standard deviation (mm)	Confidence interval (99.5%)
1	0.815	0.82	0.0072	0.13
2	0.816			
3	0.828			

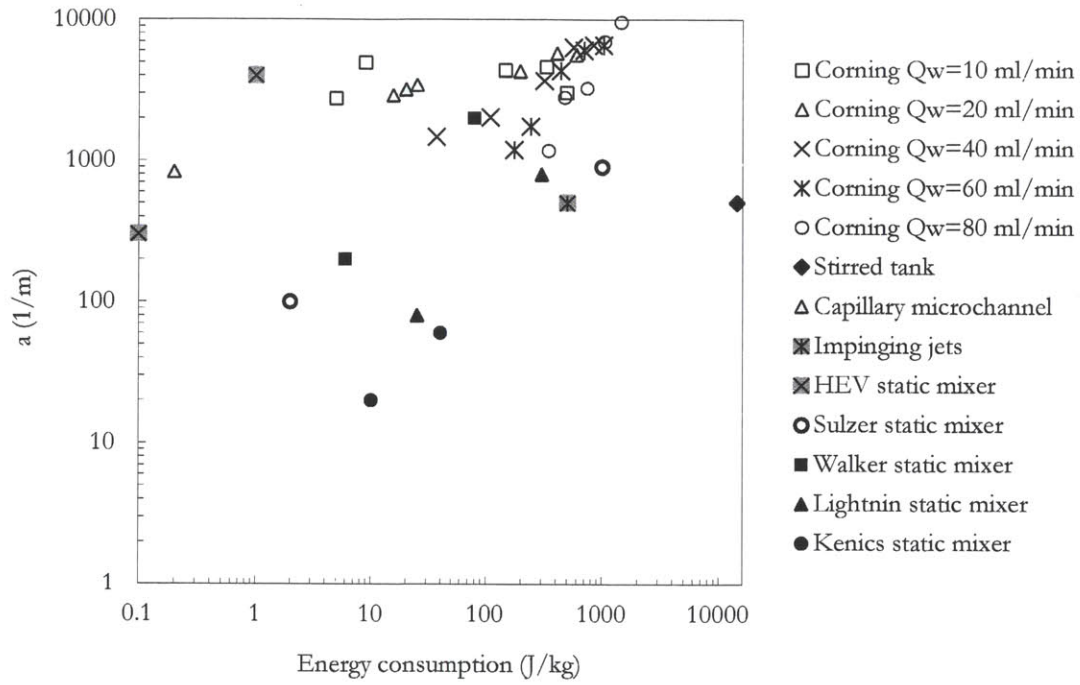


Figure A.8: Comparison of effective interfacial area (m^2/m^3) vs. power consumption for different liquid-liquid contactors.

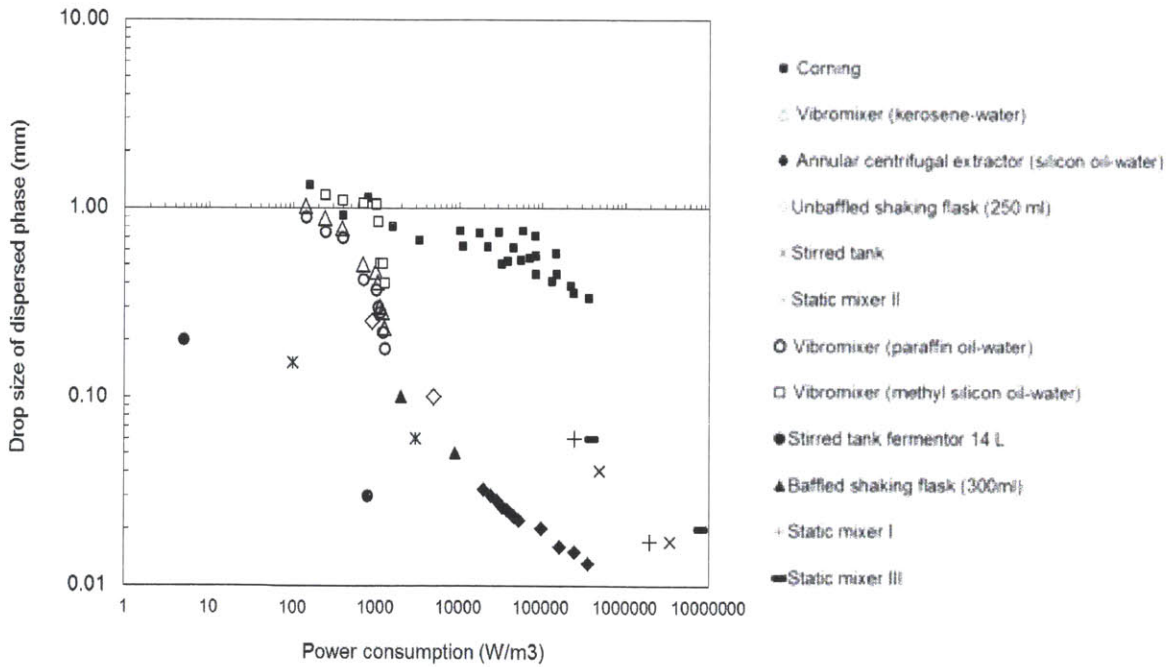


Figure A.9: Drop size of dispersed phase versus power consumption for different liquid-liquid contactors.

CFD single-phase simulations

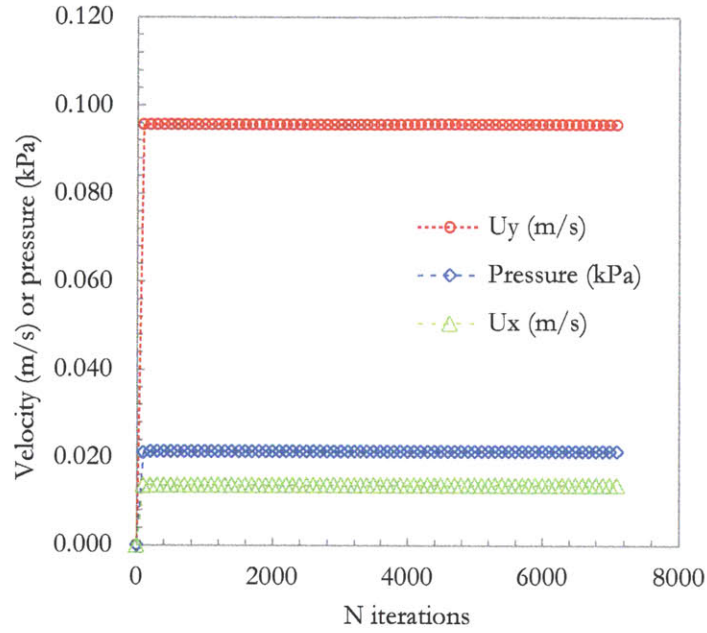


Figure A.10: Evolution of pressure and velocity components at fixed location (center of inlet of heart cell) with number of iterations for 2D unstructured mesh. Velocity (U_x , U_y), and pressure values remain constant after a few iterations.

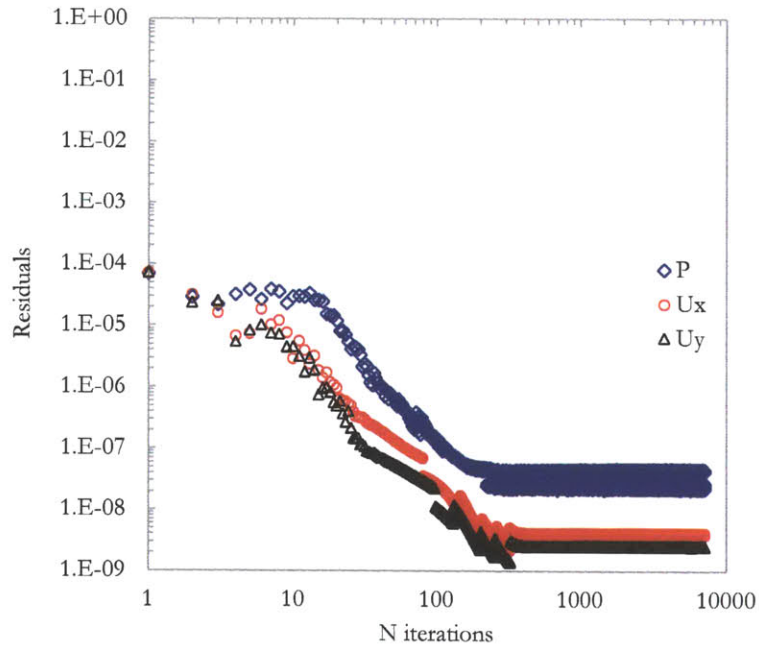


Figure A.11: Residuals for velocity and pressure evolution with number of iterations for 2D unstructured mesh.

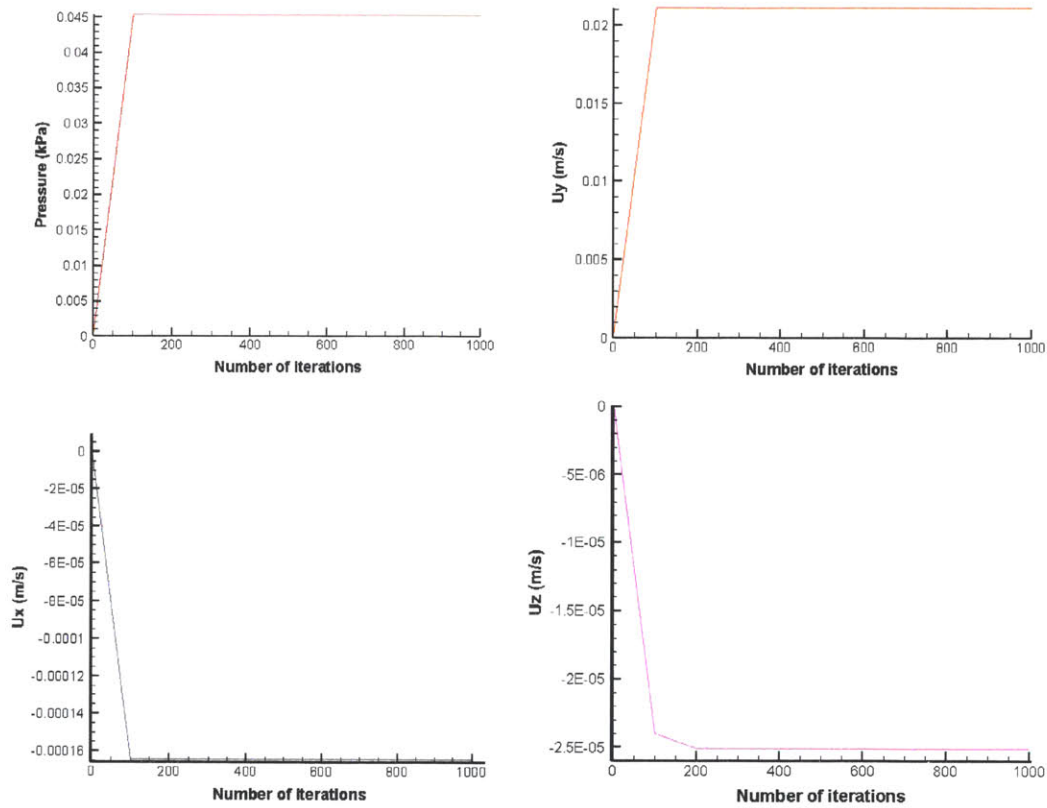


Figure A.12: Evolution of pressure (kPa) and velocity components at a fixed location with number of iterations in 3D unstructured mesh.

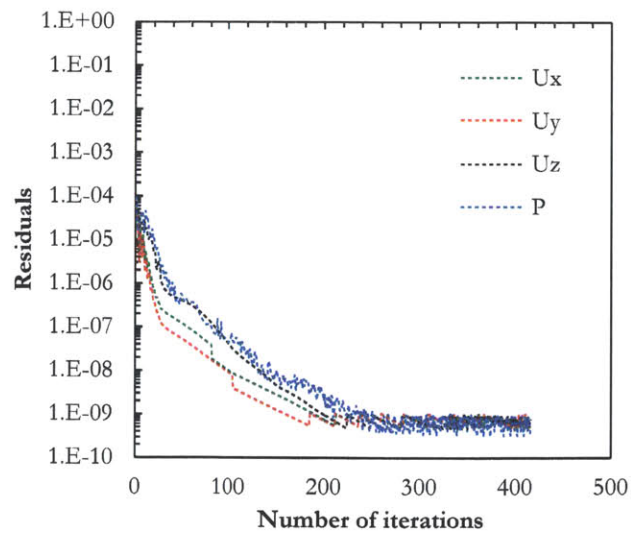


Figure A.13: Evolution of residuals for pressure and velocity components with number of iterations in 3D unstructured mesh.

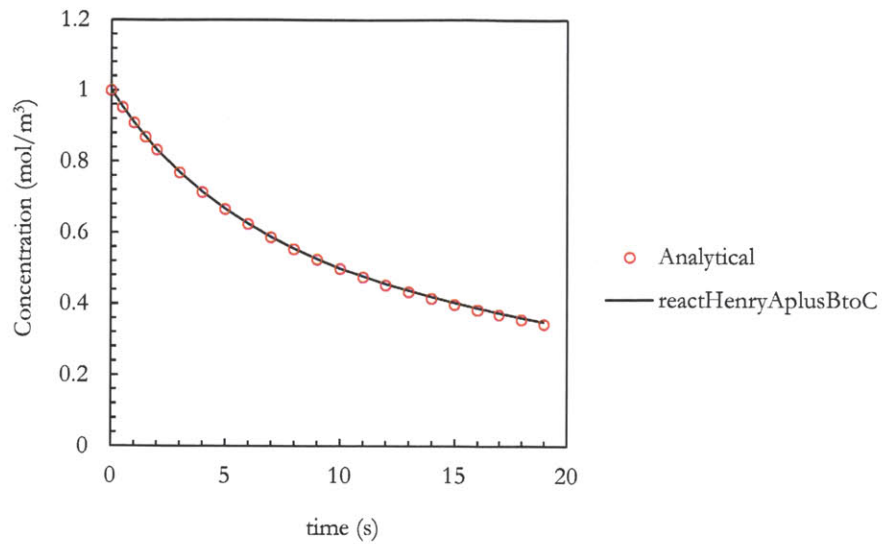


Figure A.14: Validation of modified interFoam solver based on two-phase scalarTransportFoam for a irreversible reaction $A + B \rightarrow C$ and Henry constant = 1.

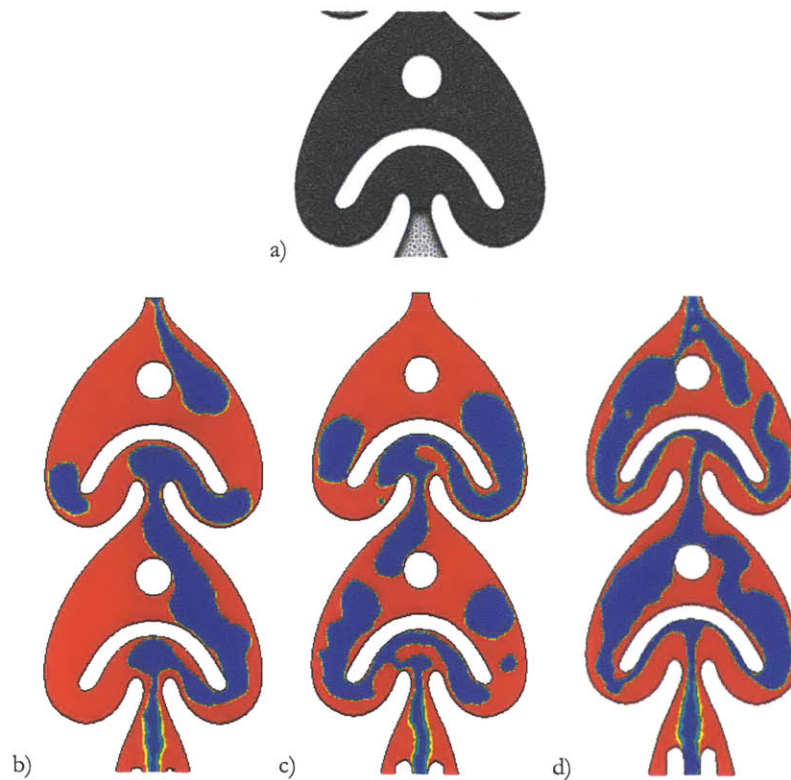


Figure A.15: Hexane/water two-phase flow simulated with interFoam using a 2D unstructured mesh, and turbulent flow model: a) detail of mesh; b) $Q_w = 10$; $Q_h = 10$; c) $Q_w = 20$; $Q_h = 20$; d) $Q_w = 40$; $Q_h = 40$. Irregularities are seen in the interface prediction as opposed to structured mesh.

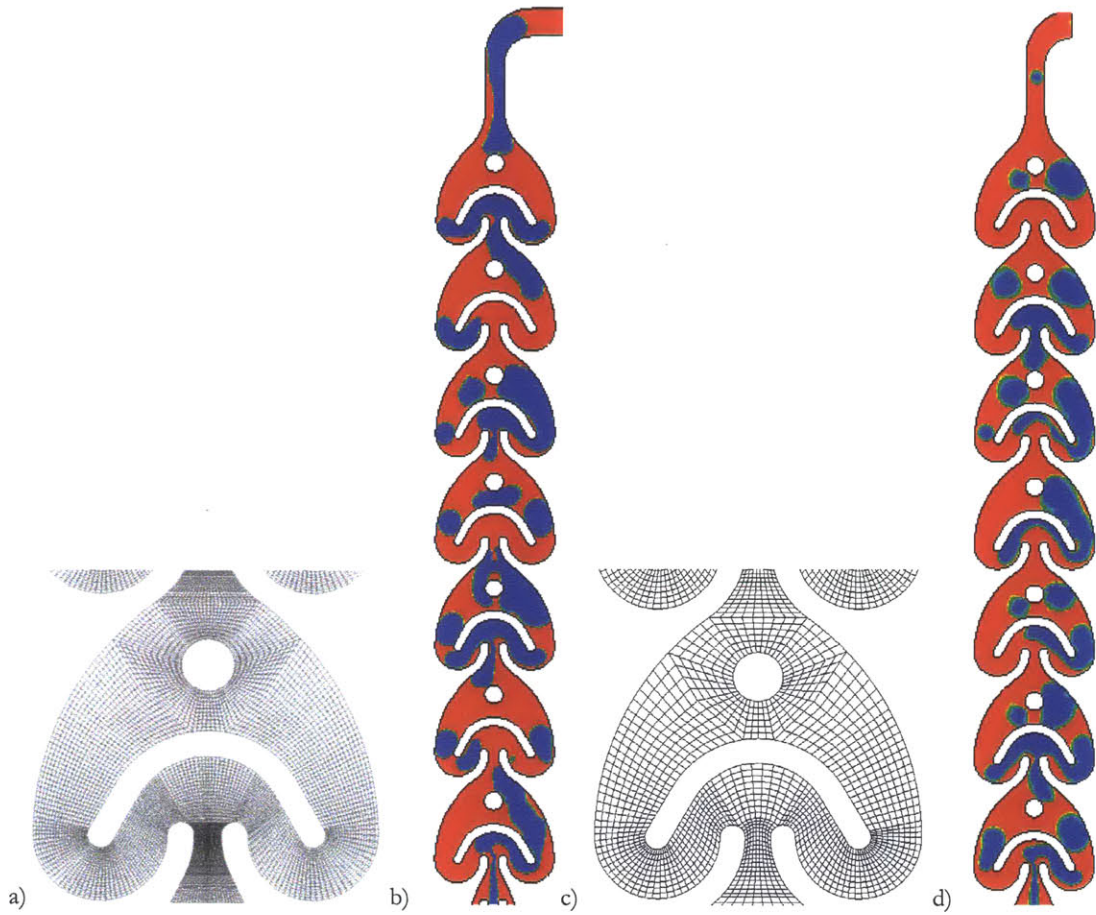


Figure A.16: Simulation of hexane/water with interFoam using a 2D structured mesh: a) detail fine structured mesh ; b) Simulation results for fine mesh in first row of AFR at 10 ml/min water and 10 ml/min hexane, time = 2.23 s; c) detail of 2D structured coarse mesh; d) Simulation results for coarse mesh in first row at 10 ml/min water and 10 ml/min hexane, time = 2.23 s;

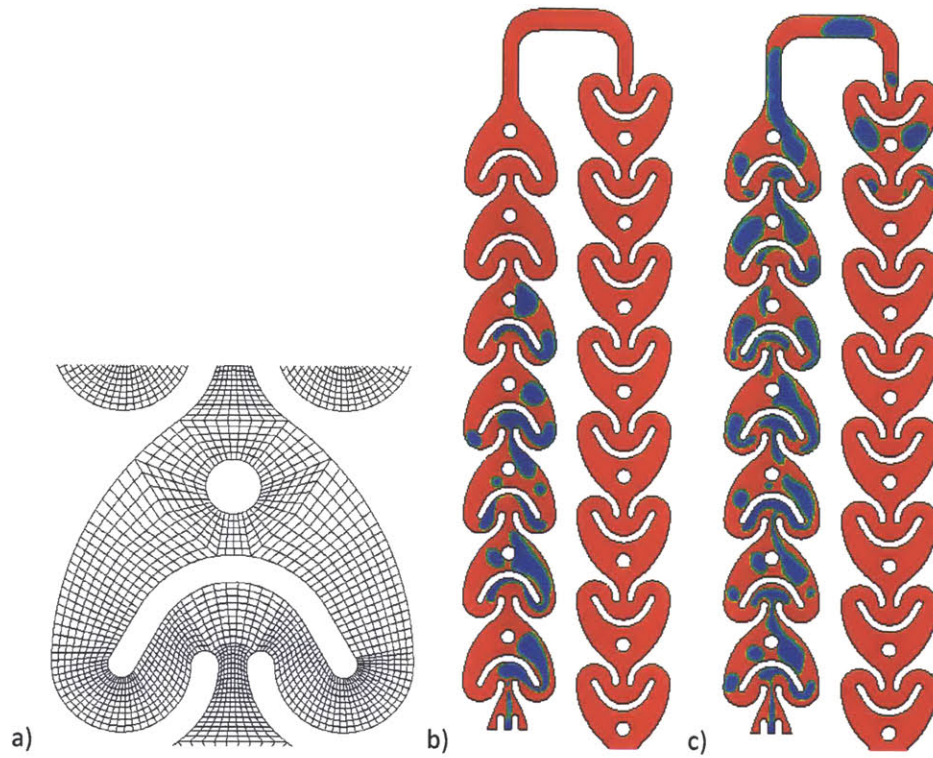


Figure A.17: Simulation of hexane/water flow using interfoam in AFR for a 3D mesh: a) detail of 3D structured mesh; b) transient simulation at time = 1.1 seconds for 10 mL/min of water and hexane flow rates; c) transient simulation at time = 1.215 seconds for 20 mL/min of water and hexane flow rates